UNIVERSITÀ
DEGLI STUDI
DI PADOVA

Università degli Studi di Padova

Dipartimento di Fisica e Astronomia "Galileo Galilei"

SCUOLA DI DOTTORATO DI RICERCA IN : Fisica
CICLO XXVII

Study of shape evolution in the neutron-rich osmium isotopes with the advanced gamma-tracking array AGATA

Direttore della Scuola : Ch.mo Prof. Andrea Vitturi
Supervisori : Dott. Daniele Mengoni
Ch.mo Prof. Santo Lunardi
Dott. José Javier Valiente Dobón

Dottorando : Philipp Rudolf John

Manchmal muss man eben Leergut zahlen.
– *Hannes Holzmann*

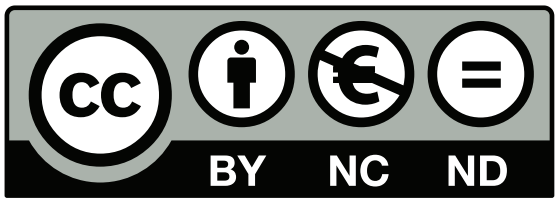

Abstract

This thesis describes the major results of a γ-ray spectroscopy experiment aiming at the investigation of the shape evolution in the neutron-rich even-even osmium isotopes. The first in-beam γ-ray spectroscopy measurement of ^{196}Os has been performed and the results are compared to state-of-the-art beyond mean-field calculations, that have revealed its presumably γ-soft character.

Finite many-body systems, such as molecules, many man-made nano materials and atomic nuclei can be understood as a drop of viscous liquids confined by an elastic membrane, where its equilibrium shape (ground state) has a unique feature: the existence of deformed (non-spherical) shapes. Non-spherical shapes represent spontaneous symmetry breaking. However, the shape of the nucleus is not a direct observable. By comparing its low-lying excited states to predictions of nuclear models, the shape of the nucleus can anyway be deduced, as it will be shown in this work. Nuclear deformation is caused by the subtle interplay between single-particle and collective degrees-of-freedom. Hence, studies of nuclear deformation open a window on the underlying NN interaction and its role in the microscopic origin of deformation. In particular, regions of the nuclear chart where oblate deformation is observed are of special interest due the paucity of oblate deformed nuclei in nature.

For the neutron-rich osmium isotopes, a shape transition from prolate to oblate deformation with increasing neutron number is predicted. Experimentally, the yrast band of ^{194}Os was interpreted to be prolate (rugby-ball) deformed, instead the low-lying excitations of ^{198}Os were suggested to be characteristic of an oblate (pumpkin) shape. The even-even nucleus in between, ^{196}Os, was investigated in the eighties and two excited levels were proposed. The uncertainties in the energy and in the spin assignment of the 2$^{\text{nd}}$ level prevented a clear comparison with nuclear models. With the current stable beam and target combinations the exotic nucleus ^{196}Os can not be populated in fusion-evaporation reactions. It is reachable via fragmentation reactions or multi-nucleon transfer reactions. ^{196}Os was produced via fragmentation reactions in the large-scale radioactive ion beam facility GSI, Germany. However, in the isomeric decay spectroscopy no γ-rays were observed. Multi-nucleon transfer reactions are complementary to fragmentation reactions and were performed using the most powerful γ-detector array, *Gammasphere*, in Lawrence Berkeley

and Argonne National laboratories, USA. However, the experiment setup was not sensitive enough to identify ^{196}Os among the reaction products.

In order to study the structure of ^{196}Os by means of γ-ray spectroscopy, a multi-nucleon transfer experiment was performed at the Laboratori Nazionali di Legnaro (Italy) using the new-generation Advanced Gamma Tracking Array (*AGATA*) demonstrator in coincidence with the magnetic spectrometer *PRISMA* using a ^{82}Se beam with an energy of 426 MeV on a ^{198}Pt target. The very selective binary partner method was applied, i.e. the lighter beam-like recoil was identified in the magnetic spectrometer and the γ rays of the corresponding heavier target-like recoil were detected in coincidence with it. The *AGATA* demonstrator is a γ-tracking array which relies on Pulse Shape Analysis (PSA) for the identification of the interaction points of the γ ray, which is crucial for the reconstruction of its interaction path through the detector. Being one of the first experiments performed with the *AGATA*+ *PRISMA* setup, the procedure for presorting, calibration and analysis of the data will be reported in detail.

The information of the target-like recoil (such as ^{196}Os) is reconstructed via the reaction kinematics. Due to the evaporation of neutrons a tight gate on the reconstructed Q value has to be applied in order to select the true binary partner. In the γ-ray spectrum in coincidence with ^{196}Os, three γ rays are identified (324.4 keV, 467.0 keV and 639.2 keV) that are assigned to originate from the decay of the three lowest-lying $2^+, 4^+$ and 6^+ states. The $E(4_1^+)/E(2_1^+)$ ratio extracted from the new data is 2.44, deviating less than 3% from the expectation value of a γ-soft/triaxial rotor (2.5).

The new excited states of ^{196}Os are compared, as well as the known levels in the even-even osmium isotopes $^{188-198}$Os, to state-of-the-art beyond mean field (BMF) calculations. The quality of the results allows a detailed analysis of the shape evolution from a predominantly prolate rotational in ^{188}Os to a more vibrational one in ^{198}Os. The new experimental data obtained for ^{196}Os, reveals an almost perfect γ-soft/triaxial rotor yrast-band, which is in perfect agreement with the calculations.

A great variety of nuclei were produced in the ^{82}Se + ^{198}Pt reaction. For example, the yrast band of ^{200}Pt is extended to higher spin and the shape evolution of the even-even platinum isotopes $^{190-200}$Pt is compared to calculations based on the same nuclear model. The shape evolution through the platinum isotopes is less rapid than the one of the osmium isotopes, with a potential which remains γ-soft for all these nuclei. In particular, the yrast band of ^{200}Pt has the most vibrational character among the investigated isotopes. For the beam like isotopes new data were also obtained and the yrast band of the even-even zinc isotopes $^{72-76}$Zn, populated in the 4 proton transfer channel, is reported.

Previous to the *AGATA* spectrometer, large-scale γ-ray arrays have collimators and anti-Compton shields, in order to reach a good peak-to-total ratio. The conceptual design of the *AGATA* is substantially different and no such passive material exists in the setup. Hence, the sensitivity for the measurement of the decay of isomeric states belonging to the target-like recoils implanted in the target chamber or in the *DANTE* array, is higher than that of traditional γ-ray arrays. Through the measurement of the beam-like recoils in the *PRISMA* spectrometer it is possible to observe in coincidence the γ-rays belonging to the implanted binary partner and to discover new isomeric states. In this thesis the first lifetime measurement of isomeric states with *AGATA* will be reported. In total 44 isomeric states are identified, including 3 previously unknown.

Riassunto

In questa tesi vengono presentati i risultati principali di un moderno esperimento di spettroscopia γ che aveva come scopo lo studio della evoluzione della forma dei nuclei pari-pari, ricchi di neutroni, di osmio. In particolare, si sono ottenuti i primi dati in assoluto sugli stati eccitati del nucleo ^{196}Os tramite lo studio della radiazione γ emessa. Dal confronto dei dati sperimentali con i più avanzati calcoli teorici "beyond mean-field", si si è potuto concludere che il ^{196}Os può essere considerato come un paradigma di nucleo γ-soft.

In natura, i sistemi finiti a molti corpi, come ad esempio le molecole, molti nano-materiali prodotti artificialmente e i nuclei atomici, presentano un comportamento che può essere descritto come una goccia di liquido viscoso confinata da una membrana elastica, dove la forma all'equilibrio (stato fondamentale) presenta una caratteristica unica: può essere deformata (non sferica) e rappresenta quindi una rottura spontanea di simmetria. In fisica nucleare, la forma di un nucleo non è un'osservabile diretta. È possibile tuttavia dedurre la forma di un nucleo da un confronto tra le energie di eccitazione dei primi stati eccitati con le previsioni dei modelli nucleari, e questo verrà illustrato nel presente lavoro di tesi. La deformazione in un nucleo è il risultato di un sottile gioco tra i gradi di libertà di particella singola e quelli collettivi del nucleo. Di conseguenza, lo studio della deformazione nucleare è importante non solo per indagare il comportamento della sottostante interazione nucleone-nucleone (NN), ma anche per meglio comprendere il ruolo di questa interazione nell'origine microscopica della deformazione stessa. Per questo tipo di studi, sono di particolare interesse le regioni della carta dei nuclidi dove si sono osservati nuclei con deformazione oblata, visto che in natura sono molto pochi, esendp la maggior parte con deformazione prolata.

Negli isotopi di osmio ricchi di neutroni è prevista una transizione di forma con l'aumentare del numero di neutroni, da una forma prolata (es. palla da rugby) per quelli meno ricchi di neutroni ad una forma oblata (es. zucca) per quelli più ricchi. In accordo con la teoria, gli stati yrast del ^{194}Os misurati sperimentalmente sono stati interpretati mediante una deformazione prolata, mentre quelli del ^{198}Os indicano che il nucleo ha una forma oblata. Il nucleo pari-pari ^{196}Os, che è situato proprio a metà tra i due nuclei appena citati, è stato studiato negli anni ottanta e ne sono stati proposti due livelli eccitati a bassa energia. Purtroppo, l'incertezza sulla posizione del secondo livello eccitato e sull'assegnazione del suo spin non ha permesso un confronto corretto con i modelli nucleari.

Il nucleo ^{196}Os non può essere popolato in una reazione di fusione-evaporazione che utilizzi una combinazione di fascio e di bersaglio presenti in natura e per questo è stato molto difficile studiarlo. Può però essere prodotto in reazioni di frammentazione o in reazioni di trasferimento di molti nucleoni. Il ^{196}Os è stato tra i prodotti di reazione di un esperimento di frammentazione effettuato nel laboratorio GSI in Germania, ma non è stato possibile osservare nessun raggio γ associato ad esso. Reazioni di trasferimento di molti nucleoni, complementari con quelle di frammentazione, sono state effettuate nei laboratori di Berkeley e Argonne in USA utilizzando *Gammasphere*, il più potente rivelatore di raggi γ disponible. Anche in questo caso però non è stata raggiunta la sensibilità sufficiente per identificare il ^{196}Os tra i prodotti della reazione.

Per studiare la struttura del nucleo ^{196}Os è stata utilizzata nel nostro caso una reazione di trasferimento di molti nucleoni bombardando un bersaglio di ^{198}Pt con un fascio di ^{82}Se ad una energia di 426 MeV. L'esperimento, effettuato presso i Laboratori Nazionali di Legnaro, ha fatto uso di un rivelatore al germanio di nuova generazione, l'Advanced Gamma Tracking Array (*AGATA*), in coincidenza con lo spettrometro magnetico *PRISMA*. Per identificare i prodotti pesanti delle reazione binarie di trasferimento è stato applicato un nuovo metodo molto selettivo: lo ione "beam-like" viene identificato con precisione dallo spettrometro magnetico PRISMA e si osservano in coincidenza con esso i raggi γ del nucleo più pesante associato. Il dimostratore di *AGATA* è un insieme di rivelatori al germanio elettricamente segmentati che si basa su un algoritmo di Pulse Shape Analysis (PSA) per individuare i punti di interazione di un raggio γ all'interno del rivelatore permettendo di ricostruirne quindi la sua traiettoria di interazioni nel rivelatore. Essendo stato questo uno dei primi esperimenti eseguiti con il dimostratore di *AGATA* associato a *PRISMA*, le procedure per il presorting dei dati, per la loro calibrazione e analisi verranno presentate in dettaglio.

L'informazione sullo ione più pesante (target-like), come il ^{196}Os, viene ottenuta partendo dalla cinematica della reazione. A causa però dell'evaporazione di neutroni, deve essere applicata una selezione molto restrittiva sul Q-valore ricostruito del processo binario in modo da selezionare in modo corretto lo specifico partner. Nello spettro γ in coincidenza con il ^{196}Os sono state osservate tre transizioni di energia 324,4 keV, 467,0 keV e 639,2 keV che sono state assegnate al decadimento dei tre stati di più bassa energia $2^+, 4^+$ e 6^+ del nucleo. Da questi nuovi dati si è estratto il rapporto $\mathrm{E}(4_1^+)/\mathrm{E}(2_1^+)$ che risulta essere uguale a 2.44, un valore che devia meno del 3% dal valore teorico (2.5) di un rotore triassiale/γ-soft perfetto. Questo nuovo risultato porta quindi ad un confronto con il nucleo ^{196}Pt, l'isobaro pari-pari più vicino al ^{196}Os, che è considerato in letteratura l'esempio classico di un rotore γ-soft.

I nuovi stati eccitati del ^{196}Os assieme a quelli già conosciuti degli isotopi pari-pari $^{188-198}$Os sono stati confrontati con i più avanzati calcoli teorici disponibili al momento, detti anche "beyond mean field" (BMF). La qualità dei dati ha consentito un'analisi dettagliata dell'evoluzione della forma degli isotopi dell'osmio, che passano da un carattere prevalentemente rotazionale prolato per il ^{188}Os a un comportamento più vibrazionale per il ^{198}Os. I nuovi dati sperimentali ottenuti per il ^{196}Os rivelano, come già accennato, un comportamento quasi perfetto di rotore triassiale/γ-soft, che viene riprodotto in maniera eccellente dai calcoli teorici.

Nella reazione di trasferimento di molti nucleoni ^{82}Se + ^{198}Pt descritta in questa tesi, sono stati prodotti molti altri nuclei con numeri di massa vicini sia a quello del fascio che a quello del bersaglio. Ad esempio, è stato possibile estendere ad alto spin la banda yrast

del ^{200}Pt e si è studiata l'evoluzione di forma anche per gli isotopi pari-pari del platino $^{190-200}$Pt, confrontando anche in questo caso i risultati sperimentali con i calcoli basati sullo stesso modello applicato agli isotopi di osmio. L'evoluzione della forma negli isotopi di platino è meno rapida di quella degli isotopi dell'osmio, con un potenziale che per tutti questi nuclei ha la caratteristica di essere γ-soft. In particolare, la banda yrast di ^{200}Pt presenta un carattere più vibrazionale rispetto a tutti gli isotopi discussi in questo lavoro. Anche per i nuclei con numero di massa vicino a quello del fascio si sono ottenuti nuovi dati. In particolare, verranno presentati i risultati per gli isotopi pari-pari $^{72-76}$Zn, popolati per trasferimento di 4 protoni.

Gli spettrometri γ precedenti ad AGATA erano costituiti anche da schermi anti-Compton e relativi collimatori allo scopo di avere un buon rapporto Peak to Total (P/T). Il design concettuale di *AGATA* consiste invece nel ridurre il più possibile il materiale passivo che risulta essere del tutto assente. Questo fa si che lo spettrometro può misurare con grande efficenza il decadimento gamma di stati isomerici, appartenenti a ioni target-like impiantati nella camera di reazione o in un rivelatore di *DANTE*, a differenza degli spettrometri gamma tradizionali. Una volta identificati gli ioni beam-like nello spettrometro *PRISMA* è possibile osservare in coincidenza i raggi γ appartenenti ai partner binari impiantati e scoprire quindi nuovi stati isomerici. In questa tesi verrà presentata la prima misura di vita media di stati isomerici nel range dei ns stati effettuata con *AGATA*. Nel complesso sono stati identificati 44 isomeri, di cui 3 nuovi.

Contents

1 Introduction

The pursuit of understanding the nature around us runs like a golden thread through the history of mankind. Starting from the prominent role of animals in the spiritual world of the pre-pottery neolithic culture nearly 11000 years ago in Göbekli Tepe, Turkey [1], which led the stone age people to built megalithic pillars with a huge variety of engraved animals in the presumably first temple [2] (see picture on the right[1]), the understanding of the nature has evolved and the perception was demystified. It was a long rocky road to reach the present level of knowledge. Johann Wolfgang von Goethe described in his tragedy Faust (1808) a frustrated scientist, who studied all the available knowledge, but could not find the inmost force which binds the world in its inner parts.

Drum hab ich mich der Magie ergeben,	Wherefore, from Magic I seek assistance,
Ob mir durch Geistes Kraft und Mund	That many a secret perchance I reach
Nicht manch Geheimnis würde kund;	Through spirit-power and spirit-speech,
Daß ich nicht mehr mit saurem Schweiß	And thus the bitter task forego
Zu sagen brauche, was ich nicht weiß;	Of saying the things I do not know,
Daß ich erkenne, was die Welt	**That I may detect the inmost force**
Im Innersten zusammenhält,	**Which binds the world, and guides its course;**
Schau alle Wirkenskraft und Samen,	Its germs, productive powers explore,
Und tu nicht mehr in Worten kramen.[3]	And rummage in empty words no more! [4]

Faust signed a pact with the devil and it ended in a well known tragedy. Goethe, who died in the year 1832 was not only a writer, but also well reputed interdisciplinary scientist. Most likely, he knew the pursuit at his time of finding a world theory.

Nearly two centuries later science split up in different subdisciplines and the question of the "inmost force" is still an important topic of contemporary research in physics. The current standard model of physics contains four fundamental forces, which can describe

[1] By Zhengan [CC BY-SA 4.0 (`http://creativecommons.org/licenses/by-sa/4.0`)]

most of the known physics: gravitation, electromagnetic, strong and weak force. However, some phenomena like the matter-antimatter asymmetry, neutrino oscillations, dark matter and dark energy are currently not explained. Theorist seek for a possible unification of these forces. One might naïvely believe that the knowledge of these forces is sufficient to understand what binds the world, but already the three-body system does not allow an exact analytical solution. Obviously, analytical solutions exits for subgroups of the three-body problem and numerical approaches exists to solve the general version. By increasing the number of interacting bodies N, the number of interactions increase by N^2. In general, systems of many interacting particles, like the molecules of the ink of these letters, can in general only be solved approximately.

The mean-field theory is in most cases a powerful approximation to describe finite many-particle systems: instead of describing the system of the motion of the particles simultaneously with the many-body equation, the system is represented by the sum of the motions of a single particle at a time in the average potential, which is generated by the particles itself.

For finite many-body systems, the presence of the mean-field defines the surface of the finite many-body object, which behaves like the one of a liquid drop [5]. The surface confines the motion of the particles inside the mean field. The surface can be perceived as a membrane, which can vibrate with a frequency, defined by the surface tension. Finite many-body systems have some unique features, like the existence of a non-spherical shapes in the ground state, i.e. the lowest energy. This represents a spontaneous symmetry breaking. In case of a deformed mean-field, a combination of the surface vibrations can couple to a rotation [6] and the deformed object can rotate.

Different mean-field theories exist aspiring to describe enormous large objects such as galaxies [7] over every-day sized objects like water drops in the shower and smaller molecules down to the small atomic nuclei [8]. Even though different sized objects are dominated by different fundamental forces, many analogies can be found between the systems. A deeper understanding of the mean-field can shed light at a fundamental level of the constitution of exotic objects like the creation of cosmic patterns, exotic nuclei and even man-made nanometer-sized materials [9].

In Figure 1.1 the size of objects is drawn versus the inverse of the rotational frequency. An almost linear dependence of the period of rotation on the radius is seen over nearly 30 orders of magnitude. This dependence suggest, that after applying a proper scaling, similar effects can emerge in the mean field.

One of the smallest systems, which can be experimentally accessed, is the atomic nucleus with a radius of few femtometers. The atomic nucleus is a finite quantum system of A nucleons ($A = N + Z$, N neutrons and Z protons) interacting with each other via the strong and in case of protons also the Coulomb force. In nearly 80 years of theoretical and experimental work on the subject of low-energy nuclear physics, an accurate and universal description of the atomic nucleus from first principles is still faraway. Fundamental questions are still partially unanswered, including: which is the binding between protons and neutrons and hence the limits in neutron-proton imbalance and the heaviest nucleus possible? and how do the complex phenomena emerge from the fundamental nucleon-nucleon, nucleon-nucleon-nucleon and higher order interactions?

These questions can not be answered directly. Hence, experiments needs to be performed in order to test the predictions of nuclear models, in particular mean-field models. Since

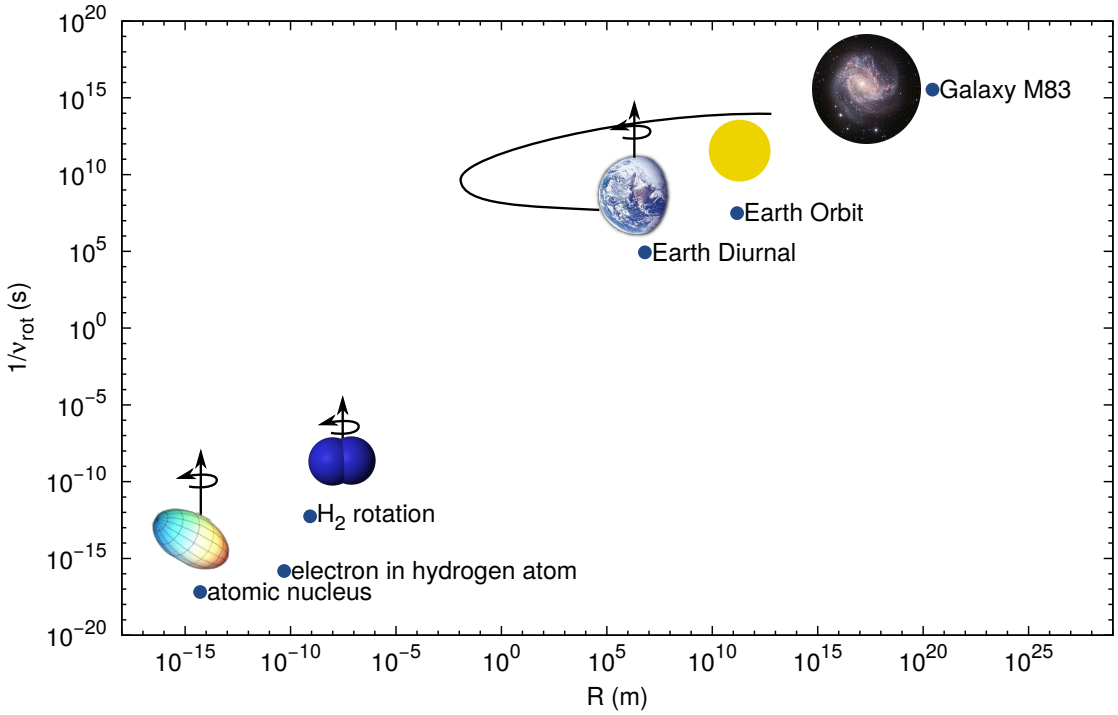

Figure 1.1: The inverse of the rotational frequency is plotted against the radius of different rotating objects. Figure based on Reference [9].

many nuclear mean-field calculations are fitted to existing experimental data, properties of nuclei close to the stability valley are in a good agreement with theoretical predictions. The cases, where different models predict different behaviour for a given nucleus are particularly important. The shape evolution along isotopic chains is a good testing ground for nuclear models, since the deformation of a nucleus depends on its inner structure and is an interplay between the proton-neutron correlation driving the deformation and shell effects restoring a spherical shape. The shape of a nucleus is not a direct observable, hence predictions of the excitation energies of a particular atomic nucleus can be used as a signature for its shape.

This thesis reports on the experimental study of the nuclear shape as a function of the neutron number for the neutron-rich osmium isotopes through γ-ray spectroscopy. For this work an experiment at the Laboratori Nazionali di Legnaro (LNL), Legnaro, Italy using a multi-nucleon transfer reaction to populate excited states of unstable isotopes was performed. These states deexcite via the emission of γ rays, which were detected with the novel γ-array *AGATA*. The level schemes deduced from the γ-ray spectrum are compared to state-of-the-art beyond-mean-field calculations.

In the following sections the nuclear theories are introduced including different geometric nuclear models and beyond mean-field calculations which are used in the interpretation of the experimental results. Furthermore, reactions close to the Coulomb barrier, in particular multi-nucleon transfer reactions, and the methods of γ-ray spectroscopy are briefly described.

1.1 Nuclear models

A great variety of theoretical models for the description of the atomic nucleus were developed, in which the nuclear Hamiltonian can be written as $H = T + V$. The potential V contains in many cases the N-body interaction of the particles, which is predominated by a two-body interaction and T denotes the kinetic energy [10]:

$$H = \sum_{i=1}^{A} \frac{p_i^2}{2m_i} + \sum_{i>k=1}^{A} V_{i,k}(r_i - r_k) + \text{ higher many-body interactions,} \tag{1.1}$$

with A interacting nucleons at the position r. $V_{i,k}$ denotes the two-body potential. The eigenstate equation of this Hamiltonian can only be solved for very light nuclei. Heavier systems can presently not be solved due to the lack of numerical calculation power of current computers.

An approach to calculate this Hamiltonian is to add and subtract a one-particle potential, which affects all i particles[2] [10]:

$$H = \sum_{i=1}^{A} \left[\frac{p_i^2}{2m_i} + U_i(r) \right] + \sum_{i>k=1}^{A} V_{i,k}(r_i - r_k) - \sum_{i}^{A} U_i(r) := H_0 + H_{residual} \ , \tag{1.2}$$

where $H_{residual}$ is a small perturbation on the system of nearly independent nucleons in a **common mean-field potential**, represented by the Hamiltonian H_0.

Many models aspiring to describe the atomic nucleus exist. Not all of them use the mean-field approach. Some examples of nuclear models are:

macroscopic models

The energy is written as a function of global properties such as volume energy, asymmetry energy, surface energy, pairing, etc. The liquid-drop model [11] is one of the macroscopic models. The parameters are then fitted to a broad range of nuclear properties. These models describe very well the general evolution of the nuclear binding energy, but close to the shell closures these models fail. In order to describe also these nuclei, shell corrections are introduced in the so called microscopic-macroscopic model.

microscopic models

The description of the atomic nucleus starts in the microscopic models from the interacting nucleons. They can use either a bare NN $(+3N)$ interaction which reproduces the nucleon-nucleon scattering (so-called nucleon-nucleon potential) or an effective interactions.

- **ab-initio methods** These approaches start from a realistic or effective interaction, which describes the nucleon-nucleon scattering, so-called nucleon-nucleon potential, and use sophisticated many-body theories to solve the nuclear Hamiltonian. These theories fail to describe the binding energy for nuclei without the inclusion of a three-body force. Due to the increasing number of the interacting nucleons, the ab-initio methods can only describe very light nuclei [12].

[2] For simplicity the calculation is restricted only to a two-body interaction.

- **shell model** The mean field is approximated via a phenomenological one-body spherical potential. The many-body states are constructed using the configuration-mixed single-nucleon states limited to the Fermi surface. The residual interaction in the limited space can be fitted phenomenologically or obtained from a general nucleon-nucleon interaction. However, by increasing the model space (i.e. including a larger fraction of states close to the Fermi surface) the efforts for computing power and memory usage increases drastically. Hence, shell model is of great success to describe light-to-medium mass nuclei and nuclei close to shell closures, where the amount of states can be restricted. The shell model was the first one, which explained the "magic numbers" as shell-closures [13, 14].
- **self-consistent mean field** Using the same effective interaction for the determination of the mean field and interaction between the particles, one can get a self-consistent description of the nucleons motion as independent (quasi)particles and hence in sum a description of the nucleus. This is performed iteratively starting from an effective force and using a self-consistent theory such as the Hartree-Fock(-Bogoliubov) theory. The effective interactions are chosen to describe nuclear properties over the whole nuclear chart.

In this thesis two different nuclear models are used to describe the experimental data: the geometric collective model, which is a macroscopic model based on the liquid drop model, and the symmetry-conserving configuration mixing calculations, which goes beyond the self-consistent mean field. These two models are introduced in the following sections.

1.1.1 Liquid-drop model of vibrations and rotations

A finite many-body system can be viewed as a drop of a liquid of interacting particles held together by an elastic surface [11]. In particular for an atomic nucleus, the drop consists of two different kinds of fermionic liquids: protons and neutrons. The nucleons can be coupled to pairs and a huge asymmetry in proton-to-neutron number is forbidden. The atomic nucleus is a very compact object with a high ratio of surface to volume and a high surface tension. Hence, its properties are dominated by surface effects [9].

The liquid-drop model arises phenomenologically and fails in describing the effects attributed to magic numbers. A refinement of this model was proposed by Leo James Rainwater: nucleons close to the surface are moving in the field of the inner nucleons. The valence nucleons interact with the core and vice versa. This can lead to a permanent deformation. The work was developed in parallel by Bohr and refined together with Mottelson for extending the macroscopic liquid drop model by considering normal modes of a non-viscous fluid drop, made of interacting protons and neutrons. This model can be used to study excitations of (deformed) nuclei. In 1975 Aage Niels Bohr, Ben Roy Mottelson and Leo James Rainwater received the Nobel prize "for the discovery of the connection between collective motion and particle motion in atomic nuclei and the development of the theory of the structure of the atomic nucleus based on this connection" [15].

The surface $R(\vartheta, \phi)$ of the nucleus can be expanded in normalised spherical harmonics [6, 16],

$$R(\vartheta, \phi) = R_0 \left(1 + \sum_{\lambda=0,1,2,\ldots} \sum_{\mu=-\lambda}^{\lambda} \alpha_{\lambda\mu} Y^*_{\lambda\mu}(\vartheta, \phi) \right) , \tag{1.3}$$

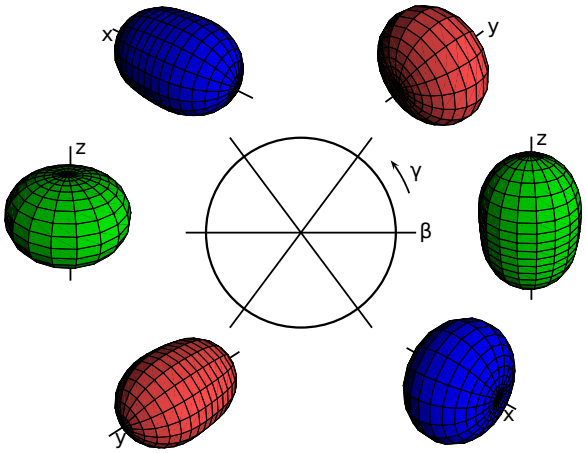

Figure 1.2: Illustration of different quadrupole-deformed shapes ($\beta = 0.4$ and $\gamma = n \cdot 60°$ with $n \in \{0, 1, 2, 3, 4, 5\}$). The different colours correspond to different principal axis (green for z, red for y and blue for x). Figure adapted from Reference [16].

with R_0 as the equilibrium radius and $\alpha_{\lambda\mu}$ the spherical tensor components, which represent the deformation. λ denotes the multipole order of the deformation. The most fundamental deformation is the quadrupole ($\lambda = 2$) deformation. In case of small values of $\|\alpha_{2\mu}\|$, the deformed nucleus is an ellipsoid randomly oriented in the system of reference. For quadrupole deformed nuclei, the 5 parameters $\alpha_{2\mu}$ can be transformed via an unitary transformation to a set of five variables $(a_0, a_2, \theta_1, \theta_2, \theta_3)$, where θ_i denotes the orientation of the ellipsoidal deformed nucleus and the parameters a_0, a_2 denote the extent of deformation: the so-called intrinsic coordinates. The transformation can be chosen, such that the principal axes of the ellipsoid are on the axes of the coordinate system.

Usually a_0 and a_2 are substituted by the two deformation parameters β and γ via $a_0 = \beta \cos\gamma$ and $a_2 = \beta/\sqrt{2} \sin\gamma$. The parameter β is given by $\beta = \sum_\mu |\alpha_{2\mu}|^2$ and hence larger absolute values of β correspond to larger deformations. In particular $\beta = 0$ represents a sphere. The γ parameter measures the angle with respect to the prolate deformed axis and characterises the deviation from an axial rotational symmetry. Two of the three semiaxes have the same length every $n \cdot 60°$, where n is an integer number. In Figure 1.2 the different quadrupole deformed shapes with $\beta = 0.4$ and $\gamma = n \cdot 60°$ $n \in \{0, 1, 2, 3, 4, 5\}$ are illustrated. Due to the rotational symmetry with respect to the choice of the principal axis, it is sufficient to restrict the plane to the wedge $0° \leq \gamma \leq 60°$ and $\beta \geq 0$.

Based on the quadrupole deformed description of the nucleus, the Bohr Hamiltonian, which has the wave function $\psi(\beta, \gamma, \theta_1, \theta_2, \theta_3)$ as the solution of the eigenstate equation $H_B\psi = E\psi$, can be built [6, 16]

$$H_B = T + V = \sum_{\mu=-2}^{2} \left(\frac{1}{2B_m} |\pi_\mu|^2 + \frac{C_2}{2} |\alpha_\mu|^2 \right) , \tag{1.4}$$

where B_m and C_2 denotes the mass and stiffness parameters, respectively. π_μ are the conjugated momenta associated to the five collective variables α_μ.

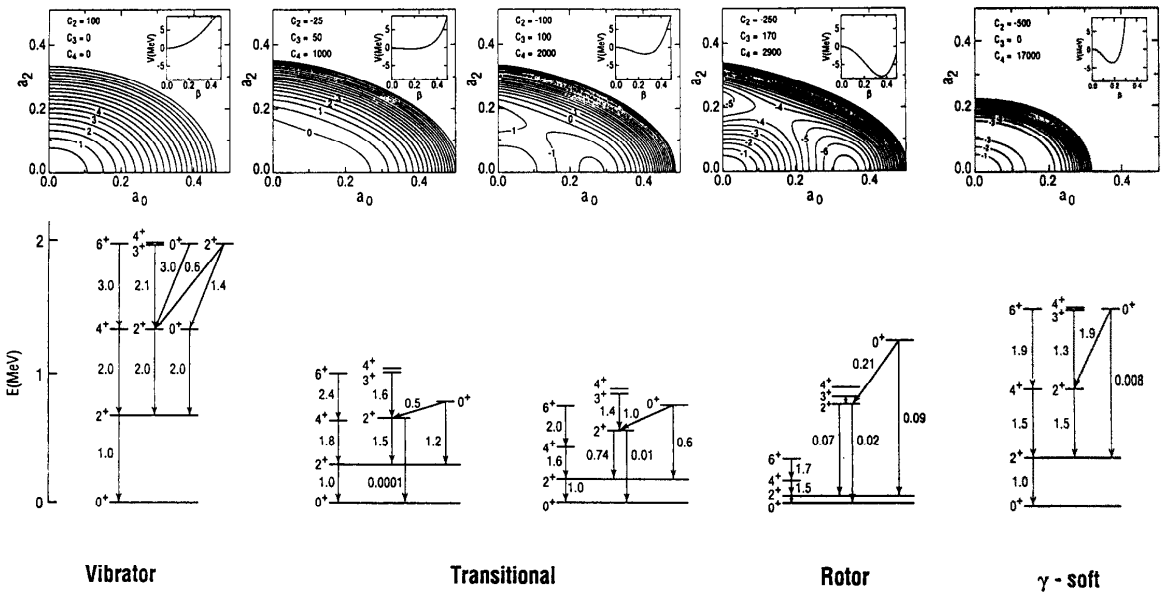

Figure 1.3: Each vertical section corresponds to a specific GCM Hamiltonian having the potential energy surface and the potential $V(a_0, a_2)$ plotted the top. The calculated energy spectrum of the Hamiltonian is at the bottom. The C_i parameters values are given in MeV. Figure adapted from Reference [18].

A large variety of solutions of the eigenstate equation of the Bohr Hamiltonian, both analytical and numeric were proposed. Each solution can be associated with a peculiar potential $V(\vartheta, \phi)$. An overview of solutions can be found in References [16, 17].

Geometric collective model

Gneuss and Greiner and coworkers developed a particular realisation of the quadrupole deformed Bohr Hamiltonian for the low-energy spectrum, the so-called **G**eometric **C**ollective **M**odel (GCM) [19–21], based on the expansion of the Bohr Hamiltonian in powers of fundamental invariants β^2 and $\beta^3 \cos 3\gamma$. The model treats the motion adiabatically, i.e. neglecting the interaction with higher lying modes of motion [19]. A rotational invariant potential $V(\theta, \phi)$ is deduced. Together with the kinetic energy terms up-to the 2$^{\text{nd}}$ order the GCM Hamiltonian can be written as [10]

$$H_{GCM} = T_{GCM} + V_{GCM} = \frac{1}{B_2}[\pi \times \pi]^{[0]} + \frac{P_3}{3}\left[[\pi \times \alpha]^{[2]} \times \pi\right]^{[0]} + C_2 \frac{1}{\sqrt{5}}\beta^2 - C_3\sqrt{\frac{2}{35}}\beta^3 \cos 3\gamma + C_4 \frac{1}{5}\beta^4 - C_5\sqrt{\frac{2}{175}}\beta^5 \cos 3\gamma + C_6 \frac{2}{35}\beta^6 \cos^2 3\gamma + D_6 \frac{1}{5\sqrt{5}}\beta^6 \ , \quad (1.5)$$

with π the momenta, α the collective coordinate tensor operator, B_2 and P_3 parameters of the kinetic energy and with the potentials stiffness parameters C_2, C_3, C_4, C_5, C_6, D_6 which are constants for every nucleus. These 8 parameters represent a good compromise between

a minimal set and the accurate description of the features of the potential. They can be calculated by a microscopic model or fitted to the low-energy spectrum. The excited states can be found by solving the eigenstate equation of the Hamiltonian using the eigenfunctions of the 5-dimensional harmonic oscillator as a basis [19].

Zhang et al. [18] proposed a simplified version of the GCM Hamiltonian, limiting the kinetic energy term to the harmonic case ($P_3 = 0$) and using only the constants C_2, C_3 and C_4. Figure 1.3 shows the calculated potentials and the level scheme for the limits of the vibrator (left) and rigid rotor and γ-soft rotor (right). Additionally, two cases of transitional nuclei are shown.

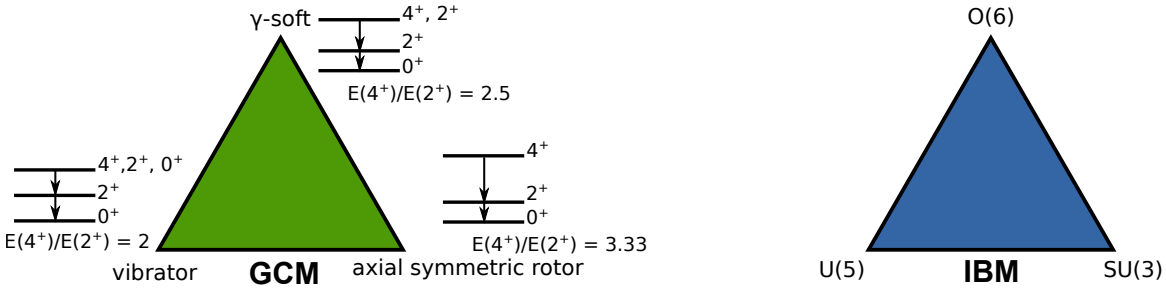

Figure 1.4: Structural triangle of the GCM (left) and the IBM (right). The limits of shapes are drawn on the edges of the triangles. The legs and the interior can be understood as transitional regions. Figure adapted from Reference [18].

Each potential produces a particular spectrum. By comparing the deduced level scheme with the expectation of the GCM, one can draw conclusions on the underlying form of the potential. The three different limits vibrator, rotator and γ-soft can be placed on the vertices of a triangle, the structural triangle, that can be understood as paradigms of nuclear structure. The legs and the interior represent transitional regions. It has strong analogies to the algebraic **I**nteracting **B**oson **M**odel (IBM) [10, 18], that is considered as an alternative description of the onset of collective spectra. In Figure 1.4 the structural triangle for the GCM and the IBM (called Casten's triangle) are shown. The triangles can be mapped into each other.

1.1.2 Self-consistent mean field using the Hartree-Fock-Bogoliubov method

The **S**elf-**C**onsistent **M**ean **F**ield (SCMF) approach calculated via the **H**artree-**F**ock-**B**ogoliubov (HFB) method is based on the variational principle. The energy of the system is minimised in a restricted variational space made of many-body wave functions which are generalised Slater determinants. This minimisation procedure brings automatically the original Hamiltonian into the form given in Equation 1.2. Only the basic concept is presented here. More detailed descriptions can be found in textbooks like Reference [22]. Besides the described approach, also a relativistic mean-field treatment was developed and recent review articles can be found in References [23, 24].

The basic building block of nuclear mean-field models is the construction of a set of N_{wf} single-nucleon wave functions $\psi_i(r, \sigma, \tau)$, where r stands for the spatial coordinates, $\sigma = \pm 1/2$ and $\tau = \pm 1/2$ for the spin and isospin, respectively. The number of wave

functions is bigger than the number of nucleons in the nucleus. Using this set of wave functions, a creation operator ($\widehat{a}_i^+$) for a nucleon in the single-particle state $\psi(r,\sigma,\tau)$ [8] employing the creation operators for position $\widehat{a}_x$ can be constructed:

$$\widehat{a}_i^+ = \int d^3r \sum_{\sigma,\tau} \psi_i(r,\sigma,\tau)\widehat{a}_x \ . \tag{1.6}$$

The state of the nucleus, Φ, can be identified as the Slater determinant [8], that is asymmetric by definition as it should be for a system of fermions

$$|\Phi\rangle = \det\{\psi_1(r,\sigma,\tau),\psi_2(r,\sigma,\tau),...,\psi_A(r,\sigma,\tau)\} \ . \tag{1.7}$$

Hence, $\widehat{a}_i^+ |\Phi\rangle = 0$ for occupied states ($i \leq A$) and $\widehat{a}_i |\Phi\rangle = 0$ for unoccupied states ($i > A$).

These single-particle states can be combined to independent quasi-particles via the unitary Bogoliubov transformation (U,V) [8]:

$$\widehat{b}_n^+ = \sum_i (U_{i,n}\widehat{a}_i^+ + V_{i,n}\widehat{a}_i) \tag{1.8}$$

These quasi-particles include the pairing correlation between the nucleons. From the quasi-particle states, the density matrix ρ and the pair tensor κ can be calculated by [8]

$$\rho_{i,j} = \langle\Phi|\widehat{a}_j^+\widehat{a}_i|\Phi\rangle = \left(V^*V^T\right)_{i,j} = \rho_{j,i}^* \tag{1.9}$$

$$\kappa_{i,j} = \langle\Phi|\widehat{a}_j\widehat{a}_i|\Phi\rangle = \left(V^*U^T\right)_{i,j} = -\kappa_{j,i}^* \ . \tag{1.10}$$

Since the particle number is not conserved in this approximation, the ground state $|\Phi_{gs}\rangle$ of the nucleus with N neutrons and Z protons can be found by minimisation of the total energy E under the constraint that the expectation value of the operators for the neutron and proton number is N and Z, respectively [8]:

$$E = \langle\psi|H|\psi\rangle = E(\rho,\kappa,\kappa^*) \ . \tag{1.11}$$

Among the empirical forces, developed for the description of the nuclear mean-field the Skyrme [25] and Gogny [26] interaction are commonly used. For the theoretical predictions used in this thesis, the Gogny 1DS force [27] is used. It is a finite-range interaction in form of the sum of two Gaussians with space-, spin-, and isospin-mixtures [8] and a density dependent spin-orbit term. It is a well adjusted empirical force, which has proven to give a reliable description of many observables and phenomena across the whole nuclear chart [28].

Using the Gogny 1DS interaction and the HFB method, the axial quadrupole deformation of the nuclei was calculated for the whole nuclear chart [29]. In Figure 1.5 the results are presented. The region of nuclei, where we have performed the study of shape evolution described in this thesis is highlighted. A shape transition from prolate to oblate deformation is predicted in that region.

1.1.3 Symmetry-conserving configuration mixing calculations

The self-consistent mean field can describe well the ground state binding energy and its trend over the whole nuclear chart. For a more realistic description of a given nucleus, one

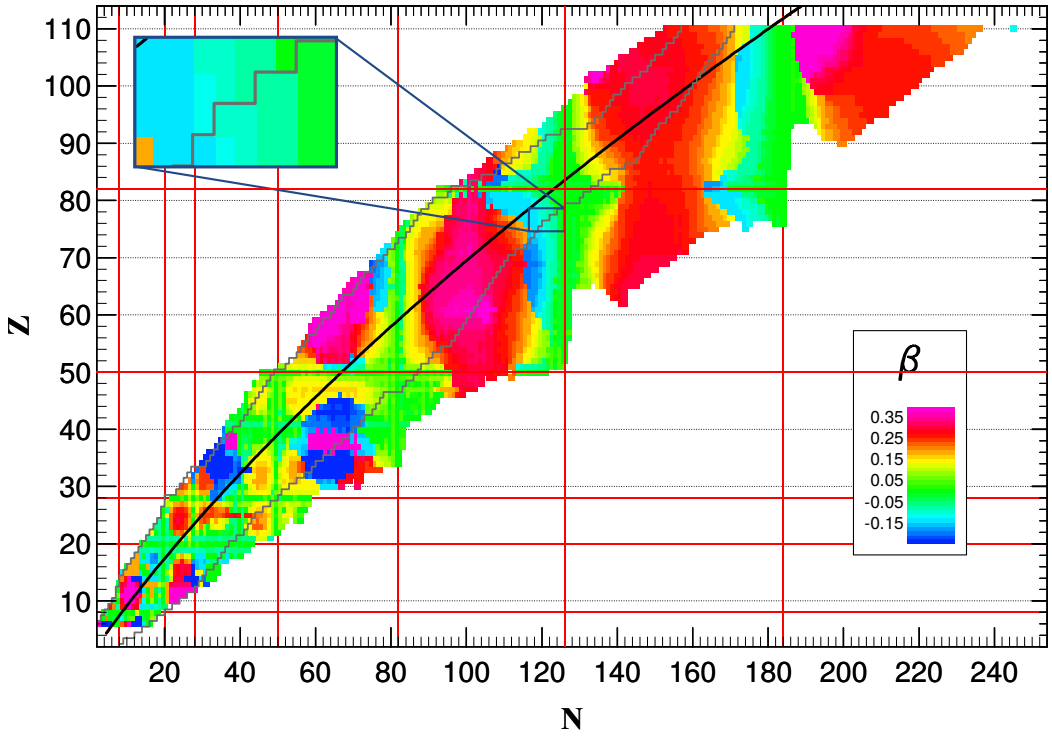

Figure 1.5: Nuclear chart showing the calculated deformation using the HFB method for axial symmetry and the Gogny 1DS interaction. The region around ^{196}Os (highlighted) described in this thesis presents a prolate-to-oblate shape transition. The nuclei inside the black polygon are the known nuclei. Figure adapted from Reference [29].

has to introduce additional correlations in the mean field, i.e. to go beyond it. Additionally, the HFB wave functions are not eigenstates of the particle number (N, Z) and angular momentum (I) operators anymore.

T.R. Rodríguez and J.L Egido developed a beyond-mean field approach including triaxial quadrupole deformation and the Gogny 1DS functional. Details of this approach, the **S**ymmetry-**C**onserving **C**onfiguration **M**ixing **C**alculations (SCCM), can be found in References [30–32]. Similar approaches were developed using the Skyrme functional [33] and the relativistic mean-field [34].

It uses the Variation after Particle Number Projection (VAP-PN) [35] for obtaining wave functions, which have a good particle number and good angular momentum quantum number [35]. To restore the particle number symmetry the HFB states with a quadrupole deformation $|\Phi(\beta, \gamma)\rangle$ are projected on HFB states, which are eigenstates of the particle number operators.

Using the variational principle on the energy $\delta E^{N,Z}[\Phi(\beta, \gamma)] = 0$ with restriction on a set of quadrupole-deformation parameters (β, γ) through Lagrange multipliers, one can find the minimal energy wave function, which is constraint to a specific pair of (β, γ) values. The wave functions are calculated for a triangular mesh of points in the (β, γ) plane. These HFB

wave functions do not break neither parity nor time-reversal symmetries. This restriction limits the calculation to positive parity states and the quantitative description of the moment of inertia.

Each of these HFB states are expanded into a single particle basis using harmonic oscillator shells. The final wave function is a linear combination of angular momentum and particle number projected wave functions, found using the generator coordinate method [22].

This approach was used to the calculate the spectra of the even-even ^{24}Mg [31], ^{44}S [30], $^{70-74}$Zn [36], $^{68-98}$Kr [32], $^{122-126}$Cd [37] and ^{140}Ba [38] isotopes. The new experimental data presented in thesis has triggered new calculations for the $^{188-198}$Os and $^{190-200}$Pt with this method. They are presented in Chapter 6.

1.2 Shape evolution in the neutron-rich osmium isotopes

A transition in nuclear shape from oblate to prolate deformation is in particular important for testing nuclear models such as those presented in the previous section. Assuming a particle-hole symmetry in a very simplified view, the number of prolate and oblate deformed nuclei would be expected to be approximately equal. However, current knowledge from both theory and experiment is that an extreme paucity of axial-oblate shapes exists for atomic nuclei [39, and References therein]). Hence, this shape transition regions are scarce in the nuclear chart.

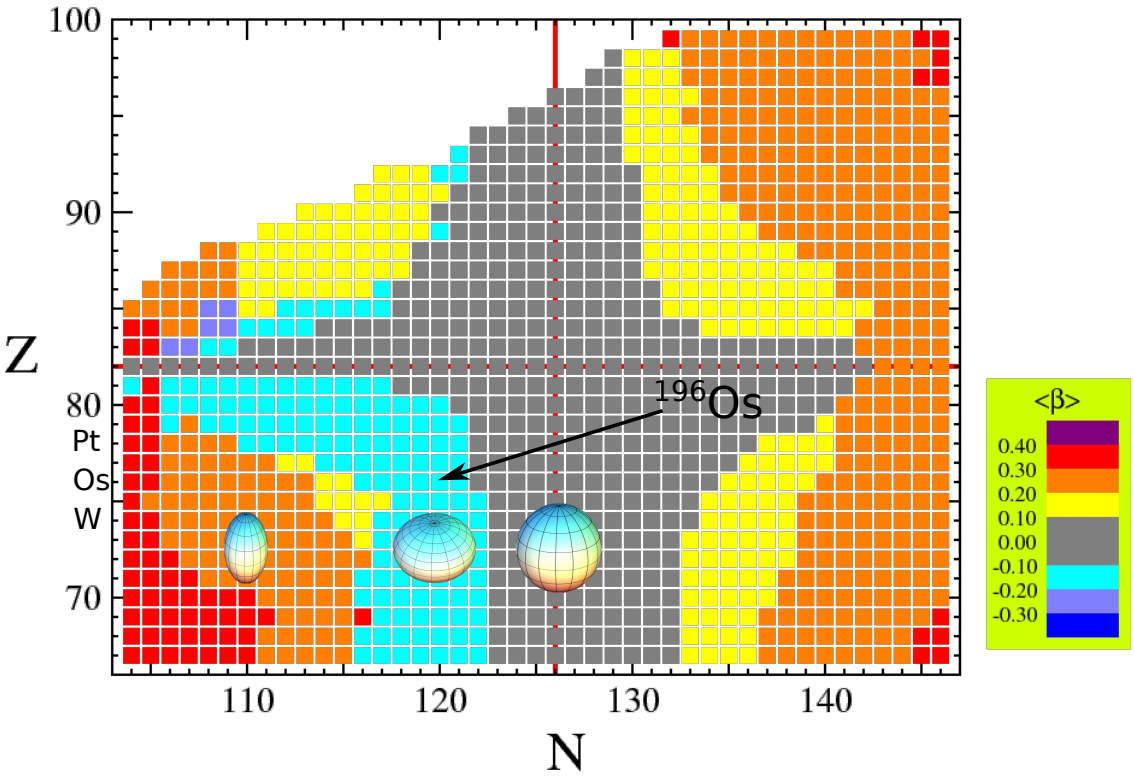

Figure 1.6: Extract of the nuclear chart around ^{198}Pt showing the axial deformation encoded in the colour. This figure presents the same calculations as Figure 1.5.

As seen in Figure 1.6 a shape transition from prolate to oblate deformation is predicted for the neutron-rich osmium isotopes. Not only the calculation of Hilaire and Girod [29] predicts a prolate-to-oblate shape transition in this region, but also a huge variety of nuclear models predict the shape transition. Among them mean-field calculations based on a variety of interactions the SLy4 Skyrme and Gogny D1S functional [40], Hartree-Fock+BCS [41], Interacting Boson Model based on a potential energy surface calculated by the HFB mechanism and the Gogny D1S functional [42] or Gogny 1DM functional [43], realistic mean field with the NL3 interaction [44], axially-deformed Hartree-Fock calculations with a separable monopole interaction [45].

The shape transition from the less neutron-rich prolate deformed osmium isotopes to the oblate deformed, when approaching the $N = 126$ shell closure is predicted, but the path between these limits has yet to be expounded.

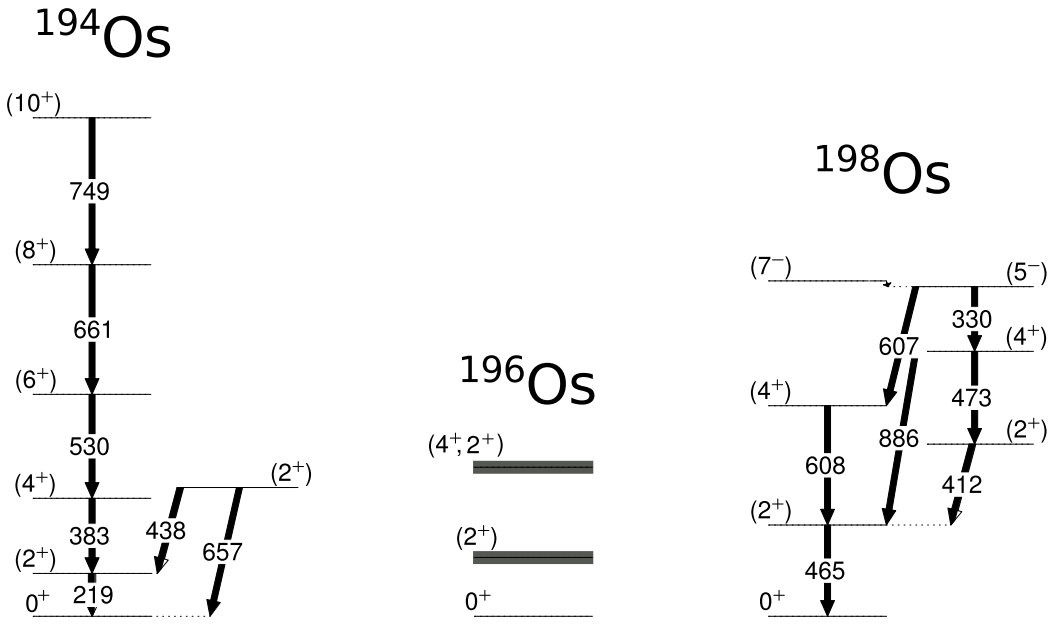

Figure 1.7: Partial level scheme of ^{194,196,198}Os as known prior to this thesis. The level schemes are based on data reported in References [46–48].

The heaviest stable isotope, ^{192}Os, has a prolate $J^\pi = 10^-$ isomer [49, 50], but additionally, its γ-vibrational band is the lowest-lying in this region with the bandhead at 489 keV [50], a clear signature of γ-softness.

On the other hand, ^{194}Os, populated up to $J^\pi = (10^+)$ via a multi-nucleon-transfer reaction [51], has a level scheme suggestive of prolate deformation, at variance with the interpretation of previous experimental results [52].

In recent years, isomer-decay spectroscopy combined with fragmentation reactions at relativistic energies, has enabled the study of, for example, ^{198}Os; the most neutron-rich osmium isotope for which any spectroscopic information is available. The (2_1^+) and (4_1^+) states in ^{198}Os were identified following the decay of the (7_1^-) isomer and a weak oblate deformation was deduced from their excitation energies [47].

Prior to the present study, in 1983, two excited states in ^{196}Os were established, populated via the two-proton transfer reaction ^{198}Pt(^{14}C, ^{16}O)^{196}Os [48]. These states lie at 300 (20) keV and 760 (20) keV. Whereas the first excited state was assumed to be the 2_1^+ state, for the second excited state a 2_2^+, 4_1^+ or doublet of these two states was suggested. However, prior this thesis, no γ-ray transitions have been measured in ^{196}Os. The partial level schemes of ^{194,196,198}Os are drawn in Figure 1.7.

The experimental endeavour to perform γ-ray spectroscopic studies of ^{196}Os continued from the finding of two excited states in the eighties. ^{196}Os was produced via fragmentation reactions using relativistic beam energies, however, no γ rays were observed in coinci-

dence [47, 53–55]. The reason might be absence of an isomer in this nucleus, or an isomer with a very short or very long half-life. Many experiments using deep-inelastic or multi-nucleon transfer reactions are reported in literature: the combination of a ^{198}Pt target and a ^{136}Xe beam was used in thick [51] and thin target [56] experiments. Additionally, the combination of a ^{192}Os target with a ^{136}Xe beam [49] or a ^{82}Se beam [57] was employed with a thick target. However, the selectivity was not sufficient to find a trace of ^{196}Os.

The selectivity of the reaction channel in a multi-nucleon transfer reaction using a magnetic spectrometer is superior to the γ-γ or γ-γ-γ coincidences used in thick target experiments if no γ-ray transitions are known. Hence, an experiment using a magnetic spectrometer was performed in the search of performing in-beam γ-ray spectroscopy of the key nucleus ^{196}Os. This thesis reports on the γ-ray spectroscopic study of ^{196}Os. Selected results including the first lifetime measurement of isomeric states with *AGATA* are also presented. The following two sections introduce the multi-nucleon transfer reaction and the γ-ray spectroscopic methods.

1.3 Nuclear reactions close to the Coulomb barrier

In order to produce the osmium isotopes of interest in an excited state a nuclear reaction is necessary. Using a combination of a stable beam and a stable target, in this case ^{82}Se impinging on ^{198}Pt target, and a beam energy high enough to overcome the repulsion of the positively charge nuclei different reactions occur. The one, which populates the neutron-rich nuclei isotopes described in this thesis, is a multi-nucleon transfer reaction.

In a reaction between two nuclei two forces are dominant: the long ranged repelling Coulomb force between positively charged nuclei and the short range attracting nuclear force. The nuclear surface-surface interaction between two nuclei, the so-called folding potential, can be simply written in the form of a Woods-Saxon potential $U_{pt}^{N}(r)$ [58] in terms of the relative distance (r) between the target t and the projectile p:

$$U_{pt}^{N}(r) = -\frac{R_p R_t}{R_p + R_t} \frac{16\pi\,\gamma\,\alpha}{1 + \exp\left[(r - R_p - r_t)/\alpha\right]} \quad \text{for} \quad r > R_p + R_t \ . \tag{1.12}$$

$R_{\{p,t\}}$ denotes the radius of the nuclei, α the diffuseness of the potential and γ the surface tension. These parameters can be found for example in Reference [58].

In a first approximation, the motion of the projectile takes place in the surface-surface interaction potential combined with the Coulomb potential, which can be written as:

$$U_s(r) = \frac{Z_p Z_t e^2}{r} + U_{pt}^{N}(r) \ . \tag{1.13}$$

For medium mass to heavy reaction partners ($A_p \cdot A_t < 23400$) at a certain distance r_B a maximum in the potential appears, the so called Coulomb barrier. It can be approximately calculated by [58]

$$r_B = 1.08(A_p/3 + A_t/3) + 1.20 + 0.34\sqrt{28.6 - A_p^{1/3} A_p^{1/3}}\,\text{fm} \ . \tag{1.14}$$

The impact parameter b has a corresponding angular momentum

$$L_s = b\sqrt{2 m_{pt} E(s)} \ . \tag{1.15}$$

For centre of mass energies below the Coulomb barrier, i.e. $E(s) < U_s(r_B)$, the distance of the closest approach is bigger than r_B. For centre of mass energies higher than the Coulomb barrier, the potential may show a maximum, which has the value of the kinetic energy. This orbiting solution happens for the grazing angular momentum L_g and is defined by the following two equations [58]

$$\left.\frac{\partial U_s(r)}{\partial r}\right|_{r=r_g} = \frac{L_g^2}{m_{pt} r_g^3} \quad \text{and} \quad U_s(r_g) + \frac{L_g^2}{m_{pt} r_g^2} = E_s \ . \tag{1.16}$$

Depending on the impact parameter b, different nuclear reactions can occur in the vicinity of the Coulomb barrier. In Figure 1.8 different types of reactions are illustrated [59]:

Quasi-elastic scattering In a direct reaction[3] one or few nucleons can be exchanged between the target and the projectile. A nucleon transfer from the projectile to the target

[3] time for the reaction $\approx$ time of transit of the projectile on the length of the target nucleus ($\approx 10^{-23} - 10^{-22}$ s)

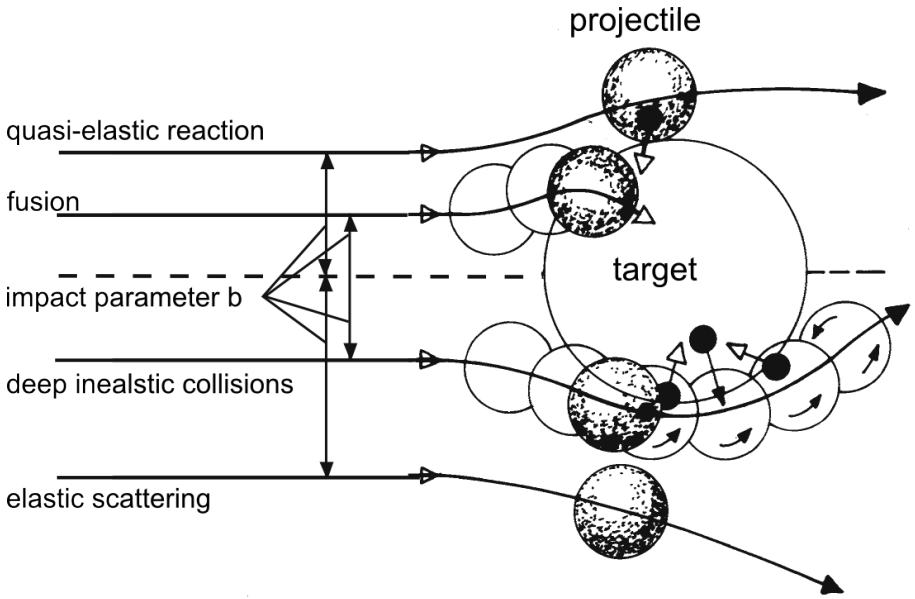

Figure 1.8: Classification of heavy-ion collisions with energies in the vicinity of the Coulomb barrier as a function of the impact parameter. Figure adapted from Reference [59].

nucleus is called "stripping" and the transfer of a nucleon from the target to the projectile is called "pick-up". The reaction is fast enough, that no rearrangement in the participants occur. In case of a transfer of more than one nucleon, this direct reaction is called **M**ulti-**N**ucleon-**T**ransfer (MNT) reaction.

Fusion The two nuclei form a compound nucleus and the projectiles kinetic energy is completely absorbed. The time scale of this reaction is long enough to loose the signatures of the projectile and the target nucleus. A symmetric reaction, i.e. the same nucleus as a target and projectile provides the highest possible spin transfer. Fusion reactions are used to study high-spin states. Depending on the excitation energy and on the angular momentum, the compound nucleus can fission, emit charged particles, neutrons and γ rays.

Deep inelastic collisions Close to the classical grazing angle of the reaction, the projectile touches the target nucleus. A transfer of several nucleons can occur and the kinetic energy of the projectile is partly converted into excitation energy. Since it is a peripheral collision, a high angular momentum can be transferred. In case of the excitation of the projectile or the target nucleus over the neutron separation energy, neutrons can be emitted. The same phenomenon was also observed for protons [60].

Elastic scattering The centre of mass energy of the projectile is conserved, hence no excitation of the participants occur. However, the energy and the angle of the projectile in the laboratory frame can change.

1.3.1 Multi-nucleon transfer reactions

Nucleons can be transferred between the reaction partners either in sequence or in pairs and clusters. The reaction products are close to the N/Z ratio of the compound nucleus of the reaction [60]. Hence, for the production of neutron-rich nuclei, a neutron-rich beam and target combination is most suited. The possible evaporation of neutrons limits its use for the investigation of very neutron-rich nuclei.

Nuclear structure investigation using MNT

Since the character of the binary reaction partners are conserved, MNT reactions are frequently used as a tool for γ-ray spectroscopy. Two approaches are commonly utilised using different target thicknesses. In a thick-target experiment, all the reaction products are stopped in the target or backing. In a thin-target experiment at least one recoil is identified in a detector or a magnetic spectrometer.

Thick target experiments The thick-target method was successfully used with several 4π γ detector arrays. The efficiency and peak-to-total ratio of Compton-suppressed γ arrays enables the construction of γ-γ-γ (or higher fold) coincidences and to select the ion of interest by gating on its γ rays or the γ-rays of its binary partner. A recent review can be found in Reference [60]. However, for weak reaction channels or for nuclei where the level scheme is unknown, this method is limited.

Thin target experiment with a magnetic spectrometer Besides the great success of the thick-target experiments, γ-ray spectrometers coupled with a magnetic spectrometer provide a huge selectivity. The magnetic spectrometer can identify the recoiling ion. Hence, the selectivity is higher and the coincident γ-ray spectrum has no contamination of other reaction products. The drawback of such a combination is the reduced target material and the limited acceptance of the spectrometer, reducing the statistics significantly. Additionally, the fragments emit the γ rays in flight and hence it is necessary to apply a Doppler correction.

Presently, there are two magnetic spectrometers which were coupled with γ-detector array and used for MNT reactions: *VAMOS* [61] and its upgraded version *Vamos++* [62] coupled with *EXOGAM* [63] and *PRISMA* [64] coupled with *CLARA* [65] and the *AGATA* demonstrator, which was used for the experiment reported in this thesis.

This method is very suitable for the study of unknown or barely known nuclei, especially for neutron-rich isotopes. Extensive studies have been conducted for spectroscopy of the detected recoils (e.g. for the iron isotopes [66], ^{40}S [67], around ^{48}Ca [68–70]). Since the identification of the magnetic spectrometers are limited to medium-mass nuclei (compare section 2.2.1), these studies are focused mainly on the spectroscopy up-to the $Z \approx 60$.

For heavier nuclei, the binary partner method can be used: the lighter beam-like isotope is detected in the spectrometer and the velocity vector of the heavier target-like recoil is reconstructed via the reaction kinematics. Since an excitation energy higher than the neutron-separation energy can be transferred, neutron evaporation occurs for the target-like and the beam-like recoils. A condition on the reconstructed Q value can be used to suppress the contamination of lower-mass isotopes [71].

Only few studies are reported in literature using the binary partner method and a magnetic spectrometer. One of the highlights is the spectroscopic study of the neutron-rich dysprosium isotopes [72]. In the study by Söderström et al. [72], a γ ray was assigned to ^{170}Dy, where the isotope and hence the level scheme was completely unknown. Unpublished results using the *CLARA-PRISMA* setup [73] and the *AGATA-PRISMA* setup [74, 75] were obtained for the uranium and thorium isotopes in the vicinity of ^{238}U. The known level scheme could be extended to higher spins.

In this thesis, the aim is to study the neutron-rich ^{196}Os isotope, few nucleons away from the stable ^{198}Pt target, using a thin-target and the binary partner method.

1.4 Gamma-ray spectroscopy

The nuclei produced in an excited state through a the multi-nucleon reaction deexcite via emission of a cascade of γ rays. The spectrum of the measured γ rays can be used to construct the level scheme of the nucleus, which then can be compared to the predictions of nuclear models. For this thesis an array of new generation γ-ray detectors was used to for the γ-ray spectroscopic study of the nuclei detected in coincidence with the magnetic spectrometer *PRISMA*.

1.4.1 Electromagnetic transitions in atomic nuclei

An excited nuclear state with an energy E_i, spin J_i and parity π_i can decay via the emission of a γ ray to a lower energetic level with an energy E_f, spin J_f and parity π_f [59]:

$$E_\gamma = E_i - E_f \ . \tag{1.17}$$

Here, the recoil energy of the nucleus is neglected. The decay follows the exponential decay rule $e^{-\lambda\, t}$, where λ is the decay constant.

Since a γ ray is just a high energetic photon which is emitted from the nucleus, in addition to the energy also the angular momentum and the parity is conserved. Hence, the angular momentum of the γ ray has to satisfy the unequation [59]

$$\|J_i - J_f\| \leq L \leq J_i + J_f \text{ with } \Delta L > 0 \ , \tag{1.18}$$

and the change in parity is given by [59]

$$\Delta\pi(EL) = (-1)^L \text{ and } \Delta\pi(ML) = (-1)^{L+1} \tag{1.19}$$

for electric (EL) and electric (ML) character, respectively.

The reduced transition probability $B(\sigma l, J_i \rightarrow J_f)$ can be written as the sum over the participating nucleons p of the single particle transition operators $\widehat{Q}^{m_l}_{\sigma,l}$ [76]

$$B(\sigma L, J_i \rightarrow J_f) = \frac{1}{2J_i+1} \sum_{m_i} \sum_{m_f} \sum_{m_l} \left| \langle J_f, m_f | \sum_p \widehat{Q}^{m_l}_{\sigma,l}(p) \, | J_i, m_i \rangle \right|^2 \ . \tag{1.20}$$

If many nucleons are involved in the transition, the $B(\sigma L, J_i \rightarrow J_f)$-value can be significantly higher than the single-particle matrix elements and hence, this value can be naïvely understood as a measure for collectively. For the calculation, the matrix elements of the reduced transition operators are needed, which are provided by different nuclear models. The transition strength is not a direct observable, it is related to the lifetime τ, and accordingly to the width T of the excited level [77]:

$$T = \frac{\hbar}{\tau} = \frac{8\pi(l+1)}{l(2l+1)!!)^2} \left(\frac{E_\gamma}{\hbar c} \right)^{2l+1} \ B(\sigma l, J_i \rightarrow J_f) \ . \tag{1.21}$$

Internal conversion

In addition to the deexcitation of the nuclear level via the emission of a γ ray, the excitation energy can get transferred via electromagnetic interaction to the electronic shell of the nucleus, resulting in emission of an electron or, in case of a energy higher than the pair-production threshold, of a electron-positron pair from the atom, so called internal conversion and internal pair production, respectively.

The probability of the emission of a shell electron depends on the overlap of the electronic and nuclear wave functions and the internal conversion is always accompanied with the emission of a X-ray quanta or an Auger electron. The total conversion probability is a sum over all the different electronic shells ν [59]:

$$\alpha = \frac{N_{ic}}{N_\gamma} = \sum_\nu \alpha_\nu = \alpha_K + \alpha_{L_I} + \alpha_{L_{II}} + \alpha_{L_{III}} + \alpha_{ML_I} + \dots \quad . \tag{1.22}$$

For the calculation of internal conversion coefficient, the same difficulties as for the transition strengths occur. However, under the assumption that $Ze^2/c \ll 1$ and $E_B(e) \ll E_\gamma \ll E_0(e)$, a approximate formula for the internal conversion coefficient can be found [59]:

$$\alpha_K(EL) \approx \frac{L}{L+1} Z^3 \left(\frac{e^2}{\hbar c}\right)^4 \left(\frac{2E_o(e)}{E_\gamma}^{L+\frac{5}{2}}\right) \tag{1.23}$$

$$\alpha_K(ML) \approx Z^3 \left(\frac{e^2}{\hbar c}\right)^4 \left(\frac{2E_o(e)}{E_\gamma}^{L+\frac{3}{2}}\right) \quad . \tag{1.24}$$

The internal conversion coefficient increases with Z^3 and and with the angular momentum L. A lower energy of the transition (E_γ) increases the internal conversion coefficient. Hence, this effect is important for small transition energies, higher multipole orders of heavy elements. The measured γ-ray intensities need to be corrected for the, in this experiment not detected, internal conversion. The internal conversion coefficients are tabulated (for example in Reference [78]).

1.4.2 Gamma-ray detection

For γ-ray spectroscopic studies a complete absorption of the energy of the γ ray is most important. A γ ray with an energy relevant for nuclear physics ($\approx 100\,\text{keV} - \approx 10\,\text{MeV}$) interacts with matter through the photoelectric effect ($\sigma_{\text{photo}} \sim Z^{4-5}$), Rayleigh scattering ($\sigma_{\text{Rayleigh}} \sim Z^2$), Compton effect ($\sigma_{\text{Compton}} \sim Z$) and pair production ($\sigma_{\text{pair}} \sim Z^2$)[4]. The other effects, like photofission, nucleon-antinucleon and meson production, have a higher threshold energy. Due to the the cross sections of the involved processes, a high atomic number Z of the detector material and a large volume is preferred to detect the γ rays. Scintillation detectors like NaI(Tl), BGO or $LaBr_3$(Ce) have a high Z, but their energy resolution is limited to a few percent. Semiconductor detectors, like germanium detectors have a superior energy resolution, but for γ rays with energies above $\approx 150\,\text{keV}$, the Compton effect is the predominant interaction. Only above $\approx 8\,\text{MeV}$ the pair production has a higher cross section than the Compton scattering (see Figure 1.9).

[4]The threshold for the pair production is in the nuclear field $E_\gamma \geq 1.02\,\text{MeV}$ and in the atomic shell surrounding the nucleus $E_\gamma \geq 2.04\,\text{MeV}$

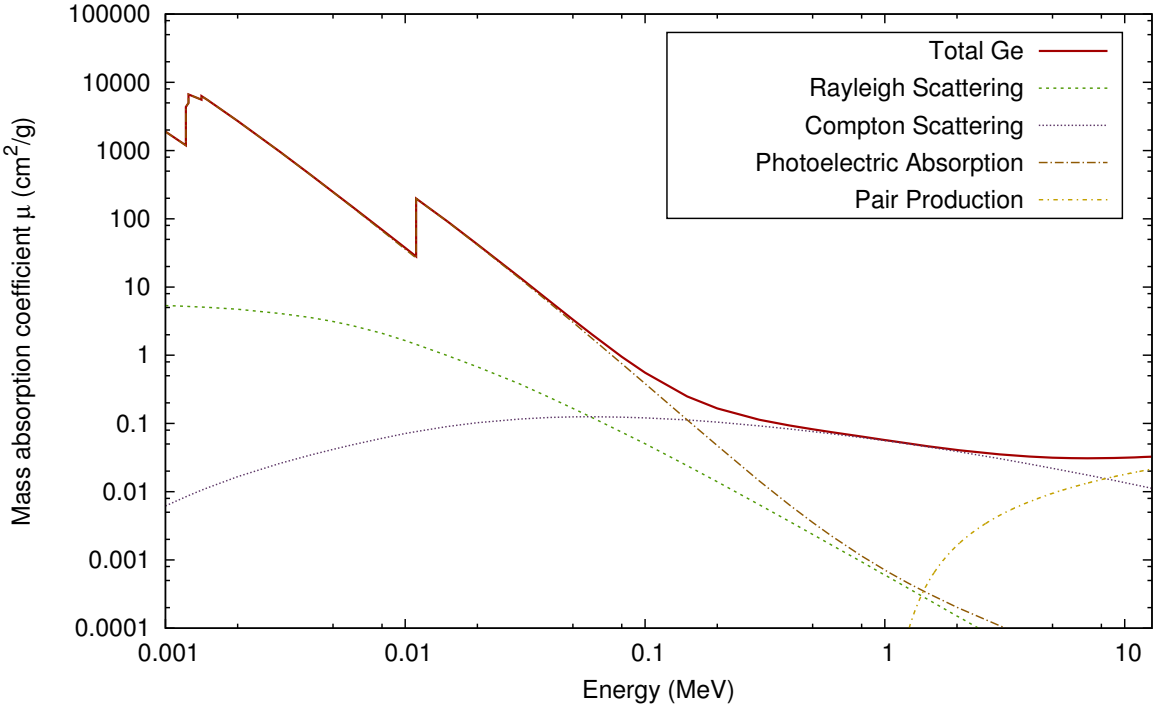

Figure 1.9: Mass absorption coefficient of γ radiation in germanium. Data taken from Reference [79].

Due to the finite volume of the germanium detectors, a Compton scattered γ ray can exit the detector and hence only deposit partly its energy. The same effect can occur after a pair production process for the γ rays originate from the annihilation of the positron. These events appear as a continuous background in the measured γ-ray spectrum or as additional peaks having the full energy minus 511 keV (single-escape peak) or 1022 keV (double-escape peak). To suppress these events, shields of a highly efficient scintillator surrounding the detector were developed. These shields serve as a veto for the events where only parts of the energy are deposited in the germanium crystal. The first escape suppressed γ array was the *TESSA* array [80]. Over the years, more efficient and bigger arrays covering 4π of solid angle were constructed, like *GASP* [81], *EUROBALL* [82] and *GAMMASPHERE* [83]. The solid angle covered by the germanium detectors in escape suppressed arrays is limited by the size of the anti-Compton shields.

To overcome this limitations, spheres built of germanium detectors with the accurate reconstruction of the interaction path of the γ rays were proposed and are currently under construction in Europe (*AGATA*) [80, 84–87] and the United States of America (**G**amma **R**ay **E**nergy **T**racking **I**n beam **N**uclear **A**rray *GRETINA*) [88]. These arrays consist of highly-segmented high-purity germanium detectors and rely on a pulse-shape analysis to deduce the interaction position and a reconstruction of the interaction path of the γ ray. The *AGATA* in the full configuration will consist of 180 high-purity germanium detectors (HPGe), each having 36 outer electrodes with a common inner core contact. The detectors

are arranged in triple clusters, with a common cryostat and dewar. A drawing of the full 4π configuration of the *AGATA* with a simulation of the efficiency is drawn in Figure 1.10. Section 2.2.3 describes the *AGATA* more detailed.

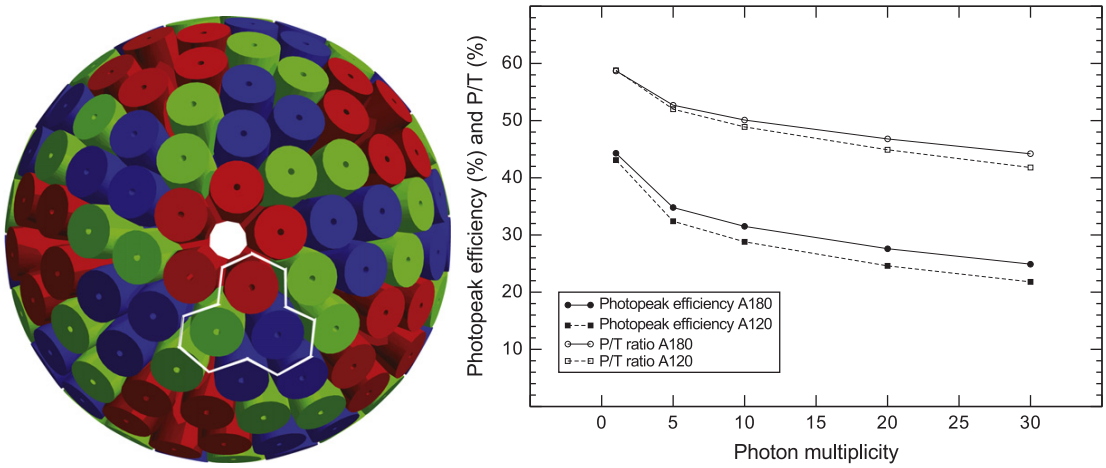

Figure 1.10: (left) The crystals of the full 4π *AGATA* array are drawn without any additional material. The different shapes of the crystals are indicated by different colours. (right) Monte Carlo simulation of the efficiency and the peak-to-total ratio of the full *AGATA* array (A180). Figures are taken from Reference [84].

1.5 Outline of the thesis

The thesis is organised as follows:

Chapter 1 Introduction The nuclear many-body problem with its treatment in terms of the mean-field approximation is introduced. Multi-nucleon transfer reactions and γ-ray spectroscopy is briefly described.

Chapter 2 Setup The experimental setup is described in detail: γ-rays were measured with the Advanced Gamma Tracking Array in coincidence with the heavy-ion spectrometer *PRISMA* and an array of *DANTE* detectors for the detection of the coincident reaction products.

Chapter 3 Presorting and calibration This experiment is one of the first *AGATA-PRISMA* experiments. The presorting and the calibration is described in detail with an emphasise on the experimental challenges.

Chapter 4 Data analysis Due to the novelty of this setup, the data analysis differs from experiments using traditional γ arrays. The procedure for the in-beam γ-ray spectroscopy as well as the delayed γ-ray spectroscopy is presented. The analysis of the data is outlined step-by-step until the final results.

Chapter 5 Results Selected results of this experiment are presented among the the first γ-ray spectroscopic measurement of ^{196}Os, in-beam γ-ray spectroscopy of ^{200}Pt, the even-even $^{70-76}$Zn and the first life-time measurement of isomeric states with *AGATA*.

Chapter 6 Theoretical interpretation The newly found yrast band of ^{196}Os is compared with beyond mean-field symmetry conserving configuration mixing calculations and geometrical models. Furthermore, the shape evolution in the even-even platinum isotopes is investigated, where the extended yrast band of ^{200}Pt plays an integral role.

Chapter 7 Conclusions and further perspectives The results are summarised and an outlook on future experiments in the transitional region around ^{196}Os is given.

2 Setup

In this chapter the experimental setup is described. A ^{82}Se beam with an energy of 426 MeV was provided by the *Tandem-ALPI* accelerator complex at LNL, Italy (section 2.1) impinging on a ^{198}Pt target. The large acceptance magnetic spectrometer *PRISMA* (section 2.2.1) and an array of 4 heavy-ion detectors *DANTE* (section 2.2.2) were used to identify the reaction products. The coincident γ rays were measured with the *AGATA* demonstrator (section 2.2.3).

2.1 Laboratori Nazionali di Legnaro

The experiment described in this thesis was conducted at the *Laboratori Nazionali di Legnaro* (LNL) [89] of the Italian *Istituto Nazionale di Fisica Nucleare* (INFN) located in northern Italy in the proximity of Padova. The accelerator complex ranges from the low-energy electrostatic Van de Graaff accelerator *AN 2000* (3 MV) and *CN* (7 MV) to the heavy-ion accelerator *XTU Tandem* and the superconducting post accelerator *ALPI* and its positive ion injector *PIAVE*. The radioactive ion beam facility *SPES* [90, 91] is currently under construction and will provide in future the possibility to accelerate mainly uranium fission products to energies above the Coulomb barrier.

The stable ^{82}Se beam for this experiment was provided by the *XTU Tandem* and the post accelerator *ALPI* with a final energy of 426 MeV. The layout of these two accelerators is drawn in Figure 2.1.

2.1.1 Tandem accelerator

The installation of the *XTU Tandem* [93, 94] with a design voltage of 16 MV was started in the year 1977. Five years later it became operational. An ion source provides negative charged ions, which are injected in the beam tube of the Tandem accelerator. The Tandem consists of two high-voltage columns placed inside a pressure tank, filled with a SF_6 gas to prevent sparks. Two laddertrons transport positive charge to the high-voltage terminal at the centre of the vessel. The ions are accelerated by the electric field gradient from the grounded source position to the positive charged high-voltage terminal. In the centre of the vessel, a carbon foil is placed to act as a stripper of the electrons: the ions are positively

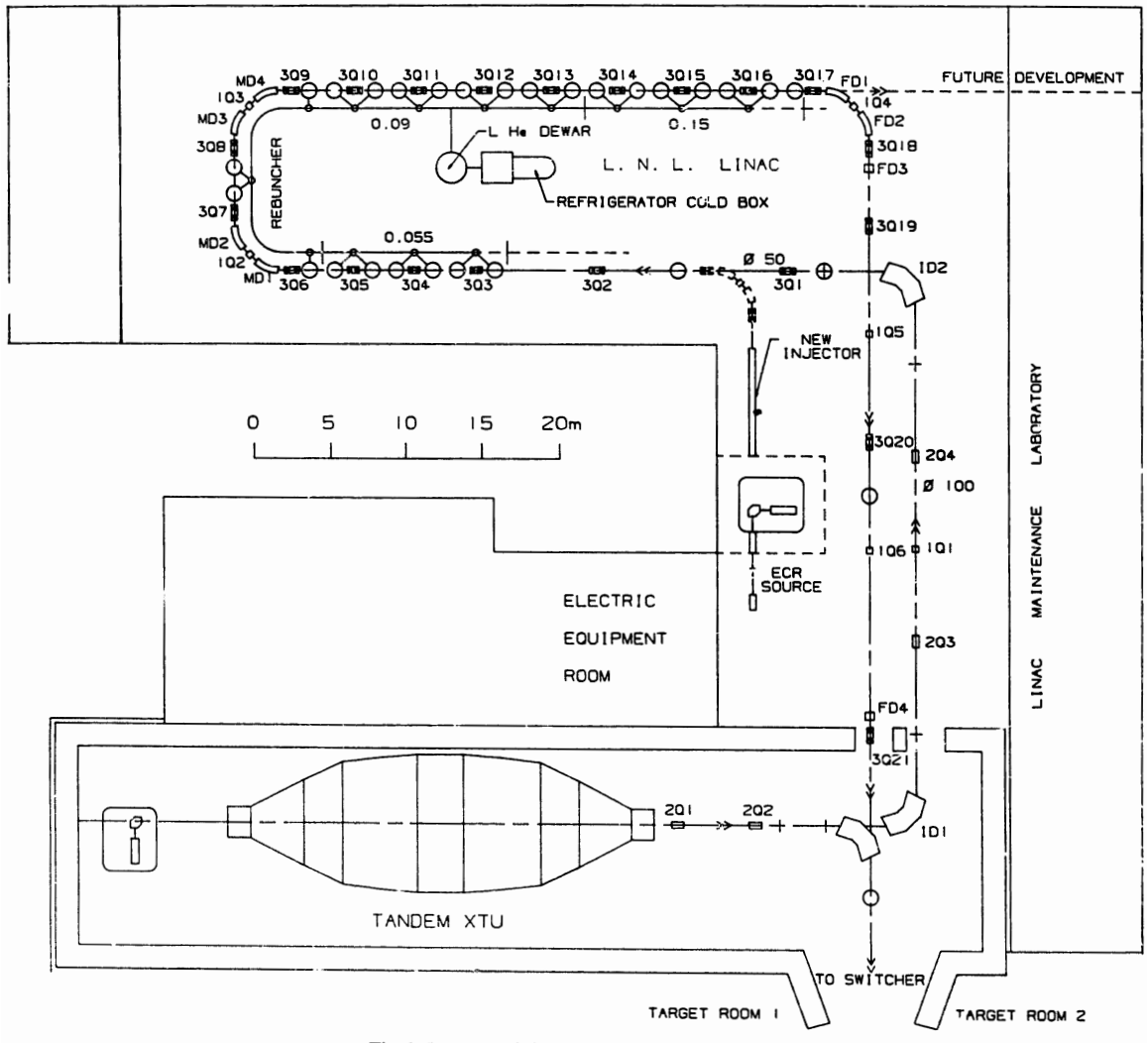

Figure 2.1: The *XTU Tandem-ALPI* accelerator complex. The pressure vessel of the *XTU Tandem* with its source is sketched at the bottom of this figure. At the top, the *ALPI* building and the accelerator is shown. Adapted from Reference [92].

charged after passing the foil in the centre and the electric field accelerates the ion until the end of the accelerator vessel. An additional foil might be placed inside the outgoing beam pipe to increase the charge state of the ion and hence to increase the energy of the accelerated ions.

The beam, which is accelerated by the *Tandem*, can be injected over a transfer beam line to the *ALPI* post accelerator.

2.1.2 ALPI post accelerator

The ALPI post accelerator [92, 95, 96] is based on superconducting **Q**uater **W**ave **R**esonance (QWR) cavities, grouped in three different sections: low-, medium- and high-β sections. The cavities are placed inside cryostats and cooled down by liquid helium, to maintain them in a superconducting state. A buncher, operating at 80 MHz, is located in front of the low-β section. It provides the bunch structure needed for the acceleration in an oscillating electric field. The bunches are further accelerated by the electric field produced by a radio frequency electromagnetic wave coupled into the cavities.

After the acceleration in *ALPI*, the ions are transferred to the experimental hall, where a switching magnet bends the ions to the beam line corresponding to a dedicated experimental apparatus.

2.2 Experimental setup

The experimental setup consisted of the large-acceptance magnetic spectrometer *PRISMA* and an array of 4 *DANTE* detectors for the identification of the reaction products. The coincident γ rays were detected by the *AGATA* demonstrator.

Figure 2.2 shows the mounted *AGATA* demonstrator (centre) together with the *PRISMA* spectrometer (right). The *DANTE* array was not mounted, when the picture was taken.

2.2.1 PRISMA spectrometer

The large-acceptance magnetic spectrometer *PRISMA* [64, 71, 98] was designed to detect and identify the medium-mass reaction products of heavy-ion collisions above and below the Coulomb barrier. It has an acceptance of ~ 80 msr in solid angle and $\pm 10\,\%$ in momentum combined with an energy resolution of 1/1000 and a mass resolution of 1/300. This is achieved by the reconstruction of the trajectory in the spectrometer. Hence, it is a hybrid between the high-energy tracking and the low-energy small acceptance spectrometer, where the correction of the trajectory is done by a set of complex magnetic lenses. It consists of a simple magnetic optics with a quadrupole and a dipole, a position sensitive entrance detector a **M**ulti **W**ire **P**arallel **P**late **A**valanche **C**ounter (MWPPAC) at the focal plane and a segmented ionisation chamber, having 40 active pads. A schematic top-down view of the spectrometer is presented in Figure 2.3.

The **M**icro-**C**hannel **P**late (MCP) start detector provides the entrance vector of the incoming ion, the quadrupole focuses the ion in the vertical plane and defocuses on the horizontal axis. The dipole is the dispersive element in the spectrometer and after a drift section, the position (horizontal and vertical) of the ion is measured. The time of flight between the start and the focal plane detector provides, with the reconstructed trajectory

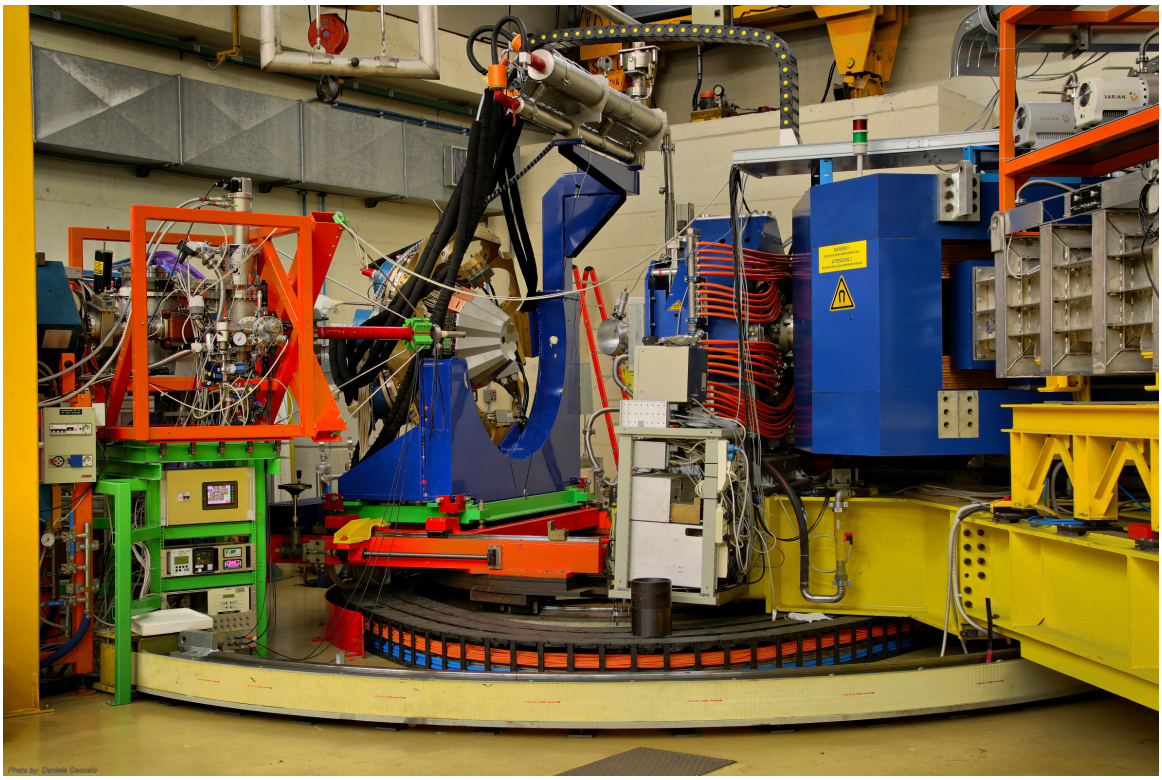

Figure 2.2: Photograph of the *AGATA-PRISMA* setup in the experimental hall. On the left side, the beam pipe is visible. The *AGATA* demonstrator is located in the centre. On the right side, the magnets and the beginning of the drift section of *PRISMA* is seen. The open target chamber is visible in the centre. Picture taken from Reference [97].

the velocity of the recoil. The ionisation chamber is used for the $\Delta E - E$ measurement, i.e. for the identification of the atomic number. The charge state of the ion after passing the carbon foil in the MCP start detector and its mass is reconstructed via a software procedure.

MCP start detector

The start detector is placed 25 cm from the target position and based on two large-area **M**icro-**C**hannel **P**lates (MCP) [99], mounted in a chevron configuration. Figure 2.4 shows a sketch of the detector as well as a picture before mounting it. In the start detector, the ions pass a thin carbon foil and induce secondary electrons, which are accelerated by an electric field, between the foil and position-sensitive anode, where they are collected. The MCPs are placed in front of the anode and amplify the charge. The anode is made of two orthogonal delay lines (horizontal and vertical). The difference in arrival time of the signals provides the position. By reconstructing the position information of both lines, the entrance point and angle of the ion in *PRISMA* can be identified. The detector has a time resolution of ≤ 350 ps and a position resolution of 1 mm on both the x and y axis with an efficiency of

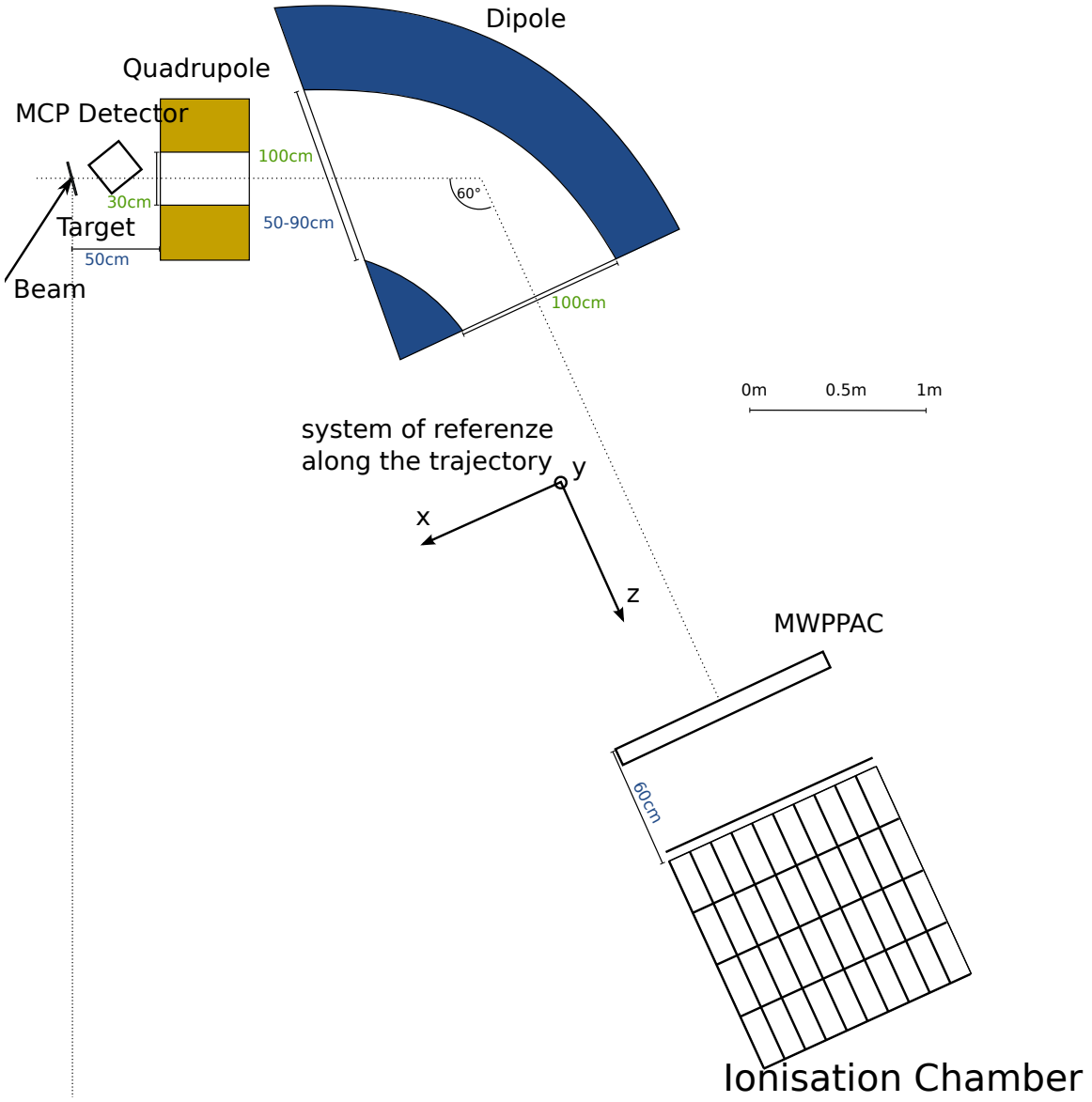

Figure 2.3: Schematic top-down view of the *PRISMA* spectrometer. The beam-pipe is not drawn. The distances between the elements are labelled in blue and the diameter of the beam tube in green. The sketch is based on Reference [64].

around 100 % [99].

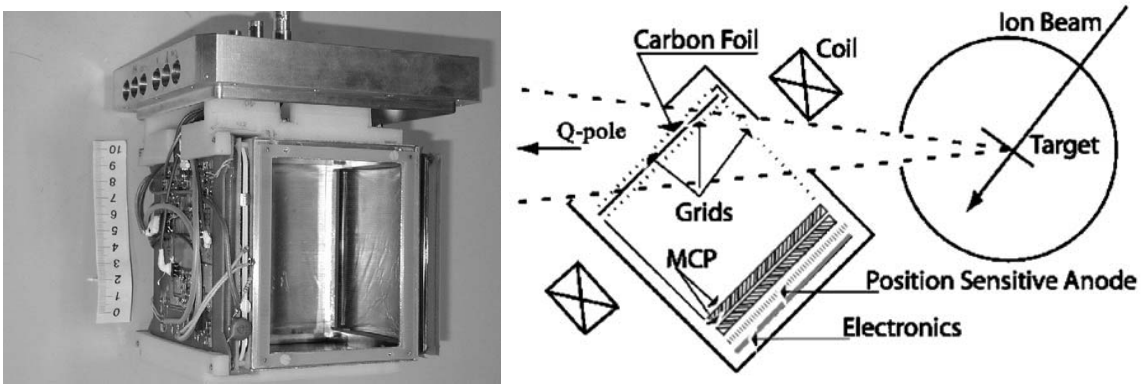

Figure 2.4: (left) Picture of the MCP start detector before the mounting into the *PRISMA* spectrometer. (right) A sketch of the MCP detector and its position in respect to the reaction chamber. The pictures are taken from Reference [99].

Magnetic optics

PRISMA has two magnetic lenses: a quadrupole and a dipole. They focus and bend the incoming particles to the focal plane and are constructed in such a way that the entrance together with the exit position determines the ions trajectory across the spectrometer.

Quadrupole The quadrupole magnet is located 50 cm away from the target position. It has a length of 50 cm and an inner diameter for the beam pipe of 30 cm. The magnetic field is set to focus the incoming particles in the vertical plane and defocus in the horizontal plane.

Dipole The dipole is located downstream of the quadrupole, at a distance of 1.6 m from the target. It is manufactured to have an homogeneous field in the 1 m wide beam pipe. The bending angle is fixed to 60° with a curvature of 1.2 m. The maximum magnetic field is 1 T and hence the maximal magnetic rigidity $B\rho$ is 1.2 T m. It is the dispersive element, which analyses the momentum of the recoils with a momentum dispersion of around $\Delta x \frac{p}{\Delta p} \approx \frac{4\,\mathrm{cm}}{\%}$.

Multi wire parallel plate avalanche counter

After the dipole and a 3.21 m long drift section in vacuum, the large-area **M**ulti **W**ire **P**arallel **P**late **A**valanche **C**ounter (MWPPAC) [100] is placed. It is used as a stop detector for the **T**ime **O**f **F**light (TOF) and to measure the position of the ions after the dispersive dipole. An exploded CAD drawing of the MWPPAC and the mounted MWPPAC is shown in Figure 2.5. It is segmented on the horizontal axis in 10 different sections, each having an area of 10 mm × 13 mm. The detector has two orthogonal anode wire planes (x and y position) combined with a central wire-based cathode 2.4 cm downstream. The 1000 anode wires are equidistantly placed on the horizontal axis each 1 mm and on each 2 mm on

the vertical axis. Due to the compact configuration, the avalanche of secondary electrons created by the ion is well localised and typically only one wire is firing. Hence, the position resolution is 1 mm on the x axis and 2 mm on the y axis. The MWPPAC is operated with isobutane (C_4H_{10}) and at a voltage between 500 V to 600 V. The acquisition of the position is based on $\sqrt{LC}$ delay lines, which are read out on the left and the right side of each section.

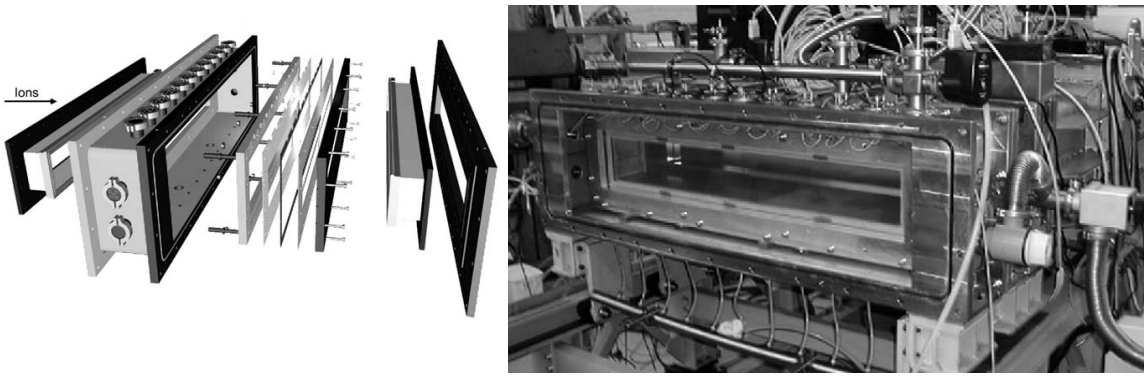

Figure 2.5: (left) Exploded drawing of the MWPPAC. (right) Picture of the MWPPAC, mounted in the vacuum vessel. Pictures adapted from Reference [100].

The MWPPAC provides the focal plane position x, y of the ions and combined with the MCP detector the TOF. The TOF for the elastic scattering on a subset of the trajectories between the start detector and the MWPPAC was found to have a FWHM time resolution of 630 ps. Taking into account the energy straggling and the finite size of the beam spot, the intrinsic time resolution of the MWPPAC is ≈ 300 ps [100].

Ionisation chamber

The ionisation chamber [100] (compare Figure 2.6) is located 60 cm downstream of the MWPPAC. The anode and the cathode are segmented in total 68 pads. The active area for the ΔE-E measurement consists of 40 pads, divided in 10 sections each having 4 pads along straight trajectories. An active pad covers an area of 99 mm × 265 mm and measures an independent energy loss (ΔE). 28 pads with a width of 55 mm surround the active area to ensure the linearity of the electric field in that area. Additionally, the 4 pads on the left and on the right of the active area are digitised and used as a veto detector (side pads). This allows to veto events having a highly distorted trajectory (see Figure 2.7). Close to the anode a Frisch grid is installed assuring the signal amplitude being independent of the position of ionisation. The dimensions of the ionisation chamber allow to stop the recoils in gas. For this experiment, methane (C_1H_4) was used. The sum energy of all pads gives the total kinetic energy of the recoil. The segmentation allows to construct the energy loss by each row and the possibility to veto an event whose reconstructed trajectory does not meet the measured energy loss. See Figure 2.7 for an example.

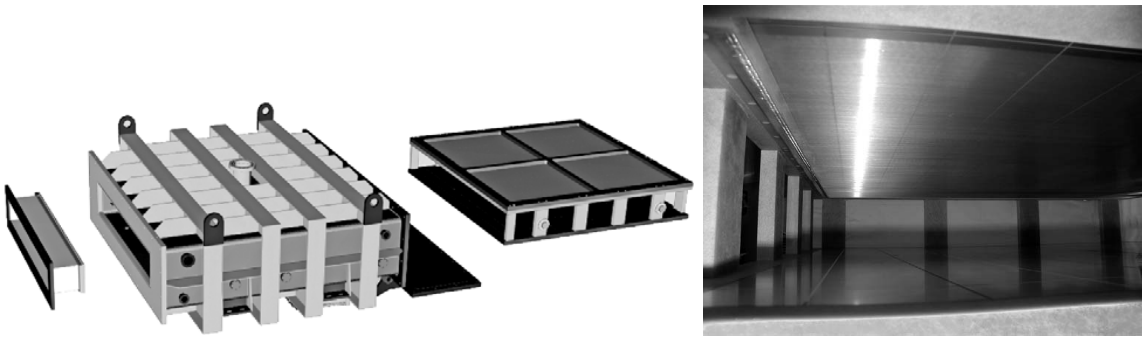

Figure 2.6: (left) Schematic view of the ionisation chamber. From left to right, entrance window, vacuum vessel and electrodes. (right) Inner view of the ionisation chamber. The pads of the anode are on the top, below is the Frisch grid and at the bottom are the pads of the cathode. Pictures are taken from Reference [100].

Determination of the atomic number

Fast ions passing through matter interact primarily through Coulomb interaction between their positive charge and the atomic shell of the matters ions. They can excite the electrons of the shell or ionise the atoms in the matter it travels through. The ion loses kinetic energy and slows down. The maximum transferred energy of an ion with the a mass m and a kinetic energy E_{kin} is $4E_{kin}m_e/m$, which is approximately 1/500 of the ions energy per nucleon. For losing the full energy, many interactions and hence ionisations are needed. Such processes occur in the ionisation chamber, which multiplies the charge carriers produced by the fast ion in an external electric field and collects them. The energy loss $\frac{dE}{dx}$ of the ion passing through matter can be described by the Bethe formula [101]

$$-\frac{dE}{dx} = \frac{4\pi e^4 q^2 c^2}{m_e \beta^2} \cdot nZ \cdot \left[\ln \frac{2m_e \beta^2 c^2}{I} - \ln\left(1-\beta^2\right) - \beta^2\right] \ . \tag{2.1}$$

Here n and Z denote the number density and the atomic number of the absorber. q and β are the charge number and the velocity of the ion, respectively. The ionisation potential of the ion I is tabulated and an can be approximated by $I \approx (10\,\mathrm{eV})Z$.

In the non-relativistic approximation this equation simplifies to

$$-\frac{dE}{dx} = C_1 \frac{mq^2}{E_{kin}} \ln\left(C_2 \frac{E_{kin}}{m}\right) \tag{2.2}$$

where C_1 and C_2 are constants.

In the gas of the ionisation chamber the charge state equalises. The average charge state can be calculated as a function of the velocity and the atomic number of the ion [102]. According to the Bohr's criterion, that the electrons of the ion with a velocity calculated in the Bohr's atom model smaller than the ions velocity gets stripped in matter, the averaged charge state $\overline{z}$ can be calculated by

$$\frac{\overline{q}}{Z} = \frac{v}{v_0 Z^{2/3}} \quad \text{for} \quad 1 < v/v_0 < z^{2/3} \ , \tag{2.3}$$

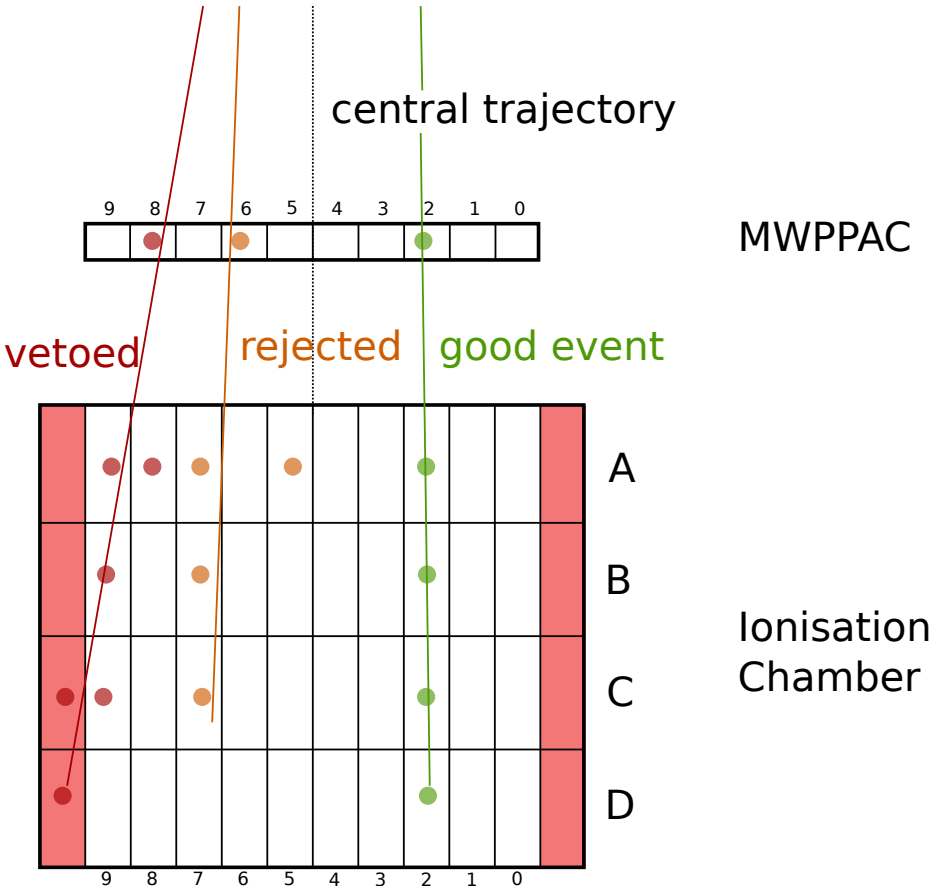

Figure 2.7: Sketch of the ionisation chamber and the MWPPAC combined with three example trajectories. The firing sections are marked with a dot. The ions releasing an energy higher than a certain threshold in one of the side pads are vetoed (red) and ions whose energy loss does not correspond to the reconstructed trajectory are rejected (orange). The remaining events are used for the analysis (green).

where $v_0 = e^2/\hbar$ denotes the Bohr velocity [102]. Hence, the average charge state $\overline{q}$ is proportional to $Z^{1/3}$.

Therefore, a matrix of the total kinetic energy versus the energy loss can be used to deduce and separate the different $m\overline{q}^2 \approx mZ^{2/3}$. For medium-mass ions the relative mass difference has a lower impact than the change of the atomic charge number ($\frac{\Delta m}{m} \ll \frac{\Delta Z}{Z}$) and consequently the different atomic numbers show a higher separation in the ΔE-E matrix than different masses for the same atomic number. Figure 2.8 shows a matrix of the energy loss measured by the first section versus the total energy measured by the ionisation chamber. The different atomic numbers are visible as bands. An additional matrix using the energy loss measured by the sum of the first two sections can be used to enhance the selectivity of the higher energetic recoils.

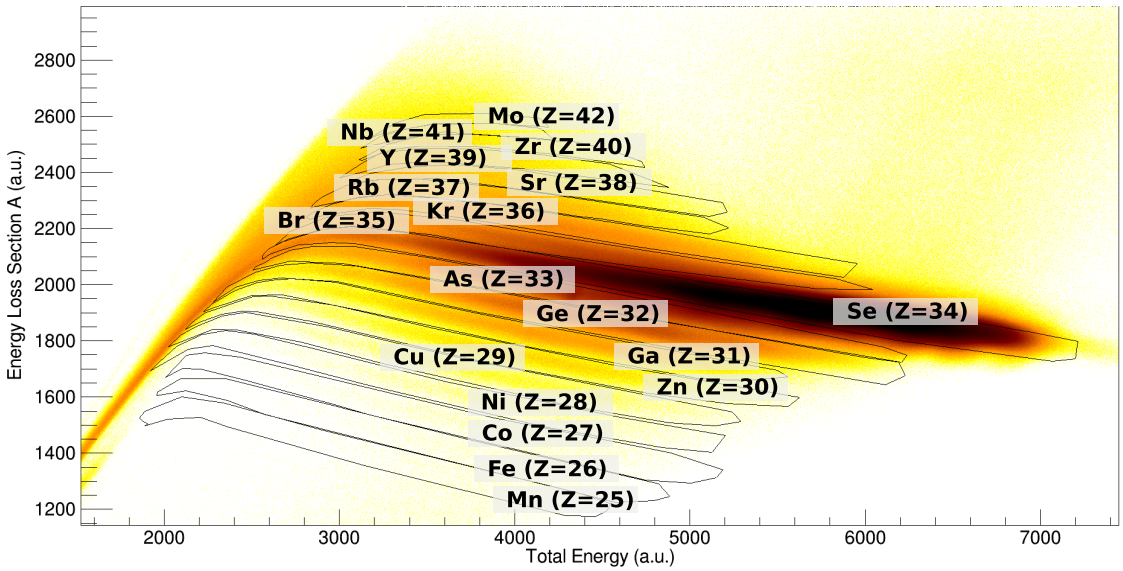

Figure 2.8: Matrix of the energy loss measured by the first section of the ionisation chamber versus the total energy, i.e. the sum of all pads of the ionisation chamber. The different atomic numbers are highlighted.

Ion trajectory reconstruction

The trajectory of the ions inside the spectrometer is reconstructed via an iterative software procedure. From the entrance position, the incident vector of the ion entering *PRISMA* can be reconstructed under the assumption, that the ion is emitted from the centre of the target position. The ion passes through the quadruple and enters the dipole. In the homogeneous magnetic field of the dipole, the ion gets deviated according to the Lorentz force. Using the valid approximation that the ion passes the dipole only in the spectrometer plane and an initial guess that the ion passes the dipole in the central radius, the position of the ion at the focal plane is calculated. The calculated position is compared with the measured position at the focal plane. The guessed radius is modified in the direction of the measured position and the transmission is recalculated. This iterative procedure is continued until the calculated position matches the measured one. The result is the bending radius ρ of the ion. The final length of the trajectory is calculated by the sum of the three dimensional straight lines, from the MCP start detector to the quadrupole entrance, quadrupole entrance to the exit, quadrupole exit to the dipole entrance, the circular motion in the dipole and a straight line in spectrometer plane from the exit of the dipole to the MWPPAC focal plane detector. The trajectory length combined with the time of flight is used to calculate the velocity of the ion.

Since this calculated length is an approximation of the real length of the trajectory, some aberration effects occur at lower order. In Figure 2.9 the results of the above described algorithm are compared to a Monte Carlo simulation, which takes the fringe fields of the magnets into account. The ratio of the reconstructed path length to the simulated one is plotted as a histogram. While the reconstruction works well for the central trajectories, for

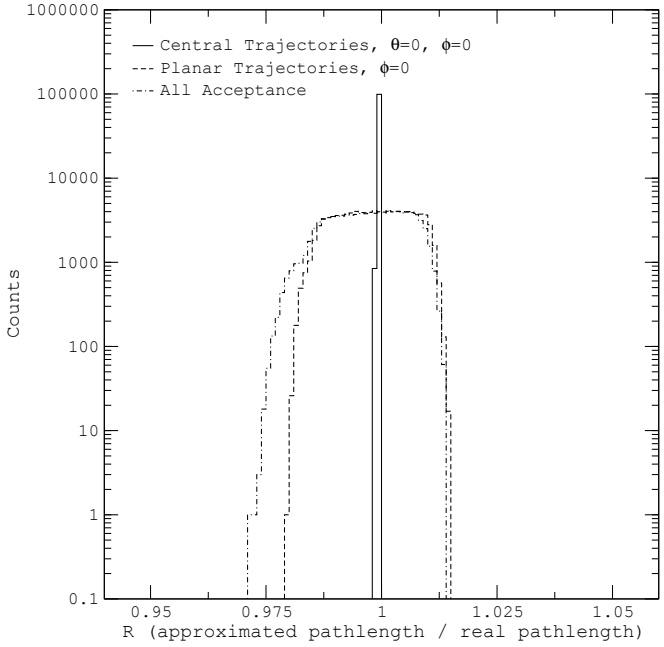

Figure 2.9: Deviation of the length of the trajectory as reconstructed by software to the length obtained from a Monte Carlo simulation taking the fringe fields of the magnets into account. Continuous line: central events; Dashed line: events belonging to the dispersion plane; Dashed and dashed-dotted line: all trajectories. Figure taken from Reference [103].

non-central trajectories an error of up-to $\approx 2.5\%$ is estimated [103].

The mass and the charge state of the ion is calculated via software using the motion of the ion in the spectrometer: equating the Lorentz force with the centrifugal force (still under the assumption of a planar trajectory in the dipole) leads to the formula

$$\frac{mv^2}{\rho} = qvB_D \ , \tag{2.4}$$

where m denotes the mass of the ion, v its velocity, q its charge state and B_D the magnetic field in the dipole. Hence, the mass-charge ratio can be calibrated by

$$\frac{m}{q} = \frac{B_D\rho}{v} \ . \tag{2.5}$$

The total kinetic energy in the non-relativistic limit is

$$E_{kin} = \frac{1}{2}mv^2 \ . \tag{2.6}$$

By combining equations (2.4) and (2.6), the charge state can be obtained by

$$E_{kin} = \frac{qvB_D\rho}{2} = \text{const} \cdot \ \rho \cdot \beta \ \cdot q \ . \tag{2.7}$$

Consequently, in a plot of the energy of the ion versus the product of β and ρ, the charge states appear as straight diagonal lines, which are parallel to each other (see Figure 2.10). Hence such a matrix can be used for the identification of the charge state.

A gate on each charge state produces a spectrum with the mass-over-charge ratio. Multiplying this spectrum by the charge state leads to the mass spectrum.

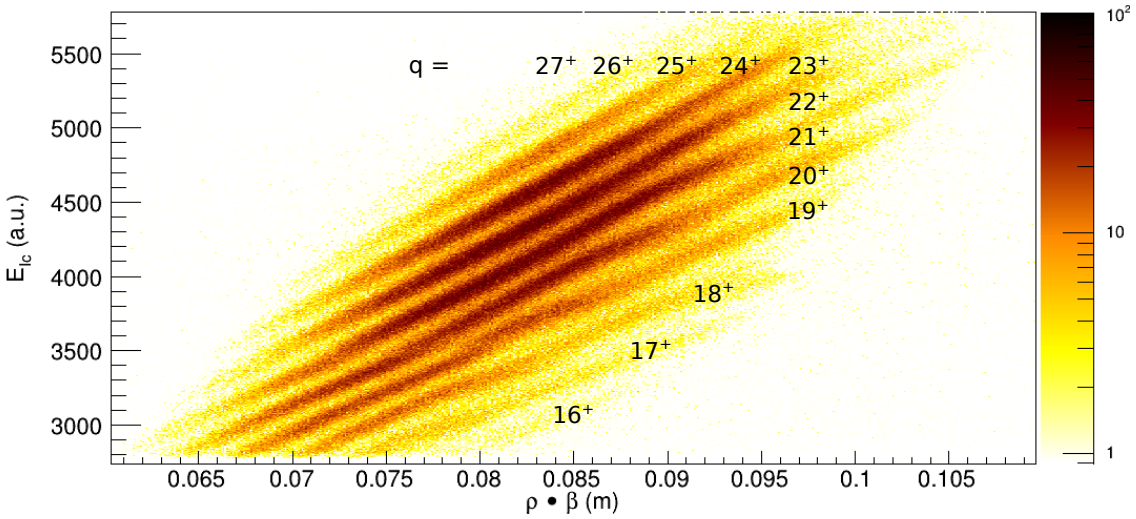

Figure 2.10: Matrix of the kinetic energy measured by the ionisation chamber versus the magnetic rigidity $\beta \cdot \rho$, gated on the atomic number $Z = 32$, for the selection of the atomic charge state. Each of the straight lines represent a charge state. The different charge states are indicated.

2.2.2 DANTE array

The **D**etector **A**rray for multi-**N**ucleon **T**ransfer **E**jectiles (*DANTE* [87, 104]) is a general purpose heavy-ion position-sensitive detector, which can be placed inside the target chamber. It is a very compact detector with a position resolution of $\approx 1\,\text{mm}$ and a time resolution of $\approx 130\,\text{ps}$. Its construction is similar to the start detector of *PRISMA*, with a Mylar foil, two micro channel plates mounted directly after the foil in a chevron configuration and two orthogonal delay lines for the x and y position.

An array of 4 heavy-ion *DANTE* detectors was placed on a forward cone at an angle of 58° around the beam axis. Figure 2.11 shows a schematic drawing of the support structure and the dismounted support structure with the mounted *DANTE* detectors on it. The ring on the left side of the picture faces the entrance position of the *PRISMA* spectrometer.

The reaction products of the binary ^{82}Se+^{198}Pt reaction can be detected in two opposed *DANTE* detectors and kinematic coincidences between the reaction partners can be obtained. The time difference between opposing detectors is recorded and from this information the velocity of the ions can be deduced.

Since a *DANTE* detector is mounted opposed to the *PRISMA* spectrometer, also kinematic coincidences with *PRISMA* are possible and done.

2.2.3 AGATA spectrometer

The energy of the γ rays, which emitted by the nuclei produced in the ^{82}Se+^{198}Pt reaction, range from the energies of X rays of elements in the region around ^{198}Pt up-to 4 MeV. These energies are typical for discrete γ-ray spectroscopy. In this energy range, the interaction

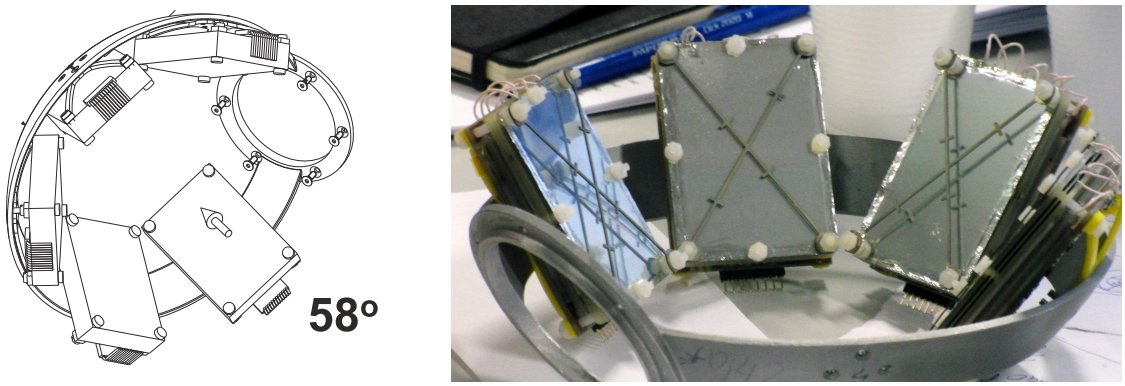

Figure 2.11: (left) Drawing of the support structure for 58° with the mounted detectors. The beam direction is indicated with an arrow. Drawing is taken from Reference [87]. (right) The dismounted support structure for the *DANTE* detectors.

of γ rays with the germanium detector material is dominated by the photoelectric effect ($\lessapprox 150\,\mathrm{keV}$) and the Compton scattering ($\gtrapprox 150\,\mathrm{keV}$ and $\lessapprox 8\,\mathrm{MeV}$). For a high detection efficiency, the solid angle coverage of the γ spectrometer should be as high as possible. Putting big detectors close to the target can lead to the summing of the γ-ray energies and hence spectroscopy is not possible. Additionally, the opening angle of the detectors and hence the position uncertainty of the γ ray should be as small as possible for a good Doppler correction. To achieve a good peak-to total ratio, the escaped Compton scattered events were suppressed in the previous γ arrays by veto detectors surrounding the germanium crystals. These detectors take a significant part of the solid angle and limit the maximal efficiency.

In order to overcome these limitations, the **A**dvanced **G**amma **T**racking **A**rray (*AGATA*) was proposed: a highly segmented germanium sphere allowing for tracking of the interaction path of the γ rays. The first implementation of this concept is used for this experiment.

AGATA demonstrator

The first realisation of a subarray of *AGATA*, the so-called *AGATA* demonstrator, was installed at LNL [87]. The aim was to demonstrate the feasibility of a tracking array, to evaluate its performance and to perform a physics campaign with stable beams. The demonstrator was mounted around the target position of the *PRISMA* spectrometer, replacing the *CLARA* array [65], which was using the clover detectors from *EUROBALL* [82]. The *AGATA* demonstrator had the unprecedent property of not having a defined focus since no collimators and anti-Compton shields were used, therefore it could be placed closer to the target chamber, to enhance the efficiency with respect to the nominal distance, while maintaining the good Doppler correction capability. It consisted in the final configuration of 5 *AGATA* triple clusters, as it was used in the present experiment.

AGATA triple cluster

Each *AGATA* triple cluster [85] has three differently shaped hexagonal tapered coaxial high-purity germanium detectors, as depicted in Figure 2.12. These crystals are encapsulated in a sealed thin aluminium case, minimising the passive material between the crystals. Each crystal has a length of 90 mm and a diameter at the rear of 80 mm. The crystal is segmented in 6 rings each having 6 segments, orthogonally segmented to the centre of the hexagonal face. The segmentation is shown in Figure 2.13.

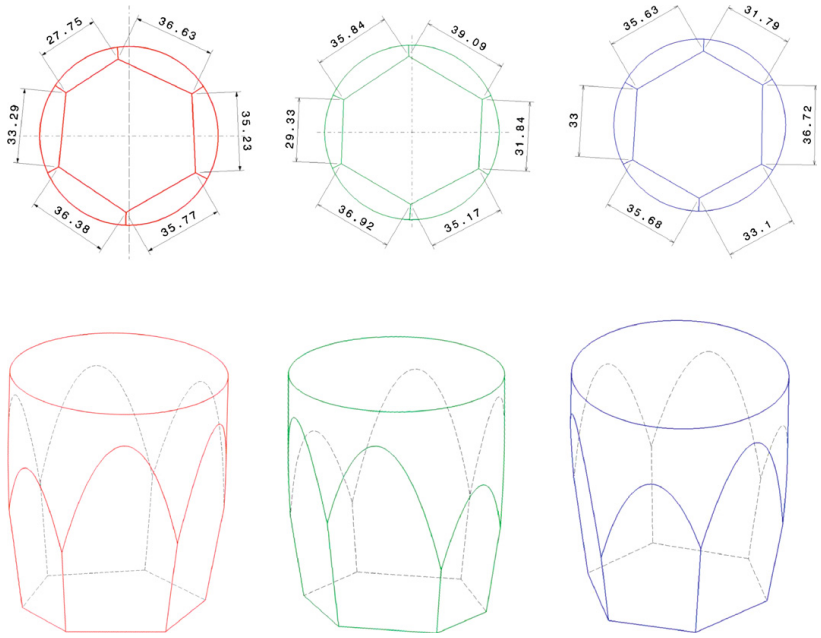

Figure 2.12: Design of the three different shapes of the *AGATA* crystals, that form a triple cluster. Figure adapted from Reference [85].

Each segment has its own preamplifier, which is divided into a cold and a warm part. The cold part is located close to the crystal and operated at cryogenic temperatures. The core has two different preamplifier gains, hence each cluster has in total $38 \cdot 3 = 111$ electronic channels. A cross talk of the level 10^{-3} between the segments has been observed, while the cross talk between the crystals is negligible [85].

The detectors, together with the cold part of the preamplifiers are mounted on the cold finger of a cryostat and placed in an aluminum end-cap. Figure 2.14 shows an *AGATA* triple cluster and the location of the preamplifiers inside the cryostat with the end cap. On the left side, one can see the mounted detectors inside the end cap.

Pulse shape analysis

For the reconstruction of the interaction path of the γ rays, their interaction position needs to be known. Furthermore, the opening angle of a detector and hence the detection-position uncertainty plays an important role for the Doppler correction. The high segmentation of the detector would already allow a better Doppler correction than traditional non-segmented

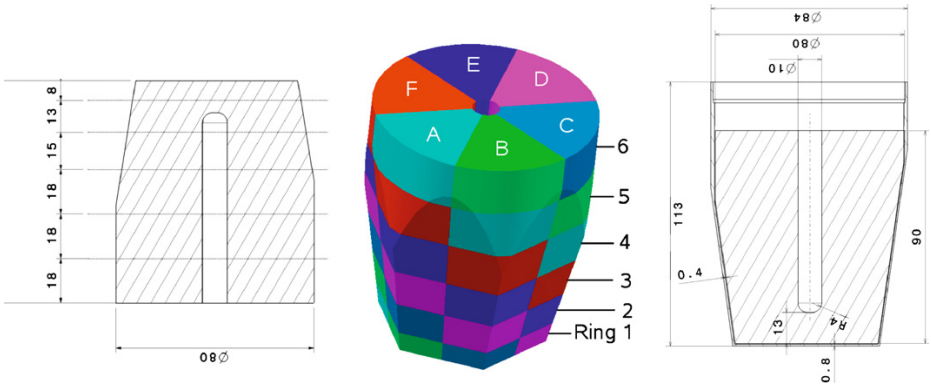

Figure 2.13: Schematic view of an *AGATA* detector (left and middle), that shows the electrical segmentation. The dimensions are given in mm. On the right side the encapsulation is drawn. Figure taken from Reference [85]

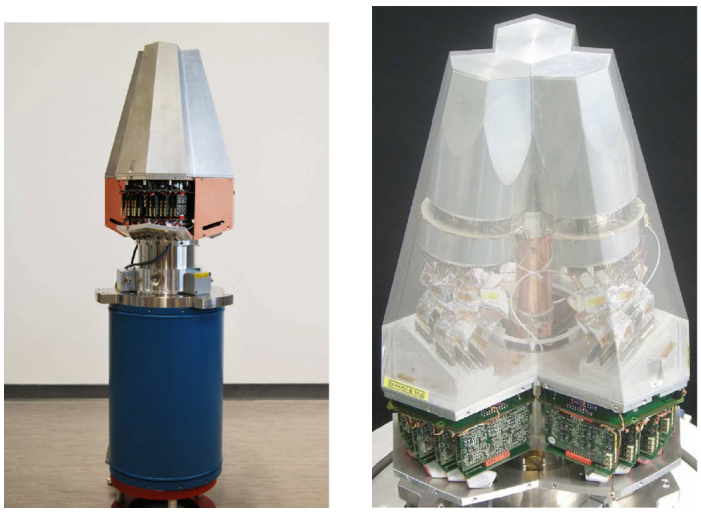

Figure 2.14: The mounted *AGATA* triple cluster, with the Dewar. The cover of the warm parts of the preamplifiers is removed. On the right side the picture is digitally edited so that the end cap is transparent. Figure adapted from Reference [85].

detectors. By applying a pulse-shape analysis technique, the interaction position in the segment can be determined. Hence, the position uncertainty is smaller than the size of the segmentation.

The energetic electron produced by the photo-electric or Compton effect is slowed down in the germanium detector material and produces electron-hole pairs and hence a net charge. This charge induces mirror charges in the neighbouring segments. A high voltage is applied to the electrodes. When the net charge drifts to the electrodes, the mirror charge causes a current into and out of the segments. After the collection of the charge in the segment also the image charge vanishes. The total integrated induced charge in the neighbouring segments is 0, but the measured signal depends on the position of the interaction. Figure 2.15 shows the pulse shape of the six segments and the core of a *MINIBALL* [105] detector. The data were taken with a collimated ^{137}Cs source illuminating the segment number 4. From the amplitude and the rise time of of the mirror-charge signals, the point of the interaction can be deduced.

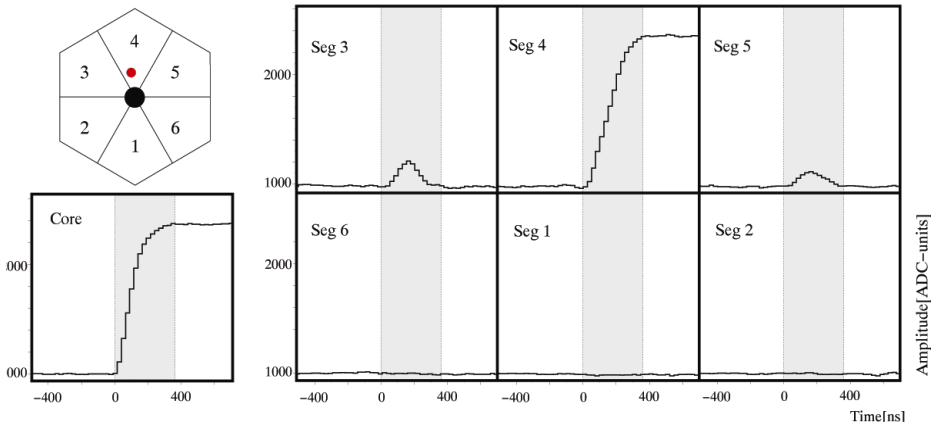

Figure 2.15: The pulse shape of an interaction in the 4$^{\text{th}}$ segment of a *MINIBALL* detector. The positive induced signals in the other segments can be used to deduce the position of the interaction. Figure taken from Reference [86].

For the determination of the interaction point depending on the measured signals, a base of reference signals is needed. In order to obtain the reference base signals, it is possible to scan each detector with a collimated source. For a grid having cells with the size of $(2\,\text{mm})^3$, more than 30000 reference positions are needed. Scanning systems for the *AGATA* crystals exists [106–108], however due to time restrictions, a simulation of the basis is currently used. Some crystals were already scanned and the simulations are tuned to reproduce the measured data. A comparison between the experimental pulse shapes and the simulated one for *AGATA* is depicted in Figure 2.16. The agreement between the simulation and the experimental measured data justifies the usage of the calculated database as a reference base for the PSA.

Digital electronics which record the signals shape are crucial for the PSA. The measured traces with the length of 1 µs (100 ADC samples each 10 ns) are compared to a reference database. The adaptive grid search algorithm [109] is used to identify the signal in the base, which is the closest to the measured one. The implementation of the algorithm used on this

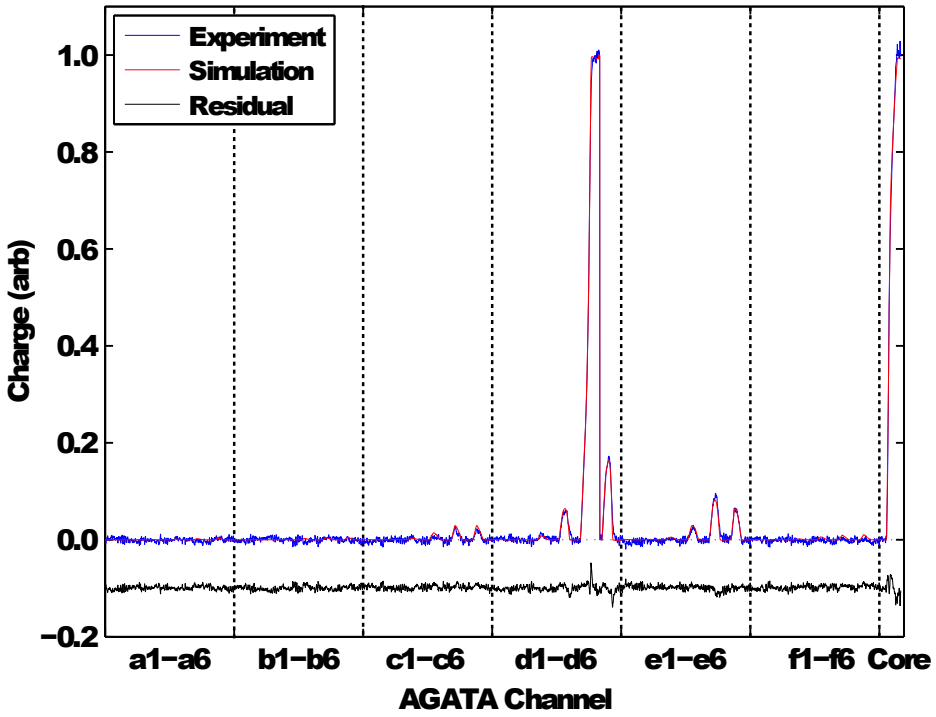

Figure 2.16: Averaged pulse form for 36 segments and the core of an interaction in the true coaxial part of an *AGATA* detector (blue) compared to the simulated signal form (red). The difference between the simulated and measured signal is drawn in black and shifted by a constant. The segments are labelled with a letter number combination. A single hit in d5 is shown. The transient signals in the neighbouring segments have a smaller amplitude and return faster to the base line. Figure taken from Reference [84].

thesis only supports single hits in a segment. Multiple hits will be treated like a single hit, with a potentially wrong interaction position.

The position resolution of the PSA depends on the energy. Higher energies lead to a lower position uncertainty. The typical position resolution of an *AGATA* crystal is 5 mm FWHM [110, 111].

Gamma-ray tracking

The pulse shape analysis provides the interaction point[1], and the energy deposited in a segment. A tracking algorithm is used to reconstruct the trajectories of the γ ray in order to determine their energy and direction. Due to the position uncertainty of the PSA and the possibility, that not the total charge is detected, the reconstruction is done by a dedicated software procedure. Currently, there are two different versions of the tracking algorithm available for *AGATA*: **O**rsay **F**orward **T**racking (OFT) [112] and the **M**ars **G**amma

[1] the algorithm used in this thesis "Adaptive Grid Search" provides only one hit per segment. A newly developed "Adaptive Grid Search two hits" algorithm can also handle two interaction points per segment

Tracking [113]. Both share the same principle of forward tracking.

The first step of the tracking algorithm is to group the interaction points in the crystal, deduced by the PSA, into clusters in the (Θ, Φ) plane. The clusters are chosen based on their angular separation, which is adapted depending on the multiplicity of interaction points. The Compton cross section has a maximum at forward scattering and the mean free path of a γ ray decreases with decreasing energy, hence each cluster is treated independently. For each cluster and each permutation of the interaction points using the target position as the source of the γ ray, a figure of merit is calculated. It is based on the distance and the interaction probability of the γ ray between the interaction points, the Compton and the photo-electric effect cross sections and for the Compton scattering a compliance of the deposited energy and the scattering angle. The interaction sequence with the best figure of merit is chosen as the γ-ray track. If the figure of merit of the reconstructed γ ray is over a certain threshold, it is accepted. Otherwise, the interactions are rejected. The threshold influences the peak-to-total ratio and the efficiency. Figure 2.17 illustrates the interaction path and the information calculated by the tracking algorithm.

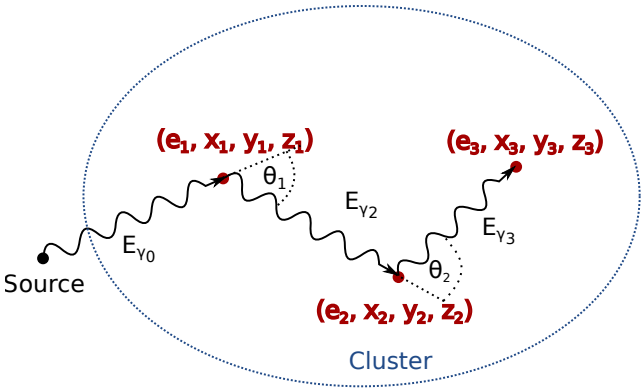

Figure 2.17: Schematic example of the tracking of a cluster (inside the big dashed oval) of a γ ray $E_{\gamma 0}$. It undergoes two Compton scattering (position 1 and 2) and gets totally absorbed via a photoelectric effect at point 3.

Passive materials, like the target-chamber, absorbers, the end cap and the crystal encapsulation affect the tracking procedure. Simulations show, that the effect is at the same level for both γ-ray tracking and conventional spectrometers. However, at low energies, where the Rayleigh scattering has a non-negligible cross section, the change in direction can produce a wrong interaction path.

3 Presorting and calibration

This chapter presents the presorting of the data and calibration of the detectors described in the previous chapter: *PRISMA* (section 3.1), *DANTE* (section 3.2) and the *AGATA* array (section 3.4).

3.1 PRISMA spectrometer

The *PRISMA* spectrometer identifies the atomic number, mass and charge state of the beam-like ion entering it. The spectrometer also provides the ions velocity vector. The start detector and the focal plane detection system provide the entrance and focal plane position, the time of flight through the spectrometer, the total energy and the energy loss. Afterwards, the calibrated positions and the time of flight can be used to deduce the charge and the mass of the ion.

As a first step of the ion identification, the individual detector systems of the *PRISMA* spectrometer are calibrated. The measured information is used as a second step to identify the ion. Empirical corrections are applied to improve the mass resolution. At the end of this section, the experimental yield of the ^{82}Se+^{198}Pt reaction identified in the present experiment is presented as the outcome of the calibration procedure of the *PRISMA* spectrometer.

3.1.1 MCP start detector

The detector consists of a carbon foil, where the ions pass through, and a MCP detector, read out by two orthogonal delay lines measuring the entrance point (x, y). Upstream of the carbon foil, a mask having 5 reference points is mounted. The mask is permanently installed inside the detector a few mm away from the foil and thus also used for monitoring eventual drifts in the position during the experiment. The position on the carbon foil is calibrated according to the reference positions given in Table 3.1. The centre of the cross is close to the centre of the trajectory. Before the calibration of the x and the y signals a linear transformation is applied in order to rotate and stretch the raw coordinates: $(x', y') = A \cdot (x, y)_{\mathrm{raw}}$. The transformed coordinates (x', y') are calibrated using a linear polynomial (y coordinate) or a cubic polynomial (x coordinate). The parameters for the calibration and for the transformation are obtained by a least-square fit of the distance

between the calibrated points and the reference points.

	position x (mm)	position y (mm)
centre	0	0
top left	-21.5	26.5
top right	21.5	26.5
bottom left	-21.5	-26.5
bottom right	21.5	-26.5

Table 3.1: References positions of the cross installed in the MCP start detector. Taken from Reference [114].

Figure 3.1 shows the calibration procedure. On the left side the calibrated points are shown together with the reference points. For improving the fit, additional reference points on the half length of the arms of the cross and nails, which are installed in centre if the beam tube, are used. Since these points are not real reference points, the uncertainty of the position of these points is increased for the fit. Without these additional reference points, there are more parameters than reference points for the fit.

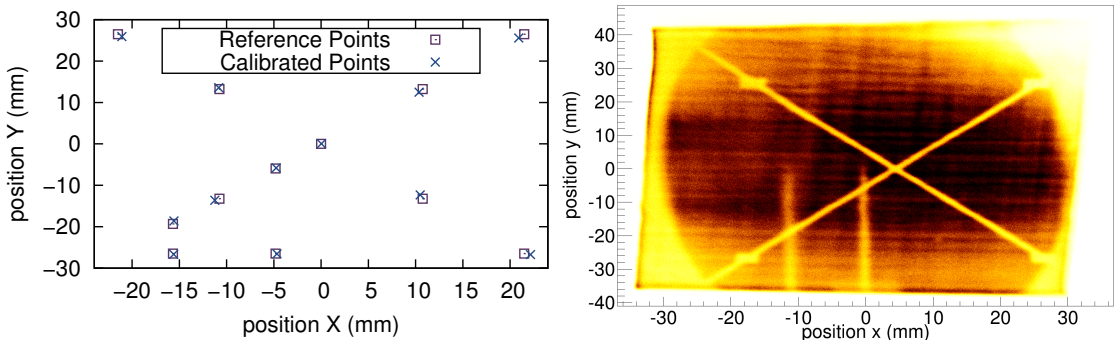

Figure 3.1: (left) Illustration of the calibration procedure of the MCP. The reference points are drawn as red squares and the data points after the fit are plotted as red crosses. The calibration parameters are obtained by a least-square fit of the distance from the calibrated data points to the reference position. (right) The calibrated position of the MCP. The calibration is shifted in order to have it on the central trajectory.

The final position of the reference points is found by shifting the position and optimising the Doppler correction. The final calibrated points are shown in Figure 3.1 (right).

3.1.2 Multi wire parallel plate avalanche counter

Three different signals for each section determine the position on the x axis on the focal plane: left, right and cathode. Since only two signals are needed for the determination of the position, a missing signal can be reconstructed by using the remaining two signals.

The first step is to select only events with a real signal. Therefore, a common threshold is applied for all the signals provided by the MWPPAC. All signals with an amplitude smaller than the threshold are discarded. Since the sum of the left and right signals must have the same amplitude as the cathode signal, a condition is placed for the sum of the left and right signals: in case, that either the left or the right signal is missing, the remaining value is reconstructed by subtracting the available signal from the cathode signal. Hence, the condition includes events, where the signals correspond to each other and the events, where the sum of the left and right signal is lower than the cathode. Figure 3.2 (left) illustrates this condition for the section 5. The wires are used as a reference position for the calibration of the MWPPAC: they appear as valleys in the spectrum and are mounted equidistantly. The final reconstructed spectrum of the x position in the focal plane x_{fp} is shown in Figure 3.2 (right).

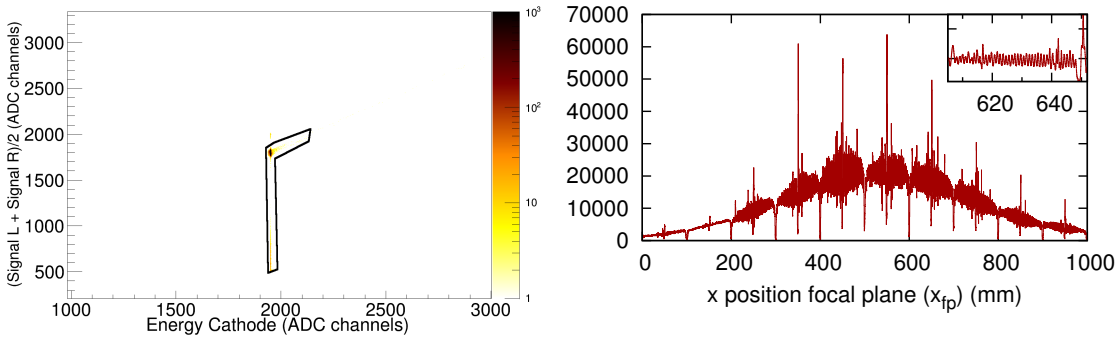

Figure 3.2: (left) Selection of valid events for the reconstruction of the position of the MWPPAC. (right) The final spectrum of the position on the focal plane x_{fp}. The inset shows the details of the spectrum, including the effect of the wires.

Time of flight

The **T**ime **O**f **Fl**ight (TOF) of the ions is measured by the time difference between each section of the MWPPAC (start signal) and the MCP (delayed stop signal). The signals of the 10 **T**ime to **A**mplitude **C**onverters (TAC) are calibrated using a linear transformation from ADC values to ns. The sections are aligned to each other by adjusting the offset between them. The final TOF has an additional common offset and is chosen so that elastic scattering of the beam-ions has the correct velocity. For this purpose the centre of the MCP is selected and the velocity is calculated for the central trajectory. In Figure 3.3 the final TOF is plotted against the x position on the focal plane x_{fp}. The different masses can be seen as diagonal parallel lines in this plot.

The fine tuning of the TOF offset is done by optimising the Doppler correction for the peaks of dominant transitions in ^{82}Se ions entering the *PRISMA* spectrometer.

Drifts in the TACs Certain TACs, corresponding to the MWPPAC sections 7-10 exhibit a shift in the spectrum mid-experiment (see Figure 3.4): all peaks have after the shift a different offset. It leads to shifts in the mass spectra and also affects the prompt peak

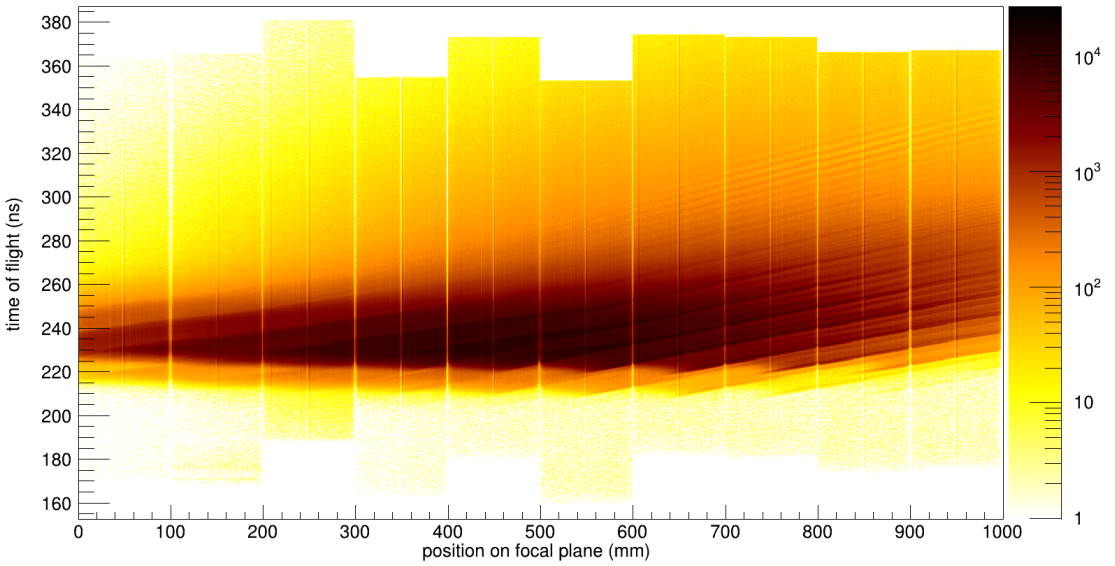

Figure 3.3: The final spectrum of the time of flight is plotted against the position on the focal plane. x_{fp}

position of the corrected γ-*PRISMA* coincidence peak in the time spectrum. For each TAC a matrix between the time stamp and the TOF gated on the beam nucleus is produced for extracting the shifts. A correction parameter is extracted by aligning the TOF before and after the shift. A similar drift in the TAC spectrum of the *PRISMA* spectrometer was observed before [74].

3.1.3 Ionisation chamber

A calibration or alignment of the ionisation chamber was performed neither just before nor after the experiment. For the measurement of the energy and the energy loss of the ions, a good alignment between the 40 pads is necessary. For the analysis of this experiment the alignment coefficients for a previous experiment is used. The alignment shows small misalignments for the pads. Hence, instead of a global threshold, for each pad an individual threshold is applied.

Besides the small misalignments, some pads have a wrong gain coefficients. These can be seen in the $\Delta E - E$ plot and the charge state selection, as plotted in Figure 3.5 (left). The coefficients are recalculated for these pads. Only the central trajectories of the beam ions with a small energy loss are selected and in the plot of the focal plane position versus the energy loss in a certain section the different charge states appear as thin lines. A discontinuity in these lines reveals the misalignment of the pads. The alignment coefficients are adjusted to obtain continuous lines. The charge state selection plot using the recalibration shows less distortion (see Figure 3.5 (right)) and the charge states can be selected with less contamination.

One of the pads (C0) was malfunctioning, it was firing only occasionally and with a signal resulting in an overflow at the ADC. This segments signal is set to 0 for all the events. All

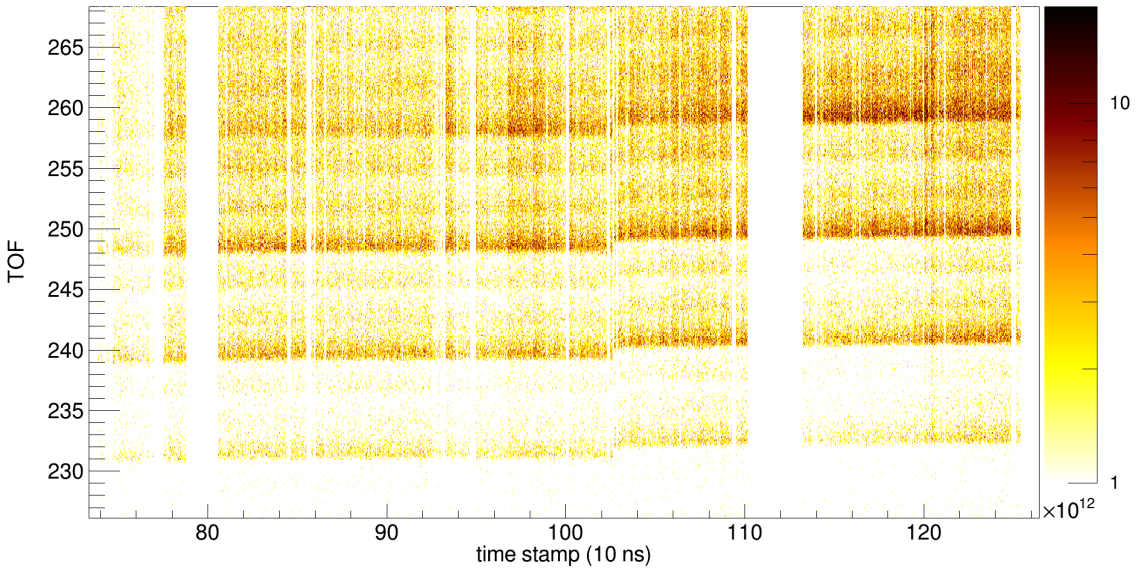

Figure 3.4: The drift in the TAC of the 10^{th} section of the MWPPAC before applying the correction.

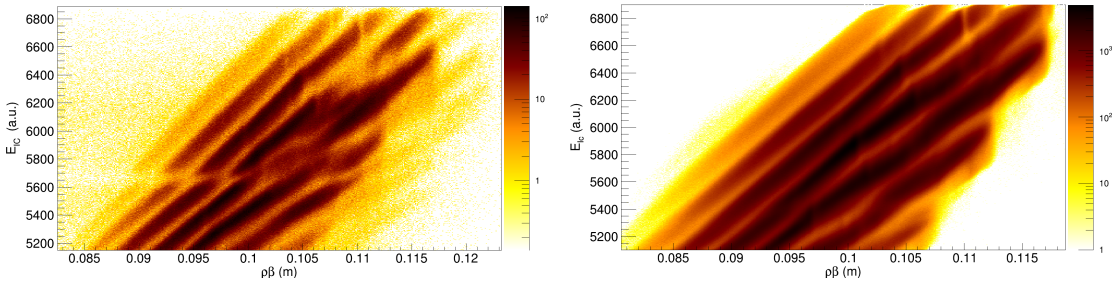

Figure 3.5: (left) Due to a misalignment of some pads of the ionisation chamber, the matrix for selecting the charge state (see 2.2.1) shows a tail overlapping with other charge states. (right) The same matrix, but with the applied corrections discussed in the text.

additional pads, when not firing in coincidence with surrounding pads with an an energy close to the ADC overflow are set to 0. Additionally, all events in which more than 2 pads in the first row firing are vetoed.

Side pads

The four pads on each side of the ionisation chamber are read out. These pads are only used to veto an event with a partial energy release in the ionisation chamber. Therefore, no gain matching was performed before the experiment. The ADCs used for digitising the signals of the side pads show a pedestal. An individual threshold in the measured energy of each pad is applied. All events with an energy above the threshold in at least one side pad are discarded. The spectra with the threshold indicated as a red background are drawn in Figure 3.6.

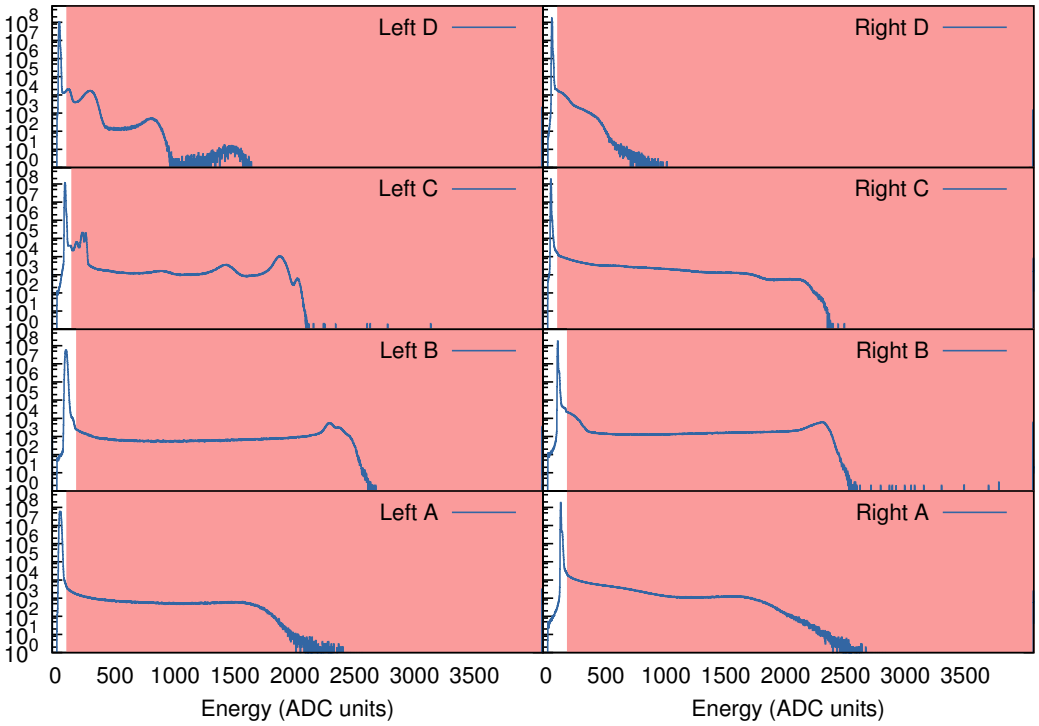

Figure 3.6: Spectra of the side pads. The events inside of the red marked area serve as a veto for the energy measurement in the ionisation chamber.

3.1.4 Empirical corrections

For improving the mass resolution, empirical corrections are applied. These include corrections for the approximate reconstruction of the trajectory, the magnetic aberration and

drifts in the electronics. The procedure foresees the construction of a matrix of the mass versus a chosen parameter and then correct the effect for the dependence of the mass spectra from this parameter. The resulting correction parameters are used to eliminate the non-physical dependences of the reconstructed masses of the position entrance and focal plane position. Using the same method with the duration of the experiment, represented by a time stamp, the drifts can be corrected.

Effective quadrupole length

Even though the magnets of the *PRISMA* spectrometer are manufactured to have a linear field, higher order magnetic fields and fringe fields play an important role in the transportation of the ions to the focal plane. The trajectory reconstruction uses only the first order approximation for the ion optics and furthermore uses continuous straight lines and a circular motion in the dipole for the length calculation. This leads to aberrations, which can be partially treated by using an effective length and position of the quadrupole. The optimisation is done by hand, by changing these values and looking at the resulted mass spectra with respect to the entrance position and focal plane position. The values, which introduce the smallest aberration are used: effective quadrupole length $L_{Q,eff} = 470\,\mathrm{mm}$ and distance of the target to the quadrupole $L_{Q,dist} = 505\,\mathrm{mm}$.

Aberrations

The change of the effective quadrupole length helps to decrease the effect of the aberrations. However, the reconstructed mass depends on the position at the start detector and the focal plane position due to the approximate treatment of the transmission through the magnets. For selecting unambiguously a certain mass, several empirical corrections are applied. The common procedure is to apply a cut on ^{82}Se and produce a matrix of a position (MCP, focal plane) versus the mass-over-charge ratio.

First, the aberrations in respect with the entrance position measured by the MCP start detector are corrected. A matrix of the x entrance position versus the mass-over-charge ratio is produced. For each bin of the matrix, the maximum value is determined. A least-square fit of an 11^{th} order polynomial on these points is performed. The polynomial is used to correct the mass-over-charge ratio. Afterwards, the corrected mass is plotted against the y position on the MCP detector. The same procedure is done using a 4^{th} order polynomial (see Figure 3.7 top and centre).

For the aberrations regarding the x position on the focal plane, a simple fit of one line is not possible, since there is no single mass-to-charge which is detected on all focal plane positions. Hence, a 6^{th} order polynomial is fitted simultaneously for several mass-to-charge ratios. This polynomial is used to correct the final mass-to-charge ratio. Figure 3.7 shows the matrices and the fitted functions. In this figure the decreasing width of the line is visible.

Side effects on the sections of the MWPPAC Figure 3.7 bottom right shows the mass-over-charge ratio plotted versus the x position on the focal plane. At the sides of the MWPPAC, the mass-over-charge ratio bends up. This leads to a tail in the final mass spectrum. In order to overcome this effect, for each point on the x position on the focal

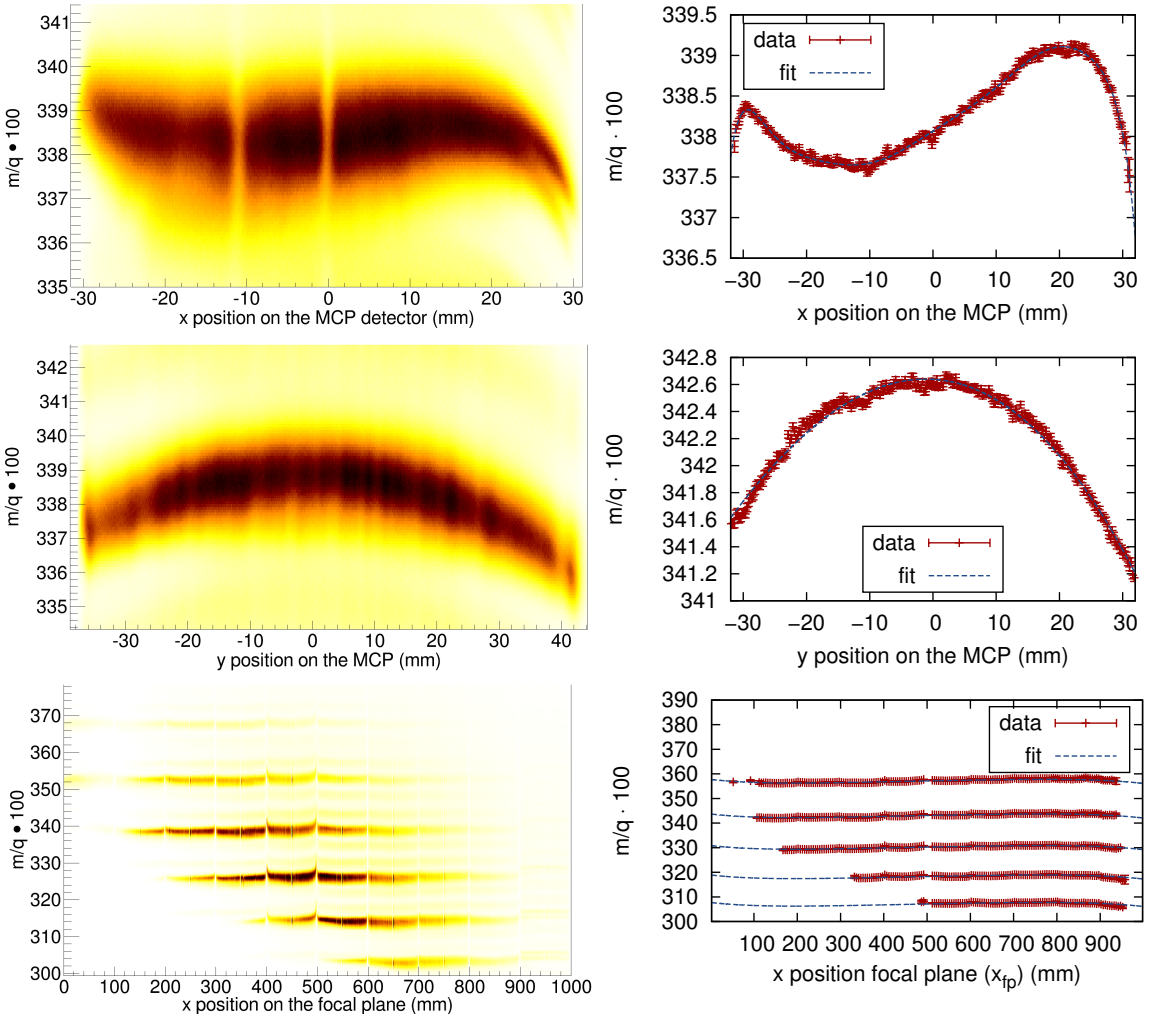

Figure 3.7: Procedure for the empirical correction of the aberration. On the left side, a matrix of the various positions versus the mass-over-charge ratio is drawn. The right side shows the position of the maximum for each position and the fitted polynomial. From the top to the bottom: MCP x position, MCP y position and x position in the focal plane. The mass resolution improves successively from top to bottom.

plane a correction coefficient is deduced. This correction removes fully the dependence of the mass-over-charge ratio on the position of the ion in the spectrometer.

Drifts in time of the mass-over-charge ratio

A drift in the mass-over-charge ratio is observed over time. Instead of analysing runs with similar shifts, a time dependent correction is applied. A matrix of the mass-over-charge ratio plotted versus the timestamp is produced and a time dependent correction factor is deduced. Figure 3.8 shows the drift and shifts of the mass-over-charge ratio for the whole experiment. Most of the shifts can be identified with changes of the experimental run.

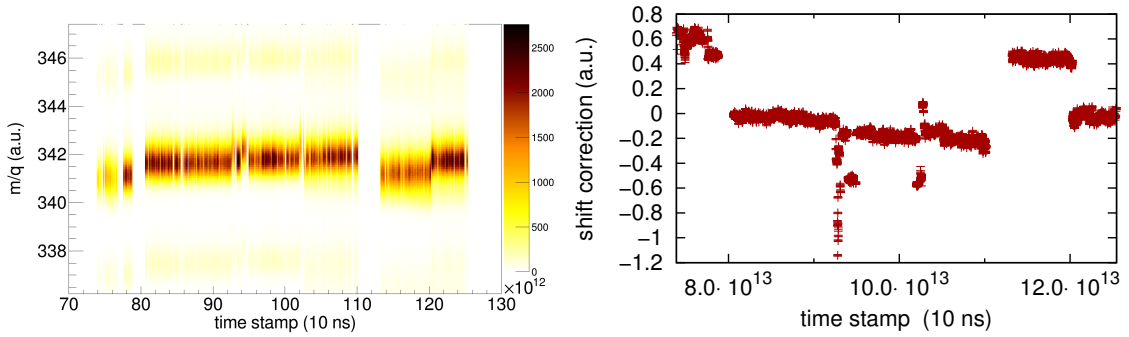

Figure 3.8: (left) The drift in the mass-over-charge ratio over time of the experiment, expressed in time stamps, is illustrated for the mass-over-charge ratio for $^{82}Se^{24+}$. A general drift is observed with some abrupt changes, which can be mostly identified with the changes in the experimental runs. (right) The deduced correction for the mass-over-charge ratio with respect to the experimental time allows to shift the mass-over-charge ratio to a value, which is constant over time.

The drift over the duration of the experiment is in the order of 2% of the measured mass.

3.1.5 Identification of the ion entering PRISMA

The identification of the recoil with Z, q and A is done by placing consecutive gates on different matrices. First the atomic number gets selected, than the charge state and finally from the resulting mass-over-charge ratio, the mass number can be deduced.

Atomic number

The ionisation chamber consists of 4 rows of each 10 pads for the measurement of the energy loss and total energy. Figure 3.9 shows the gates applied on the energy loss measured in the first row versus total total energy measured by the whole ionisation chamber. The conditions for the atomic number cuts are indicated. For higher energetic ions, the energy loss can be measured by the sum of the first two rows. The higher energy loss results in a better separation of the atomic numbers and hence a second cut on the energy loss measured by the first two rows is additionally used for these events.

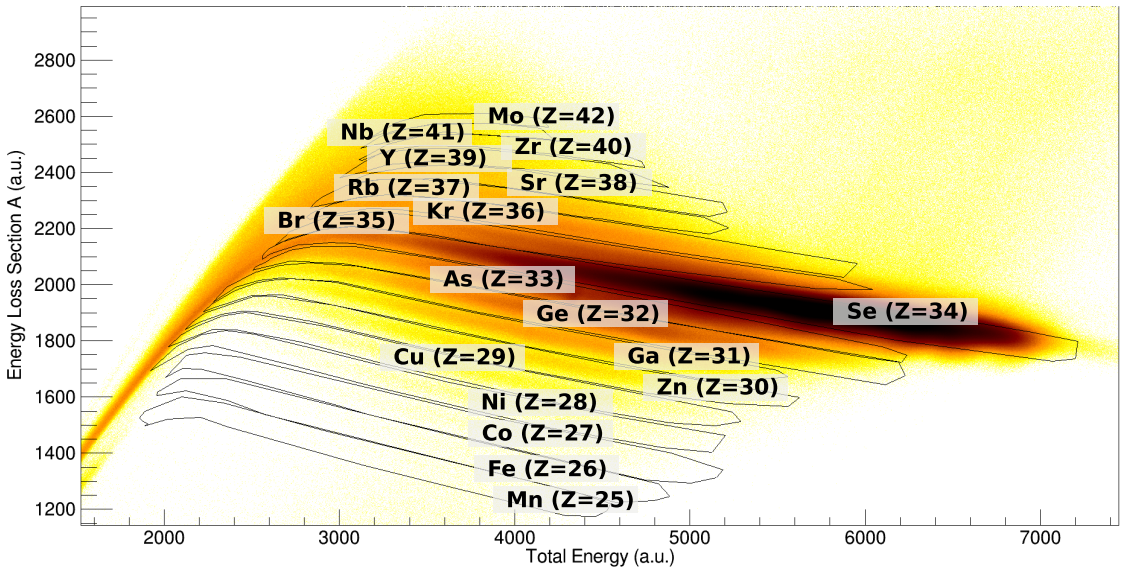

Figure 3.9: Matrix of the total energy measured by the ionisation chamber versus the energy loss in the first row (A) of the ionisation chamber. The gates for the selection of the different atomic numbers are indicated.

Charge state selection

As described in section 2.2.1, the product of the bending radius of the ion ρ, its velocity β and the charge state q is proportional to the total kinetic energy. For the selection of the charge state, a matrix of $\beta\rho$ versus the total energy measured in the ionisation chamber is produced. Figure 3.10 shows this matrix for the germanium isotopes. Each diagonal line represents a charge state and a tight gate on this line is used to select the charge state.

Reconstruction of the mass

Each gate on an atomic number and a charge state provides a mass-over-charge spectrum. Figure 3.11 shows the mass-over-charge spectra for each charge state of the germanium recoils.

Due to nonlinearities, a multiplication with an integer charge does not provide the best result. Hence, for each charge state an effective charge state is used. Additionally, a common offset for all the mass-over-charge spectra is applied. For each charge state q_i, the mass number is calculated by

$$A = q_{eff,i}(offset + (m/q)_i) \tag{3.1}$$

The effective charge state $q_{eff,i}$ is found by looking at the γ-ray spectra for a known unique strong transition.

The obtained masses are plotted in Figure 3.12. The peaks in the mass spectrum have a FWHM resolution between $\frac{\Delta M}{M} \approx \frac{1}{240}$ and $\frac{\Delta M}{M} \approx \frac{1}{280}$ for the whole range of transfer channels (see insets). This value is close to the design value of the *PRISMA* spectrometer

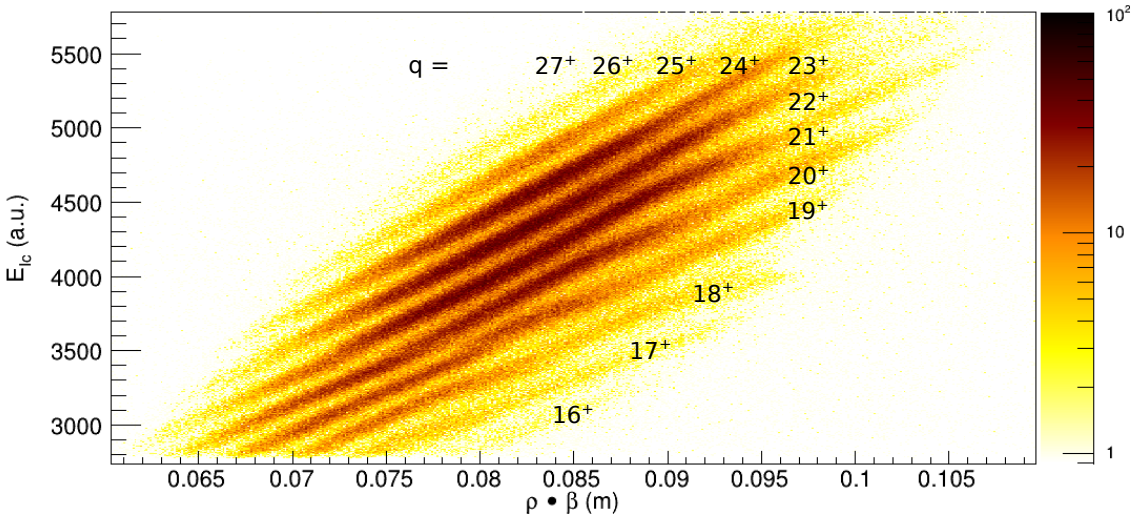

Figure 3.10: Matrix of the energy for the selection of the charge states, gated on the atomic number $Z = 32$. The product of β and ρ is plotted against the total energy measured by the ionisation chamber. Each of these diagonal lines represent a charge state and has been indicated in the plot.

of 1/300 (see section 2.2.1). The different peaks in the mass spectrum show no overlap and hence no contamination of the neighbouring masses are visible in the γ-ray spectra.

3.1.6 Yield of the beam-like recoils

The procedure for obtaining the mass distribution is done for all the atomic numbers. The result is the experimental yield of the beam-like recoils produced in the reaction. Due to the acceptance of the *PRISMA* spectrometer the yield is not directly related to the cross section. For the cross section estimation, a detailed simulation of the response function of *PRISMA* needs to be performed [98].

The yield measured in this experiment is depicted in Figure 3.13. One can observe a transfer of up-to 24 nucleons. A statistics of $\approx 10^4$ ions for a specific A and Z is in most cases sufficient for the observation of γ-ray transitions in the corresponding nucleus.

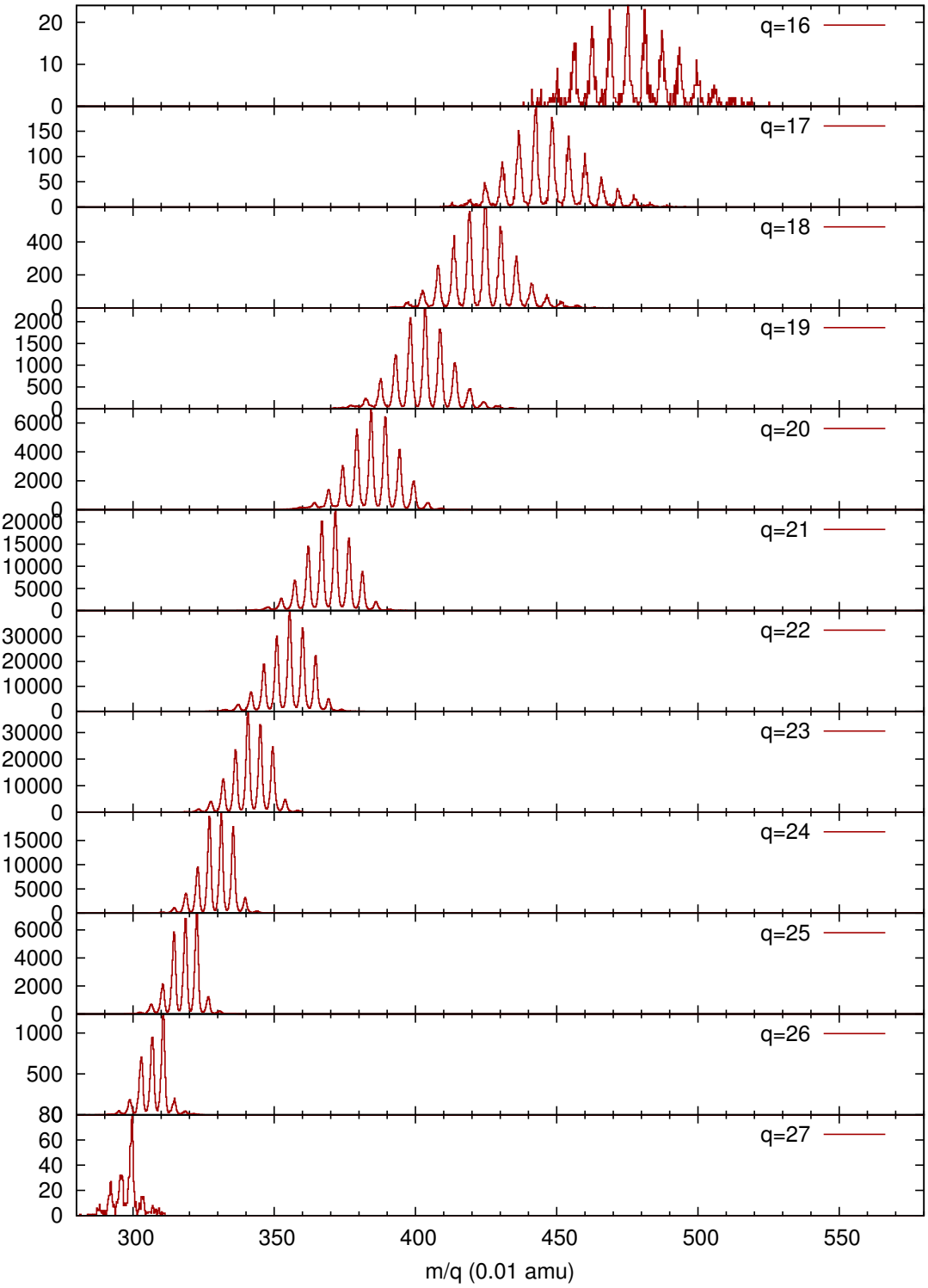

Figure 3.11: The mass-over-charge ratio for the different charge states of the germanium isotopes ($Z = 32$) as identified in Figure 3.10.

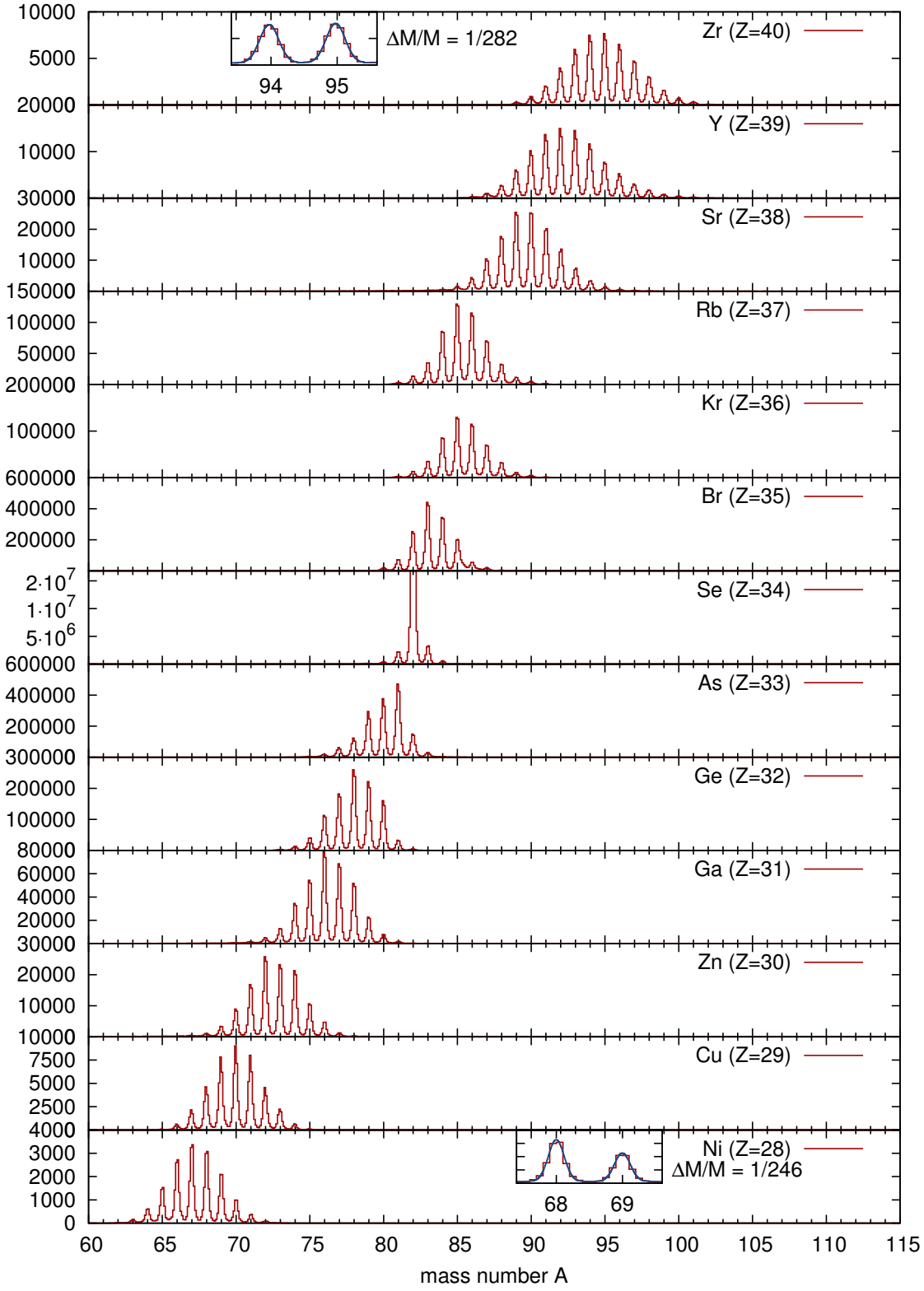

Figure 3.12: Spectrum of the masses for each an atomic number. The peak of ^{82}Se is only partially shown in order to make the neutron-transfer channels visible. The inset on the top and the bottom highlights the obtained mass resolution.

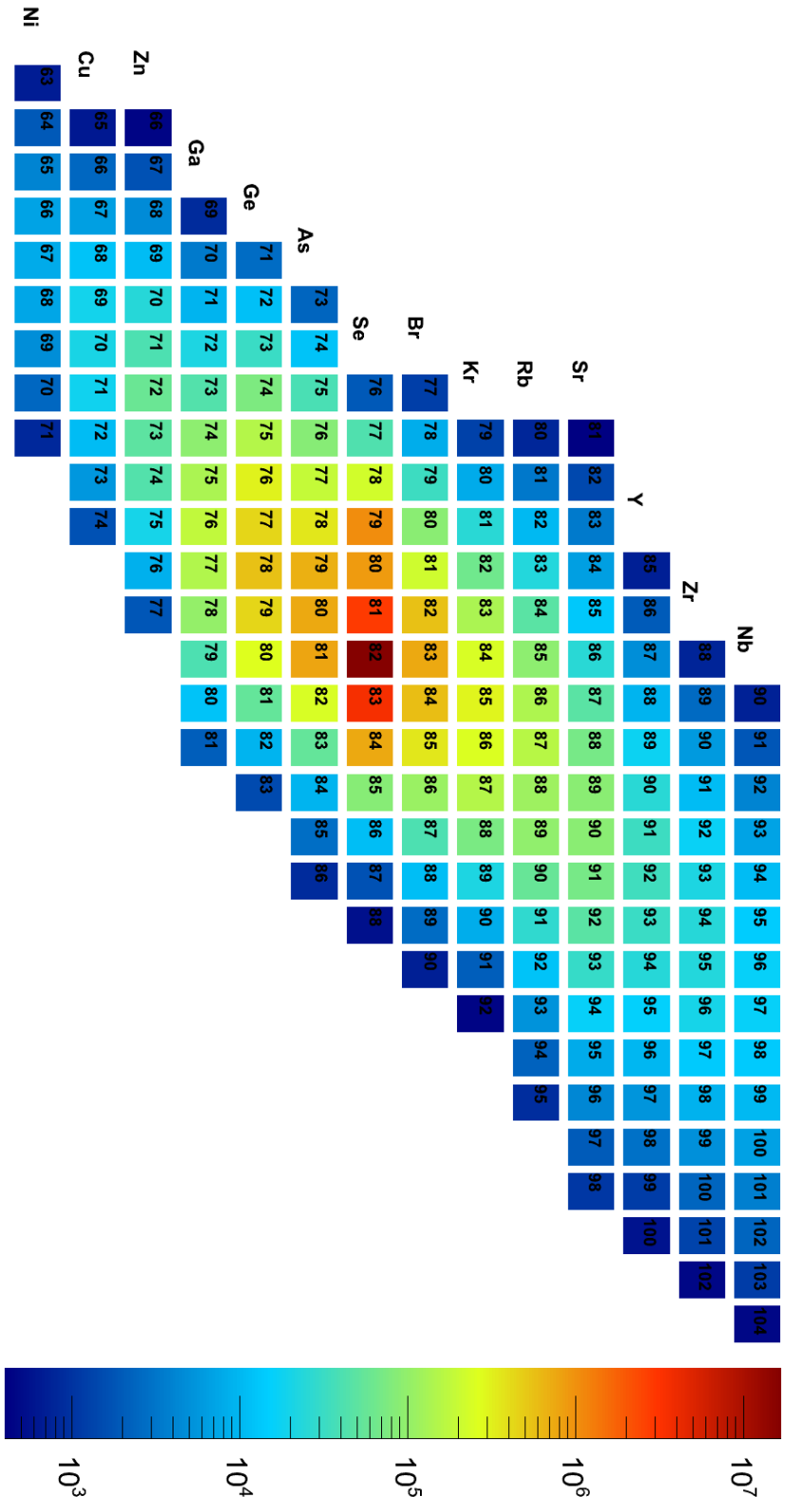

Figure 3.13: Yield of the beam-like recoils identified in the *PRISMA* spectrometer in coincidence with the *AGATA* demonstrator.

3.2 DANTE array

Each *DANTE* detector provides 4 different information: the position of the ion (x, y coordinates), its time of arrival and the amplitude of the signal. The time between opposite placed *DANTE* detectors is measured by a TAC. Due to the construction similar to the MCP start detector, a similar calibration procedure is used (see section 3.1.1).

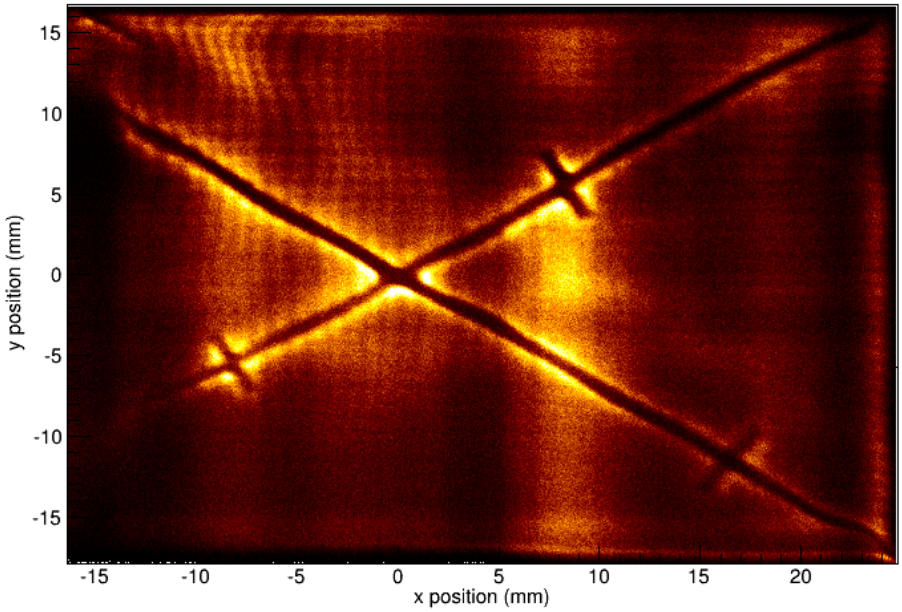

Figure 3.14: The measured distribution of the hits on the 2nd *DANTE* detector. The cross with its reference positions is visible as a shadow. The left side is shadowed by the target holder.

For the calibration a plastic mask is mounted on the top of each *DANTE* detector. The mask is a cross centred at the middle of the detector with 4 calibration points on the legs of the cross. The mask and the points are visible as a shadow on the MCP. Their reference positions are given in Table 3.2. Only events with physical valid signals are selected by placing a condition on position lying on the MCP of each *DANTE* detector. The uncalibrated points are then fitted to their reference position, by minimising the squared distance of the calibrated point from the reference position. Due to the linearity of the position information and the amount of reference points, a linear calibration is used. Figure 3.14 shows the distribution of the hits on the 2nd *DANTE* detector.

3.2.1 Spatial position

In the present experiment the *DANTE* structure, which holds the detector on a cone with an angle of 58° with respect to the beam axis is used. The interaction positions on each detector are translated to match the physical position in the *PRISMA* reference frame by a sequential rotation and translation. Using the positions calculated in this way one can

	position x (mm)	position y (mm)
centre	0	0
top left	-16.48	11.33
top right	8.24	5.66
bottom left	-8.24	-5.66
bottom right	16.48	-11.33

Table 3.2: References positions of the cross mounted on top of each *DANTE* detector.

perform the Doppler correction. Figure 3.15 shows the positions of the *DANTE* detectors from a virtual observer at the entrance position of the *PRISMA* spectrometer.

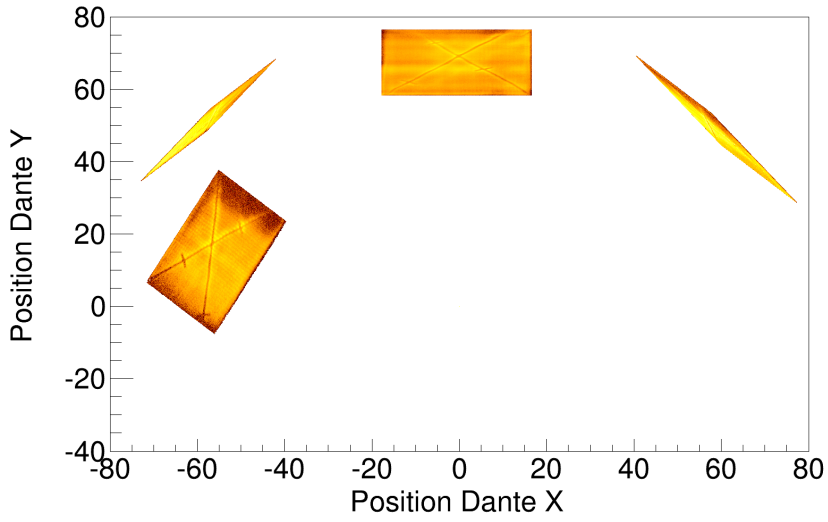

Figure 3.15: View from a virtual observer placed at the entrance position of the *PRISMA* spectrometer looking at the *DANTE* structure. The target is positioned at the point $(0, 0)$.

3.2.2 Time of flight calibration

The calibration of the time of flight between the detectors uses peaks associated to beam pulses in the recorded time spectrum of the coincidences between *DANTE* and *PRISMA*. The ALPI accelerator operates the cavities with a frequency of 80 MHz, which corresponds to a time difference between two pulses of 12.5 ns. In the time spectrum of Figure 3.16 on the right side eight small peaks appear. Using this information a linear calibration can be extracted with a channel in the *DANTE* time spectra corresponding to ≈ 0.1016 ns.

3.2.3 Separation of TLF and BLF

Two *DANTE* detectors are on the opposite site to the entrance window of the *PRISMA* spectrometer. Hence, the binary partner of the ion entering the *PRISMA* spectrometer can be detected on one of those two detectors. In the time difference spectrum between the *DANTE* detectors and the MCP start-detector, two peaks can be identified: one, when the beam-like fragment enters the *PRISMA* spectrometer and a second one, when the target-like recoil hits the start detector. In Figure 3.16 the two peaks are highlighted.

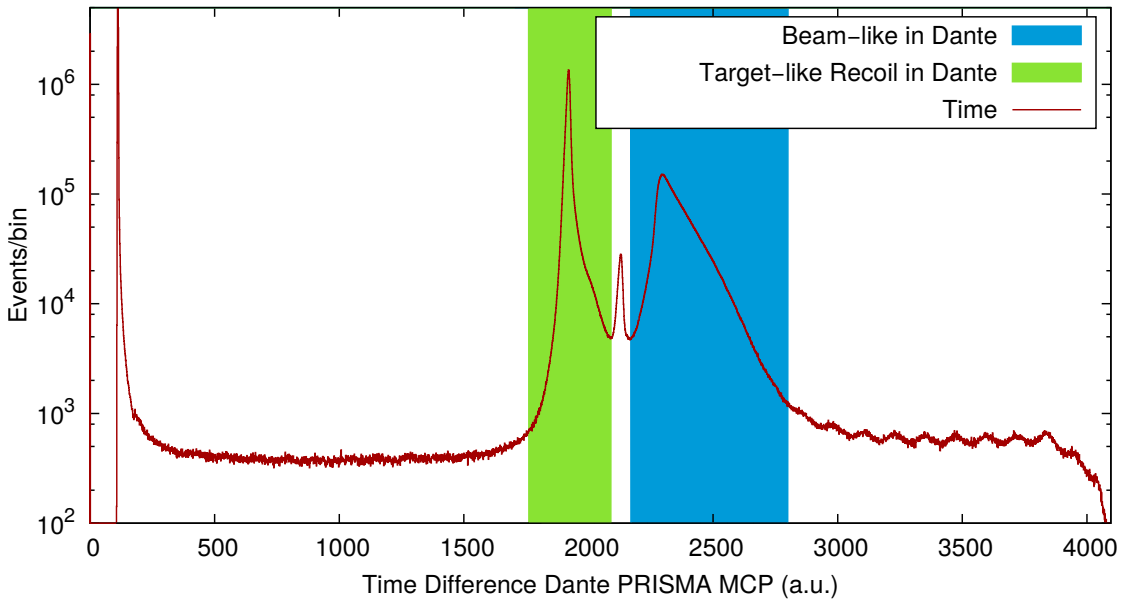

Figure 3.16: Separation of the beam-like recoils from the target-like recoils using the time spectrum of the MCP start-detector - *DANTE* coincidence.

For the second trigger condition, i.e. two kinematical opposed *DANTE* detectors, a similar condition is not possible.

In this thesis no further discussion on the *DANTE* array is done and its results will be discussed in further publications.

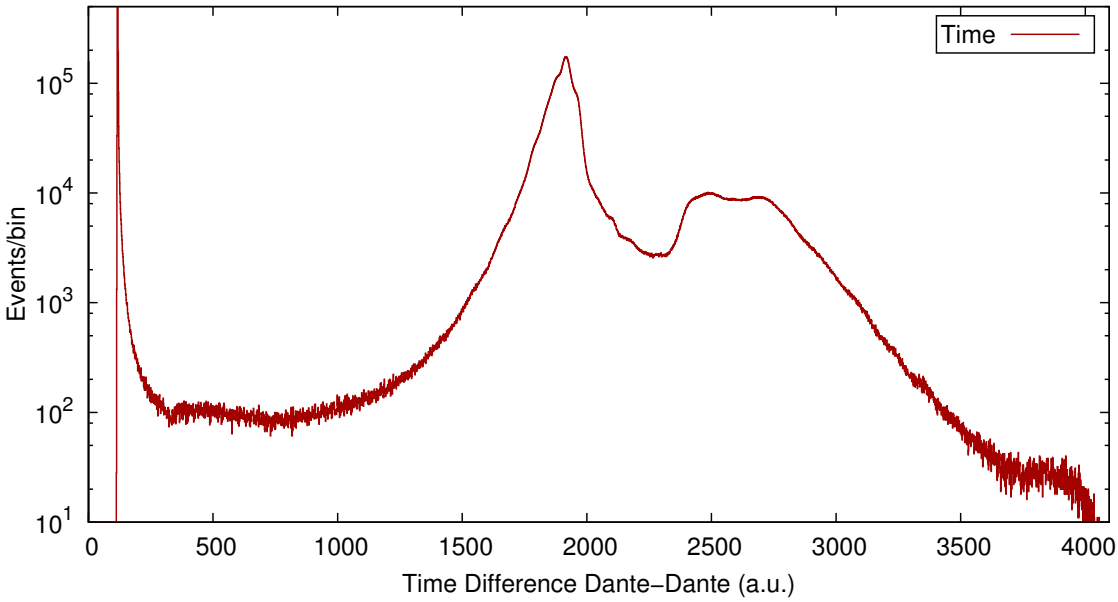

Figure 3.17: Time spectrum of the *DANTE-DANTE* coincidences.

3.3 Time difference between γ-rays and heavy-ion detectors

The γ rays are measured in coincidence with a heavy ion detected in either the *PRISMA* spectrometer or the *DANTE* array. These heavy ion detectors are complementary detectors for the *AGATA*. For the selection of the promptly emitted γ rays the time information of the complementary detectors and the *AGATA* is recorded in terms of timestamps.

3.3.1 Removal of the phase difference

The data of the complementary detectors and *AGATA* are merged on the basis of the timestamp: all events lying on a window of 2200 µs are considered as being in coincidence. The clock rate for the timestamps is 100 MHz, i.e. each 10 ns the timestamp is increased by one. An intrinsic jitter of 10 ns exists between the complementary detectors and *AGATA* after the merging. To overcome this limitation of the time difference resolution a logical signal of the validation was returned to the VME crate of *PRISMA* and digitised by a TDC. This signal gives the phase difference between the two systems which is calibrated in the offline sorting. The matrix of the time difference of complementary detectors and *AGATA* versus the phase is sorted (see Figure 3.18 (left)). For each channel in the phase spectrum, a time difference projection is produced. The mean value of each projection is calculated. A linear fit on these obtained values provides the calibration (Figure 3.18 (right)). This

calibration of the phase signal is used to correct the time difference between *AGATA* and complementary detectors.

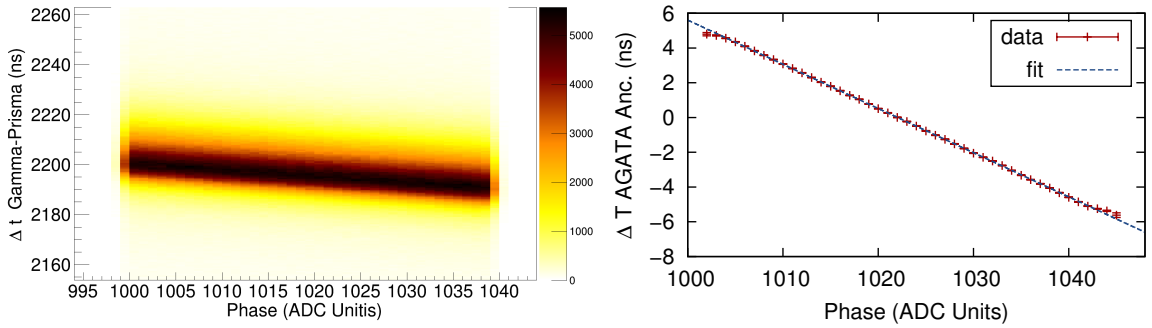

Figure 3.18: (left) Matrix of the time difference of complementary detectors and *AGATA* versus the phase. (right) Linear fit of the phase versus the time difference of complementary detectors and *AGATA*.

3.3.2 Adjusting the trigger time for PRISMA

The trigger condition for the *PRISMA* spectrometer is that an ion arrives at the focal plane, i.e. one section of the MWPPAC fires. Hence, the differences of the time of flight of ions in *PRISMA* broadens the prompt peak for the coincidence between *PRISMA* and *AGATA*. To overcome this effect, the time of flight for each ion is subtracted from the time difference. Additionally, the time difference depends on which section fires. As a correction, the trigger time of all sections are aligned to each other, in order to increase the resolution of the prompt peak. Figure 3.19 shows the prompt peak in coincidence with *PRISMA* without the corrections, by subtracting the TOF and by adjusting the trigger times.

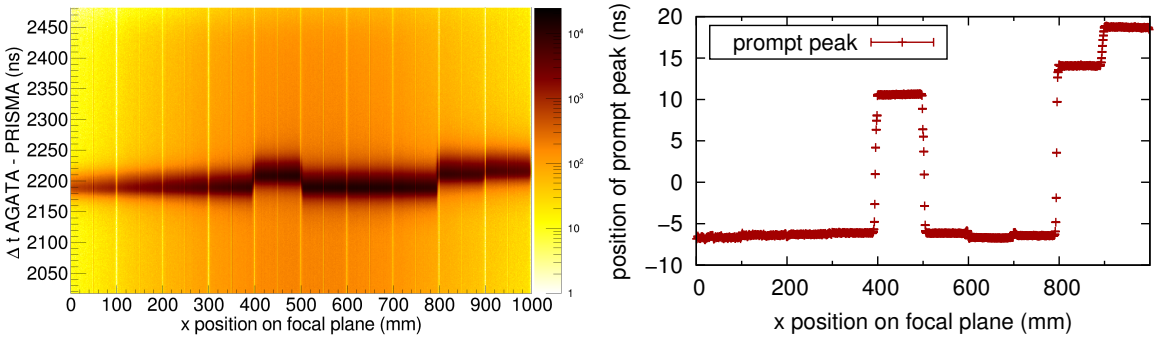

Figure 3.19: (left) Matrix of the reconstructed time difference of complementary detectors and *AGATA* versus the x position on the focal plane. (right) Deduced shift for each position. These values are used to straighten the line.

3.4 AGATA spectrometer

The analysis of the *AGATA* data starts from the recorded traces of the signals for the 36 segments and the 2 gains of the core signal of each of the 15 crystals. From this information the position and energy of each interaction is deduced via a pulse shape analysis. The obtained hits in the detector volume are passed to the tracking algorithm, which provides a list containing the reconstructed γ rays. Due to the conceptual differences with a traditional γ array, the procedure of the calibration and data analysis is very different and is described in detail in the following sections.

3.4.1 Energy calibration

Each *AGATA* crystal is segmented into 36 outer contacts (segments) with a common core contact. The preamplifier of the central core contact has two different gain outputs. The energy calibration has to be done for each channel. Therefore, for the full *AGATA* demonstrator, as present for this experiment, $(36 + 1 + 1) \cdot 15 = 570$ channels are present.

The energy calibration was done by placing a strong ^{60}Co source in front of *AGATA*. The recorded data is sorted into energy spectra for each preamplifier, with a condition, that just one segment per crystal fires. This condition allows to treat each segment as an individual detector. In each spectrum the peaks of the 1173.2 keV and 1332.5 keV transition are automatically fitted with the program *Recal* [115]. A linear fit with no offset is used. The calibration coefficients are applied to the energy information and also to scale the recorded traces used for the PSA. For the core signals a ^{152}Eu source was used to refine the calibration, where 10 peaks are used for the least-square fit.

3.4.2 Crosstalk correction

If the γ-ray energy is deposited in more than one segment in the same crystal, the observed sum energy of the segments is smaller than in case of a single segment firing, i.e. the segments energy sum is shifted to lower energies. The dependence of this shift is nearly linear with respect to the segment multiplicity [116]. A ^{60}Co source was placed in front of the *AGATA* spectrometer. The crosstalk correction coefficients are obtained by sorting the energies recorded in the segments with respect to the numbers of firing segments and deducing the shift from the nominal energy of the two strong transitions of the ^{60}Co source. The derived matrices are used for the correction of the measured energies and the restoration of the baseline. The inverse of the correction matrix is folded to the calculated signal bases to include crosstalk effects in the pulse shape analysis.

3.4.3 Dead and unstable segments

A segment without any signal is regarded as a dead segment. If the charge does not get collected by this segment, the spectra of neighbouring segments show additional peaks and/or noise. If only one segment in a crystal is missing, the energy deposited in this segment can be recovered by the induced charge signal in the neighbouring segments and the energy deposited in the core contact. In our experiment one crystal has one broken segment (2G). The energy of the broken segment is recovered assuming, that the sum of

the segments net charges is equal to the charge collected in the core contact. A correction to the cross talk coefficients is applied to correct for the dead segment.

The same procedure can be used to treat gain-unstable segments. However, in the present experiment unstable segments are not observed.

3.4.4 Determination of the interaction time

During the experiment a leading edge trigger for the core signal is used. Therefore, a walk effect depending on the energy is observed: high energy signals having a high amplitude trigger later than signals with a smaller amplitude. To correct for this walk, a linear interpolation of the rising edge of the signal is done and its intersection with the baseline is calculated. The start of the signal obtained in such way is placed for all the events to the same time, i.e. shifting the trace of the signals. This improves the time resolution of each *AGATA* crystal significantly, as shown in Figure 3.20. On the left side the spectrum of the γ energy of the core is drawn for the case of the leading edge trigger. On the right side, the walk is corrected with this method.

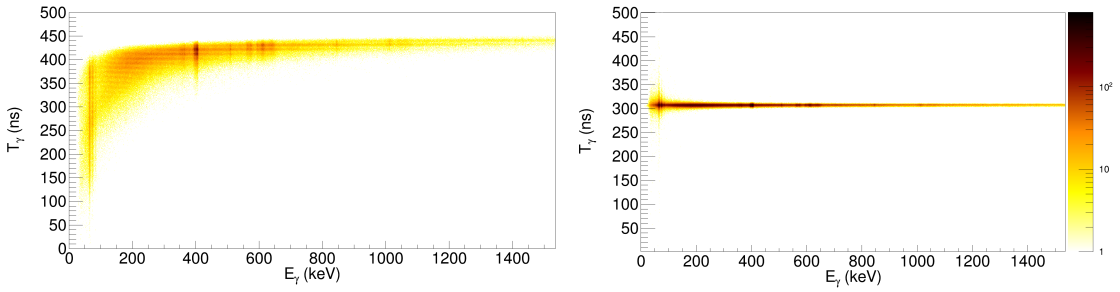

Figure 3.20: Matrix of the γ-ray interaction energy versus its time, measured from the core of crystal 1B. (left) Using a leading edge trigger, an energy walk is visible. (right) After applying the correction, the dependence of the trigger time from the energy is improved significantly.

3.4.5 Alignment of the signal traces

Different lengths in the cables can lead to a certain difference in the timing between the segments of the crystal and the core to the segments. The offset between the different signals can lead to a misinterpretation of the interaction point: the signals in the database used for the PSA are calculated for an ideal detector and hence are well aligned. A difference in time between the measured signal and the calculated one could lead to a different reconstructed position, since the set of signals is chosen from a χ^2 minimisation between the database and the signal. A negative offset favours faster signals, while a positive offset might result in slower signals. An individual correction for each segment is applied.

The signals of the segments are aligned to each other by aligning all the segments to the core contact with a condition on a segment multiplicity of one. After this alignment the core and the segment signals occur at the same time, which is nonphysical, hence the traces of all segments are shifted relative to the core signal. This procedure has a direct impact on

the distribution of hits, reconstructed by the PSA. Comparing the FWHM of the Doppler corrected peak for different shifts, the optimum value is deduced. Figure 3.21 shows an example for the crystal 1B.

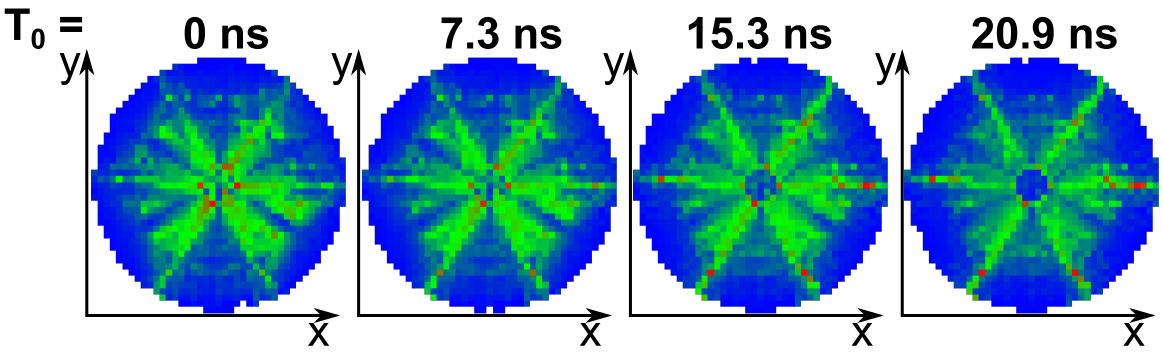

Figure 3.21: Distribution of the γ-ray interactions (looking at the front face of the crystal) as reconstructed by the pulse shape analysis of the crystal 1B for different relative shifts of the core signal to the aligned segment signals. From left to right 0 ns, 7.3 ns, 15.3 ns and 20.9 ns. By looking at the best Doppler corrected spectrum, the shift of 15.3 ns is chosen.

3.4.6 Rise time of the preamplifiers

The calculated signal shape is convoluted with an experimental response of the preamplifiers for the comparison with the measured signal. At the present stage there is no automated way to determine the rise time of the preamplifiers. This information is crucial for the comparison of the calculated PSA basis to the measured signals. Especially for the first layer of segments, where the distribution of the interaction positions after the PSA is concentrated at the edges of the segments. To reduce this effect, the rise time of the preamplifiers is set for the frontal row of the segments to 25 ns instead of the standard value 35 ns. This reduces the clusterisation and improves the Doppler correction slightly. However, the chosen value does not imply that it is the real risetime of the preamplifiers. For a different *AGATA* experiment, higher values for the rise time were reported to result in a more homogeneous distribution [117].

3.4.7 Neutron damage correction

The interaction of fast neutrons with the germanium crystals induces lattice defects, which act as efficient charge carrier traps. Therefore, the efficiency of the charge collection is reduced due to these defects. This effect can be observed as a tail on the left side of the full-energy peak, i.e. for the lower energy part of the γ-ray peak. The segments of the *AGATA* crystals are more sensitive to the hole trapping than the core contact [118]. Hence, as a simple solution to recover the good energy resolution of the *AGATA* detectors, the sum energy of all segments is normalised to the energy measured in the core contact.

3.4.8 Time alignment between the crystals

A time alignment between the 15 crystals is performed by creating a histogram of the time difference between each combination of detectors. A fit using a Gaussian function with a left and right tail on each peak gives the time difference between each pair of crystals. The optimal shift for each detector is calculated and applied to the data.

3.4.9 Tracking

For the current analysis package of *AGATA* data, there are two different tracking algorithms available: **O**rsay **f**orward **t**racking (*OFT*) [112] and **M**ARS **G**amma **T**racking (*MGT*)[113]. Both implement the forward tracking algorithm showing similar results, except for the pair production. The pair production has a threshold of 1022 keV and thus above the energy of the transitions of interest for this experiment. For this work the *OFT* algorithm is used. To enhance the peak-to-total ratio an acceptance level of 0.95 was chosen. In case of a full acceptance, all the hits, which are not reconstructed as a Compton scattering, will be treated like a single-hit photo effect. Therefore, the acceptance level smaller than one increases the quality of the spectra with the trade off of reducing the efficiency. The rest of the parameters of the tracking algorithm *OFT* was not changed from the standard values.

3.4.10 Efficiency calibration

For the efficiency calibration of *AGATA* a source of ^{133}Ba and ^{152}Eu source were placed successively at the target position. The calibration runs were performed before the experiment and directly after an preceding experiment. Concurrently with the calibration run, the beam for the experiment was prepared. The beam hit material upstream the beam line. Hence, the calibration run was contaminated by reaction products of the previous experiment and the beam-induced reaction products. The contamination has transitions with a similar or equal energy of the calibration sources. To minimise the effect of the beam preparation, only the time intervals with a lower background are used in the analysis (see Figure 3.22 for an example of the ^{152}Eu calibration run): for this procedure a matrix with the tracked γ-ray energy versus the time of the calibration run, expressed in time stamps is produced. The time intervals revealing a higher background are excluded from the calibration run. However, some transitions of the calibration sources can not be used for the efficiency calibration. Due to the unknown contamination, the errors of the fit of the peaks of the calibration runs are just a lower limit for the uncertainty of true errors.

The efficiency is fitted with the standard efficiency function [119],

$$\epsilon_\gamma(E_\gamma) = \exp\left(\left[\left(A + B\cdot\frac{E_\gamma}{100\,\mathrm{keV}}\right)^{-G} + \left(D + E\cdot\frac{E_\gamma}{1\,\mathrm{MeV}} + F\cdot\left(\frac{E_\gamma}{1\,\mathrm{MeV}}\right)^2\right)^{-G}\right]^{\frac{-1}{G}}\right), \tag{3.2}$$

where the constants A, B, D, E, F, G are free parameters. The result of the fit is drawn in Figure 3.23.

The efficiency calibration was performed without an absorber. For the experiment an absorber, consisting of two tin foils of 300 µm is placed in front of the *AGATA* crystals. These foils were used to reduce the counting rate in the first segments due to X rays. The

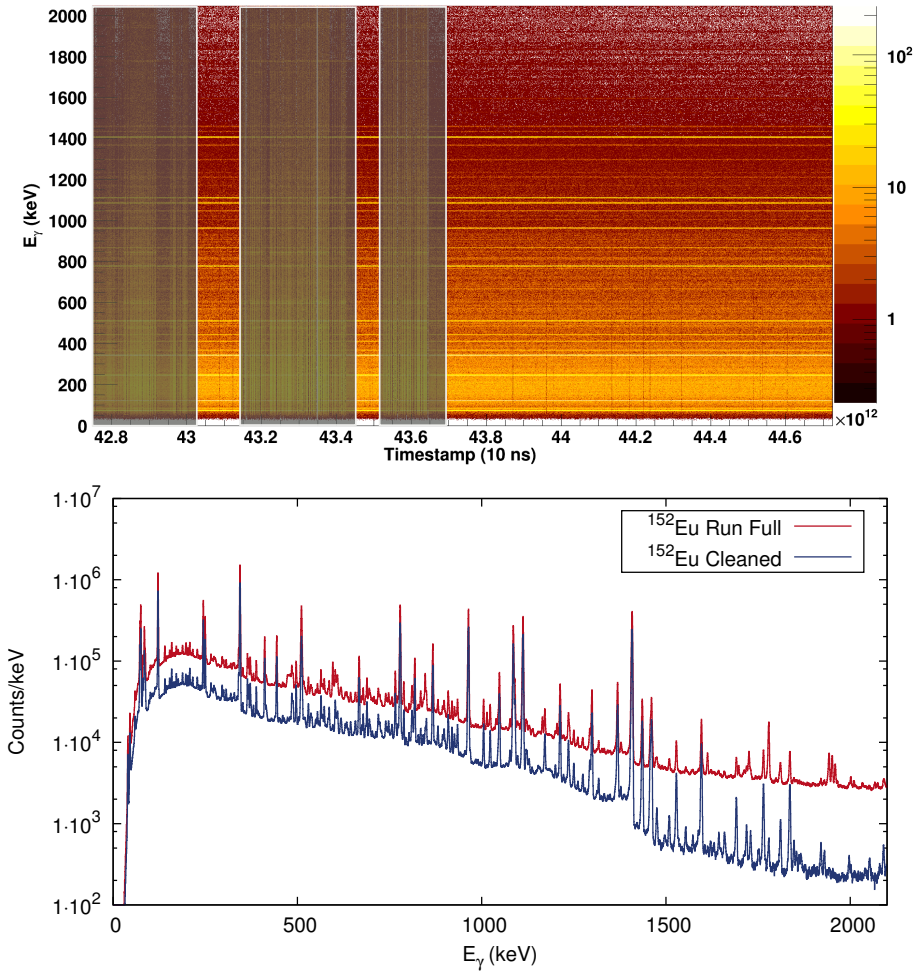

Figure 3.22: (top) Matrix of the time stamp (time during the run) versus the tracked γ-ray energy. The time intervals with a higher background are excluded in the analysis. (bottom) The total spectrum from the ^{152}Eu source run (red) and the final spectrum, after the rejection of the higher-background time intervals which is used for the efficiency calibration (blue).

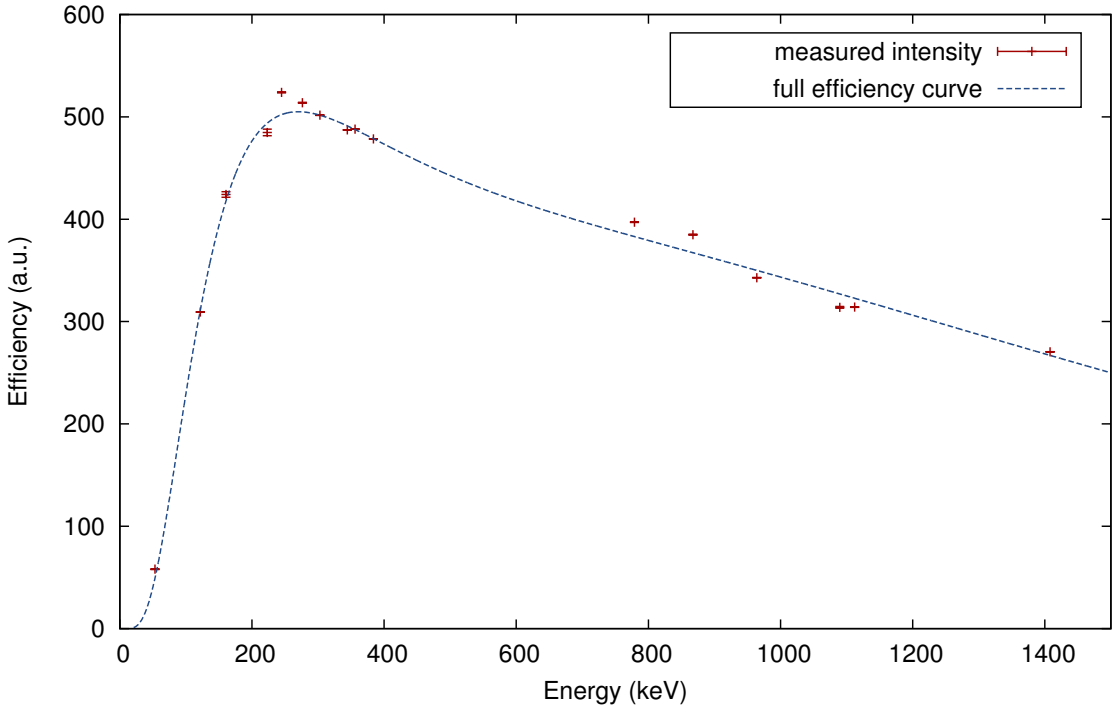

Figure 3.23: Relative efficiency curve deduced from a ^{133}Ba and a ^{152}Eu γ-ray source. See text for details.

efficiency during the experimental run is affected by the attenuation of the foils in the low-energy part of the spectrum. The attenuation coefficient for the tin absorber is taken from the XCOM database [79]. The fraction according to the Beer-Lambert law of the total absorption and the attenuation due to Compton- and Rayleigh scattering are plotted in Figure 3.24 (left). The majority of the attenuation is due to the photoelectric effect. The cross section of Rayleigh scattering drops steady with increasing energy and above 100 keV the Compton scattering becomes predominant. The Compton effect has a contribution of around 5% for a wide energy range above the energy of the X rays. This adds up to a background. The Rayleigh scattering is negligible for energies above 100 keV. Hence, it is a valid approximation to fold the measured efficiency without an absorber with the attenuation curve. The result is plotted in Figure 3.24 (right).

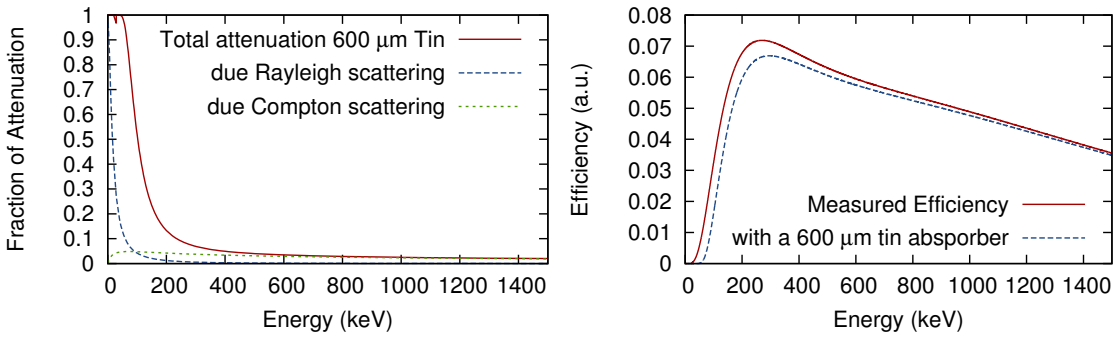

Figure 3.24: (left) Fraction of the attenuation of a 600 µm thick tin absorber. (right) Efficiency curve including the effect of the attenuation of the absorber.

The absolute efficiency of the *AGATA* demonstrator was deduced with a ^{60}Co source at the nominal distance to be 1.77% [120]. An estimation of the absolute efficiency of the configuration at a distance of 16.5 mm from the target can be done by scaling this value to the increase in the solid angle. This leads to an absolute efficiency of $\approx 4\%$. Due to the shorter distance, the position uncertainty of the PSA leads to an higher uncertainty of the angle between the target and the first interaction point. This effect changes slightly the efficiency of the tracking algorithm and is not taken into account for this estimation.

4 Data analysis

The *AGATA* acquisition system delivers besides the energies of the signal also a snapshot of 1 µs around the rising edge of the digitised signals of the segments and of the core. From the signals, the interaction energy, position and time can be deduced. Dedicated software was developed for the analysis of the *AGATA* data, which contain significantly more information than data of traditional germanium arrays. During the experiment a total of ≈ 15 TB of data were collected.

In Figure 4.1, the data flow of the analysis process is outlined. The raw data (stored digitised signals of the *AGATA* crystals and raw data of the complementary, i.e. heavy-ion detectors) are drawn in blue. The program *femul* [121] is used for the so called replay, i.e. the pulse shape analysis, the energy calculation, merging of the data and a production of a binary list mode file, which contains the tracked γ rays and the merged complementary data.

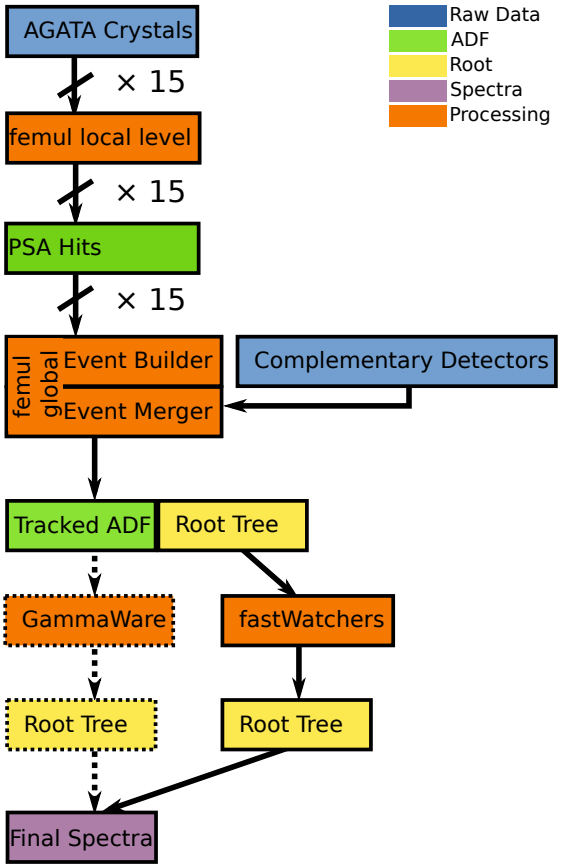

Figure 4.1: Scheme of the procedure and data flow of the analysis. See text for details.

This list mode file can be either analysed with *GammaWare* [122] or similar software. For the present thesis a dedicated software was developed (*fastWatchers*), which uses a modified version of *libPRISMA*, which was initially developed by A. Latina [103] and E. Farnea to analyse the data from the *PRISMA* part. The modification consists of the calculation of the kinematics of the binary partner and the reconstruction of the reaction Q value. The program *fastWatchers* produces a

ROOT tree [123, 124] with all the necessary information stored in its branches. The final spectra are then produced by correlating the observables and by projecting the variables of interest out of the tree.

4.1 Replay with femul

During the experiment an array of dedicated computers were used for preprocessing the data stream, performing also the pulse shape analysis and the tracking. The collected data, including the tracked events, were stored on disk. The *femul* [121] package is able to replay the stored data for a reanalysis of the PSA and the tracking. The analysis is divided in two different steps: the local level, which handles every crystal independently and the global level, which combines the data from the different crystals and the complementary detectors.

For each crystal, the stored digitised signals are read by the *femul* program and mapped to the different segments and core contact. The signals are then passed to the preprocessing actor which subtracts the crosstalk and handles the energy calibration and time alignment of the traces. The preprocessed signals are then passed to the pulse shape analysis, which compares the measured signals to the simulated ones stored in a database. The final information for each interaction is a tuple consisting of (E, x, y, z, t) and is stored in a binary list mode file using the **A**GATA **D**ata **F**low (ADF) format.

At the global level of the replay, the data of all the crystals are merged based on the time of each interaction. The time differences between the crystals due to different cable lengths and offsets in the time stamp distribution system **G**lobal **T**rigger **S**ystem (GTS) are corrected on this step. The database of the calculated pulses contains voxels in form of a $2\,\text{mm} \times 2\,\text{mm} \times 2\,\text{mm}$ cube. The interaction positions are spread out uniformly over the size of this voxel. The tracking is performed and produces a list of γ rays. Each γ-ray entry contains its energy, the time of the first interaction and the positions of the first and second interaction. Additionally, the data stream is merged with the data from the complementary detectors on the bases of the time stamp. The final output is a root tree with these data and a binary list mode file containing the tracked γ rays and the merged coincident complementary data.

4.2 Data reduction with fastWatchers and libPRISMA

The root tree produced by the global level of *femul* is analysed by the program *fastWatchers*. It uses parts of the *PrismaWatchers*, developed for *GammaWare*. It reads the stored raw data from the VME crate and maps it to the individual detectors of the *PRISMA* spectrometer. The mapped data are then passed to a modified version of the PRISMA library (*libPRISMA*), which performs the calibration of the detectors and calculates from the detector output, the information needed for the final analysis including the identification and the velocity vectors for the beam-like fragment and the target-like fragment. The returned information is stored together with the list of the γ rays in a *ROOT* [123, 124] tree.

The final root tree is used to produce the spectra and matrices, by applying different conditions and projecting the variables out of the tree.

4.3 Binary partner reconstruction

In this experiment, a ^{82}Se with 426 MeV impinging on a ^{198}Pt target, only the lighter beam-like recoil is identified in the *PRISMA* spectrometer. The information of the heavier target-like recoil, e.g. ^{196}Os which is the main goal of this work, is reconstructed under the assumption of a pure binary reaction, i.e. a two-body reaction. Due to the velocity of the beam ($\beta = 10.5\%$), the calculation is performed using a relativistic approach taken from Baldin et al. [125].

4.3.1 Reaction kinematics

Figure 4.2 shows a sketch of the reaction. The ^{82}Se beam impinges on the ^{198}Pt target (mass m_t) with a kinetic energy T_b. The squared four momentum vector s of the initial two-body system is Lorentz invariant and given by

$$s = (m_b + m_t)^2 + 2m_t T_b \ . \tag{4.1}$$

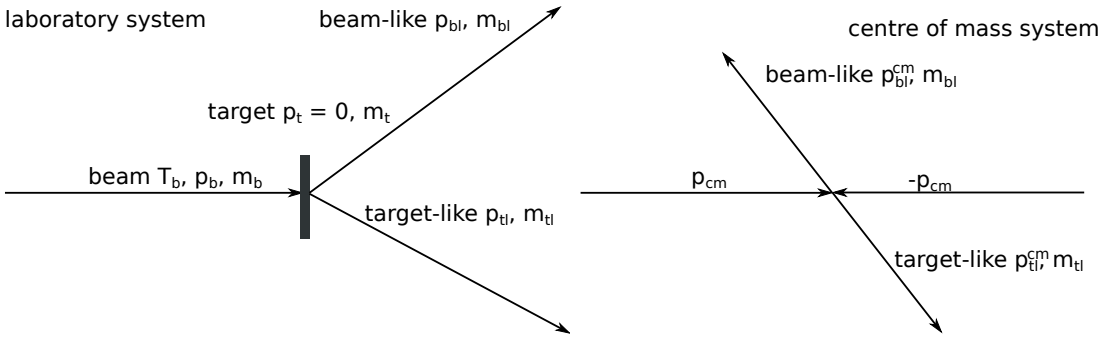

Figure 4.2: (left) Sketch of the reaction in the laboratory frame. The momenta of the beam (p_b) and fragments (p_{tl}) for the target-like and (p_{bl}) for the beam-like recoil are sketched. (right) Sketch of the same reaction in the centre of mass system.

In the centre of mass system the momentum of the beam and the target have the same absolute value, but are opposed to each other. Since s is Lorentz invariant, it can also be calculated by

$$s = \left(\sqrt{m_b^2 + p_{cm}^2} + \sqrt{m_t^2 + p_{cm}^2}\right)^2 \ . \tag{4.2}$$

Hence, this equation combined with equation 4.1 determines the centre of mass momentum

$$p_{cm} = \sqrt{\frac{(s - m_b^2 - m_t^2)^2 - 4m_b m_t}{4s}} \ . \tag{4.3}$$

The rapidity χ of the centre of mass system can be calculated by the transformation of the target nucleus at rest to the centre of mass system with the momentum p_{cm}

$$\begin{pmatrix} m_t \\ 0 \end{pmatrix} \rightsquigarrow \begin{pmatrix} E_t \\ p_{cm} \end{pmatrix} = \begin{pmatrix} \sqrt{m_t^2 + p_{cm}^2} \\ p_{cm} \end{pmatrix} = \begin{pmatrix} m_t \sinh\chi \\ m_t \cosh\chi \end{pmatrix} \tag{4.4}$$

and solving for χ

$$\chi = \ln\left(\frac{p_{cm} + \sqrt{m_t^2 + p_c m^2}}{m_t}\right) . \tag{4.5}$$

Similar considerations lead to the centre-of-mass momentum after the reaction

$$p'_{cm} = \sqrt{\frac{(s - m_{tl}^2 - m_{bl}^2)^2 - 4m_{tl}^2 m_{bl}^2}{4s}} . \tag{4.6}$$

By applying the boost to p'_{cm} and the assumption, that the beam-like recoil is the forward scattered one, the energy (E_{bl}) and momentum (p_{bl}) of the beam-like recoil in the lab frame can be calculated.

$$E_{bl} = \sqrt{p'^2_{cm} + m_{bl}^2}\cosh\chi + p'_{cm}\cos\Theta_{cm}\sinh\chi \tag{4.7}$$

$$p_{bl}\cos\Theta_{bl} = p'_{cm}\cos\Theta_{cm}\cosh\chi + \sqrt{p'^2_{cm} + m_{bl}^2}\sinh\chi \tag{4.8}$$

$$p_{bl}\sin\Theta_{bl} = p'_{cm}\sin\Theta_{cm} \tag{4.9}$$

Since the momentum of the beam-like and the target-like recoil are opposed to each other in the centre-of-mass system, the boost needs to be applied for $-p'_{cm}$, leading to the energy (E_{tl}) and momentum (p_{tl}) of the target-like recoil:

$$E_{tl} = \sqrt{p'^2_{cm} + m_{tl}^2}\cosh\chi - p'_{cm}\cos\Theta_{cm}\sinh\chi \tag{4.10}$$

$$p_{tl}\cos\Theta_{tl} = -p'_{cm}\cos\Theta_{cm}\cosh\chi + \sqrt{p'^2_{cm} + m_{tl}^2}\sinh\chi \tag{4.11}$$

$$p_{tl}\sin\Theta_{tl} = p'_{cm}\sin\Theta_{cm} . \tag{4.12}$$

Isolating p'_{cm} in the momentum equations, squaring them, equating them and solving for the momentum in the laboratory frame leads to the momentum as a function of the laboratory angle:

$$p_{bl} = \frac{\sinh\chi\sqrt{p'^2_{cm} + m_{bl}^2}\cos\Theta_{bl} \pm \cosh\chi\sqrt{p'^2_{cm} - m_{bl}^2\sin^2\Theta_{bl}\sinh^2\chi}}{1 + \sin^2\Theta_{bl}\sinh^2\chi} \tag{4.13}$$

$$p_{tl} = \frac{\sinh\chi\sqrt{p'^2_{cm} + m_{tl}^2}\cos\Theta_{tl} \pm \cosh\chi\sqrt{p'^2_{cm} - m_{tl}^2\sin^2\Theta_{tl}\sinh^2\chi}}{1 + \sin^2\Theta_{tl}\sinh^2\chi} \tag{4.14}$$

Since the momentum needs to be a real number, the maximum scattering angle is limited by the expression under the root in the numerator:

$$\Theta_{max} = \arcsin\left(\frac{p'_{cm}}{m\sinh\chi}\right) . \tag{4.15}$$

4.3.2 Implementation of the reaction kinematics in software

The measured incident angle of the beam-like recoil, entering the *PRISMA* spectrometer, together with the identification of the nucleus is used to calculate the centre-of-mass momentum. The masses are taken from the *NUBASE2012* database of evaluated nuclear

properties [126]. The binary partner is deduced by assuming no particle evaporation. A transformation back to the laboratory system for the binary partner leads to its momentum vector.

Figure 4.3 shows the relation between the angle of the beam-like recoil and the target-like recoil for the elastic scattering and the two-proton transfer channel ^{198}Pt(^{82}Se, ^{84}Kr)^{196}Os. These plots are produced for a beam energy of 426 MeV, without considering the energy loss in the target and excitation energy. The angular coverage of the entrance window of the *PRISMA* spectrometer, which is rotated to the grazing angle of the reaction at $\Theta_g = 57°$, is highlighted in blue.

The energy loss of the binary partner through the target material is calculated event-by-event using the Northcliffe-Schilling approximation [127].

4.3.3 Reconstruction of the reaction Q value

The simultaneous measurement of the angle and the energy of the beam-like recoil entering *PRISMA* enables the deduction of the Q value of the reaction under the assumption of a binary reaction without particle evaporation. The *PRISMA* spectrometer analyses the momentum in the dipole magnet and measures the energy in the ionisation chamber. As described in section 2.2.1, the resolution of the time of flight measurement is higher than the energy measurement in the ionisation chamber. Hence, the momentum is deduced by the measurement of the velocity of the ion and the identified mass. For the reconstruction it is assumed, that the reaction occurs in the centre of the target. The energy of the beam ion at the centre of the target ($E_{reaction}$) is calculated by subtracting the energy loss of the beam ion estimated by the Northcliffe-Schilling approximation [127]. The same procedure is done to calculate the energy at the reaction point of the ion detected by the *PRISMA* spectrometer. Using the non-relativistic formula [128]

$$Q = \frac{m_{tl} + m_{bl}}{2m_{tl}m_{bl}} p_{bl}^2 - \frac{m_{tl} - m_{bl}}{m_{tl}} E_{reaction} - \frac{1}{m_{tl}} \sqrt{2m_b E_{reaction}} p_{bl} \cos\Theta_{bl} \tag{4.16}$$

the Q value of the reaction can be reconstructed.

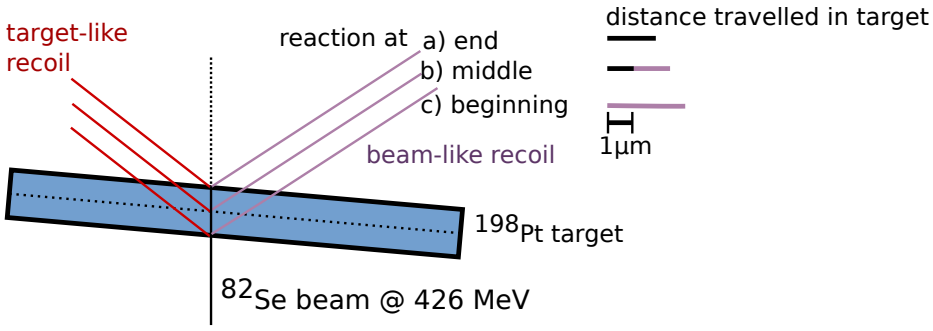

Figure 4.4: Sketch of the different reaction depths showing the target-like and beam-like recoils trajectory for a given detection angle. The length of the total distance in the target is divided into before (black) and after the reaction (light violet).

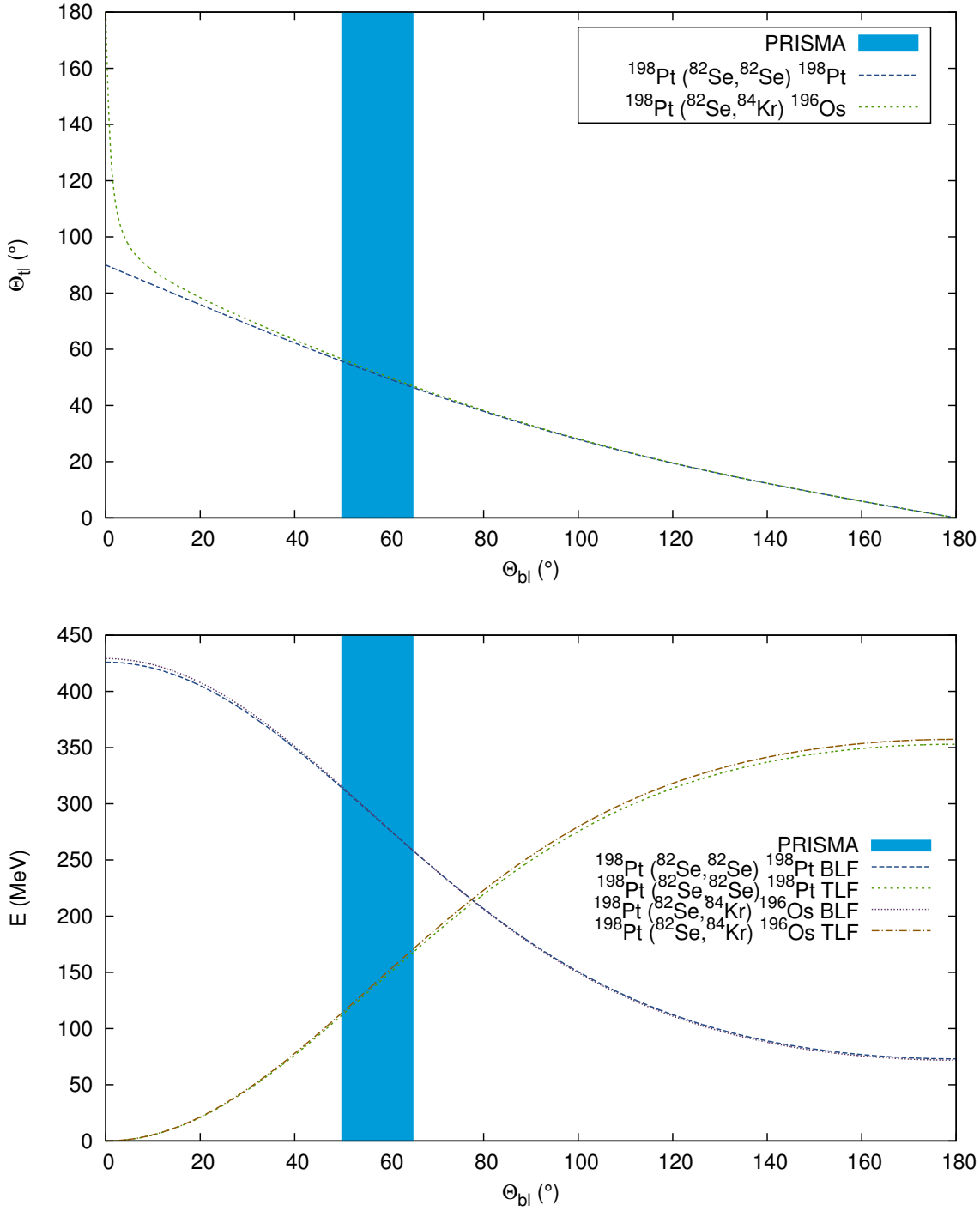

Figure 4.3: (top) Angle in the laboratory system of the beam-like recoil (Θ_{bl}) plotted versus the angle of the target-like recoil (Θ_{tl}) for the elastic channel and the two-proton transfer channel. The area covered by the entrance window of the *PRISMA* spectrometer is highlighted in blue. (bottom) The energy of the recoils is plotted versus the scattering angle of the beam-like fragment.

There are several uncertainties of the reconstructed Q-value. The major contribution to the uncertainty is the thickness $2\,\mathrm{mg/cm^2}$ of the target and hence the different energy loss of the ions in the target. Figure 4.4 illustrates this effect for 3 different trajectories, with the reaction occurs at the beginning of the target, at the centre of the target and finally one at the exit of the target. From this figure it is obvious, that the distance of the ions travelled in the target changes accordingly to the position where the reaction occurs. The energy loss of an ion in matter depends on its mass, atomic charge number and energy. For elastic scattering, the change of the ion energy changes slightly the energy loss in addition to the change in the length in the target. Even though the energy loss of the recoil is calculated for the identified ion, the difference of energy loss between the beam ion is higher for the transfer channels. Especially for the transfer of many protons this effect is important.

The straggling and the unknown position of the beam spot on the target increases the uncertainty of the reconstructed Q value. In total, an uncertainty of around 30 MeV can be expected, by combining all these effects. A thinner target would decrease the uncertainty, but on the other hand would decrease drastically the final yield.

The reconstructed Q value and the suppression of neutron evaporation

If an energy greater than the neutron separation energy is transferred to the nucleus, it might de-excite via the emission of a neutron. The emission of charged particles is hindered by the Coulomb barrier. In this experiment no emission of charged particles is observed. Figure 4.5 shows a detail of the nuclear chart around ^{198}Pt with the neutron separation energy S_n encoded in colour. The neutron separation energy drops when adding neutrons. The decreasing neutron-separation energy hinders the spectroscopy of very neutron-rich isotopes via the binary-partner method, since the x-neutron evaporation channels are present in the corresponding γ-ray spectra. Especially for the nuclei in the proton-pick-up channels, the neutron separation energy drops significantly: the neutron-separation energy of ^{196}Os is with 6.8 MeV [129] lower than the resolution of the reconstructed Q value.

However, the neutron evaporation effect can be controlled by limiting the excitation energy of the system, i.e. by gating on the reconstructed Q value. This method is a trade off between statistics and cleanliness. Hence, for each reaction channel, the optimum condition on the reconstructed Q value needs to be extracted. A condition on a lighter beam-like fragment of the nucleus of interest can be used to recover additional statistics.

Suppression of elastic beam scattering

Due to the finite resolution of the ionisation chamber the conditions on the atomic number of the $\pm 1pxn$-transfer channels contains also events originated from elastic scattering. Each transfer channel has a threshold energy for a transfer to the ground state, hence a condition on a matrix of the mass versus the reconstructed Q value can also be used to select the events without the contamination from the elastic scattered beam.

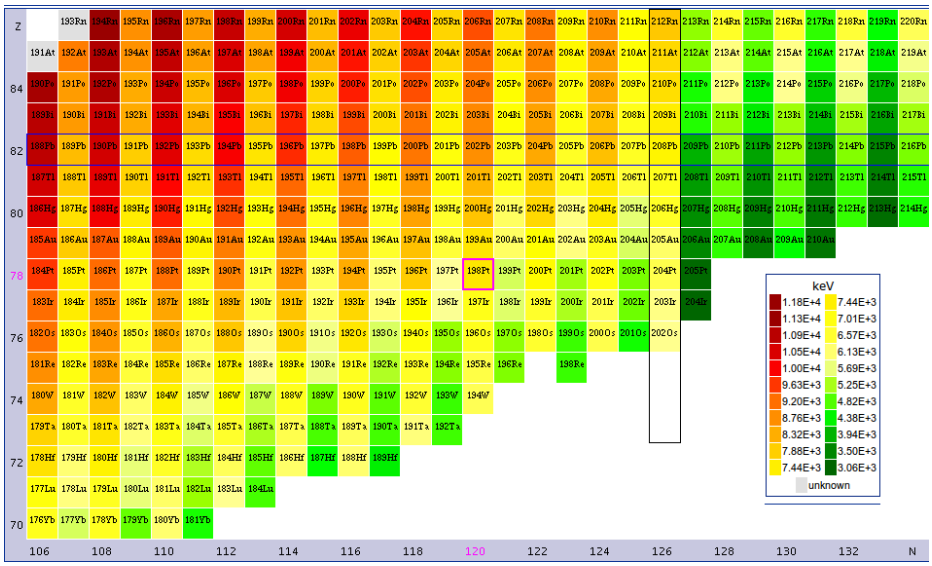

Figure 4.5: The neutron separation energy S_n plotted for the region of the target-like partner. Figure taken from [129].

4.4 Prompt γ-ray spectroscopy

The *PRISMA* spectrometer and the *AGATA* array are used in coincident mode: the trigger condition is an ion detected at the focal plane of *PRISMA* and at least one *AGATA* crystal fired. A 2.2 µs (220 timestamps) long coincidence window is used for the coincidences. Besides the true prompt coincidences, also random coincidences (e.g. decay of reaction products) can occur and add up to the background of the spectrum. Figure 4.6 shows the time difference between the *PRISMA* spectrometer and *AGATA* without corrections, with the beam-like recoil time-of-flight correction and with the phase correction between *AGATA* and the complementary detectors (compare Section 3.3.1). The prompt-peak condition is indicated in blue. In order to remove the background due to random coincidences, two equally sized gates before and after the prompt peak are placed. The background spectrum is scaled by the ratio of the sizes of the windows and subtracted from the prompt-peak spectrum. Due to the tight prompt gate and the low background level, such background subtractions for this experiment are typically less than 1%.

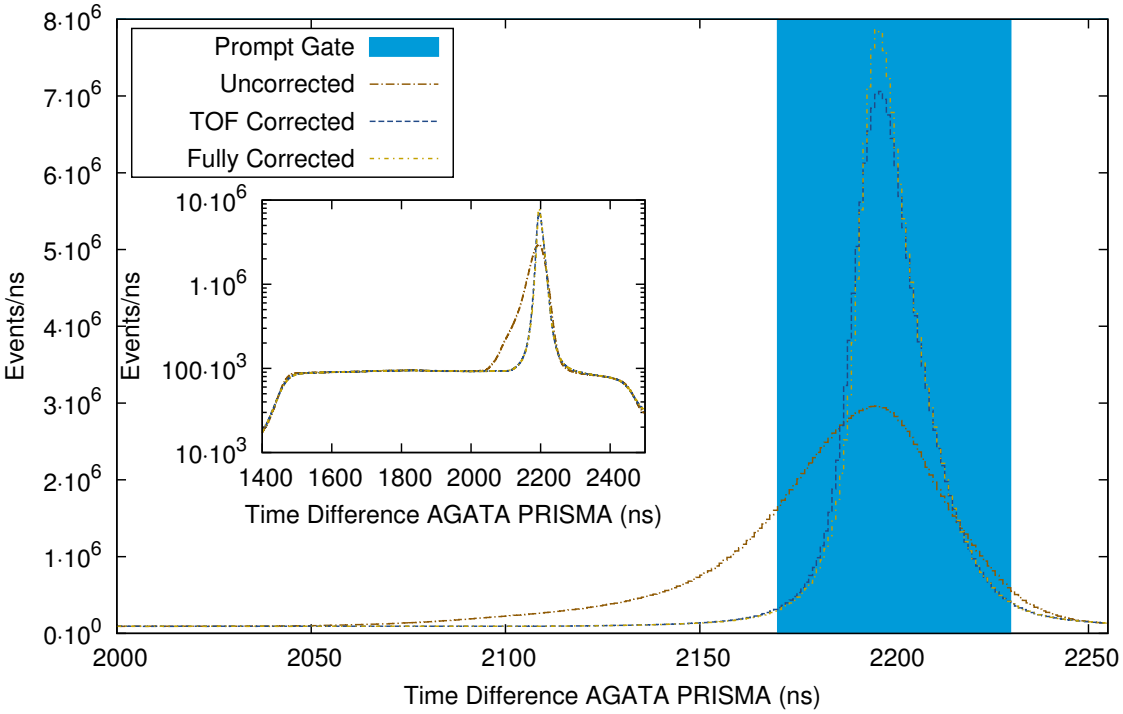

Figure 4.6: Spectrum of the time difference between *AGATA* and *PRISMA* without correction (orange), time of flight correction (dark blue) and full correction (yellow). The gate for a prompt event is indicated by the blue strip. The inset shows the full coincidence window.

4.4.1 Doppler correction

The excited reaction partners can de-excite by emitting γ rays in flight, which is depicted in Figure 4.7. The γ detectors (at rest) measure the Doppler shifted energy E'_γ of the emitted γ ray E^0_γ.

$$E'_\gamma = E^0_\gamma \frac{\sqrt{1-\beta^2_{bl,tl}}}{1-\beta_{bl,tl}\cos(\vartheta_{bl,tl})} \,, \tag{4.17}$$

where $\theta_{bl,tl}$ denotes the angle between the direction of the ion (beam-like or target-like recoil) and the γ-ray direction. The direction of the ion entering the *PRISMA* spectrometer is measured by the MCP start detector and the velocity of the beam-like recoil ($\beta_{bl}c$) is deduced by the time-of-flight measurement combined with the length of the reconstructed trajectory. The velocity of the target-like recoil ($\beta_{tl}c$) is deduced by the two-body reaction kinematics (see section 4.3.1). The velocity distribution for the measured selenium and platinum isotopes is drawn as an example in Figure 4.8.

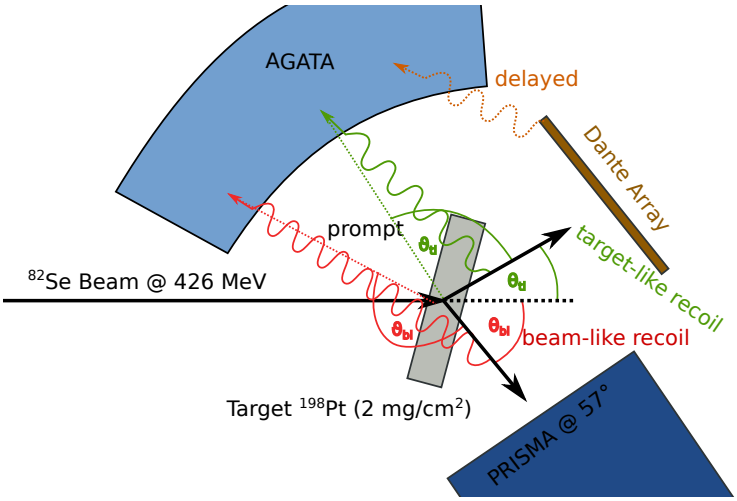

Figure 4.7: Sketch of the reaction and the angles used for the Doppler correction for the target-like and beam-like recoils. The dimensions are not to scale and hence the difference in angle is smaller than indicated.

Due to the short typical lifetime of excited nuclear levels, most of the γ rays are emitted directly after leaving the target. However, it is assumed that the γ ray is emitted at the target position. Hence, the position of the first interaction, as reconstructed by the tracking algorithm is used for the emission angle. Nevertheless, the tracking algorithm is not very sensitive to small changes of the emission position of the γ rays [112].

In Figure 4.9, the γ-ray spectrum gated on the prompt peak and ^{82}Se Doppler corrected for the beam-like recoil (top) and for the target-like recoil (bottom ^{198}Pt) is shown. Intense transitions are labelled with their known spin assignment. Besides the sharp peaks of ^{82}Se large bumps originating from wrongly Doppler corrected peaks of the target-like recoil ^{198}Pt appear in the spectrum at the top. Consequently wrongly Doppler corrected peaks of ^{82}Se appear as bumps in the spectrum Doppler corrected for ^{198}Pt. In addition to the peaks of ^{198}Pt also transitions of ^{196}Pt appear in the spectrum, indicating a two-neutron evaporation channel. Since the two-neutron separation energy of ^{198}Pt is 13.4 MeV and the excitation energies are larger, this effect of neutron evaporation is expected [130].

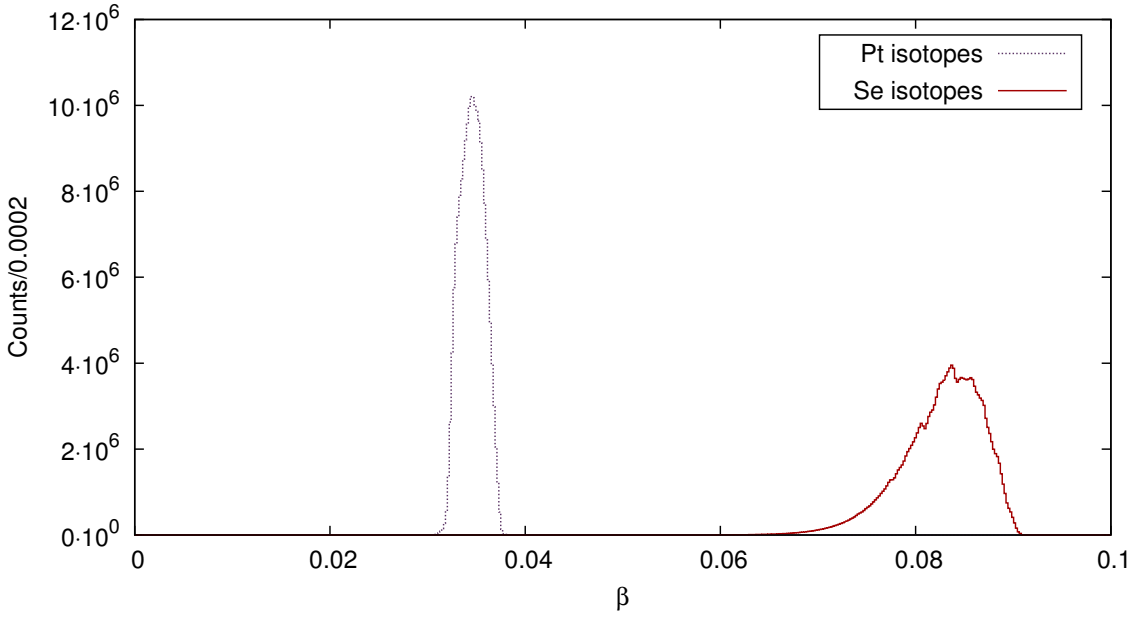

Figure 4.8: Histogram of the distribution of the measured velocities of the selenium isotopes (red peak on the right) and the corresponding calculated velocities for the binary partner, i.e. the platinum isotopes (violet peak left).

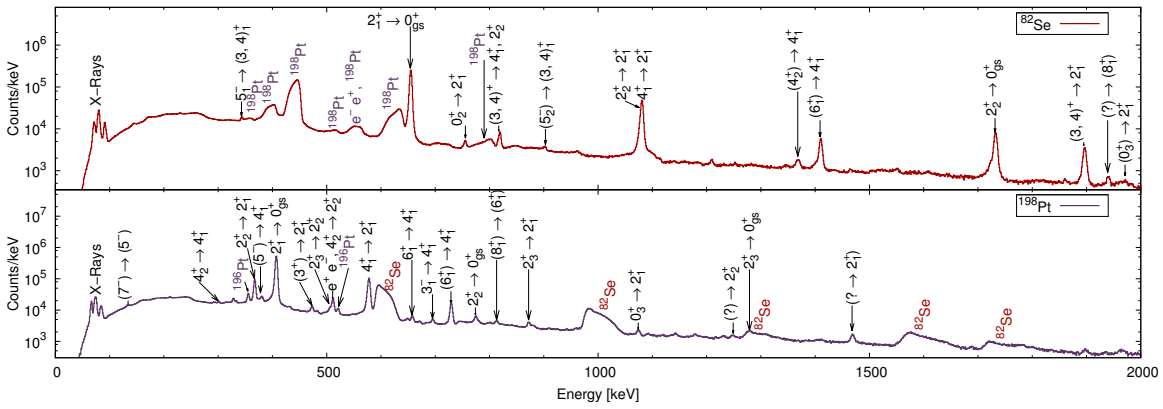

Figure 4.9: Gamma-ray spectra with a condition on the ^{82}Se ions, identified by the *PRISMA* spectrometer, and Doppler corrected for ^{82}Se (top) and ^{198}Pt (bottom). The spectra show the perfectly Doppler corrected γ-ray peaks as well as the wrongly Doppler corrected peaks of the binary partner, which are highlighted in the opposite colour of the spectrum. In the spectrum Doppler corrected for the target recoil, ^{198}Pt, peaks from ^{196}Pt, populated after neutron evaporation, appear in the spectrum.

Figure 4.10 shows the FWHM resolution of different γ-ray peaks for calibration sources and the FWHM of the Doppler corrected γ-ray peaks for the beam (^{82}Se) and the target (^{198}Pt) recoils as a function of their energy. The FWHM of the target-like recoils γ-ray peaks is comparable or slightly worse than the FWHM of the beam-like recoils. In particular, the resolution of the Doppler corrected $2_2^+ \rightarrow 0_{gs}^+$ transition of ^{82}Se at 1731.5 keV is 6.21 keV (3.59‰) and for the $(6_1^+) \rightarrow 4_1^+$ transition of ^{198}Pt at 729.1 keV 4.9 keV (6.7‰).

These results show the superior capabilities of *AGATA* compared to the *CLARA* array, mounted at the same position as the *AGATA* demonstrator. A typical FWHM resolution of 10 keV at $\approx$ 1 MeV was achieved for the detected beam-like recoil [65, 131].

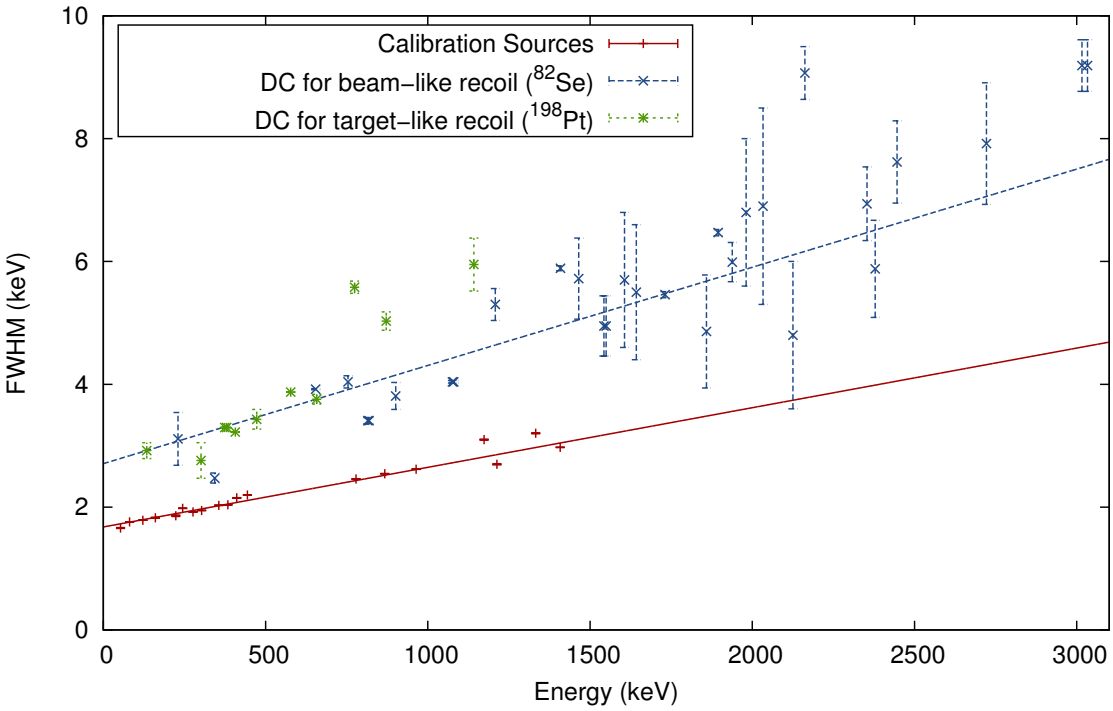

Figure 4.10: Measured FWHM of the γ-ray peaks from the calibration sources (^{60}Co,^{133}Ba and ^{152}Eu) and the Doppler corrected γ-ray peaks from transitions of ^{82}Se and ^{198}Pt are drawn as a function of the energy. The lines are drawn to guide the eye.

4.4.2 Time distribution for the γ -γ analysis

For the γ-γ analysis, matrices gated on different identified ions and reconstructed Q values are produced. Additionally, a condition on the time difference between two γ rays is required. The time of a γ ray is deduced by the time of its first interaction point, which is deduced from the recorded signal. Hence, the time difference of the γ rays is not measured by TACs, but by subtracting the two interaction times in the germanium crystals (see section 3.4). Due to the reconstruction of the time of the interaction, two γ rays, which have the first interaction in the same crystal have the same time information. This results in a peak at

$\Delta t_\gamma = 0$. Figure 4.11 illustrates the condition used for the $\gamma - \gamma$ matrix of ^{82}Se without any condition on the reconstructed Q value, where the peak at $\Delta t_\gamma = 0$ appears.

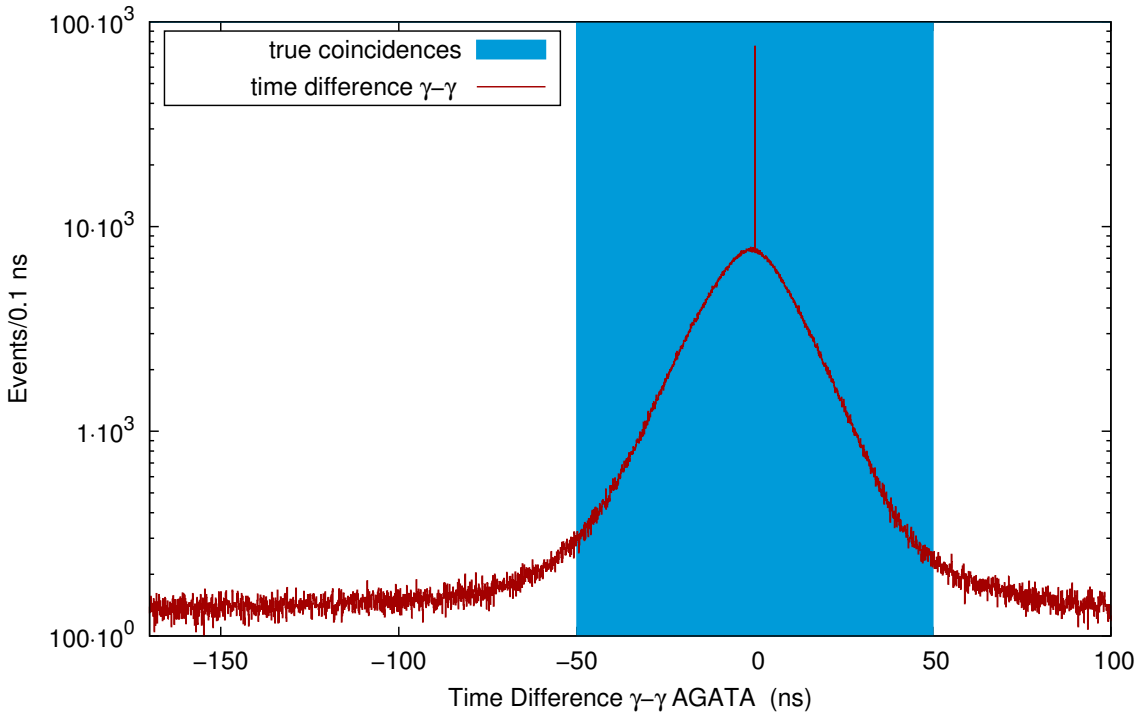

Figure 4.11: Spectrum of the time difference between two γ rays measured with *AGATA*. The time of the first γ ray is required to lie in the prompt peak. The spike at $\Delta t_\gamma = 0$ is caused by two first interactions in the same crystal.

A similar condition excluding the prompt peak from the time difference is imposed for the construction of a $\gamma - \gamma$ matrix of the delayed γ rays. The γ-γ matrices are analysed either with *ROOT* [123, 124] or the *tv* [132] analysis packages.

4.5 Delayed γ−ray spectroscopy

After a time of flight of around 10 ns-15 ns, the target-like recoils are collected in either one of the *DANTE* detectors or implanted in the target chamber. If the implanted ion is in a long living excited nuclear level, i.e. isomeric state, it can deexcite via emission of γ rays. Gamma rays emitted at rest are present in the γ-ray spectra after the prompt peak (right hand side, see Figure 4.13). Since *AGATA* has no collimators and no anti-Compton shields, the γ rays can be detected with a high efficiency. However, the figure of merit of the tracking algorithm of the delayed γ rays emitted by stopped ions far away from the target position might be smaller and thus some delayed γ rays get rejected by the tracking algorithm. The FWHM of the prompt γ-ray peak in coincidence with the *PRISMA* spectrometer is around 15 ns-18 ns depending on the reaction channel.

The data analysis procedure used in this thesis is exemplarily performed for two different isomeric states: the (7_1^-) of ^{200}Pt [53, 54, 133] and the $(27/2^+), (31/2^+)$ level of ^{197}Au [46]. The known partial level schemes for the decay of these two isomers are presented in Figure 4.12.

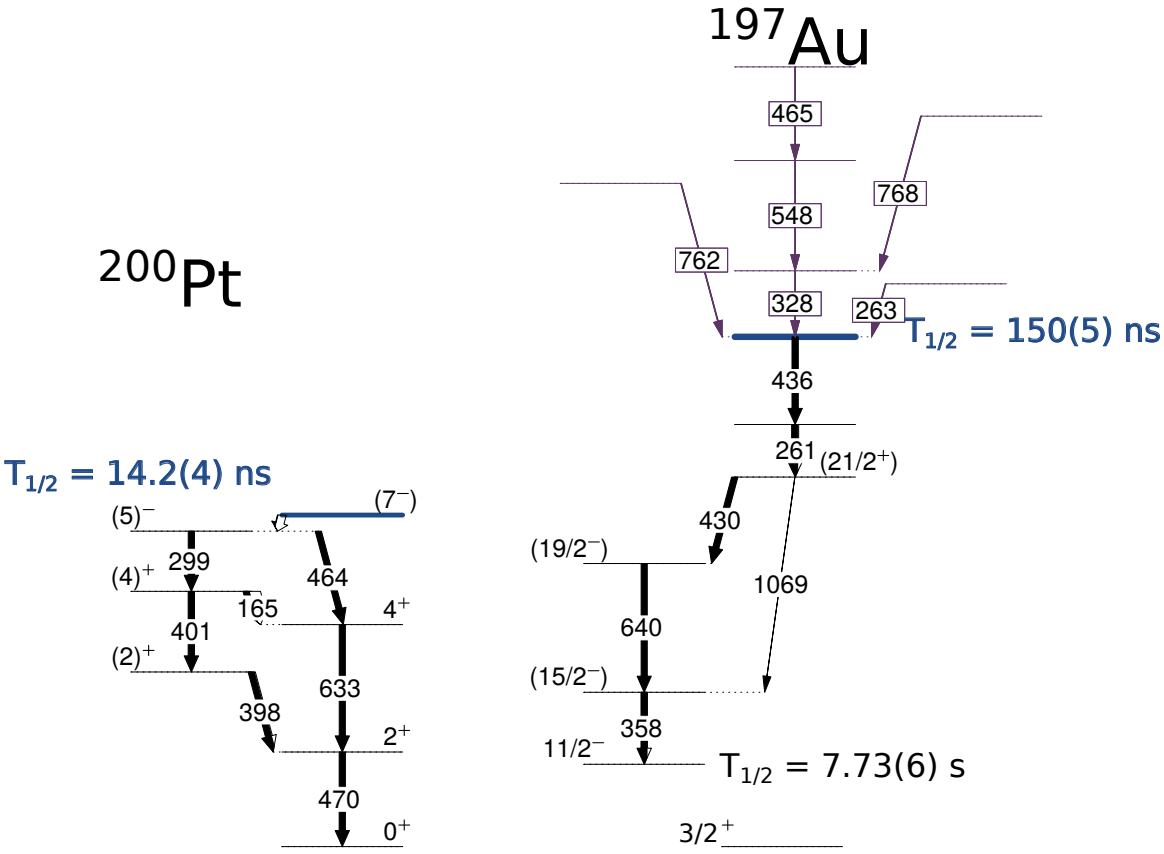

Figure 4.12: (left) Partial level scheme from the decay of the (7_1^+) level in ^{200}Pt. (right) Partial level scheme of ^{197}Au showing states populated by the 150(5) ns isomer and also states above the isomer, that are reported to feed it (violet boxes). Figure based on data from References [46, 53, 54, 133]

The decay from the (7_1^-) isomeric state was observed in isomeric decay spectroscopic experiments [53, 54], after multi-nucleon transfer reactions [134] and two-neutron transfer [133]. The transition from the (7_1^-) state to the 5_1^- state is not yet observed, however, it is believed to be below 90 keV, and hence also outside of the sensitivity of this experiment. The weighted average of the half-life is 14.3(6) ns. This isomeric states is populated in the present experiment via the two-neutron transfer, i.e. its binary partner is ^{80}Se.

The other case, which is presented in detail is the isomeric state in ^{197}Au observed by Wheldon et al. [46] with a half-life of 150(5) ns. The proposed spin of the isomeric state is $(\frac{25}{2}^+)$ or $(\frac{27}{2}^+)$ and $(\frac{31}{2}^+)$ or $(\frac{33}{2}^+)$, assuming a direct de-excitation and an unobserved transition, respectively [46].

Figure 4.13 shows the matrix of the γ-ray time versus energy, gated on ^{80}Se, the binary partner of ^{200}Pt. Due to the evaporation of neutrons, this spectrum contains also γ rays from other platinum isotopes with a lower mass. The prompt peak has an arbitrary offset and is located at 2200 ns. On the right hand side delayed γ rays can be observed.

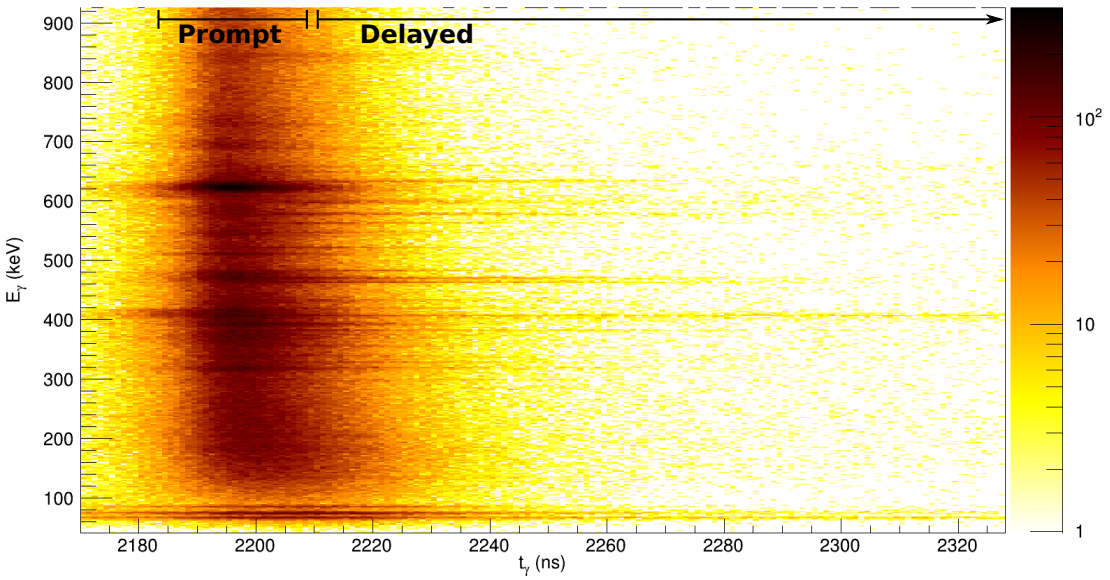

Figure 4.13: Matrix of the γ-ray time versus the γ-ray energy gated on ^{80}Se, the binary partner of ^{200}Pt. Delayed γ rays can be clearly seen to extend in time beyond the prompt peak.

The reconstructed Q value can be used to suppress the neutron evaporation events. A gate on a small reconstructed Q value enhances the contribution of the true binary partner. Figure 4.14 shows the matrix of the reconstructed Q value versus the γ-ray transitions for the interval 20 ns $-$ 100 ns after the prompt peak and a gate on ^{80}Se, the binary partner of ^{200}Pt. Additionally, the energy thresholds for the population of the ground state of the even-even platinum isotopes produced after neutron evaporation are indicated. A dominant transition for each nucleus is indicated. A certain isotope gets only produced on a specific range of the reconstructed Q value. In this figure the appearance of the different neutron-evaporation channels for a given reconstructed Q value can be clearly seen.

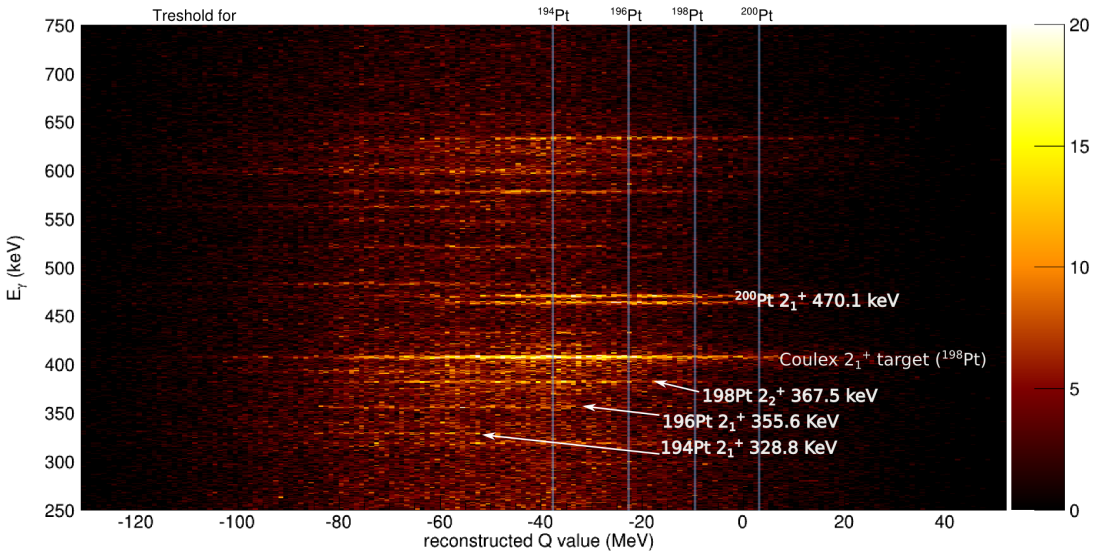

Figure 4.14: Matrix of reconstructed Q value versus the early delayed (20 ns − 100 ns after the prompt incident) γ-ray energy gated on ^{80}Se, the binary partner of ^{200}Pt. The thresholds for the population of the ground state of lighter platinum isotopes via neutron evaporation are indicated.

Therefore, a gate with the condition on the reconstructed Q value smaller than 60 MeV produces a γ-time versus energy matrix, with less contamination of neutron-evaporation channels. Figure 4.15 shows this matrix with the transitions belonging to ^{200}Pt highlighted in green. This matrix is used as a base for the measurement of the half-life of the isomeric state, which is explained in the next section.

The matrix shown on Figure 4.13 is gated on the binary partner of ^{200}Pt. The neutron-evaporation channels up-to the evaporation of 6 neutrons are clearly visible. A condition on the range of reconstructed Q values, where the $x\,n$-evaporation channel appears, can be used to produce a delayed γ-ray spectrum for the nuclei produced in the $x\,n$-evaporation channel. The delayed γ-ray spectrum of a specific target-like nucleus can be obtained by a sum of the spectra obtained for the $x\,n$-evaporation channels.

Figure 4.16 shows this procedure for the delayed sum spectrum of ^{197}Au [46]. Transitions belonging to the dexcitation of the 150 ns-isomeric state in ^{197}Au appear in the delayed γ-ray spectra with a gate on the nuclei $^{75-82}$As, the binary partners of $^{198-205}$Au. For each mass-gated spectrum, the optimal reconstructed Q value condition is found and the final spectrum is the sum of all these spectra. The gates on the reconstructed Q value improves the selectivity for the isomeric state and helps to clean the spectrum (compare top spectrum to the spectra at the bottom). The loss in statistics is negligible. The non-correlated beam-induced background is constant over the coincidence window. In order to subtract this background, a gate on the left side of the prompt peak is applied and the corresponding spectrum is subtracted from the delayed γ-ray spectrum. The background-subtracted spectrum is presented at the bottom of Figure 4.16.

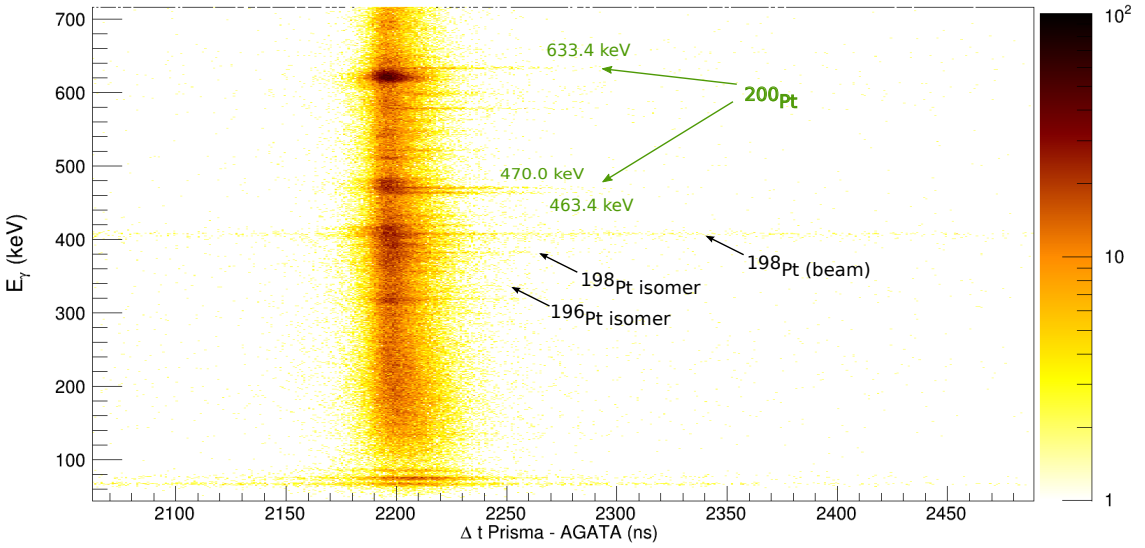

Figure 4.15: Matrix of the γ-ray time versus the γ-ray energy gated on ^{80}Se, the binary partner of ^{200}Pt, and a reconstructed Q value smaller than 60 MeV. The background in the matrix is diminished compared to Figure 4.13.

4.5.1 Lifetime measurements of isomeric states

Using the same conditions on the reconstructed Q value and masses, the time distribution of the delayed γ rays can be obtained. The usage of these conditions produces cleaner time spectra with lower background than the full spectra without a condition on the reconstructed Q value. Furthermore transitions originating from other isomeric states can be suppressed. In order to obtain the time distribution of a specific γ-ray transition, a gate on it is placed. The non-correlated background is subtracted by placing a background gates on on either sides of the γ-ray peak. The time spectrum can be either fitted via an exponential decay with a decay constant $\lambda = \frac{1}{\tau}$

$$N(t) = N_0 e^{-\lambda t} \tag{4.18}$$

or via an exponential convoluted Gaussian (with its parameters σ and μ) when the lifetime is very short and the prompt peak can not be excluded in the fitting process

$$ECG(t) = A\left[\frac{\lambda}{2}\, e^{\frac{\lambda}{2}\cdot(2\mu+\lambda\sigma^2-2t)} \cdot \left(1 - \mathrm{erf}\frac{\mu+\lambda\sigma^2-t}{\sqrt{2}\sigma}\right)\right] . \tag{4.19}$$

The fit of an exponential decay is only valid, if the fitted range is outside of the prompt peak. Due to the different time of flight of the target-like recoils, a range starting at 25 ns after the prompt peak is a safe assumption. However, for longer living isomeric states a range starting from 50 ns after the prompt peak is better suited due to the cleaner spectra. A fit with the exponential convoluted Gaussian has the shape of the Gaussian prompt peak inside the function. A good fit needs an estimation of the position in time (μ) and the width (σ) of the peak. These parameters can be deduced from the background above and below

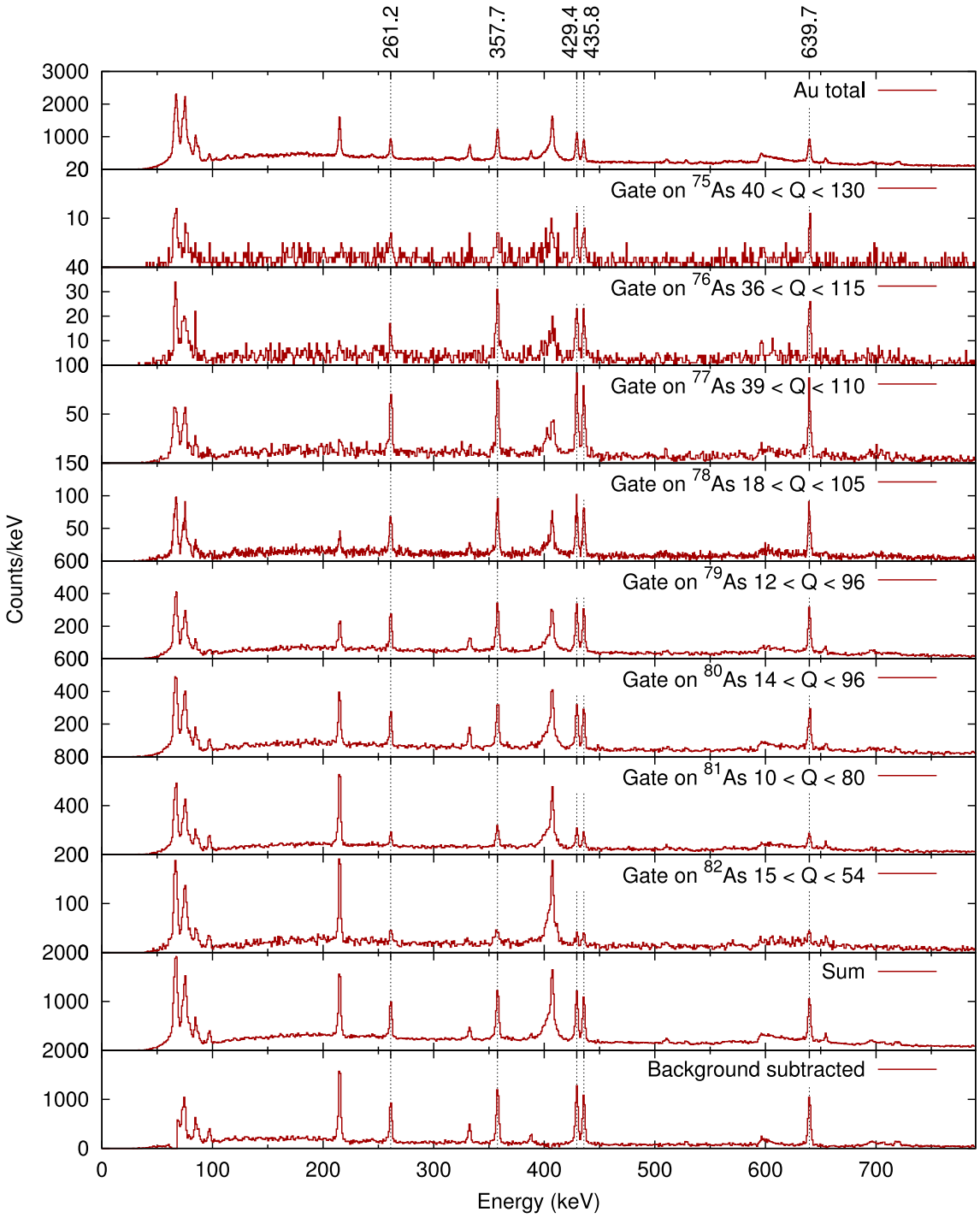

Figure 4.16: Procedure for obtaining a spectrum of the isomeric decay in ^{197}Au by summing all the evaporation channels leading to ^{197}Au. At the bottom the sum spectrum is presented together with the background-subtracted spectrum.

in energy with respect to the energy of the transition of interest. Figure 4.17 shows the sum of the time distribution for two transitions following the decay of the 7^- isomeric state in ^{200}Pt. The half-life $T_{1/2} = \ln 2\,\tau$ is determined with both the exponential convoluted Gaussian function and an exponential decay. The half-life measured with the two methods agree within one σ.

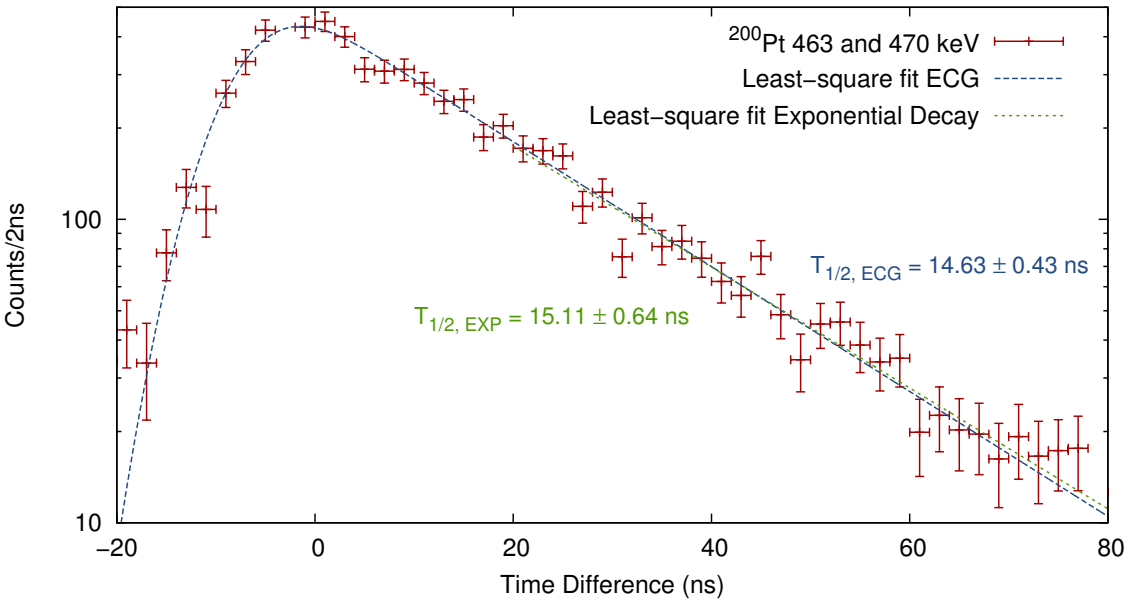

Figure 4.17: Determination of the half-life of the 7^- isomeric state in ^{200}Pt using two different functions.

If the lifetime of the levels in the decay cascade following a dexcitation of an isomeric state is negligible small, the life time of the isomeric state can be calculated by the weighted average [135] of the n measured lifetimes $(\tau_i \pm \sigma_i)$ of each transition populated by the de-excitation of this state:

$$\overline{\tau} = \frac{\sum_{i=1}^{n} g_i \tau_i}{\sum_{i=1}^{n} g_i} \text{ , with } g_i = \frac{\sigma_1^2}{\sigma_i^2} \text{ .} \tag{4.20}$$

The error of the weighted average can be calculated by

$$\sigma_{AM} = \sqrt{\frac{\sum_{i=1}^{n} g_i (\overline{\tau} - \tau_i)^2}{(n-1)\sum_{i=1}^{n} g_i}} \text{ .} \tag{4.21}$$

In case of an intermediate state, which has a measurable lifetime, a gate on transitions above the state and below shows a difference in the time spectrum. Due to the low statistics of the γ-γ events, the measurement of the lifetime of intermediate states with the centroid shift method is not possible for this experiment.

The half-life of the isomeric state in ^{197}Au, described in this thesis, measured using conditions on the different transitions in ^{197}Au are: 164(29) ns, 142(18) ns, 131(15) ns, 136(15) ns

and 167(22) ns. The weighted average computes to 155(7) ns, which agrees well with the literature value of 150(5) ns [46].

4.5.2 Prompt-delayed coincidences

A gate on the delayed γ rays can be used to look at the prompt γ rays feeding the isomeric state. For this a prompt-delayed matrix with the conditions on the reconstructed masses and reconstructed Q values (see Figure 4.16) can be produced. A gate on the delayed γ rays produces spectra of the transitions feeding the isomer. Figure 4.18 shows the analysis of the transitions feeding the 150 ns isomeric state in ^{197}Au. On the top panel the delayed γ rays of the ^{197}Au in coincidences with at least one prompt γ ray is shown. The conditions on the reconstructed Q value and masses are the same as in Figure 4.16. For each delayed transition a spectrum of the prompt γ rays feeding the isomeric state is produced. The final spectrum of the feeding transitions is the sum of all the conditions on the delayed γ rays (bottom). Three previously reported prompt γ rays can be identified in the sum spectrum: 328 keV, 548 keV and 768 keV.

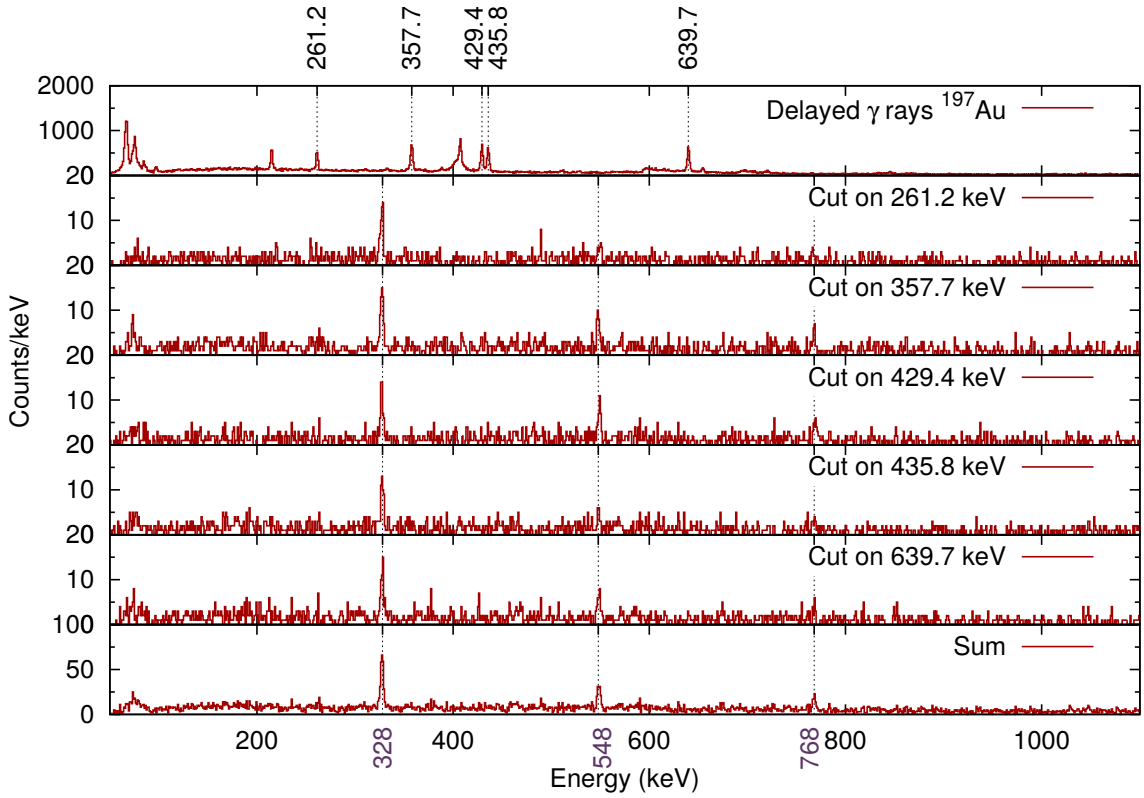

Figure 4.18: Illustration of the procedure for the prompt-delayed coincidences. On the top the delayed γ rays of the ^{197}Au in coincidences with at least one prompt γ ray is shown. In the subsequent 5 panels the prompt spectrum with a condition on the delayed γ ray is shown. The bottom shows the sum of the gates with three γ rays populating the Isomeric state in ^{197}Au. The prompt γ rays feeding the isomeric state are indicated in violet.

5 Results

The main aim of this experiment was to perform the first γ-ray spectroscopic measurement of the nucleus ^{196}Os, which is reported in detail in section 5.1.1. Further results, such as the γ-ray spectroscopy of the even-odd neighbours ^{195}Os and ^{197}Os and ^{200}Pt are reported in the following sections. Besides the γ-ray spectroscopic measurement of the binary partner, this experiment provided higher quality data on the neutron-rich beam-like recoils. As an example of the quality of the data, the spectra of the even-even $^{70-76}$Zn isotopes are presented in section 5.3. The combination of *AGATA* and a magnetic spectrometer is unique combination for the measurement of isomeric states with half-life between ≈ 8 ns and ≈ 250 ns. A survey of the isomeric states populated in the ^{82}Se + ^{198}Pt reaction is presented in section 5.4.

5.1 Shape evolution in the neutron-rich osmium isotopes

In the neutron-rich osmium isotopes a shape transition from prolate deformation to oblate deformation is predicted by a large variety of nuclear models. Experimentally, ^{194}Os was found to have a ground state band suggestive of a prolate deformation. ^{198}Os has an (7_1^+) isomeric state and low-lying levels were found via an isomeric decay spectroscopic experiment at the radioactive ion beam facility GSI, Germany. The path between those two shapes was unknown prior to this thesis, in particular γ-ray spectroscopic data on ^{196}Os were missing.

5.1.1 Prompt γ-ray spectroscopy of ^{196}Os

The ^{196}Os isotope was synthesised for the first time in 1977 via the ^{198}Pt$(n, 2pn)^{196}$Os reaction [136]. The osmium isotopes produced in this way where chemically separated from the irradiated target and the β^- decay of ^{196}Os was observed for the first time.

Six years later, two excited states in ^{196}Os were reported by Bond et al. [48]: 300(20) keV and 760(20) keV. They were populated by the two-proton transfer ^{198}Pt$(^{14}$C$, ^{16}$O$)^{196}$Os. These states were identified in a Q value spectrum measured via a split-pole quadruple spectrometer for the analysis of the momentum of the recoiling ^{16}O ions. However, the setup did not contain any γ-ray detector and hence no γ spectroscopic information was obtained.

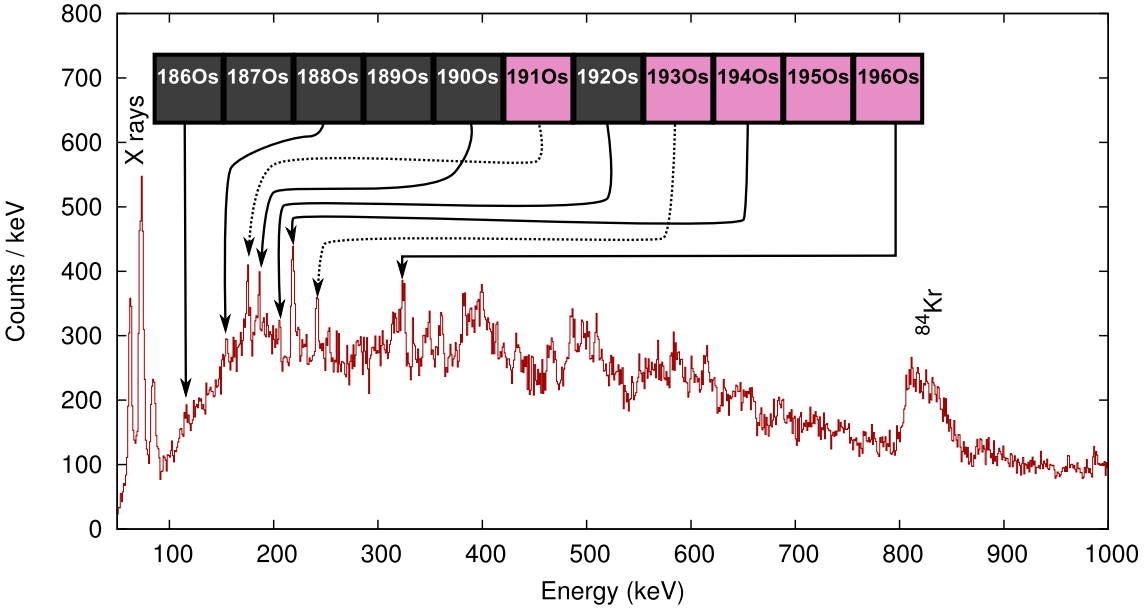

Figure 5.1: Gamma-ray spectrum gated on ^{84}Kr and Doppler corrected for ^{196}Os. The $(2_1^+) \rightarrow 0_{gs}^+$ transition of ^{196}Os is indicated by an arrow. The most prominent transitions from lighter osmium isotopes produced after the evaporation of neutrons are indicated.

Additionally, no angular correlation measurements were possible in this experiment. The proposed spin assignment of the first excited state was (2_1^+). For the second excited state a 2_2^+, 4_1^+ or a doublet of these states was proposed.

Later on, ^{196}Os was produced in fragmentation reactions using a beam at relativistic energies and identified via the fragment separator at GSI, Darmstadt [47, 53–55]. The ions were stopped in a silicon detector or a passive stopper surrounded by γ-ray detectors. No γ-rays in coincidence with ^{196}Os were reported, which indicates an absence of an isomeric state or that the half-life is too short and it deexcites in-flight inside the fragment separator or too long for the observation with the used coincidence window. Therefore, prior to the experiment, reported in this thesis, no γ rays were known in ^{196}Os.

In the present experiment experiment the nucleus ^{196}Os was populated via the two-proton transfer reaction ^{198}Pt(^{82}Se, ^{84}Kr)^{196}Os. Figure 5.1 shows the prompt γ-ray spectrum gated on ^{84}Kr and Doppler corrected for ^{196}Os. In this spectrum peaks from osmium isotopes with lower masses appear due to the evaporation of neutrons. In particular, transitions from ^{186}Os are present, indicating the evaporation of up-to 10 neutrons. Besides the known transitions of the osmium isotopes produced via neutron evaporation a peak at 324.4 keV appears that we assign to originate from ^{196}Os, which is in agreement with the deexcitation of the first excited state found by Bond et al. This peak is less intense than the known $2_1^+ \rightarrow 0_{gs}^+$ peak of ^{194}Os at 218.5 keV. This indicates that the spectrum is dominated by evaporation channels, which is expected since the lighter isotopes of a given nuclear species

are predominantly populated via neutron evaporation [130]. Since the beam energy is ≈ 10% above the Coulomb barrier, part of the excitation energy is dissipated via the emission of neutrons.

The high background and the broad structure peaks in the spectrum presented in Figure 5.1 prevent to identify states with spin higher than 2^+. In order to produce a cleaner spectrum a condition on low energies transferred into the system, i.e. a condition on a small reconstructed Q value (as introduced in section 4.3.3) has to be applied. However, the resolution of the reconstructed Q value (≈ 30 MeV) is not sufficient enough to select a single nucleus. This method is also used to prove the assignment of the 324.4 keV γ ray to ^{196}Os. A matrix of the reconstructed Q value versus the Doppler corrected γ-ray energy is produced. A condition on a low reconstructed Q value suppresses the contribution of neutron-evaporation channels in the γ-ray spectrum and hence enhances the peak-to-total ratio. A further condition on a low number of reconstructed γ rays[1] produces cleaner spectra. Figure 5.2 shows the spectrum for ^{196}Os obtained by applying successive more stringent conditions on the reconstructed Q value (left row from bottom to top) and additionally with a condition on only one reconstructed γ ray (central row).

Three γ rays at 324 keV, 467 keV and 639 keV can be identified in the spectra with a lower cut on the reconstructed Q value. Gamma rays with such energies are not present in the spectra gated on ^{85}Kr and higher masses (i.e. the binary partner of ^{195}Os (compare section 5.1.2) and osmium isotopes with lower masses). Hence, these three γ rays are all assigned to come from the decay of excited states in ^{196}Os. The condition on a reconstructed Q value smaller than 12 MeV and only one reconstructed γ ray produces the cleanest spectrum, which is drawn in Figure 5.3. The corresponding intensities corrected for efficiency and electron conversion under the assumption of pure E2 transitions are reported in Table 5.1.

In order to verify that these 3 transitions belong to the same decay sequence, γ-γ-coincidence matrices with different conditions on the reconstructed Q value are produced. A γ-γ matrix with a condition on the reconstructed Q value smaller than 30 MeV provides the optimal peak-to-background ratio. The intensities of the γ-ray peaks in the spectrum with this condition are reported also in Table 5.1 and are compatible with the intensities of the previous spectrum. A cut on a higher reconstructed Q value produces spectra having higher background. The results from the γ-γ analysis are shown in Figure 5.4. A gate without any background subtraction on the 324 keV or 467 keV γ ray shows that these two transitions are in mutual coincidence with 3-4 counts on a background level of 0-1 counts.

However, a gate on the 639.2 keV transition shows not even a single count in coincidence with the former two transitions.

For the 639 keV transition, two different placements in the level scheme are possible. Its energy corresponds to the value expected from systematics for both the $6_1^+ \rightarrow 4_1^+$ and $2_2^+ \rightarrow 0_{gs}^+$ transitions. The two possibilities are drawn together with the partial level scheme of the neighbouring even-even osmium isotopes in Figure 5.5.

In the neighbouring even-even osmium isotopes the 2_2^+ state is known. In the clean spectrum from the isomeric decay spectroscopy of ^{198}Os only the 2_2^+ to the 2_1^+ transition

[1] Due to the conceptual difference between *AGATA* and traditional γ arrays, this number is not the multiplicity. A different value in the acceptance level of the tracking algorithm can lead to a different number of reconstructed γ rays

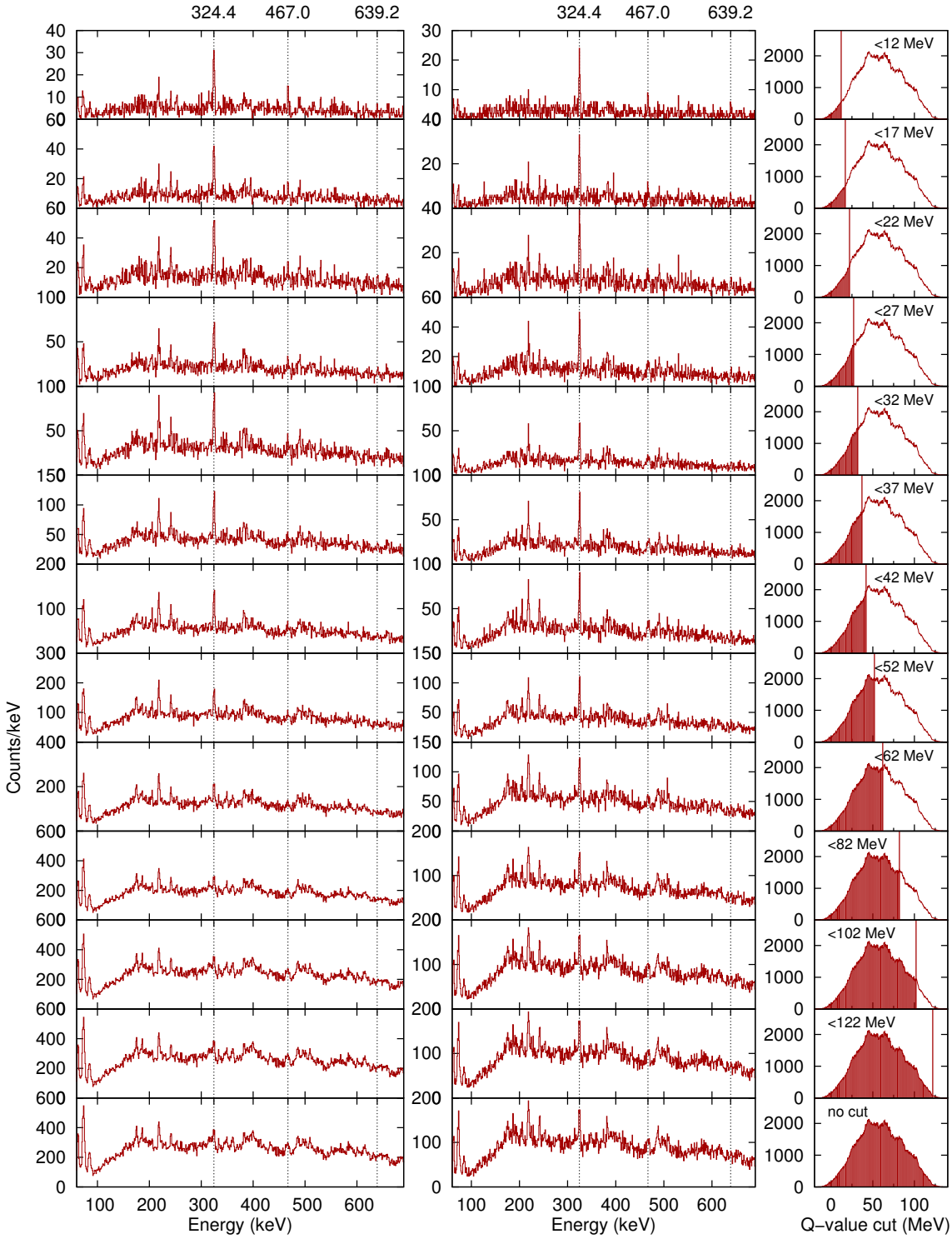

Figure 5.2: The left column shows the γ-ray spectra gated on ^{84}Kr and Doppler corrected for ^{196}Os with a condition on the reconstructed Q value (right column). The spectra in the middle row are the same as in the left row with an additional condition on one reconstructed γ ray. The γ-ray energies assigned to ^{196}Os are shown on the top of the spectra.

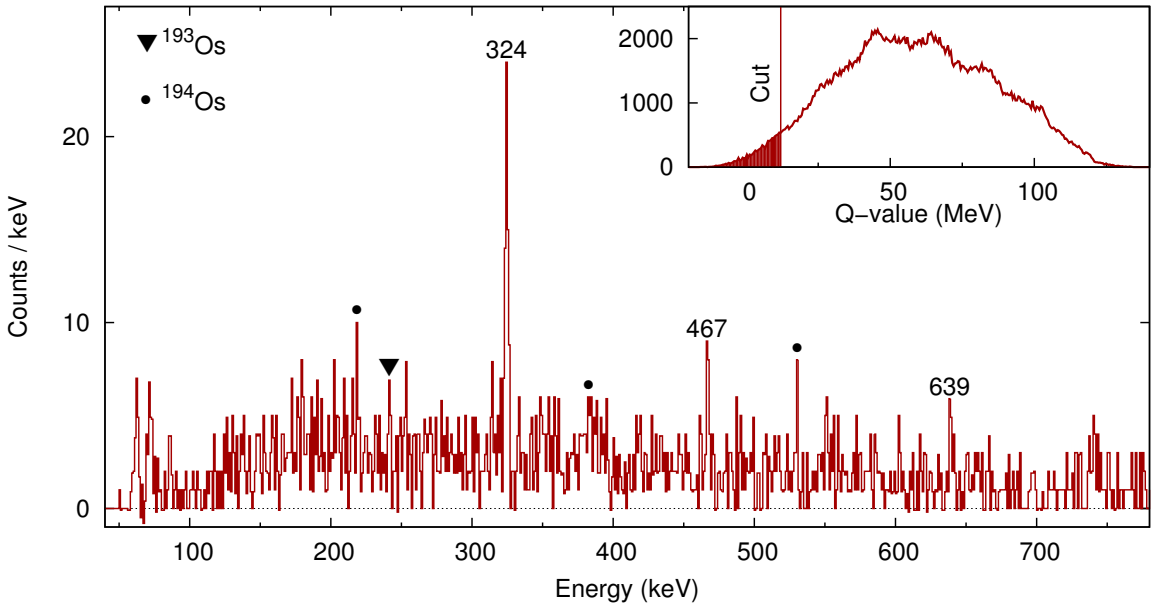

Figure 5.3: Gamma-ray spectrum gated on ^{84}Kr and Doppler corrected for ^{196}Os. Transition assigned to ^{196}Os are labelled by their energy. The transitions from lighter osmium isotopes produced after the evaporation of neutrons are indicated by different symbols.

was observed [47]. A direct deexcitation to the ground state was not seen. In ^{194}Os the 2_2^+ state has been identified which decays to both the 2_1^+ and 0_{gs}^+ states with the transition to the ground state having almost twice the intensity of the transition to the 2_2^+ state. A similar situation in ^{196}Os would lead to the presence of a strong 314.8 keV transition from the 2_2^+ to the 2_1^+ state, which is not observed in the present data.

In literature many cases exist, where non-yrast 2^+ states were populated via a multi-nucleon transfer reaction. Chiara et al. [137] observed the deexcitation of the 2_2^+ level of ^{68}Ni with an intensity of 25% of the $4_1^+ \rightarrow 2_1^+$ transition in the two-proton transfer channel. This behaviour is believed to originate from the structure of the 2_2^+ state. Szilner et al. [71] reported the population of non-yrast 2^+ states of ^{92}Zr and ^{40}Ar. No intensities are given, however the spectra suggest, that the intensity of the non-yrast 2^+ states is just a small

Table 5.1: Energies (E_γ) and relative intensities (I_γ) of the observed γ-ray transitions for ^{196}Os. The spin assignment of the transitions and the energy of the initial level $E(J_i)$ are also given.

E_γ (keV)	$I_{\gamma,M=1,Q<12}$	$I_{\gamma,Q<30}$	$J_i^\pi \rightarrow J_f^\pi$	$E(J_i)$ (keV)
324.4 (10)	100 (17)	100 (12)	$(2_1^+) \rightarrow 0_{gs}^+$	324.4
467.0 (10)	31 (11)	41 (10)	$(4_1^+) \rightarrow (2_1^+)$	791.4
639.2 (10)	22 (10)	12 (8)	$(6_1^+) \rightarrow (4_1^+)$	(1430.6)

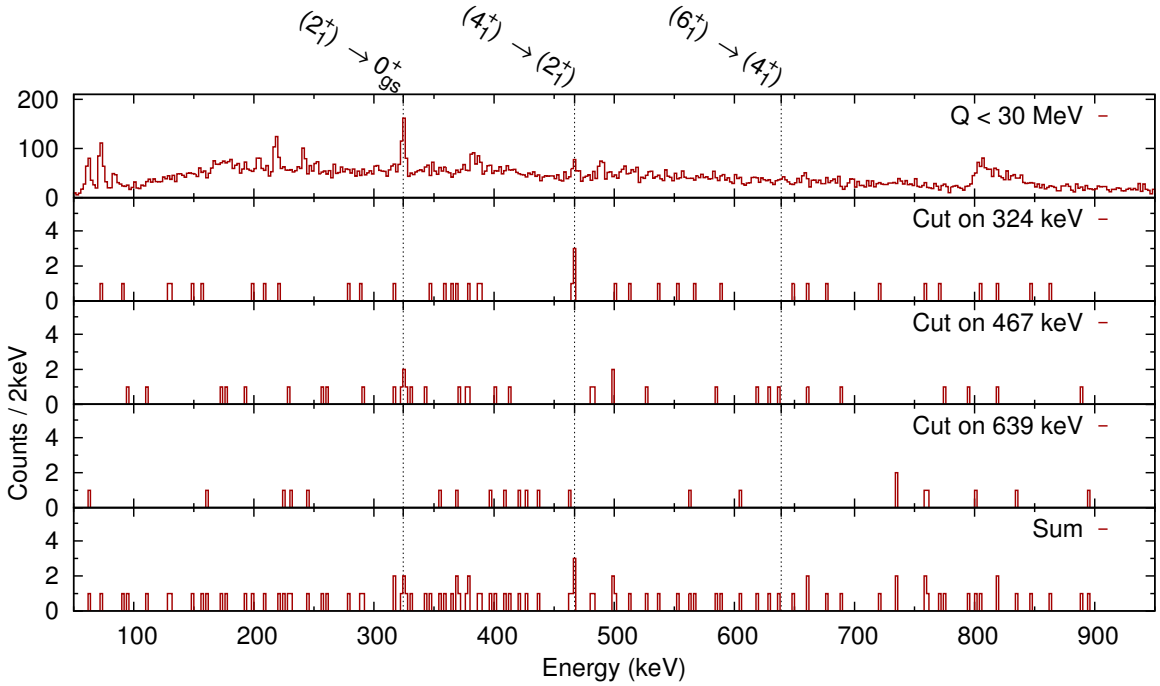

Figure 5.4: Gamma-ray spectra obtained for ^{196}Os after gating on the beam-like recoils ^{84}Kr having a reconstructed Q value smaller than 30 MeV and with a gate on the γ rays at 324 keV, 467 keV and 639 keV.

fraction of the intensity of the first 2^+ state. The general trend is, that the population of a non-yrast 2^+ state via multi-nucleon transfer reactions is very weak (few percent of the first 2^+) whereas that of a yrast 6_1^+ state is usually much larger.

Therefore, the assignment of the 639 keV transition to the de-excitation of the 6_1^+ state is preferable. The fact that the 639 keV transition does not appear in coincidence with the 324 keV and 467 keV transitions can be explained through the low statistics in the γ-γ matrix. In the projection shown in Figure 5.4 the intensities of the three relevant transitions are compatible within errors with those of the singles spectrum of Figure 5.3 have different absolute values with the 639 keV transition resulting more than three times weaker with respect to the 467 keV one. Considering the number of counts of the 324 keV and 467 keV peaks in the projection, the expected number of counts in coincidence between them, taking into account the efficiency of the AGATA demonstrator and a binomial distribution, is 3, which indeed is what is observed in the two middle spectra of Figure 5.4.

Accordingly, the 639 keV transition is expected to have at most 1 event in coincidence with the 324 keV and 467 keV lines. This is just at the level of the background observed in our coincidence spectra of Figure 5.4.

Hence, the present low-statistics data can not prove the assignment of the 639 keV transition to be the γ ray emitted by the de-excitation of the (6_1^+) level. However, the data is compatible with this assumption.

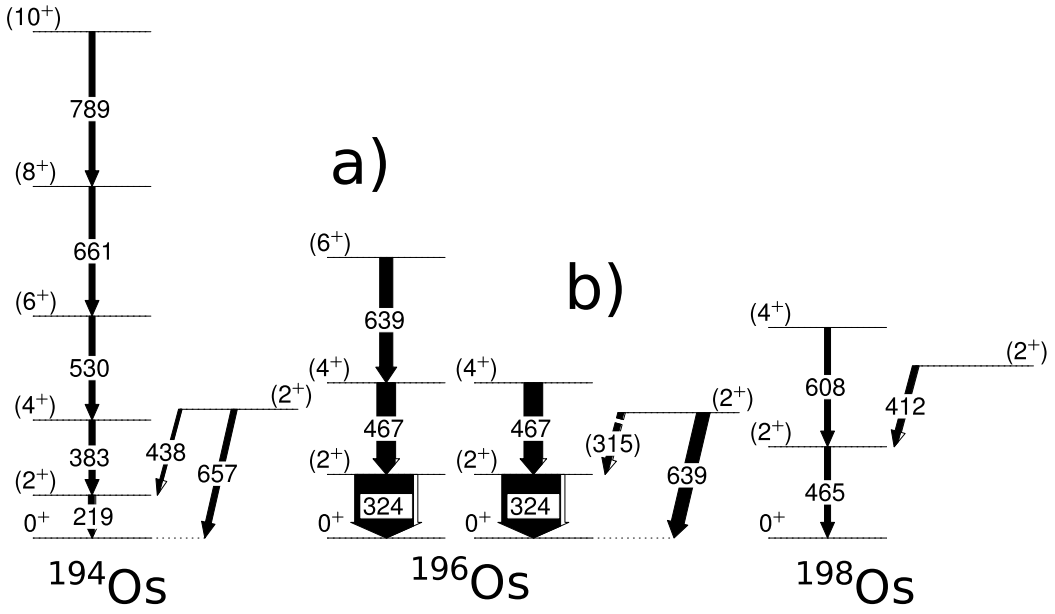

Figure 5.5: Level scheme of ^{194}Os (left) and ^{198}Os (right) based on reference [46] and [47], respectively. In the middle the two possible level schemes of ^{196}Os considering just γ-γ coincidences, placing the 639 keV transition as deexciting the (6_1^+) (a) or the (2_2^+) level (b), are drawn.

The energies of the 2_1^+ and the 4_1^+ level are in agreement with the previously reported levels (see Figure 5.6), although being slightly higher in energy.

A previous experiment using a ^{136}Xe beam impinging on a ^{198}Pt target was reported in literature [56, 134]. A prompt γ-ray spectrum with a condition on the delayed γ rays emitted by ^{136}Ba, the binary partner of ^{196}Os, was produced (see Figure 5.1.1). In this spectrum a small peak appears on the right hand side of the $4_1^+ \rightarrow 2_1^+$ transition of ^{188}Os at 322.9 keV. The energy of the small peak is compatible with the presently found $(2_1^+) \rightarrow 0_{gs}^+$ transition in ^{196}Os.

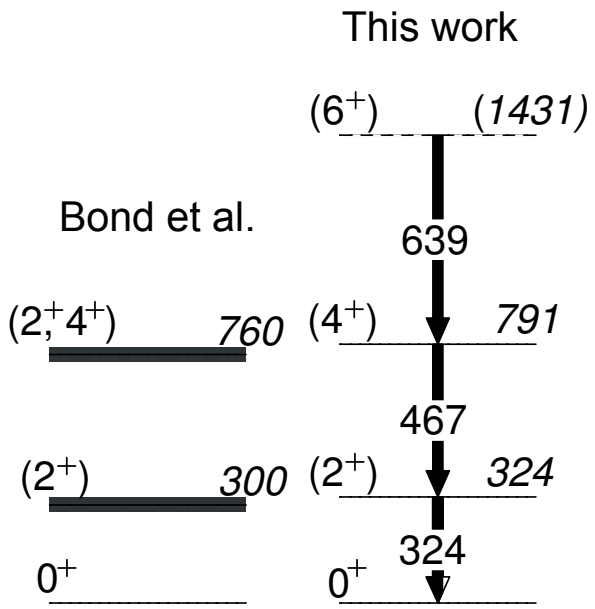

Figure 5.6: Deduced level scheme (right) compared to the study by Bond et al. [48]. The error of the exited states is proportional to the width of the level.

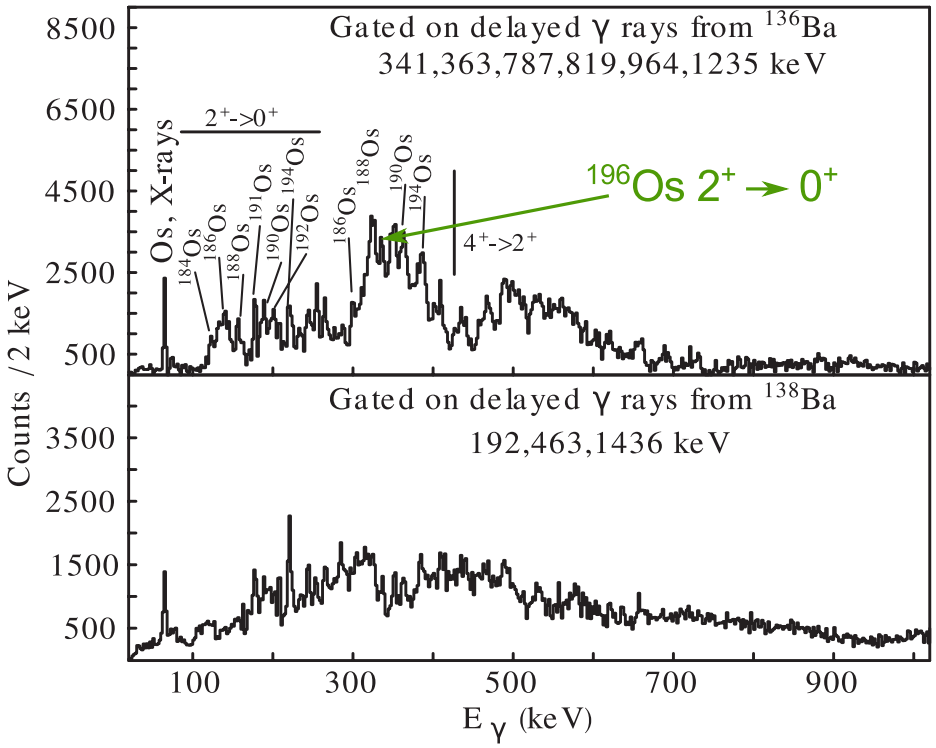

Figure 5.7: A previous study of the ^{136}Xe on ^{198}Pt reaction. A hint of the $(2_1^+) \rightarrow 0_{gs}^+$ transition of ^{196}Os is indicted. Figure adopted from reference [56].

5.1.2 Excited states in ^{195}Os

An isomeric state with a half-life of $T_{1/2} = 26\,\text{ns}$ exists in ^{195}Os [53, 54, 138] as shown in Figure 5.9. The current knowledge of its excited states is based on isomeric decay spectroscopic experiments and of this isomer and an additional long-lived isomeric state [139] with an energy of 454(10) keV, observed in a storage ring experiment at GSI, Germany.

The highest yield among the krypton isotopes populated in the reaction is ^{85}Kr, the binary partner of ^{195}Os. Due to the low neutron-evaporation threshold of 5267 keV [140], a spectrum gated on ^{85}Kr shows even with a very stringent condition on the reconstructed Q value, transitions of ^{194}Os. Figure 5.8 shows the spectrum gated on ^{85}Kr and a reconstructed Q value smaller than 3 MeV. The most intense transition is the 219 keV $2_1^+ \rightarrow 0_{gs}^+$ γ ray in ^{194}Os. The γ rays observed for ^{196}Os are not present in this spectrum, supporting the assignment to ^{196}Os. A peak at 439.2 keV appears in the spectrum that corresponds to the energy of a transition reported in three previous isomeric decay studies [53, 54, 138] of ^{195}Os and the $2_2^+ \rightarrow 2_1^+$ transition in ^{194}Os [46]. However, the depopulation of the 2_2^+ level of ^{194}Os has a branching to the ground state twice as intense as to the first 2^+ state. The $2_2^+ \rightarrow 0_{gs}^+$ transition in ^{194}Os has an energy of 656.5 keV, which is not observed in this spectrum. Additionally, in spectra with a less stringent condition on the reconstructed Q value, the ratio of intensity of the 439.2 keV to the $2_1^+ \rightarrow 0_{gs}^+$ transition of ^{194}Os shrinks. Hence, this γ ray is assigned to ^{195}Os.

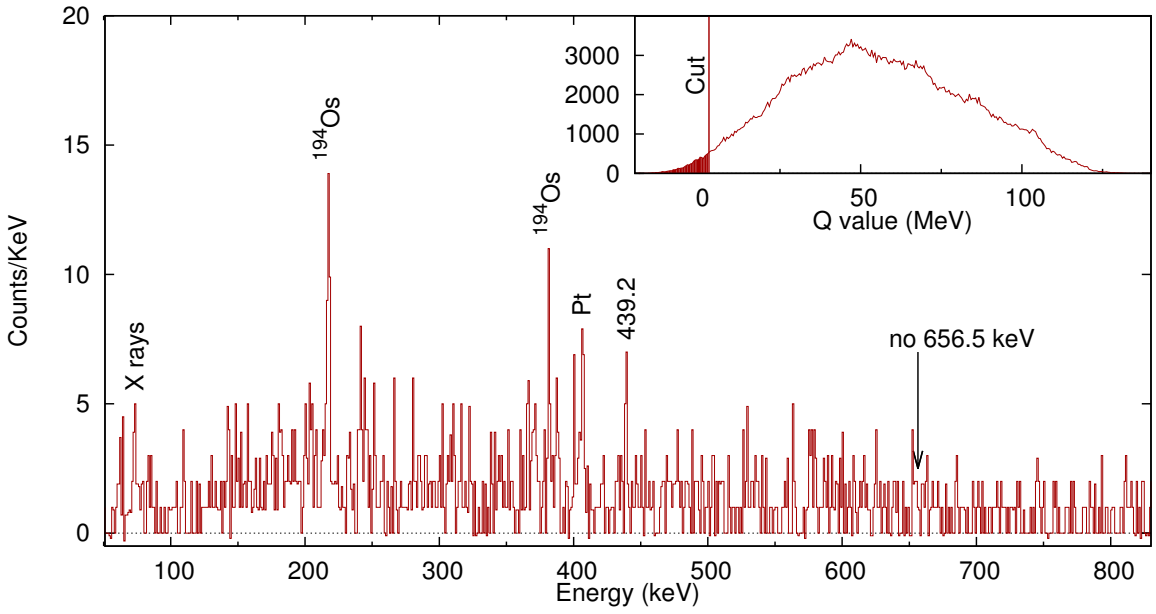

Figure 5.8: Gamma-ray spectrum with a gate on ^{85}Kr, a reconstructed Q value $\leq$ 3 MeV (see inset), on a multiplicity of γ rays of one and Doppler corrected for ^{195}Os. The transition identified in ^{195}Os is labelled by its energy. Transitions from lighter osmium isotopes produced after the evaporation of neutrons are labelled. The excitation of the target is indicated by "Pt".

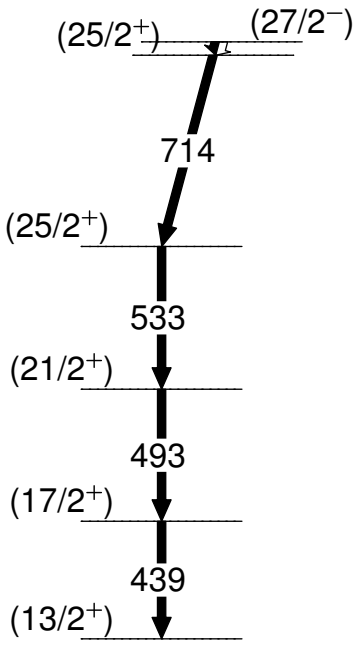

Figure 5.9: Level scheme of ^{195}Os previously reported in References [53, 138]

5.1.3 Search for excited states in ^{197}Os

An isomeric state with a half-life of 78.2(66) ns has been reported in ^{197}Os [53]. It was suggested, that the isomeric state has a $25/2^-$ or $27/2^-$ character. From its deexcitation four γ rays were observed: 204.4 keV, 415.9 keV, 486.5 keV and 628.8 keV.

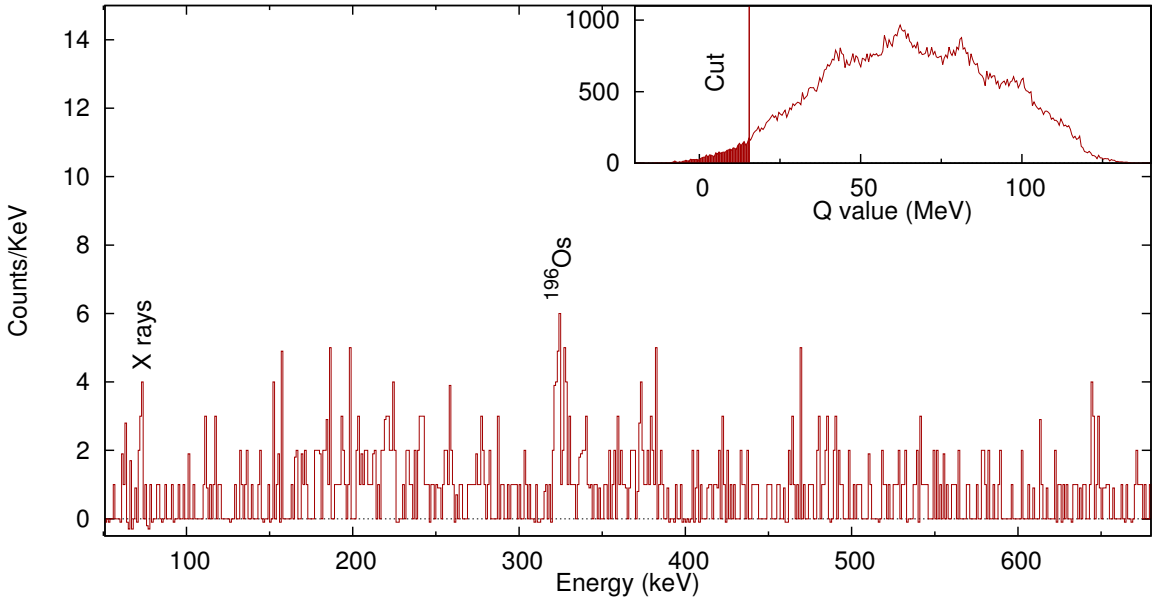

Figure 5.10: Gamma-ray spectrum gated on ^{83}Kr, a reconstructed Q value $\leq$ 15.5 MeV (see inset) and on a multiplicity of γ rays of one and Doppler corrected for ^{197}Os. The transition identified in ^{196}Os are indicated

Figure 5.10 shows the spectrum gated on ^{83}Kr and a reconstructed Q value smaller than 15.5 MeV. The 324.4 keV transition of ^{196}Os is visible, which is present due to the evaporation of one neutron, that populates ^{196}Os. Some peaks appear in this spectrum, in particular at 327 keV and 645 kev: however the statistics is too low for any assignment. The previously reported γ rays are not observed.

5.2 Shape evolution in the neutron-rich platinum isotopes

The shape transition from prolate deformation to oblate deformation is observed for the platinum isotopes, where ^{196}Pt is the textbook example of a γ-soft nucleus [18]. The $^{190-198}$Pt isotopes are stable and therefore have been well studied. In our experiment large statistics for the platinum isotopes has been collected and new states are observed. The two-neutron stripping channel has a higher yield than the two-proton pick-up channel (^{196}Os) and leads to the isotope ^{200}Pt, which is reported in detail in the following.

5.2.1 In-beam γ-ray spectroscopy of ^{200}Pt

^{200}Pt has two neutrons more than the heaviest stable platinum isotope ^{198}Pt. It was investigated via a variety of methods, including the (t,p) reaction [133], β decay [141] and fragmentation reactions [53, 54]. The light-ion induced reaction and the β decay populate predominately low- to medium-spin states. The isomeric decay studies are limited to certain states in which the isomer decays to. The presently known highest ground state band level of ^{200}Pt is the 4_1^+ state. A (12^+) state was proposed as an isomeric state feeding the 7_1^- level [53, 54]. No direct de-excitation of the (12^+) level over the low-lying states of the ground state band was observed.

A gate on the binary partner of ^{200}Pt, ^{80}Se, produces a γ-ray spectrum including many peaks from lower-mass platinum isotopes, produced via neutron evaporation. In order to suppress these γ-ray transitions, a spectrum for ^{200}Pt with a condition on ^{80}Se and a reconstructed Q value higher than 30 MeV is constructed (Figure 5.11).

In this spectrum previously identified de-excitations of the two lowest-lying states of ^{200}Pt can be observed. Since a 40 ns wide gate is used for the prompt peak, γ-rays belonging to the decay of the 7^--isomeric level can also be detected. Its half-life is 14.2 ns and thus well inside the prompt condition. These peaks are broad due to the partially wrong Doppler correction. An additional γ ray at 779.6 keV appears in this spectrum. Yates et al. [133] reported a γ ray with an energy of 780.8 keV, which was placed to decay into the 4_1^+ state. A γ-γ coincidence analysis of these three γ rays (see Figure 5.12) indicates, that they are in mutual coincidence.

Table 5.2: Energies (E_γ) and relative intensities (I_γ) of the observed γ-ray transitions for ^{200}Pt. The spin assignment of the transitions based on previously reported levels [133] and the energy of the levels $E(J_i)$ are also given.

E_γ (keV)	I_γ	$J_i^\pi \rightarrow J_f^\pi$	$E(J_i)$ (keV)
469.6 (10)	100.0 (26)	$2_1^+ \rightarrow 0_{gs}^+$	469.6
632.2 (10)	51.2 (27)	$4_1^+ \rightarrow 2_1^+$	1101.8
779.6 (10)[a]	8.7 (15)	$(6_1^+) \rightarrow 4_1^+$	1881.4

[a] newly assigned transition

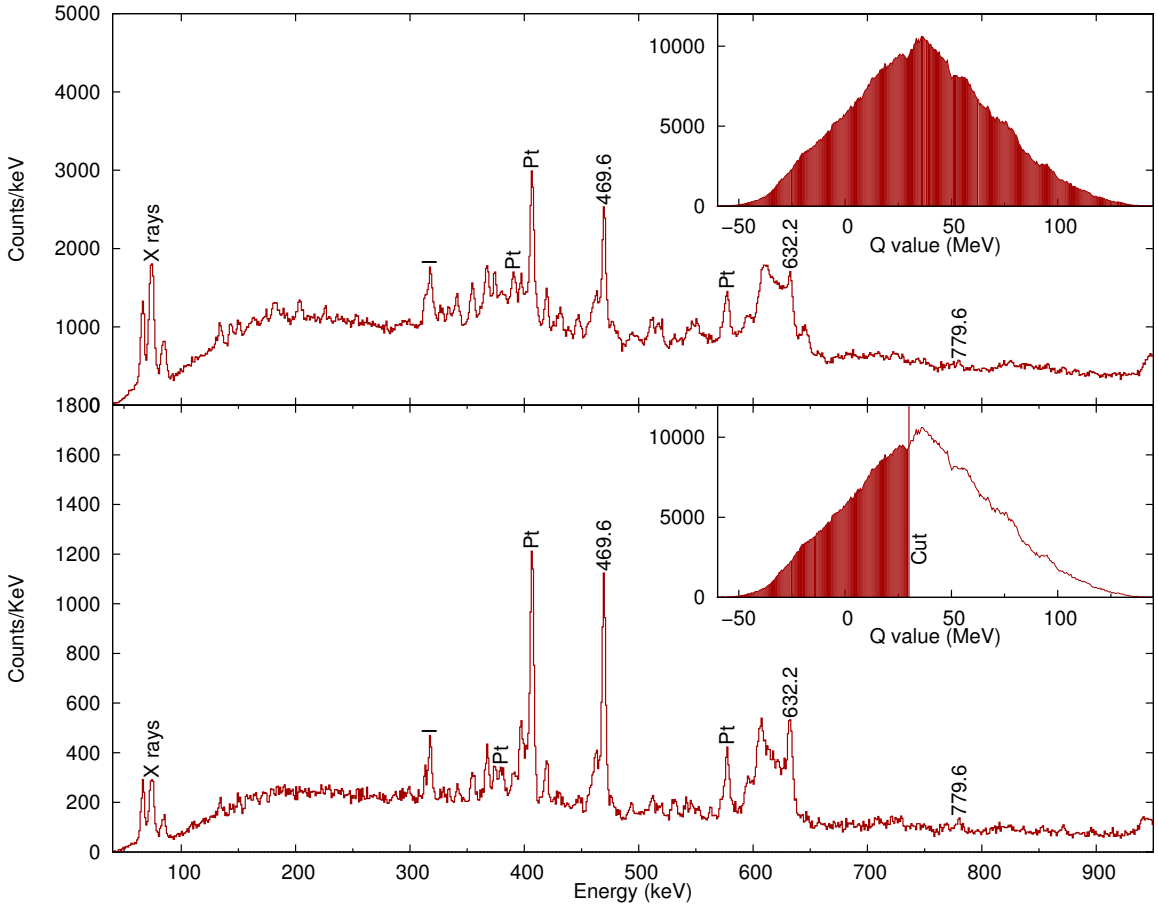

Figure 5.11: Gamma-ray spectra gated on ^{80}Se, the binary partner of ^{200}Pt, and Doppler corrected for the target-like recoil ^{200}Pt. On the bottom an additional condition on a reconstructed Q value smaller than 30 MeV is applied. Transitions assigned to ^{200}Pt are labelled by their energies. The intensities and the levels are given in Table 5.2. Contamination of lower mass platinum isotopes are indicated by Pt and decays of the isomeric states by I.

As explained before, multi-nucleon transfer reactions tend to predominantly populate yrast states. Hence, th 779.6 keV γ ray is assigned to originate from the decay of the yrast (6_1^+) state. This placement at a level energy of 1881.4 keV fits well into the systematics of steadily increasing 6^+ energies in the yrast band of the even-even platinum isotopes: when approaching the $N = 126$ shell closure at ^{204}Pt, the energies of the 2_1^+ and 4_1^+ states increase. The systematics of the yrast band of the even-even platinum isotopes is drawn in Figure 5.13.

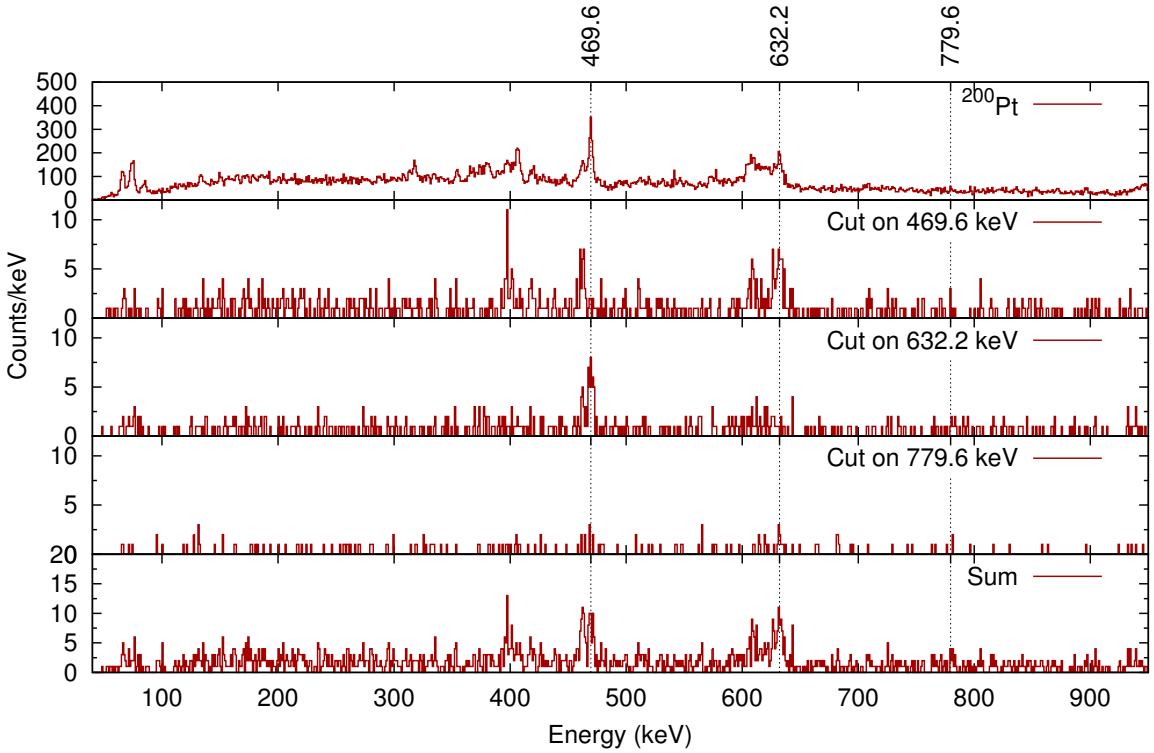

Figure 5.12: Gamma-ray spectra obtained for ^{200}Pt after gating on the beam-like recoils ^{80}Se having a reconstructed Q value smaller than 30 MeV and a multiplicity higher than one (top) and with a gate on the γ rays at 469.6 keV, 632.2 keV and 779.6 keV. The sum of the gates is presented at the bottom.

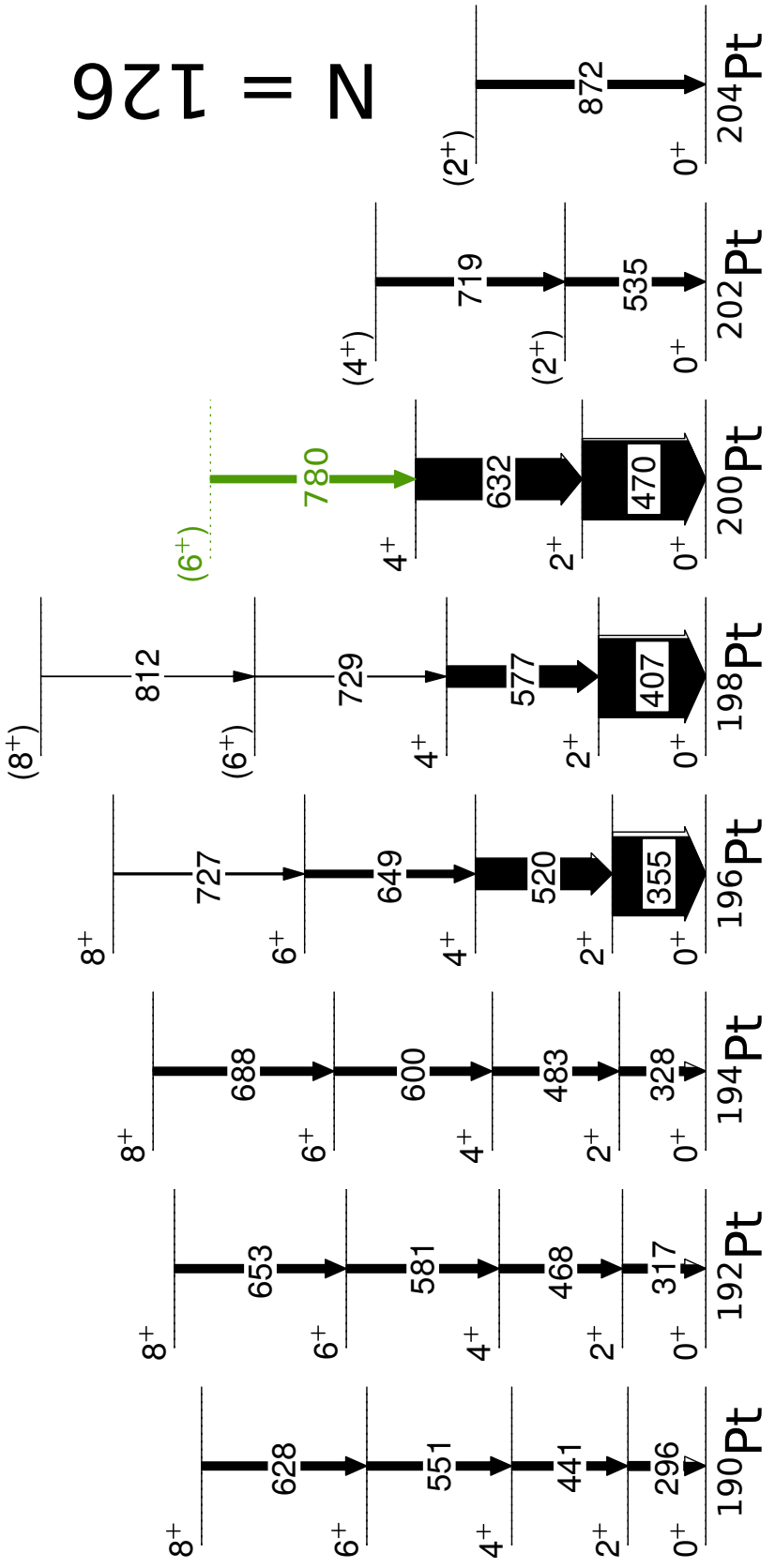

Figure 5.13: Systematics of the yrast band of the $^{190-204}$Pt isotopes. The intensities of the measured yrast bands in ^{196,198,200}Pt are proportional to the widths of the arrows. The newly assigned transition is marked in green. For the non studied platinum isotopes, the data are taken from [53, 141–145].

5.3 Results on beam-like recoils

Not only for the target-like nuclei new results are obtained, but also for the beam-like nuclei many new excited states can be identified. As an example of the quality of the obtained data, the Zinc isotopes are presented in this section.

5.3.1 Neutron-rich zinc isotopes

The zinc isotopes ($Z = 30$) have 4 protons less than the beam ($Z = 34$) and are produced via multi-nucleon transfer reactions with a sufficient yield for γ-ray spectroscopy (see Figure 5.14). The main yield in this experiment are unstable isotopes above the heaviest stable zinc isotope, ^{70}Zn. In this section only the results from the even-even isotopes are discussed. The γ-ray spectra in coincidence with the different even-even Zinc isotopes are presented in Figure 5.15. The level schemes of ^{72}Zn, ^{74}Zn and ^{76}Zn are extended in this experiment. Figure 5.17 shows the partial level scheme deduced for the even-even zinc isotopes.

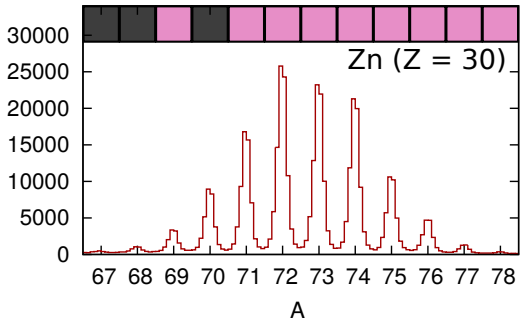

Figure 5.14: Mass spectrum of the zinc isotopes identified at the focal plane position of the *PRISMA* spectrometer. The unstable isotopes are indicated by a pink box.

^{70,72}Zn

The nuclei ^{70}Zn and ^{72}Zn were studied previously in a thick-target DIC experiment [146] using a ^{64}Ni beam on a ^{208}Pb target. From the γ-γ coincidences the yrast-band of ^{70}Zn and ^{72}Zn were established up-to the (12^+_1) and the (10^+_1) state, respectively.

In this experiment, all γ-rays were reported by Wilson et al. [146], except of a transition in ^{72}Zn at 1275.7 keV. This transition is a candidate for the $(12^+_1) \rightarrow (10^+_1)$ transition: in the γ-γ analysis, this transition indicates one count in coincidence with the deexcitation of the lower-lying yrast states. The corresponding γ-γ analysis is shown in Figure 5.16. Due to the low statistics in the γ-γ analysis the assignment is only tentative. The results are summarised in Table 5.3.

^{74}Zn

The 2^+_1 and the 4^+_1 states were identified in the β decay of ^{74}Cu [147] and by Coulomb excitation [148]. Louchart et al. measured the transition strengths of the low-lying excited states of the $^{70-76}$Zn [149] with the same *AGATA-PRISMA* setup. The (6^+_1)-state was identified and reported in the PhD thesis of Faul [150] with an energy 2 keV higher than the one reported by Louchart et al..

The level scheme of Louchart et al. is confirmed. Two additional transitions are identified. Based on intensities, systematics and the γ-γ-coincidence analysis (see Figure 5.18), candidates for the 8^+_1 and 10^+_1 states are assigned. The results are summarised in Table 5.3.

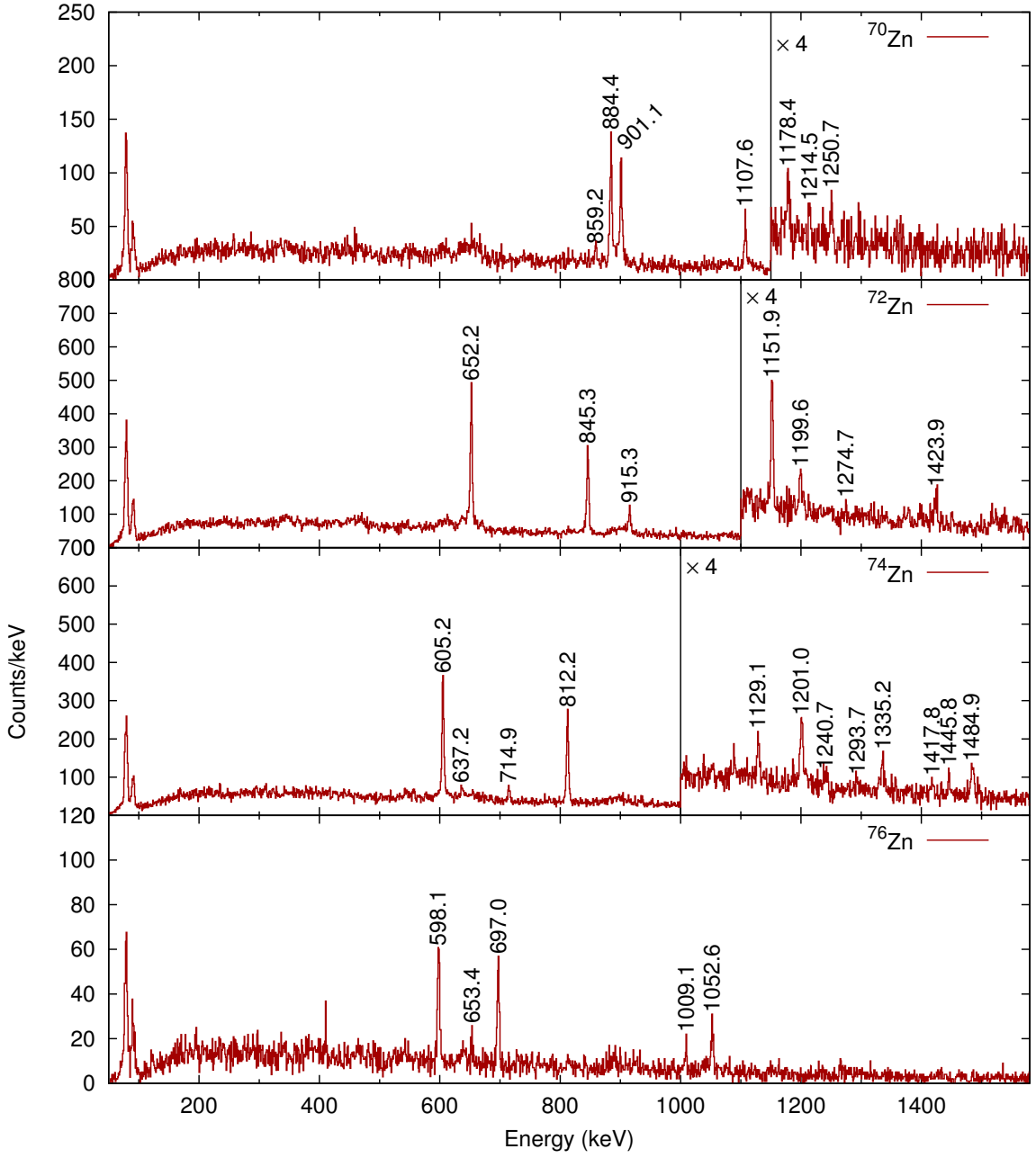

Figure 5.15: Gamma-ray spectra obtained after gating on the the even-even $^{72-76}$Zn isotopes identified in the *PRISMA* spectrometer. Transitions are labelled by their energies. The deduced level schemes are presented in Figure 5.17.

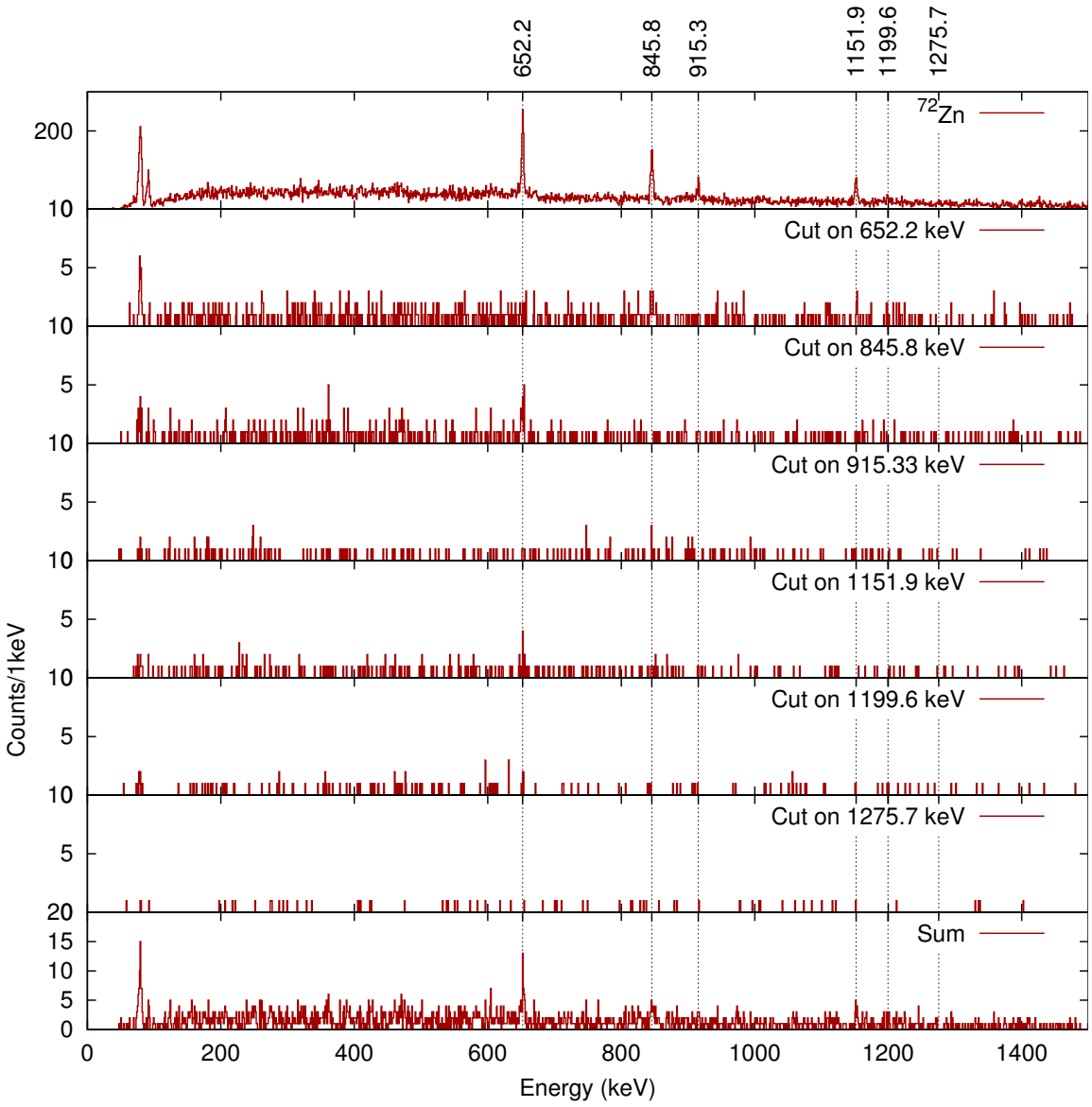

Figure 5.16: γ-γ coincidence spectra for ^{72}Zn. The top panel shows the total projection of the matrix. The middle spectra the coincidence with each transition. The bottom spectrum shows the sum of the gated spectra.

^{76}Zn

In ^{76}Zn the 2_1^+ and the 4_1^+ states were populated by β decay [147] and $\beta - n$ decay [151]. Faul [150] proposed a her PhD thesis a candidate of the $(6_1^+) \rightarrow (4_1^+)$ transition with an energy of 1055 keV.

In the γ-ray spectrum obtained for ^{76}Zn, a γ-ray peak with an energy of 1052.6 keV appears, more than 2 keV smaller than the $(6_1^+) \rightarrow (4_1^+)$ candidate of Faul [150]. Nonetheless, it is assumed to be the same transition. Furthermore, a peak at 653.4 keV is present in the spectrum, which is a candidate for the $(8_1^+) \rightarrow (6_1^+)$ transition. An additional transition can not be assigned due to the lack of γ-γ statistics. In summary, the level scheme is extended with a new transition depopulating a state for which we assume an 8^+ character based on the systematics. The results are summarised in Table 5.3.

^{78}Zn

Because of an 8_1^+-seniority isomer with a half life of $T_{1/2} = 319(9)$ ns [152], the level scheme of ^{78}Zn was established in previous experiments. Additionally, ^{78}Zn was populated by β decay [153].

Since the beam-like recoil exit the target chamber with a time of flight of around 10 ns, this experiment is not sensitive for isomeric states of the beam-like recoils.In our experiment γ rays in coincidence with ^{78}Zn are observed, but the statistics is not sufficient to add new information in this nucleus.

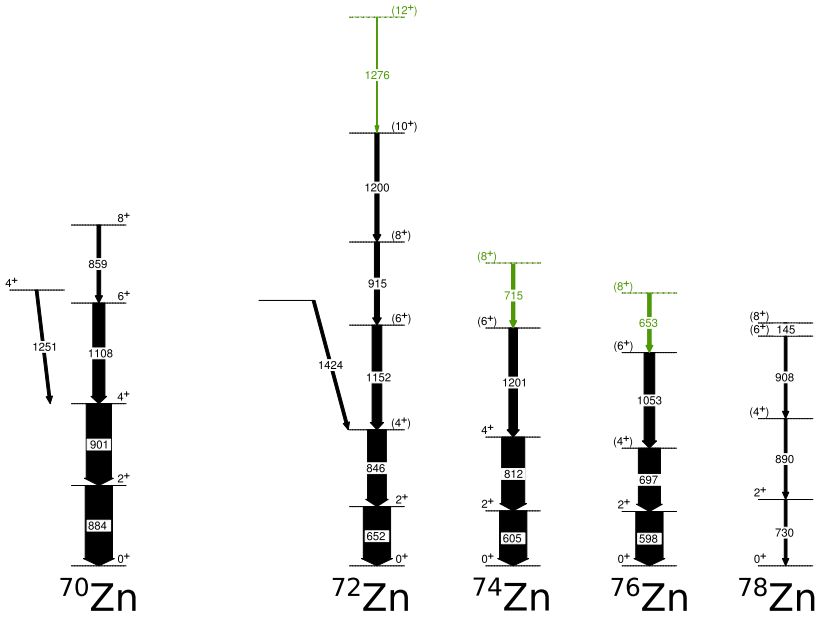

Figure 5.17: Level scheme of the even-even $^{72-76}$Zn isotopes observed in the present work. The newly found states and transitions are drawn in green. The widths of the arrows are proportional to the γ-ray intensities as given in Table 5.3. The level scheme of ^{78}Zn is based on Reference [152].

Table 5.3: Energies (E_γ) and relative intensities (I_γ) of the in this work observed γ-ray transitions for the even-even $^{70-76}$Zn. The spin assignment of the transitions and the energy of the level ($E(J_i)$) are also given. See text for details.

E_γ (keV)	I_γ	$J_i^\pi \rightarrow J_f^\pi$	$E(J_i)$(keV)
		^{70}Zn	
859.2 (10)	13.3 (28)	$8_1^+ \rightarrow 6_1^+$	3752
884.4 (10)	100.0 (53)	$2_1^+ \rightarrow 0_{gs}^+$	884
901.1 (10)	92.6 (51)	$4_1^+ \rightarrow 2_1^+$	1786
1107.6 (10)	44.4 (41)	$6_1^+ \rightarrow 4_1^+$	2893
1178.4 (10)[a]	14.8 (45)		
1214.5 (10)[a]	6.8 (37)		
1250.7 (10)	10.0 (40)	$4_2^+ \rightarrow 4_1^+$	3036
		^{72}Zn	
652.2 (10)	100.0 (30)	$2_1^+ \rightarrow 0_{gs}^+$	652
845.8 (10)	69.0 (27)	$(4_1^+) \rightarrow 2_1^+$	1498
915.3 (10)	18.5 (19)	$(8_1^+) \rightarrow (6_1^+)$	3565
1151.9 (10)	35.6 (21)	$(6_1^+) \rightarrow (4_1^+)$	2650
1199.6 (10)	15.3 (20)	$(10_1^+) \rightarrow (8_1^+)$	4765
1275.7 (10)[a]	1.2 (10)	$(12_1^+) \rightarrow (10_1^+)$	6041
1423.9 (10)	10.4 (18)	$(?) \rightarrow (4_1^+)$	2922
		^{74}Zn	
605.2 (10)	100.0 (34)	$2_1^+ \rightarrow 0_{gs}^+$	605
637.2 (10)[a]	8.4 (29)		
714.9 (10)[a]	12.1 (18)	$(8_1^+) \rightarrow (6_1^+)$	3333
812.2 (10)	84.6 (32)	$4_1^+ \rightarrow 2_1^+$	1417
1129.1 (10)[a]	13.9 (20)		
1201.0 (10)	31.5 (26)	$(6_1^+) \rightarrow 4_1^+$	2618
1240.7 (10)[a]	8.1 (21)		
1293.2 (10)[a]	3.7 (14)		
1335.1 (10)[a]	16.0 (25)		
1484.9 (10)[a]	20.2 (25)		
1417.8 (10)[a]	7.0 (20)		
1445.8 (10)[a]	5.9 (20)		
		^{76}Zn	
598.1 (10)	100 (11)	$2_1^+ \rightarrow 0_{gs}^+$	598
653.4 (10)[a]	12.3 (57)	$(8_1^+) \rightarrow (6_1^+)$	3001
697.0 (10)	81 (10)	$4_1^+ \rightarrow 2_1^+$	1295
1009.1 (10)[a]	21.7 (63)		
1052.6 (10)	39.1 (84)	$(6_1^+) \rightarrow 4_1^+$	2348

[a] new transition

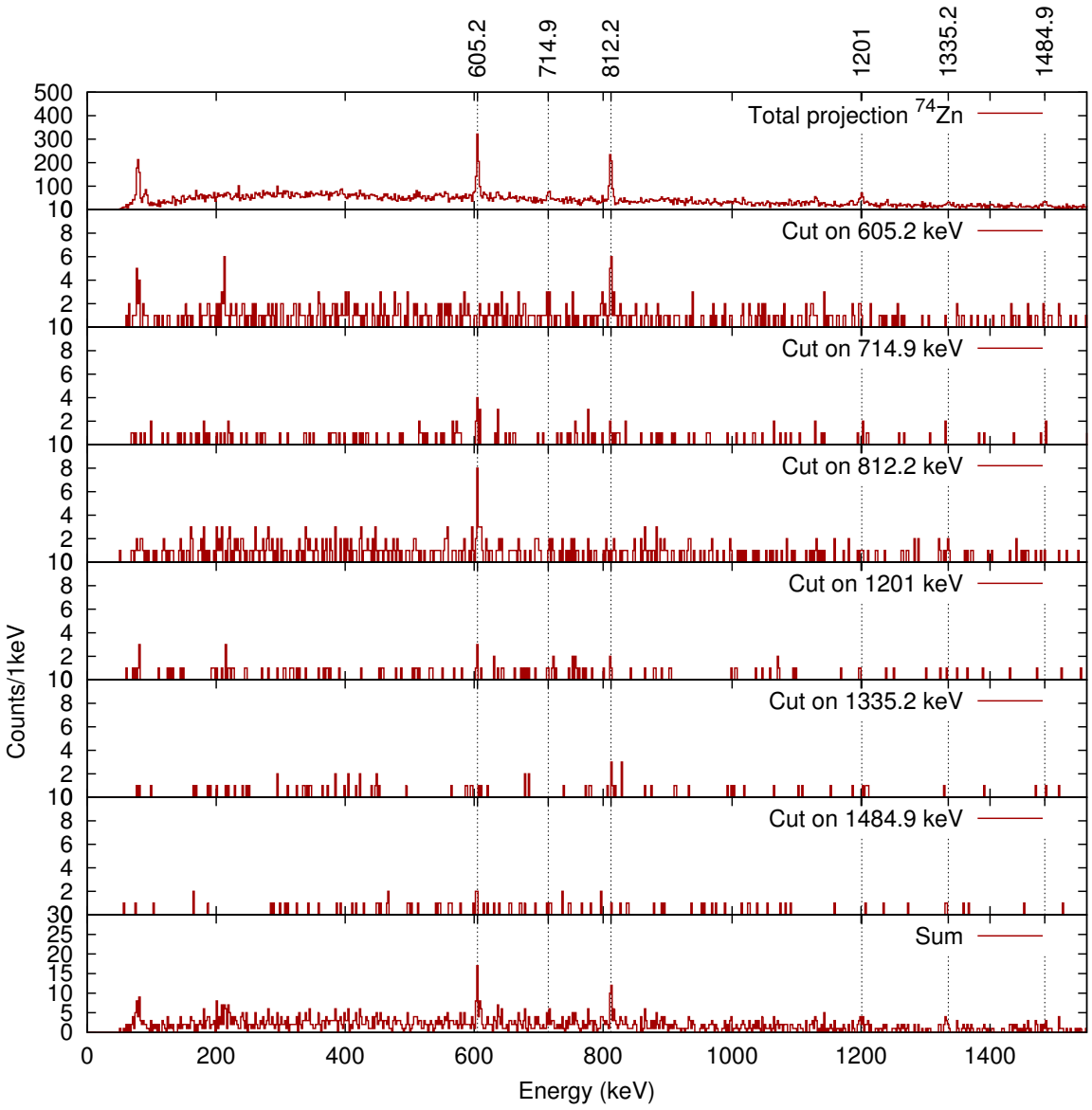

Figure 5.18: γ-γ analysis of the transitions found in ^{74}Zn. The top panel shows the total projection of the matrix. The middle spectra show the coincidence with the named transition. The bottom spectrum shows the sum of the gated spectra.

5.4 Isomeric states in the target-like recoils

The absence of collimators and anti-Compton shields of the *AGATA* array renders this setup (see Figure 5.19) very sensitive for the detection of γ rays emitted by target-like recoils stopped in the target chamber. The binary partner of the target-like recoil is identified in the *PRISMA* spectrometer and it is used to identify the isotope at rest, which emits delayed γ rays.

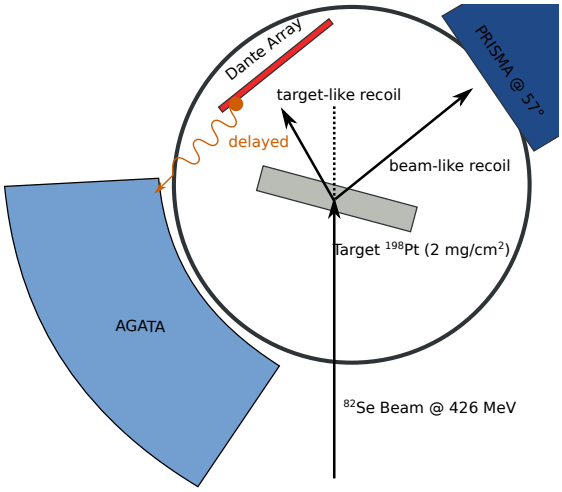

Figure 5.19: Sketch of the ^{82}Se+^{198}Pt reaction and the position of the implanted ions.

The lower time limit for the detection of isomeric states is given by the time of flight of the heavy binary partner from the target to the target chamber and from the FWHM of the prompt-peak and is around ≈ 8 ns. The upper limit is given by the acquisition-time window after the prompt peak and is around ≈ 400 ns. Due to various corrections of the γ-rays timing (compare section 3.3), which includes also the time of flight of the beam-like recoils in the *PRISMA* spectrometer, ≈ 250 ns is the upper limit for the measurement of the half-life of the isomeric states.

The region of the neutron-rich isotopes around ^{198}Pt was already investigated via i) decay spectroscopy after the fragmentation at relativistic energies of a ^{208}Pb and ^{238}U beam, ii) via deep-inelastic collisions or multi-nucleon transfer reactions with a thick target and iii) fusion-evaporation reactions for the less neutron-rich isotopes.

In the present experiment, in total 44 isomeric states are identified, including 3 previously not reported isomeric states. Figure 5.20 shows the nuclear chart of the Os-Pt region. The stable and primordial nuclei are drawn in black. The binary partners of the identified beam-like recoils (compare Figure 3.13 for the identified beam-like recoils) are inside the green polygon. The isomeric states reported in literature and the newly observed ones are indicated by coloured circles.

Due to the evaporation of neutrons, no isomeric state could be observed in the most-neutron rich isotopes, where the beam-like recoil is observed. Additionally, some isomeric states in nuclei, for which the binary partner is not observed, are identified.

In this section the newly found isomeric states are reported in detail. They are listed together with selected observed known isomeric states in Table 5.4. A complete list of the isomeric states will be part of a further publication.

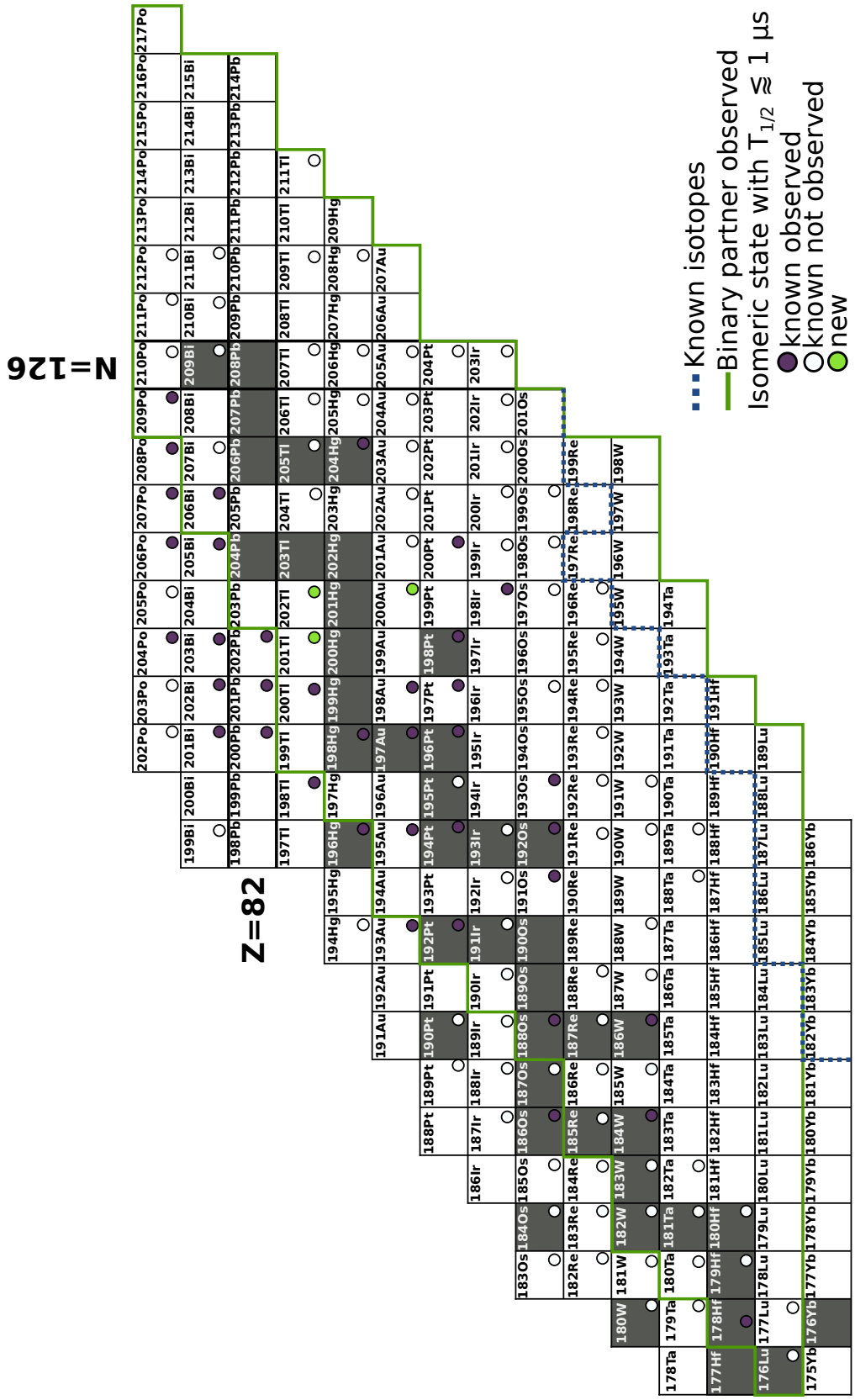

Figure 5.20: Nuclear chart in the Os-Pt region. The binary partners of the beam-like identified with the *PRISMA* spectrometer isotopes are inside the green polygon. Isomeric states with a half-life shorter than 1 µs are marked with three different circles.

Isotope	Level (J_i^π)	$E_x(J_i^\pi)$ (keV)	E_γ (keV)	$T_{1/2}$ (literature)	$T_{1/2}$ (this work)
			Osmium $Z = 76$		
^{188}Os	7_1^- [154]	1771 [154]	155.2, 323.1, 462.4, 728.5	14(1) ns [154], 14.0(2) ns [155]	15(2) ns
^{193}Os			242.5	132(29) ns [53]	117(19) ns
			Platinum $Z = 78$		
^{200}Pt	(7_1^-) [53]		463.4, 470.0, 633.4	14.2(4) ns [53]	14.9(22) ns
			Gold $Z = 79$		
^{197}Au	5^+ [156]	2532 + X? [46]	261.2, 357.7, 429.4, 435.8, 639.7	150(5) ns [46]	155(7) ns
^{198}Au		312.2 [156]	97.2, 214.9 [156]	128(15) ns, 118(5) ns, 123(4) ns [156–160]	105(4) ns
^{200}Au			332.4	new	17(1) ns
			Thallium $Z = 81$		
^{201}Tl		1987.8 [161]	749.2	new	26(5) ns
^{202}Tl			853.3	new	77.5(93) ns

Table 5.4: List of the isomeric states observed and identified in this experiment. The γ-ray energies in parenthesis are transitions previously reported, but not observed.

5.4.1 New isomeric state in ^{200}Au

Presently, only one γ-spectroscopic study of ^{200}Au is reported in literature [162]. A β^- decay of ^{200}Pt was investigated and γ-γ coincidence data were collected. However, no isomeric transition was reported. ^{200}Au was also observed in experiments using the fragment separator at GSI Darmstadt, Germany at relativistic heavy-ion beam energies [47, 53–55], but no delayed γ-rays were reported.

In the delayed γ-ray spectra of ^{78,79,80}As gated on 30 ns - 140 ns after the prompt peak (see Figure 5.22), among the known γ rays, a new γ ray with an energy of 332.4(5) keV is present. This γ ray appears when a condition on the reconstructed Q value of $\approx$ 12 MeV and on the ^{80}As isotope is applied. For the lighter arsenic isotopes a condition on a higher excitation is required to see this γ ray. This transition is not present in the spectra with a gate on ^{81}As and heavier isotopes. The 332.4 keV transition is therefore assigned to ^{200}Au, the binary partner of ^{80}As. A transition with an energy of 332.4 keV is not reported in literature. However Hill et al. [162] reported a γ ray with an energy of approximately 2 keV smaller than the newly observed one (330.28(5) keV), which is most likely an other transition.

A least square fit of the half-life via the decay curve of the 332.4 keV transition gives $T_{1/2} = 17(1)$ ns as it is shown in the inset of Figure 5.21.

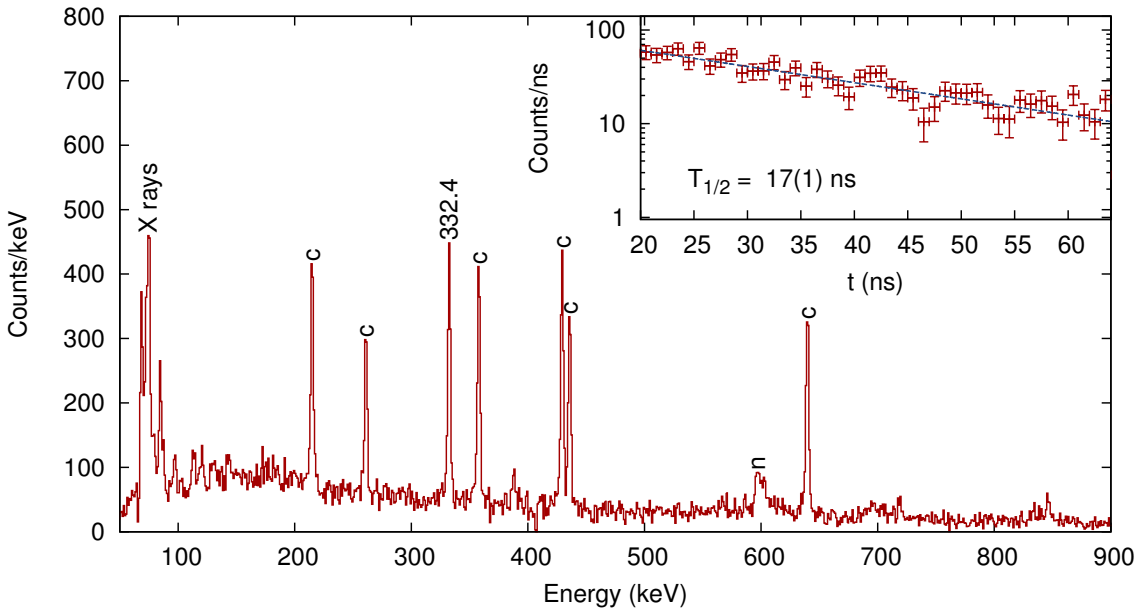

Figure 5.21: Delayed γ-ray spectrum for the isomeric state in ^{200}Au, as shown in Figure 5.22 (bottom). The new transition is labelled by its energy. Contamination from other γ rays following the deexcitation of other isomeric states and neutron-induced reactions are labelled by c and n, respectively. The inset shows the least-square fit of the half-life.

A γ-γ-coincidence analysis shows no delayed γ rays in coincidence with the 332.4 keV

transition. Furthermore, no prompt γ rays are in delayed coincidence with it. These two are extracted from the spectra in Figure 5.23.

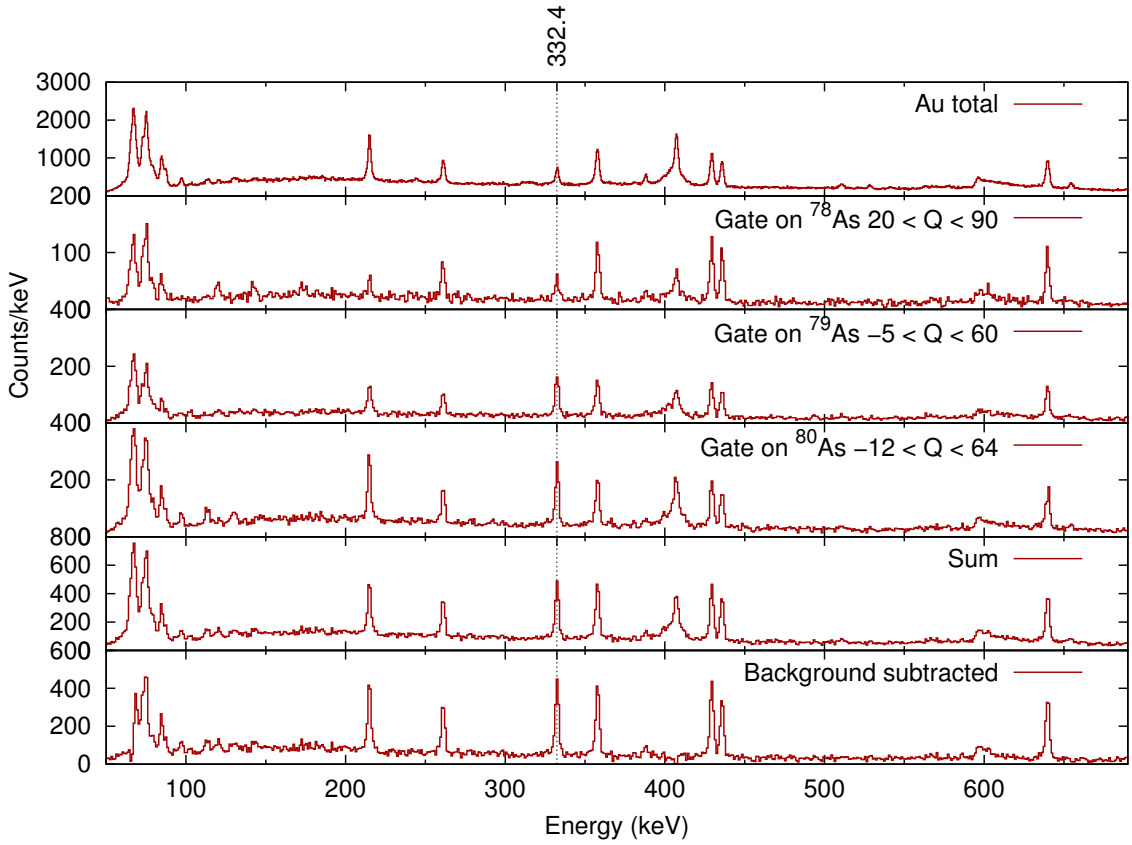

Figure 5.22: Delayed γ-ray spectra for the new isomeric state in ^{200}Au, obtained with the conditions on the reconstructed Q value shown in the panel for the nuclei $^{80-78}$As. The identified transition of ^{200}Au is labelled by its energy. The 2$^{\text{nd}}$ last panel shows the sum of the spectra for the different arsenic isotopes. The bottom spectrum shows the same spectrum after background subtraction. The not labelled peaks are due to other isomeric states in the gold isotopes.

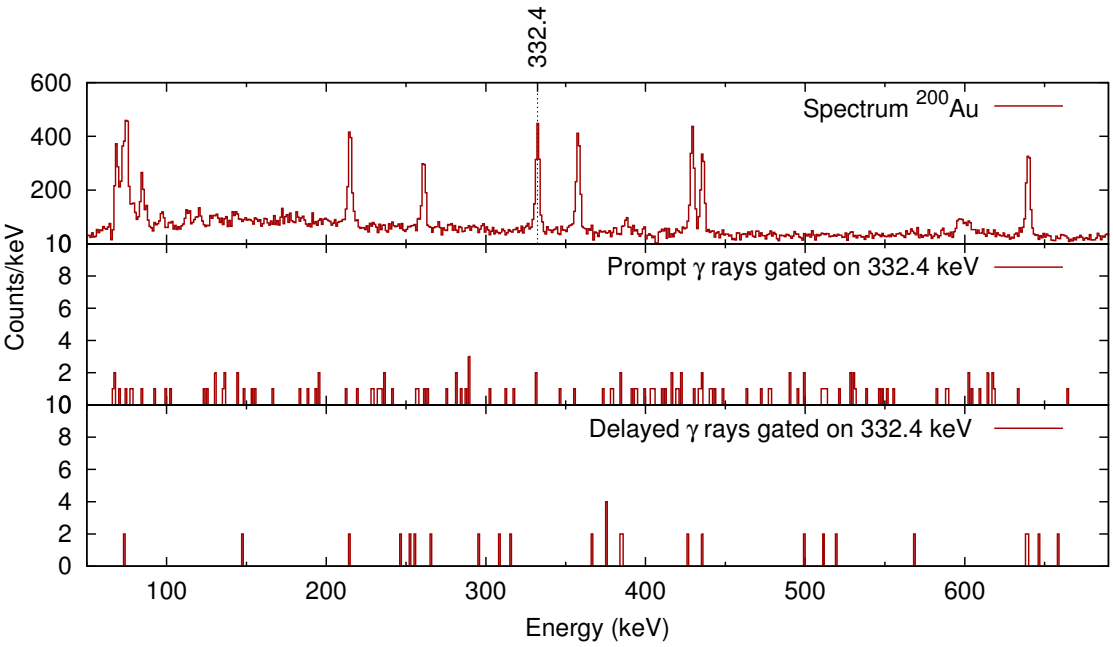

Figure 5.23: (top) Same as Figure 5.21. (middle) Prompt γ-ray spectrum using the same conditions as presented in Figure 5.22. (bottom) Delayed γ-ray spectrum in coincidence with the 332.4 keV.

5.4.2 New isomeric states in the thallium isotopes

The thallium isotopes have one proton less than the magic number at $Z = 82$. We were not able to identify all peaks appearing in the delayed γ-ray spectrum, produced with a condition on the binary partner of thallium. Therefore, some new additional isomeric states might be possible.

^{201}Tl

Slocombe et al. [161] reported a weak γ-ray transition with an energy of 749.21(30) keV feeding the $(11/2^-)$ state, which deexcites via the emission of a 319.0 keV γ ray to the $9/2^-$ isomeric state. The $9/2^-$ state has a half-life of 2 ms and thus outside our sensitivity range.

Both the 749.21(30) keV and the 319.0 keV transitions are identified in the delayed γ-ray spectrum (50 ns - 150 ns after the prompt peak), gated on the binary partners of the thallium isotopes, indicating that they follow the decay of an isomeric state previously not observed. A least-square fit of the half-life of this isomeric state using the 749.2 keV transition is presented in the inset of Figure 5.24 and reveals a half-life of 26(5) ns.

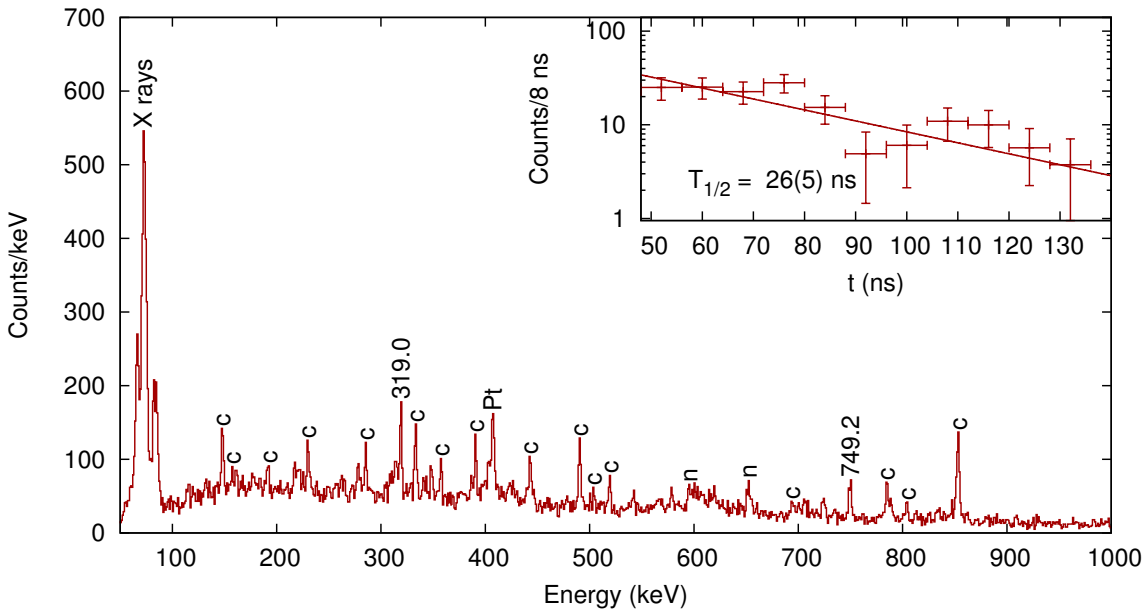

Figure 5.24: Delayed γ-ray spectrum 50 ns - 150 ns after the prompt peak for the thallium isotopes. The inset shows the least-square fit of the half-life of the isomeric state in ^{201}Tl using the 749.2 keV transition. Transitions of other isomeric states are labelled with c, neutron, beam induced and background by n and Pt, respectively.

^{202}Tl

Having one neutron less that the lightest stable thallium isotope, this nucleus was studied previously via light-charge particle and neutron induced reactions. A 7^+ isomeric state was identified in the fifties [163] and the most recent and precise measurement, using the ^{203}Tl$(n, 2n\gamma)$ reaction [164] yielded a half-life of 591(3) µs.

A γ ray with an energy of 853.3 keV appears in the delayed γ-ray spectra in coincidence with $^{72-78}$Ga. The γ-ray spectra with the condition on the reconstructed Q value where this transition appears are presented in the 7 top panels of Figure 5.25. The sum of the individual cuts is presented additionally with a gate 150 ns-250 ns after the prompt peak. Many peaks of shorter lived isomeric states, which are present in the sum spectrum disappear with the additional condition on γ-ray time, indicating the newly found isomeric state has a half-life of > 40 ns. This transition does not appear in the spectrum gated on ^{79}Ga. The pattern of the reconstructed Q value, where this transition appears, indicates, that this transition belongs to a deexcitation of an isomeric state in ^{202}Tl.

No γ-ray is found to be in coincidence with the 853.3 keV peak, whose area is of 609(30) counts in the sum spectrum. A transition in coincidence with it would have around 20 counts depending on the γ-ray energy. The background level in the γ-γ matrix gated on the 853.3 keV peak is between 0 and 2 counts. The delayed γ-ray spectrum corresponding to ^{202}Tl and the least-square fit of the half-life of the isomeric state deexciting via the 853.3 keV are shown in Figure 5.26. The deduced half-life is 77.5(93) ns.

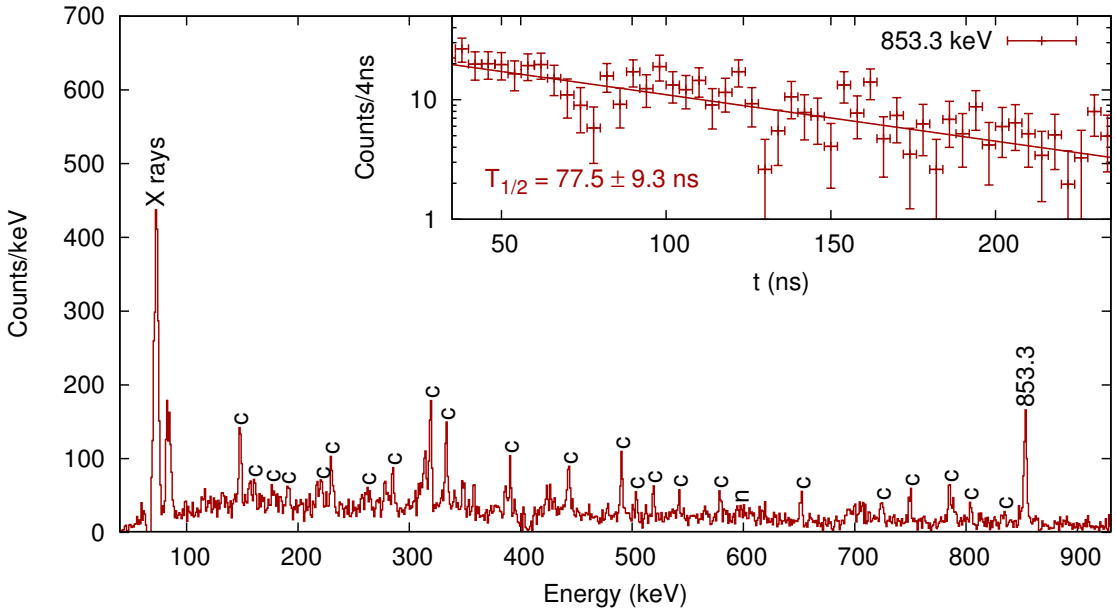

Figure 5.26: Delayed γ-ray spectrum for the new isomeric state in ^{202}Tl as presented in Figure 5.25 bottom. The inset shows the decay curve obtained by gating on the 853.3 keV transition and the least-square fit of the half-life of the isomeric state.

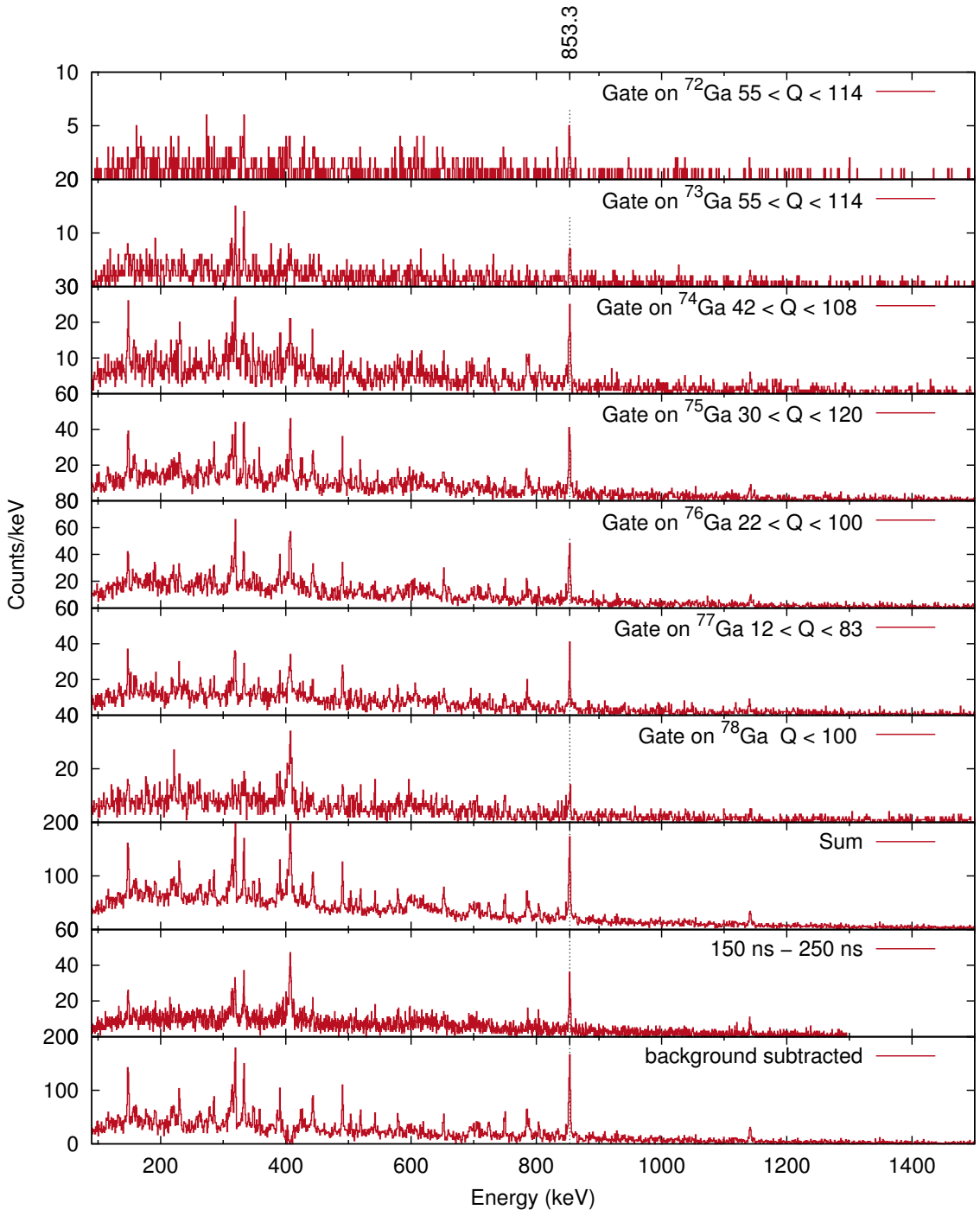

Figure 5.25: Delayed $\gamma-$ray spectrum for the isomeric state in ^{202}Tl, produced with different conditions on the reconstructed Q value as shown in the figure and by gating on the $^{72-78}$Ga isotopes. The new transition assigned to ^{202}Tl is labelled by its energy. The other peaks are due to the decay of other isomeric states. The last 3 spectra show the summed spectrum.

6 Theoretical interpretation

The shape of the nucleus and, in the case of a quadrupole deformation, the intrinsic quadrupole moment is not a direct observable. The observables measured in this experiment are the energies of low-energy excited levels. The energy spectra are compared to those calculated from configuration mixing calculations based on **P**otential **E**nergy **S**urfaces (PES) defined along the quadrupole (axial and non-axial) degrees of freedom.

The PES are calculated by state-of-the-art self-consistent beyond mean-field **S**ymmetry-**C**onserving **C**onfiguration-**M**ixing calculations (SCCM). The self-consistent mean-field theory is introduced in section 1.1.2 and the restoration of the particle number symmetries is explained in section 1.1.3.

Additionally, the **G**eometric **C**ollective **Mo**del (GCM) (introduced in section 1.1.1) is used for the comparison of the level scheme with the predictions of the limits of different shapes, i.e. typical potentials, in particular the axial rotor, vibrator and γ-soft rotor.

6.1 Shape evolution in the neutron-rich osmium isotopes

For the first time 3 $\gamma-$ray transitions are identified in ^{196}Os and assigned to deexcite the first $2^+, 4^+$ and 6^+ states. In order to compare the newly measured excited states with theoretical predictions, state-of-the-art self-consistent beyond mean-field symmetry-conserving configuration mixing calculations have been performed for the neutron-rich even-even $^{188-198}$Os.

6.1.1 Potential energy surfaces for the even-even $^{188-198}$Os isotopes

The potential energy surfaces for the neutron-rich even-even osmium isotopes $^{188-198}$Os are calculated using 60 deformed intrinsic states in the range $\beta \in [0, 0.5]$ and 9 major oscillator shells. The calculated PES are shown in Figure 6.1. The potential energy of a point with the deformation parameters (β, γ) is represented by a colour (see scale on the right border). In particular the minimum is represented by dark blue. Additionally, contour lines are drawn every 0.2 MeV.

A clear transition from prolate deformed nuclei (^{188}Os) to oblate deformed ones ($^{194-198}$Os) via a certain degree of γ softness is visible. The minimum of the PES changes from a prolate deformation, $\beta \approx 0.2$, in ^{188}Os over triaxial minima in ^{190}Os ($\gamma \approx 30°$) and ^{192}Os ($\gamma \approx 45°$)

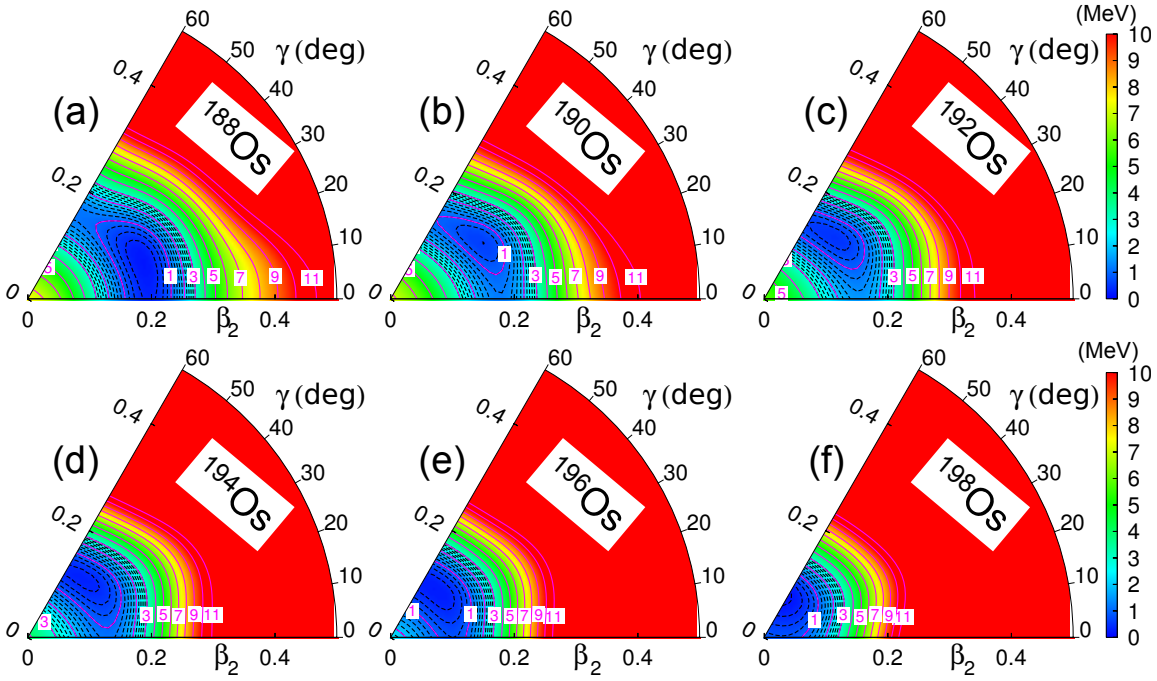

Figure 6.1: Particle number projected potential energy surfaces in the triaxial plane for the even-even $^{188-198}$Os isotopes calculated with the Gogny D1S interaction. Solid and dashed contour lines are separated 1.0 MeV and 0.2 MeV, respectively. The solid contour lines are labelled with their energy.

to oblate minima in ^{194}Os ($\beta \approx 0.14$), ^{196}Os ($\beta \approx 0.11$) and ^{198}Os ($\beta \approx 0.07$). A reduction of the deformation can be observed, when approaching the $N = 126$ shell closure, where the sphericity is restored. Additionally the PES of these nuclei show a degeneracy in the γ direction with ^{196}Os showing the strongest one: within the 1 MeV-contour line all intrinsic states from oblate to prolate deformation can be found. This indicates theoretically, that ^{196}Os is a γ-soft nucleus.

6.1.2 Theoretical predictions of excited states

The underlying structure of the PES described above is then reflected in the spectra calculated from configuration mixing calculations based on these surfaces. Figure 6.2 shows the known $E(J_i^+)/E(2_1^+)$-ratio of the yrast band of the osmium nuclei together with the newly measured ^{196}Os and the theoretical $E(J_i^+)/E(2_1^+)$ ratios. Additionally the same ratios as found from the geometric collective model in the limits of the axial rotor, γ-soft/triaxial rotor and vibrator are given [18].

The experimental spectra are close to the γ-soft/triaxial rotor limit for most of the analysed isotopes. However, a smooth transition from a more axial rotational behaviour in ^{188}Os through triaxial configurations towards more vibrational spectra in ^{198}Os can be observed when pairs of neutrons are added.

In particular, an almost perfect γ-soft/triaxial rotor yrast-band is predicted for ^{196}Os in

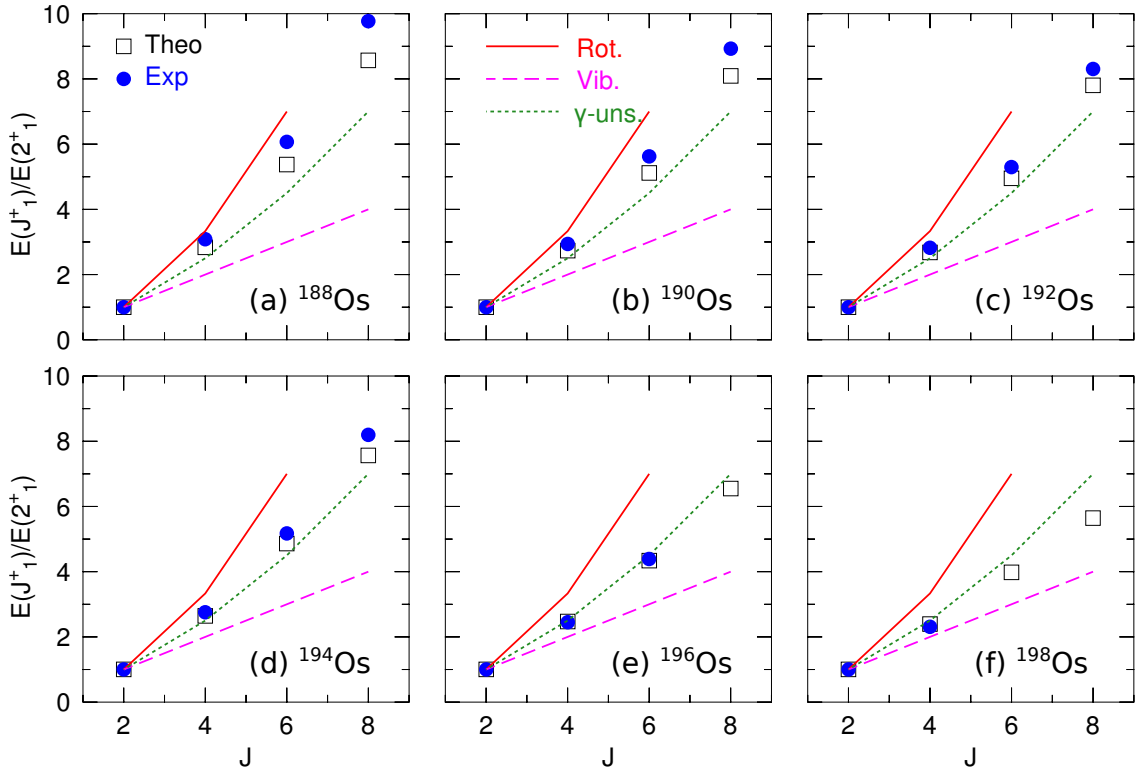

Figure 6.2: Yrast band excitation energies, normalised to the corresponding 2_1^+ energies, for $^{188-198}$Os isotopes. Blue dots and black boxes are the experimental points and theoretical beyond mean-field predictions respectively. Theoretical limits for axial rotor (red continuous line), vibrator (magenta dashed line) and γ-soft/triaxial rotor (green dotted line) geometrical models are also given. The experimental data is taken from [47, 51, 165–167] and this work for ^{196}Os.

good agreement with the experimental ratio $E(4_1^+)/E(2_1^+)$ and also with the assumption of the 639 keV transition as the γ ray corresponding to the transition $(6_1^+) \rightarrow (4_1^+)$ (see Figure 6.2(e)). The good correspondence of the measured excited states with the predictions of the γ-soft limit of the collective model is remarkable. The textbook example of a γ-soft rotor is the isobar ^{196}Pt [18]. Their $E(4_1^+)/E(2_1^+)$ and $E(6_1^+)/E(2_1^+)$ ratios are very close to each other: 2.44, 4.41 and 2.47, 4.29 for ^{196}Os and ^{196}Pt, respectively. The calculation for the platinum isotopes, including ^{196}Pt is presented in section 6.2.

For the remaining isotopes, the agreement between the theoretical predictions and the available experimental data is also very good, although $^{188-194}$Os are predicted to be more γ-soft/triaxial rotors than the actual experimental values, which are slightly more axial rotor-like. These results give confidence to the description of the shape transition from prolate/$\gamma-$soft to slightly oblate/$\gamma-$soft nuclei found in Figure 6.1 for the osmium isotopic chain.

Level scheme of ^{196}Os

The energies of the levels of the yrast band can give only the first hint of a γ-soft/triaxial rotator. A more detailed level scheme would allow to further elucidate the degree of γ-softness by comparison with the theory. In fact, theoretical predictions are not only limited to the yrast band. Figure 6.3 shows the predictions of the SCCM calculations for the level scheme of ^{196}Os compared to the experimental findings and the level scheme of a perfect γ-soft nucleus calculated via the GCM. For this second one, the level scheme is scaled to the energy of the first 2^+ level.

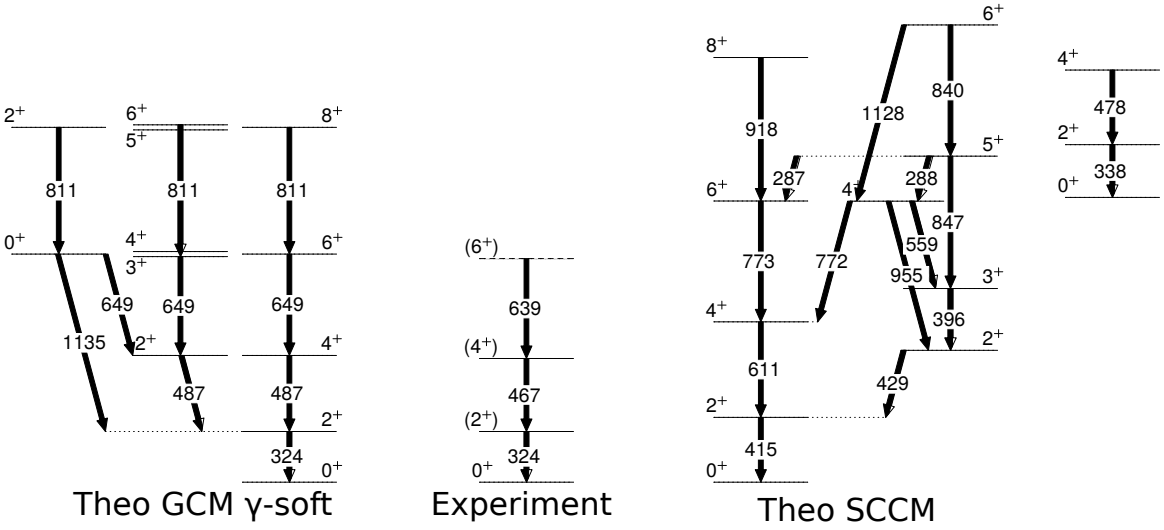

Figure 6.3: Experimentally measured level scheme of ^{196}Os (middle) compared to predictions based on a γ-soft potential in the geometric collective model (left) and the symmetry conserving configuration-mixing calculations (right).

Figure 6.3 underlines the good agreement between the different predictions. However, for the SCCM calculations, the absolute energies are slightly higher than the measured ones. This effect can be attributed to the non-restoration of the time-reversal symmetry, which results in a different moment of inertia. Since the moment of inertia can vary between different bands, a scaling of the level scheme with the to the $E(2^+_{\text{theo}})/E(2^+_{\text{exp}})$ ratio is not physical. The predicted level scheme shows, besides the characteristic energy ratios of the yrast band, also a degeneracy in energy of the 6^+_1, 4^+_2 and 0^+_1 states. However, the 3^+_1-state is not degenerated with the former levels, which is not in agreement with the expectation of a γ-soft/triaxial rotor.

To shed more light on the structure of the calculated states, the collective wave functions of the excited states in the (β, γ) plane are presented in Figure 6.4. The low-lying states of the ground state band and of the 1st excited band have a similar structure: the distribution of probability in the (β, γ) plane for each state belonging to these bands does not change significantly. The collective wave functions have triaxial maxima with $\beta \approx 0.12$ and $\gamma \approx 30° - 40°$.

The 2nd excited band, has a different structure, the wave function is more spread out in the γ direction.

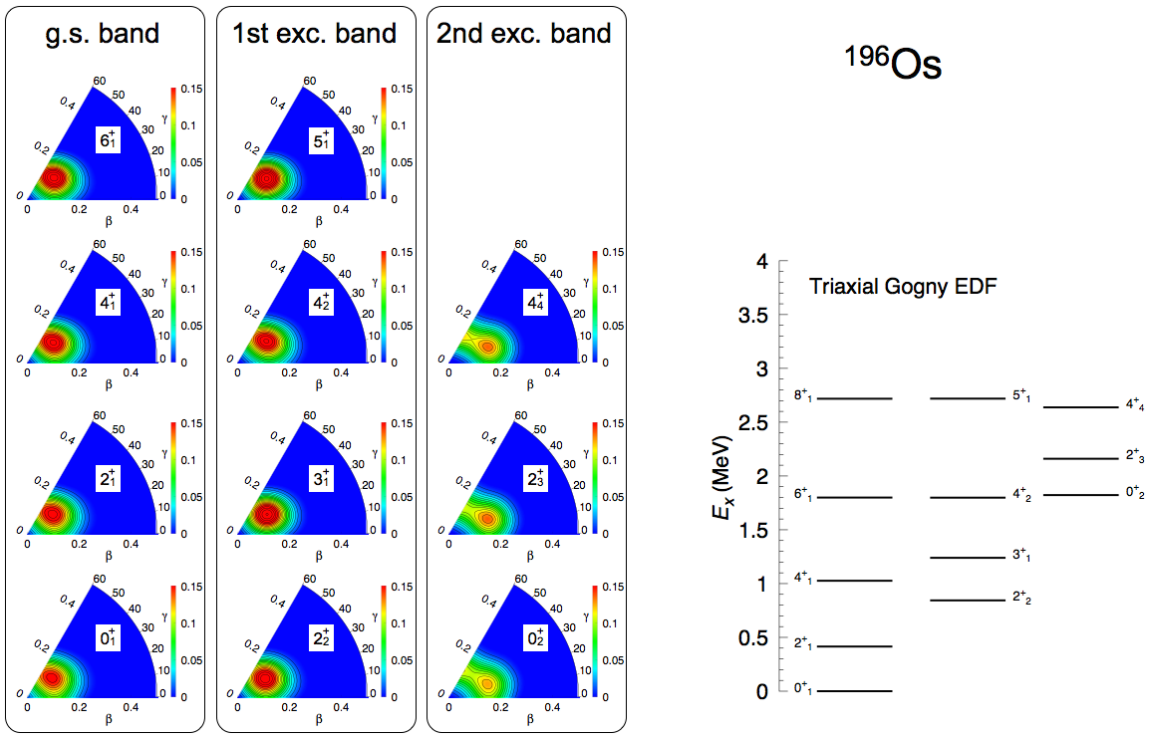

Figure 6.4: The collective wave functions of the excited states of ^{196}Os are drawn on the left side, while the level scheme is drawn on the right hand side.

6.2 The yrast structure of the even-even platinum isotopes

The textbook example of a γ-soft nucleus, ^{196}Pt is the isobar of ^{196}Os [18]. The even-even platinum isotopes undergo the shape transition from prolate to oblate deformation more smoothly than the osmium isotopes. In order to better understand the shape transition in the osmium isotopes, a comparison with the shape evolution in the neutron-rich platinum isotopes is done in this section. Furthermore, the predictions of the SCCM calculations can be tested on already available data.

Besides previously unknown non-yrast levels, the yrast band of ^{200}Pt has been extended in the present experiment to the (6_1^+) level.

The PES of the even-even neutron-rich $^{190-200}$Pt are presented in Figure 6.5. For all these nuclei, a degeneracy in the γ direction is evident. Also, like for the osmium isotopes, the deformation reduces form $\beta \approx 0.18$ (^{190}Pt) to $\beta \approx 0.1$ (^{200}Pt), when pairs of neutrons are added. The minimum in the PES for ^{190}Pt and ^{192}Pt is at $\gamma \approx 40°$ and for ^{198}Pt and ^{200}Pt it is on the oblate axis. The even-even nuclei in between, ^{194}Pt and ^{196}Pt, have both a broader minimum, which spans from $\gamma \approx 40°$ to $\gamma \approx 60°$.

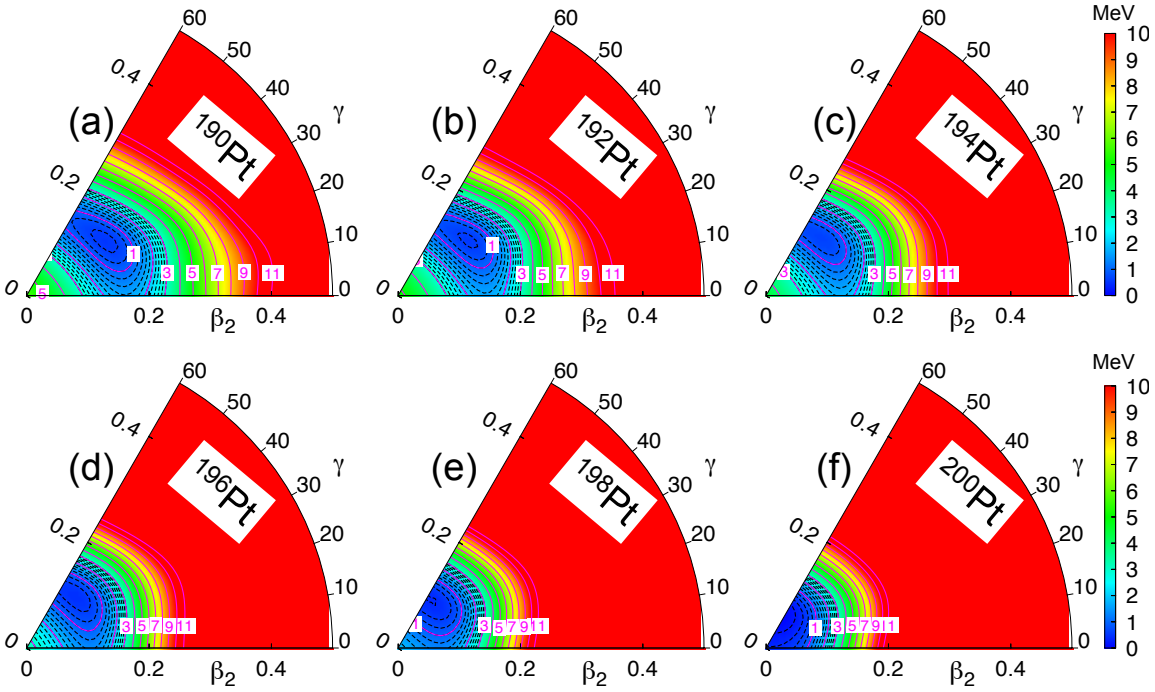

Figure 6.5: Particle number projected potential energy surfaces in the triaxial plane for $^{190-200}$Pt isotopes calculated with the Gogny D1S interaction. Solid and dashed contour lines are separated 1.0 MeV and 0.2 MeV, respectively. The solid contour lines are labelled with their energy.

Figure 6.6 shows the energies of the yrast band, normalised to the energy of the first 2_1^+ state together with the limits for the geometric models of a vibrator, rotator and γ-soft/triaxial rotor and the experimental data. The energy ratios are for all investigated

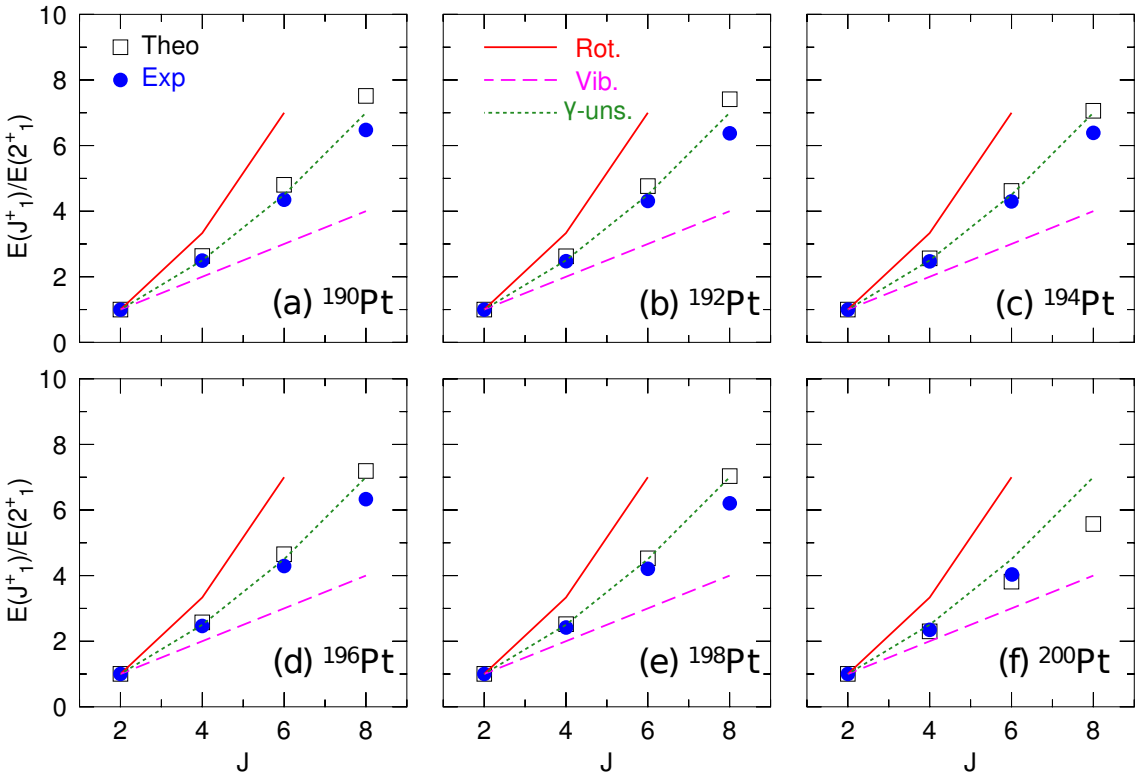

Figure 6.6: The same as Figure 6.2 for the even-even platinum isotopes $^{190-200}$Pt. The experimental data is taken from this work and references [142, 143] for ^{190,192}Pt.

nuclei close to the γ-soft/triaxial rotor limit. As indicated by the potential energy surface, the ^{200}Pt nucleus shows the most vibrational spectra among these nuclei, but the ratios are still closer to the γ-soft/triaxial rotor limit than to the vibrational limit.

Compared to the yrast band of the osmium isotopes, the energy ratios of the platinum isotopes are closer to the γ-soft rotor limit. This calculation indicates that the platinum isotopes passes the region of shape transition more smoothly than the osmium isotopes with more nuclei having a γ-soft rotor structure.

7 Conclusions and further perspectives

7.1 Conclusions

In the present thesis the results of the multi-nucleon transfer reaction ^{82}Se + ^{198}Pt at 426 MeV, with its goal to study the shape evolution in the neutron-rich osmium isotopes via the binary partner method, is presented. The beam-like recoils were detected in the *PRISMA* heavy-ion spectrometer and the coincident γ rays with the γ-tracking array *AGATA*. It has been one of the first experiments with the *AGATA-PRISMA* setup, and the analysis has been performed starting from the recorded signals of the *AGATA* spectrometer. An elaborated procedure was applied for the calibration of the individual detectors of both spectrometers. Empirical corrections are applied in order to achieve a mass resolution of $\frac{\Delta m}{m} \approx \frac{1}{260}$, which allows the selection of the beam-like recoil of interest without any observable contamination from neighbouring masses.

Prompt γ-ray spectra are taken for a great variety of nuclei down to the $-6p-12n$-channel (^{68}Ni). The high quality of the data allows to associate to them many new transitions. As an example, the level schemes of the even-even neutron-rich $^{70-76}$Zn nuclei at the onset of deformation have been extended. For the spectroscopy of the heavier binary partner, a kinematic reconstruction of the velocity vector of the target-like recoil is performed. The neutron evaporation plays anyway an important role during the deexcitation of the target-like recoil. In order to obtain a clean γ-ray spectrum belonging to the true binary partner, the reconstruction of the Q value of the reaction is used for the suppression of transitions of nuclei produced after neutron evaporation.

The major outcome of the experiment is the first in-beam γ-ray spectroscopic study of the nucleus ^{196}Os, which is the key to understand the shape evolution of the neutron-rich osmium isotopes. Three new γ rays were identified: 324.4 keV, 467.0 keV and 639.2 keV. The first two can be assigned to originate from the two previously measured excited states in ^{196}Os. The 639.2 keV transition is a candidate for the deexcitation of the (6_1^+) state. From the precise level energies of the first two excited states one can deduce a γ-soft/triaxial rotor character for ^{196}Os: in fact the $E(4_1^+)/E(2_1^+)$ ratio is 2.44, deviating less than 3% of the expectation value (2.5).

The new level scheme of ^{196}Os is compared to the predictions of the geometric collective model using a γ-soft potential and to beyond mean-field symmetry-conserving configuration

mixing calculations using the Gogny 1DS functional. The first three excited levels are in a good agreement with both models and are in particular perfectly reproduced by the beyond-mean field calculations. The same calculations are also applied to the $\gamma-$soft even-even neutron-rich $^{190-200}$Pt nuclei. For the unstable ^{200}Pt, the yrast band is extended, which provides a new important data point for the comparison with theoretical calculations at medium spin. This nucleus presents the most vibrational character among the platinum isotopes investigated in this thesis.

Due to the absence of collimators and anti-Compton shields, the *AGATA-PRISMA* setup is particularly suitable to perform delayed γ-ray spectroscopy of the target-like recoils stopped in the target chamber that are in coincidence with the beam-like recoils identified in the *PRISMA* spectrometer. The reconstructed Q value can be used to assign newly found isomeric states to a certain nucleus. In the data set of this experiment 44 isomeric states are identified, among them are 3 previously unknown.

A complete description of the atomic nucleus ^{196}Os is still out of reach due to the difficulties to study it at high spin, but the new data obtained will pave the way for the understanding of the shape evolution in the region of the neutron-rich platinum, osmium and tungsten isotopes.

7.2 Further perspectives

The low-lying levels of ^{196}Os were identified for the first time and the comparison with beyond mean-field calculations suggests a reduction in the deformation compared to lighter even-even neutron-rich osmium isotopes, while keeping a γ-soft potential. The knowledge of the energy of the second 2^+ state would be very important, for understanding better the γ-softness of ^{196}Os. A more detailed level scheme, including the transition strengths for the deexciation of the first two 2^+ states would be essential in this respect. The mass resolution of the *PRISMA* or *Vamos++* spectrometers are at the limit for the direct detection of ^{196}Os after a multi-nucleon transfer reaction and in any case the atomic number is too high to be resolved in such a spectrometer. For the lifetime measurement of the excited 2^+ states of ^{196}Os via a plunger device and a magnetic spectrometer inverse and direct kinematics are feasible: using ^{198}Pt as a beam on a light target or a light beam impinging on a ^{198}Pt target. The atomic number of the lighter recoil has to be identified in a second detector and the mass of ^{196}Os in the magnetic spectrometer.

Relativistic ion beam facilities, such as GSI [168], FAIR [169, 170] and FRIB [171, 172] could produce ^{196}Os via the fragmentation of a heavier beam (such as ^{208}Pb or ^{238}U) and use it in a Coulomb excitation experiment to deduce the quadrupole moment.

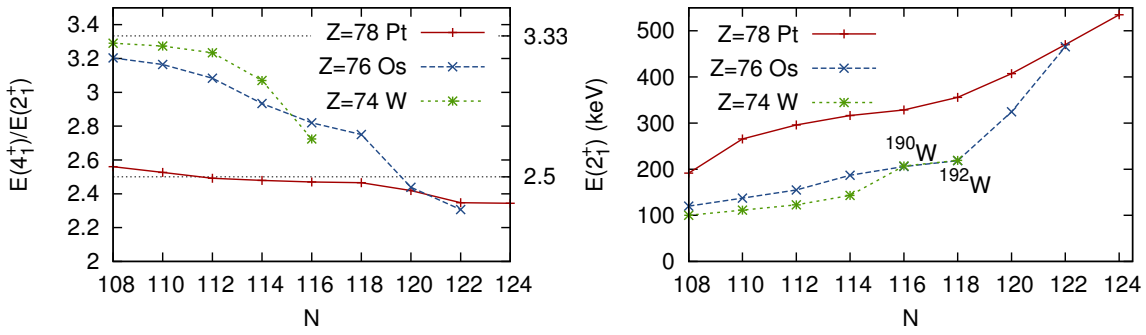

Figure 7.1: (left) $E(4_1^+)/E(2_1^+)$ ratio plotted as a function of the neutron number N for the neutron-rich even-even platinum, osmium and tungsten isotopes. (right) The first 2^+ state energies are shown for same nuclei.

The knowledge of the level schemes of the platinum and the osmium isotopes has been extended in this work and the shape evolution in such nuclei can be better understood. Also the tungsten isotopes ($Z = 74$, 2 protons less than osmium) are expected to go through a shape transition. However, it is predicted that the tungsten isotopes undergo a much more abrupt transition than the osmium and platinum isotopes. The experimental $E(4_1^+)/E(2_1^+)$ ratio, shown in Figure 7.1 (left), indicates a structural change, when approaching ^{190}W, the heaviest tungsten isotope, where the $E(4_1^+)/E(2_1^+)$ ratio was established via the decay of the 10^- isomer [55]. The change in the $E(4_1^+)/E(2_1^+)$ ratio can be partially attributed to the raise of the 2_1^+ energy from 142.9 keV in ^{188}W to 207 keV in ^{190}W, which is the most abrupt one in this region. Additionally, the 2_1^+ level in ^{192}W has an energy of 219 keV as measured in the β^- decay of ^{192}Ta [173] (see Figure 7.1 (right)). It is remarkable, that these 2_1^+ energies are very close to the ones of the corresponding osmium isotones: 205.8 keV and 218.5 keV in ^{192}Os and ^{194}Os, respectively.

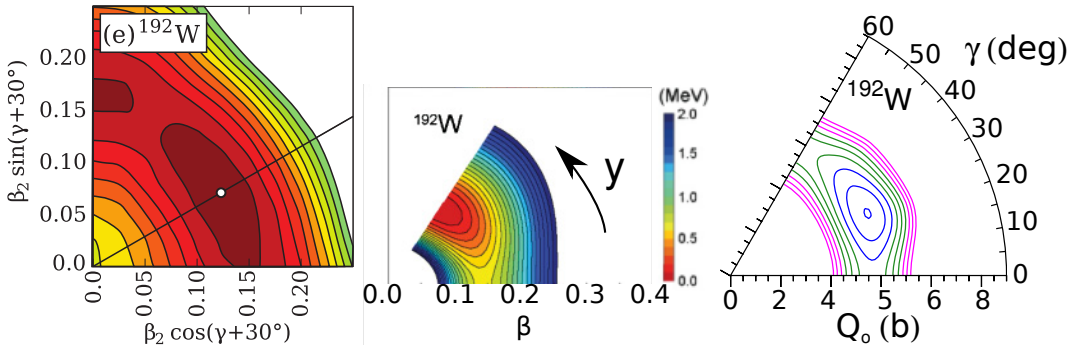

Figure 7.2: Three different recent calculations predicting very different shapes in ^{192}W. Potential energy surfaces are plotted as obtained with a nonaxial deformed Woods-Saxon (left, [174]), a IBM with Gogny1DS (middle [43]) and a HFB with Skyrme (right [40]) potential.

Theoretical calculations for ^{192}W are available, but disagree in predicting its shape. Figure 7.2 shows the potential energy surfaces reported in three recent publications. The discrepancies in the predictions of the shape of the nucleus ^{192}W call for new experimental data in order to better understand the shape evolution in the neutron-rich tungsten isotopes. The symmetry-conserving configuration-mixing calculations has shown a remarkable agreement with the experimental data in the case of the osmium and the platinum isotopes and therefore experimental data on the shape evolution in the neutron-rich tungsten would be an ideal case for a continuation of the theoretical study using this state-of-the-art beyond mean field approach.

As a followup of this thesis, an experiment aiming at the study of ^{190}W and ^{192}W using a multi-nucleon-transfer reaction was proposed and accepted for the oncoming *AGATA* campaign at GANIL, France. A setup similar to the one presented in this thesis will be used: *AGATA* will be coupled to the *Vamos++* magnetic spectrometer and to an array of $LaBr_3$ detectors. A ^{136}Xe beam impinging on a ^{192}Os target at 900 MeV will populate exotic neutron-rich nuclei around ^{192}Os. The same reaction was used before to study the decay of the 10^- isomeric state in ^{190}W [175]. The binary partner method and the analysis techniques developed in this thesis will be applied and, besides new excited states in the tungsten isotopes, also the quadrupole transition moment of the 2_1^+ levels of ^{190,192}W will be measured.

Bibliography

[1] K. Schmidt. Göbekli Tepe, southeastern Turkey: A preliminary report on the 1995-1999 excavations. **Paléorient**, pages 45–54, 2000.

[2] J. Peters and K. Schmidt. Animals in the symbolic world of Pre-Pottery Neolithic Göbekli Tepe, south-eastern Turkey: a preliminary assessment. **Anthropozoologica**, 39(1):179–218, 2004.

[3] J.W. von Goethe. **Faust: Eine Tragodie**. 1808.

[4] J.W. von Goethe. **Faust**. The World Publishing Group, CleveLand, Ohio New York, 1842. URL `http://www.gutenberg.org/files/14591/14591-h/14591-h.htm`.

[5] N. Bohr. Neutron capture and nuclear constitution. **Nature**, 137(3461):344–348, 1936.

[6] A. Bohr and B.R. Mottelson. **Nuclear structure Volume II: Nuclear deformations**, volume 2. World Scientific, 1998.

[7] R.M. Kulsrud and S.W. Anderson. The spectrum of random magnetic fields in the mean field dynamo theory of the galactic magnetic field. **The Astrophysical Journal**, 396:606–630, 1992.

[8] M. Bender, P.-H. Heenen, and P.-G. Reinhard. Self-consistent mean-field models for nuclear structure. **Reviews of Modern Physics**, 75(1):121, 2003.

[9] R.A. Broglia. The surfaces of compact systems: from nuclei to stars. **Surface science**, 500(1):759–792, 2002.

[10] R.F. Casten. **Nuclear structure from a simple perspective**, volume 6. Oxford University Press Oxford, 2000.

[11] C.F. von Weizsäcker. Zur Theorie der Kernmassen. **Zeitschrift für Physik A Hadrons and Nuclei**, 96(7):431–458, 1935.

[12] P. Navrátil, J.P. Vary, and B.R. Barrett. Large-basis ab initio no-core shell model and its application to ^{12}C. **Physical Review C**, 62(5):054311, 2000.

[13] O. Haxel, J.H.D. Jensen, and H.E. Suess. On the "magic numbers" in nuclear structure. **Physical Review**, 75(11):1766, 1949.

[14] M.G. Mayer. Nuclear configurations in the spin-orbit coupling model. I. Empirical evidence. **Physical Review**, 78(1):16, 1950.

[15] The Royal Swedish Academy of Sciences. The Nobel Prize in Physics 1975. Press Release, 1975. URL `http://www.nobelprize.org/nobel_prizes/physics/laureates/1975/press.html`.

[16] L. Fortunato. Solutions of the Bohr Hamiltonian, a compendium. **The European Physical Journal A-Hadrons and Nuclei**, 26:1–30, 2005.

[17] L. Próchniak and S.G. Rohoziński. Quadrupole collective states within the Bohr collective Hamiltonian. **Journal of Physics G: Nuclear and Particle Physics**, 36(12):123101, 2009.

[18] J. Zhang, R.F. Casten, and N.V. Zamfir. A structural triangle for the geometric collective model. **Physics Letters B**, 407:201–206, 1997.

[19] G. Gneuss, U. Mosel, and W. Greiner. A new treatment of the collective nuclear Hamiltonian. **Physics Letters B**, 30(6):397–399, 1969.

[20] G. Gneuss, U. Mosel, and W. Greiner. On the relationship between the level-structures in spherical and deformed nuclei. **Physics Letters B**, 31(5):269–272, 1970.

[21] G. Gneuss and W. Greiner. Collective potential energy surfaces and nuclear structure. **Nuclear Physics A**, 171(3):449–479, 1971.

[22] P. Ring and P. Schuck. **The nuclear many-body problem**. Springer, 2004.

[23] T. Nikšić, D. Vretenar, and P. Ring. Relativistic nuclear energy density functionals: Mean-field and beyond. **Progress in Particle and Nuclear Physics**, 66(3):519–548, 2011.

[24] P. Ring. Relativistic mean field theory in finite nuclei. **Progress in Particle and Nuclear Physics**, 37:193–263, 1996.

[25] Y.M. Engel, D.M. Brink, K. Goeke, S.J. Krieger, and D. Vautherin. Time-dependent Hartree-Fock theory with skyrme's interaction. **Nuclear Physics A**, 249(2):215–238, 1975.

[26] D.M. Brink and E. Boeker. Effective interactions for Hartree-Fock calculations. **Nuclear Physics A**, 91(1):1–26, 1967.

[27] J.F. Berger, M. Girod, and D. Gogny. Microscopic analysis of collective dynamics in low energy fission. **Nuclear Physics A**, 428:23–36, 1984.

[28] J.-P. Delaroche, M. Girod, J. Libert, H. Goutte, S. Hilaire, S. Péru, N. Pillet, and G.F. Bertsch. Structure of even-even nuclei using a mapped collective Hamiltonian and the D1S Gogny interaction. **Physical Review C**, 81:014303, 2010.

[29] S. Hilaire and M. Girod. Large-scale mean-field calculations from proton to neutron drip lines using the D1S Gogny force. **The European Physical Journal A-Hadrons and Nuclei**, 33(2):237–241, 2007.

[30] T.R. Rodríguez and J.L. Egido. Configuration mixing description of the nucleus ^{44}S. **Physical Review C**, 84(5):051307, 2011.

[31] T.R. Rodríguez and J.L. Egido. Triaxial angular momentum projection and configuration mixing calculations with the Gogny force. **Physical Review C**, 81:064323, 2010.

[32] T.R. Rodríguez. Structure of krypton isotopes calculated with symmetry-conserving configuration-mixing methods. **Physical Review C**, 90:034306, Sep 2014.

[33] M. Bender and P.-H. Heenen. Configuration mixing of angular-momentum and particle-number projected triaxial Hartree-Fock-Bogoliubov states using the Skyrme energy density functional. **Physical Review C**, 78:024309, 2008.

[34] J.M. Yao, J. Meng, P. Ring, and D. Vretenar. Configuration mixing of angular-momentum-projected triaxial relativistic mean-field wave functions. **Physical Review C**, 81(4):044311, 2010.

[35] M. Anguiano, J.L. Egido, and L.M. Robledo. Particle number projection with effective forces. **Nuclear Physics A**, 696:467–493, 2001.

[36] A. Illana, A. Jungclaus, R. Orlandi, A. Perea, C. Bauer, J.A. Briz, J.L. Egido, R. Gernhäuser, J. Leske, D. Mücher, et al. Low-velocity transient-field technique with radioactive ion beams: g factor of the first excited 2^+ state in ^{72}Zn. **Physical Review C**, 89(5):054316, 2014.

[37] S. Ilieva, M. Thürauf, Th. Kröll, R. Krücken, T. Behrens, V. Bildstein, A. Blazhev, S. Bönig, P.A. Butler, J. Cederkäll, et al. Coulomb excitation of neutron-rich Cd isotopes. **Physical Review C**, 89(1):014313, 2014.

[38] C. Bauer, T. Behrens, V. Bildstein, A. Blazhev, B. Bruyneel, J. Butterworth, E. Clément, L. Coquard, J.L. Egido, A. Ekström, et al. Prolate shape of ^{140}Ba from a first combined Doppler-shift and Coulomb-excitation measurement at the REX-ISOLDE facility. **Physical Review C**, 86(3):034310, 2012.

[39] I. Hamamoto and B. R. Mottelson. Further examination of prolate-shape dominance in nuclear deformation. **Physical Review C**, 79:034317, 2009.

[40] L.M. Robledo, R. Rodríguez-Guzmán, and P. Sarriguren. Role of triaxiality in the ground-state shape of neutron-rich Yb, Hf, W, Os, and Pt isotopes. **Journal of Physics G: Nuclear and Particle Physics**, 36(11):115104, 2009.

[41] P. Sarriguren, R. Rodríguez-Guzmán, and L.M. Robledo. Shape transitions in neutron-rich Yb, Hf, W, Os, and Pt isotopes within a Skyrme Hartree-Fock+BCS approach. **Physical Review C**, 77(6):064322, 2008.

[42] K. Nomura, T. Otsuka, R. Rodríguez-Guzmán, L.M. Robledo, P. Sarriguren, P.H. Regan, P.D. Stevenson, and Zs. Podolyák. Spectroscopic calculations of the low-lying structure in exotic Os and W isotopes. **Physical Review C**, 83:054303, 2011.

[43] K. Nomura, T. Otsuka, R. Rodríguez-Guzmán, L.M. Robledo, and Sarriguren P. Collective structural evolution in neutron-rich Yb, Hf, W, Os, and Pt isotopes. **Physical Review C**, 84(5):054316, 2011.

[44] R. Fossion, D. Bonatsos, and G.A. Lalazissis. E(5), X(5), and prolate to oblate shape phase transitions in relativistic Hartree-Bogoliubov theory. **Physical Review C**, 73 (4):044310, 2006.

[45] P.D. Stevenson, M.P. Brine, Zs. Podolyák, P.H. Regan, P.M. Walker, and J.R. Stone. Shape evolution in the neutron-rich tungsten region. **Physical Review C**, 72(4): 047303, 2005.

[46] C. Wheldon, J.J. Valiente-Dobón, P.H. Regan, C.J. Pearson, C.Y. Wu, J.F. Smith, A.O. Macchiavelli, D. Cline, R.S. Chakrawarthy, R. Chapman, et al. Observation of an isomeric state in ^{197}Au. **Physical Review C**, 74(2):027303, 2006.

[47] Zs. Podolyák, S.J. Steer, S. Pietri, F.R. Xu, H.L. Liu, P.H. Regan, D. Rudolph, A.B. Garnsworthy, R. Hoischen, M. Gorska, et al. Weakly deformed oblate structures in ^{198}Os$^{122}_{76}$. **Physical Review C**, 79:031305, Mar 2009.

[48] P.D. Bond, R.F. Casten, D.D. Warner, and D. Horn. Excited states in ^{196}Os and the structure of the Pt - Os transition region. **Physics Letters B**, 130:167–170, 1983.

[49] G.D. Dracoulis, G.J. Lane, A.P. Byrne, H. Watanabe, R.O. Hughes, N. Palalani, F.G. Kondev, M.P. Carpenter, D. Seweryniak, S. Zhu, et al. Isomers and alignments in ^{191}Ir and ^{192}Os. In **Journal of Physics: Conference Series**, volume 381, page 012060. IOP Publishing, 2012.

[50] G.D. Dracoulis, G.J. Lane, A.P. Byrne, H. Watanabe, R.O. Hughes, F.G. Kondev, M. Carpenter, R.V.F. Janssens, T. Lauritsen, C.J. Lister, et al. Isomers and excitation modes in the gamma-soft nucleus ^{192}Os. **Physics Letters B**, 720:330–335, 2013.

[51] C. Wheldon, J.G. Narro, C.J. Pearson, P.H. Regan, Zs. Podolyák, D.D. Warner, P. Fallon, A.O. Macchiavelli, and M. Cromaz. Yrast states in ^{194}Os: The prolate-oblate transition region. **Physical Review C**, 63:011304, 2000.

[52] R.F. Casten, A.I. Namenson, W.F. Davidson, D.D. Warner, and H.G. Borner. Low-lying levels in ^{194}Os and the prolate—oblate phase transition. **Physics Letters B**, 76:280–284, 1978.

[53] S.J. Steer, Zs. Podolyák, S. Pietri, M. Górska, H. Grawe, K.H. Maier, P.H. Regan, D. Rudolph, A.B. Garnsworthy, R. Hoischen, et al. Isomeric states observed in heavy

neutron-rich nuclei populated in the fragmentation of a ^{208}Pb beam. **Physical Review C**, 84:044313, 2011.

[54] M. Caamaño, P.M. Walker, P.H. Regan, M. Pfützner, Zs. Podolyák, J. Gerl, M. Hellström, P. Mayet, M.N. Mineva, A. Aprahamian, et al. Isomers in neutron-rich $A \approx 190$ nuclides from ^{208}Pb fragmentation. **The European Physical Journal A-Hadrons and Nuclei**, 23:201–215, 2005.

[55] Zs. Podolyák, P.H. Regan, M. Pfützner, J. Gerl, M. Hellström, M. Caamaño, P. Mayet, Ch. Schlegel, A. Aprahamian, J. Benlliure, et al. Isomer spectroscopy of neutron rich $^{190}W_{116}$. **Physics Letters B**, 491(3):225–231, 2000.

[56] P.H. Regan, J.J. Valiente-Dobón, C. Wheldon, C.Y. Wu, J.F. Smith, A.O. Macchiavelli, D. Cline, R.S. Chakrawarthy, R. Chapman, M. Cromaz, et al. Production of exotic nuclear isomers in multi-nucleontransfer reactions. **Laser Physics Letters**, 1 (6):317–324, 2004.

[57] G.A. Jones, Zs. Podolyák, P.M. Walker, P.H. Regan, G. de Angelis, M. Axiotis, D. Bazzacco, P.G. Bizzeti, F. Brandolini, R. Broda, et al. Population of yrast states in ^{191}Os using deep-inelastic reactions. **Journal of Physics G: Nuclear and Particle Physics**, 31(10):S1891, 2005.

[58] A. Winther. Dissipation, polarization and fluctuation in grazing heavy-ion collisions and the boundary to the chaotic regime. **Nuclear Physics A**, 594(2):203–245, 1995.

[59] K. Bethge, G. Walter, and B. Wiedemann. **Kernphysik: eine Einführung**. Springer-Verlag, 2008.

[60] R. Broda. Spectroscopic studies with the use of deep-inelastic heavy-ion reactions. **Journal of Physics G: Nuclear and Particle Physics**, 32(6):R151, 2006.

[61] H. Savajols. VAMOS: A variable mode high acceptance spectrometer for identifying reaction products induced by SPIRAL beams. **Nuclear Instruments and Methods in Physics Research Section B: Beam Interactions with Materials and Atoms**, 204:146–153, 2003.

[62] M. Rejmund, B. Lecornu, A. Navin, C. Schmitt, S. Damoy, O. Delaune, J.M. Enguerrand, G. Fremont, P. Gangnant, L. Gaudefroy, et al. Performance of the improved larger acceptance spectrometer: VAMOS++. **Nuclear Instruments and Methods in Physics Research Section A: Accelerators, Spectrometers, Detectors and Associated Equipment**, 646(1):184–191, 2011.

[63] F. Azaiez. EXOGAM: a γ-ray spectrometer for radioactive beams. **Nuclear Physics A**, 654(1):1003c–1008c, 1999.

[64] A.M. Stefanini, L. Corradi, G. Maron, A. Pisent, M. Trotta, A.M. Vinodkumar, S. Beghini, G. Montagnoli, F. Scarlassara, G.F. Segato, et al. The heavy-ion magnetic spectrometer PRISMA. **Nuclear Physics A**, 701(1):217–221, 2002.

[65] A. Gadea, N. Mărginean, L. Corradi, S.M. Lenzi, C.A. Ur, E. Farnea, G. De Angelis, E. Fioretto, D.R. Napoli, A.M. Stefanini, et al. The CLARA-PRISMA setup installed at LNL: first results. **Journal of Physics G: Nuclear and Particle Physics**, 31 (10):S1443, 2005.

[66] S. Lunardi, S.M. Lenzi, F. Della Vedova, E. Farnea, A. Gadea, N. Mărginean, D. Bazzacco, S. Beghini, P.G. Bizzeti, A.M. Bizzeti-Sona, et al. Spectroscopy of neutron-rich Fe isotopes populated in the ^{64}Ni + ^{238}U. **Physical Review C**, 76(3):034303, 2007.

[67] Z.M. Wang, R. Chapman, X. Liang, F. Haas, F. Azaiez, B.R. Behera, M. Burns, E. Caurier, L. Corradi, D. Curien, A.N. Deacon, Zs. Dombrádi, E. Farnea, E. Fioretto, A. Gadea, A. Hodsdon, F. Ibrahim, A. Jungclaus, K. Keyes, V. Kumar, A. Latina, S. Lunardi, N. Mărginean, G. Montagnoli, D.R. Napoli, F. Nowacki, J. Ollier, D. O'Donnell, A. Papenberg, G. Pollarolo, M.-D. Salsac, F. Scarlassara, J.F. Smith, K.M. Spohr, M. Stanoiu, A.M. Stefanini, S. Szilner, M. Trotta, and D. Verney. γ-ray spectroscopy of neutron-rich ^{40}S. **Physical Review C**, 81:054305, May 2010.

[68] D. Montanari, S. Leoni, D. Mengoni, J.J. Valiente-Dobón, G. Benzoni, N. Blasi, G. Bocchi, P.F. Bortignon, S. Bottoni, A. Bracco, et al. γ spectroscopy of calcium nuclei around doubly magic ^{48}Ca using heavy-ion transfer reactions. **Physical Review C**, 85(4):044301, 2012.

[69] D. Mengoni, J.J. Valiente-Dobón, E. Farnea, A. Gadea, A. Dewald, and A. Latina. Lifetime measurements of neutron-rich nuclei around ^{48}Ca with the CLARA-PRISMA setup. **The European Physical Journal A-Hadrons and Nuclei**, 42(3):387–391, 2009.

[70] J.J. Valiente-Dobón, D. Mengoni, A. Gadea, E. Farnea, S.M. Lenzi, S. Lunardi, A. Dewald, Th. Pissulla, S. Szilner, R. Broda, et al. Lifetime Measurements of the Neutron-Rich $N = 30$ Isotones ^{50}Ca and ^{51}Sc: Orbital Dependence of Effective Charges in the fp Shell. **Physical review letters**, 102(24):242502, 2009.

[71] S. Szilner, C.A. Ur, L. Corradi, N. Mărginean, G. Pollarolo, A.M. Stefanini, S. Beghini, B.R. Behera, E. Fioretto, A. Gadea, et al. Multinucleon transfer reactions in closed-shell nuclei. **Physical Review C**, 76:024604, 2007.

[72] P.-A. Söderström, J. Nyberg, P.H. Regan, A. Algora, G. De Angelis, S.F. Ashley, S. Aydin, D. Bazzacco, R.J. Casperson, W.N. Catford, et al. Spectroscopy of neutron-rich ^{168,170}Dy: Yrast band evolution close to the N_P N_N valence maximum. **Physical Review C**, 81(3):034310, 2010.

[73] K. Geibel. **Search for Proton Emission in ^{54}Fe and Multi-Nucleon Transfer Reactions in the Actinide Region**. PhD thesis, Universiät zu Köln, 08 2012.

[74] B. Birkenbach. **Gamma ray tracking with the AGATA demonstrator - A novel approach for in-beam spectroscopy**. PhD thesis, Universiät zu Köln, 04 2014.

[75] A.G.H. Vogt. In-Beam Gamma-Ray Spectroscopy of Neutron-Rich Actinides after Multi-Nucleon Transfer Reactions. Master's thesis, Universiät zu Köln, 06 2014.

[76] T. Mayer-Kuckuk. **Kernphysik**. Teubner, Wiesbaden, 7 edition, 04 2002.

[77] K. Bethge, G. Walter, and B. Wiedemann. **Kernphysik**. Springer, Heidelberg, 2 edition, 2001.

[78] T. Kibédi, T.W. Burrows, M.B. Trzhaskovskaya, P.M. Davidson, and C.W. Nestor Jr. Evaluation of theoretical conversion coefficients using *BrIcc*. **Nuclear Instruments and Methods in Physics Research Section A: Accelerators, Spectrometers, Detectors and Associated Equipment**, 589(2):202–229, 2008.

[79] M.J. Berger, J.H. Hubbell, S.M. Seltzer, J. Chang, J.S. Coursey, R. Sukumar, D.S. Zucker, and K. Olsen. XCOM: Photon Cross Sections Database. http://www.nist.gov/pml/data/xcom/, 2014.

[80] J. Eberth and J. Simpson. From Ge(Li) detectors to gamma-ray tracking arrays – 50 years of gamma spectroscopy with germanium detectors. **Progress in Particle and Nuclear Physics**, 60(2):283–337, 2008.

[81] C. Rossi Alvarez. The GASP array. **Nuclear Physics News**, 3(3):10–13, 1993.

[82] J. Simpson. The EUROBALL spectrometer. **Zeitschrift für Physik A Hadrons and Nuclei**, 358(2):139–143, 1997.

[83] I.-Y. Lee et al. The Gammasphere. **Nuclear Physics A**, 520:c641–c655, 1990.

[84] S. Akkoyun, A. Algora, B. Alikhani, F. Ameil, G. De Angelis, L. Arnold, A. Astier, A. Ataç, Y. Aubert, C. Aufranc, et al. Agata—advanced gamma tracking array. **Nuclear Instruments and Methods in Physics Research Section A: Accelerators, Spectrometers, Detectors and Associated Equipment**, 668:26–58, 2012.

[85] A. Wiens, H. Hess, B. Birkenbach, B. Bruyneel, J. Eberth, D. Lersch, Gh. Pascovici, P. Reiter, and H.-G. Thomas. The AGATA triple cluster detector. **Nuclear Instruments and Methods in Physics Research Section A: Accelerators, Spectrometers, Detectors and Associated Equipment**, 618(1):223–233, 2010.

[86] AGATA technical proposal. Technical report.

[87] A. Gadea, E. Farnea, J.J. Valiente-Dobón, B. Million, D. Mengoni, D. Bazzacco, F. Recchia, A. Dewald, Th. Pissulla, W. Rother, et al. Conceptual design and infrastructure for the installation of the first AGATA sub-array at LNL. **Nuclear Instruments and Methods in Physics Research Section A: Accelerators, Spectrometers, Detectors and Associated Equipment**, 654(1):88–96, 2011.

[88] I.-Y. Lee, R.M. Clark, M. Cromaz, M.A. Deleplanque, M. Descovich, R.M. Diamond, P. Fallon, A.O. Macchiavelli, F.S. Stephens, and D. Ward. GRETINA: A gamma ray energy tracking array. **Nuclear Physics A**, 746:255–259, 2004.

[89] Laboratori Nazionali di Legnaro Website. http://www.lnl.infn.it, 2014.

[90] A. Bracco and A. Pisent. SPES-Technical Design for an Advanced Exotic Ion Beam Facility at LNL. **INFN-LNL Report**, 181(02), 2002.

[91] A. Andrighetto, L. Biasetto, M. Manzolaro, P. Benetti, S. Carturan, P. Colombo, F. Gramegna, G. Meneghetti, B. Monelli, G. Prete, et al. The SPES project at LNL. In **APPLICATION OF ACCELERATORS IN RESEARCH AND INDUSTRY: Twentieth International Conference**, volume 1099, pages 728–732. AIP Publishing, 2009.

[92] G. Fortuna, R. Pengo, G. Bassato, I. Ben-Zvi, J.D. Larson, J.S. Sokolowski, L. Badan, A. Battistella, G. Bisoffi, G. Buso, et al. The ALPI project at the Laboratori Nazionali di Legnaro. **Nuclear Instruments and Methods in Physics Research Section A: Accelerators, Spectrometers, Detectors and Associated Equipment**, 287 (1):253–256, 1990.

[93] C. Signorini, F. Cervellera, and G. Bezzon. Status report of the Legnaro XTU tandem. **Nuclear Instruments and Methods in Physics Research Section A: Accelerators, Spectrometers, Detectors and Associated Equipment**, 244(1): 27–30, 1986.

[94] R.A. Ricci and C. Signorini. On the 16 MV XTU tandem of the laboratori nazionali di legnaro. **Nuclear Instruments and Methods in Physics Research**, 184(1): 35–47, 1981.

[95] A. Dainelli, G. Bassato, A. Battistella, M. Bellato, A. Beltramin, L. Bertazzo, G. Bezzon, G. Bisoffi, L. Boscagli, S. Canella, et al. Commissioning of the ALPI post-accelerator. **Nuclear Instruments and Methods in Physics Research Section A: Accelerators, Spectrometers, Detectors and Associated Equipment**, 382 (1):100–106, 1996.

[96] G. Fortuna, A.M. Porcellato, G. Bassato, A. Battistella, M. Bellato, L. Bertazzo, G. Bezzon, G. Bisoffi, G. Buso, S. Canella, et al. Completion of the medium-β section of the ALPI SC-booster at LNL. **Nuclear Instruments and Methods in Physics Research Section A: Accelerators, Spectrometers, Detectors and Associated Equipment**, 328(1):236–241, 1993.

[97] AGATA Demonstartor Inauguration. `http://agata.lnl.infn.it/Inaugurazione/foto/index_en.htm`, 04 2010.

[98] D. Montanari, E. Farnea, S. Leoni, G. Pollarolo, L. Corradi, G. Benzoni, A. Gadea, E. Fioretto, A. Latina, G. Montagnoli, et al. Response function of the magnetic spectrometer PRISMA. **The European Physical Journal A-Hadrons and Nuclei**, 47(1):1–7, 2011.

[99] G. Montagnoli, A.M. Stefanini, M. Trotta, S. Beghini, M. Bettini, F. Scarlassara, V. Schiavon, L. Corradi, B.R. Behera, E. Fioretto, et al. The large-area micro-channel plate entrance detector of the heavy-ion magnetic spectrometer PRISMA. **Nuclear Instruments and Methods in Physics Research Section A: Accelerators, Spectrometers, Detectors and Associated Equipment**, 547(2):455–463, 2005.

[100] S. Beghini, L. Corradi, E. Fioretto, A. Gadea, A. Latina, G. Montagnoli, F. Scarlassara, A.M. Stefanini, S. Szilner, M. Trotta, et al. The focal plane detector of the magnetic spectrometer PRISMA. **Nuclear Instruments and Methods in Physics Research Section A: Accelerators, Spectrometers, Detectors and Associated Equipment**, 551(2):364–374, 2005.

[101] G.F. Knoll. Radiation detection and measurement. **New York, John Wiley and Sons, Inc.**, 1, 1979.

[102] H.-D. Betz. Charge states and charge-changing cross sections of fast heavy ions penetrating through gaseous and solid media. **Reviews of Modern Physics**, 44(3):465, 1972.

[103] A. Latina. **Study of Heavy-Ion Reactions with the Magnetic Spectrometer PRISMA: On-line and Off-line Data Analysis**. PhD thesis, Universita degli Studi di Torino, 2005.

[104] A. Gottardo et al. Performance of the DANTE Detector. **Nuclear Physics A**, 805: 606–608, 2008.

[105] J. Eberth, Gh. Pascovici, H.G. Thomas, N. Warr, D. Weisshaar, D. Habs, P. Reiter, P. Thirolf, D. Schwalm, C. Gund, et al. MINIBALL A Ge detector array for radioactive ion beam facilities. **Progress in Particle and Nuclear Physics**, 46(1):389–398, 2001.

[106] M. Descovich, P.J. Nolan, A.J. Boston, J. Dobson, S. Gros, J.R. Cresswell, J. Simpson, I. Lazarus, P.H. Regan, J.J. Valiente-Dobón, et al. The position response of a large-volume segmented germanium detector. **Nuclear Instruments and Methods in Physics Research Section A: Accelerators, Spectrometers, Detectors and Associated Equipment**, 553(3):512–521, 2005.

[107] M.R. Dimmock, A.J. Boston, H.C. Boston, J.R. Cresswell, L. Nelson, P.J. Nolan, C. Unsworth, I.H. Lazarus, and J. Simpson. Characterisation results from an AGATA prototype detector. **IEEE Transactions on Nuclear Science**, 56(3):1593–1599, 2009.

[108] T.M.H. Ha, A. Korichi, F. Le Blanc, P. Désesquelles, N. Dosme, X. Grave, N. Karkour, S. Leboutelier, E. Legay, D. Linget, et al. New setup for the characterisation of the AGATA detectors. **Nuclear Instruments and Methods in Physics Research Section A: Accelerators, Spectrometers, Detectors and Associated Equipment**, 697:123–132, 2013.

[109] R. Venturelli and D. Bazzacco. Adaptive Grid Search as Pulse Shape Analysis Algorithm for γ-Tracking and Results . **INFN-LNL Report**, 204/205, 2004.

[110] F. Recchia, D. Bazzacco, E. Farnea, A. Gadea, R. Venturelli, T. Beck, P. Bednarczyk, A. Buerger, A. Dewald, M. Dimmock, et al. Position resolution of the prototype AGATA triple-cluster detector from an in-beam experiment. **Nuclear Instruments and Methods in Physics Research Section A: Accelerators, Spectrometers, Detectors and Associated Equipment**, 604:555–562, 2009.

[111] P.-A. Söderström, F. Recchia, J. Nyberg, A. Al-Adili, A. Ataç, S. Aydin, D. Bazzacco, P. Bednarczyk, B. Birkenbach, D. Bortolato, et al. Interaction position resolution simulations and in-beam measurements of the AGATA HPGe detectors. **Nuclear Instruments and Methods in Physics Research Section A: Accelerators, Spectrometers, Detectors and Associated Equipment**, 638(1):96–109, 2011.

[112] A. Lopez-Martens, K. Hauschild, A. Korichi, J. Roccaz, and J.P. Thibaud. γ-ray tracking algorithms: a comparison. **Nuclear Instruments and Methods in Physics Research Section A: Accelerators, Spectrometers, Detectors and Associated Equipment**, 533(3):454–466, 2004.

[113] D. Bazzacco. The Advanced Gamma Ray Tracking Array AGATA. **Nuclear Physics A**, 746(0):248–254, 2004. ISSN 0375-9474. doi: 10.1016/j.nuclphysa.2004.09.148. Proceedings of the Sixth International Conference on Radioactive Nuclear Beams (RNB6).

[114] A. Goasduff. **Etats intrus dans les noyaux de la couche sd : de 1p-1t a np-nt dans les isotopes de Si**. PhD thesis, l'Université de Strasbourg, 09 2012.

[115] D. Bazzacco. Recal – subversion repository. svn://gamma01.lnl.infn.it/agata/trunk/narval_emulator/zPrograms/.

[116] B. Bruyneel, P. Reiter, A. Wiens, J. Eberth, H. Hess, Gh. Pascovici, N. Warr, S. Aydin, D. Bazzacco, and F. Recchia. Crosstalk corrections for improved energy resolution with highly segmented HPGe-detectors. **Nuclear Instruments and Methods in Physics Research Section A: Accelerators, Spectrometers, Detectors and Associated Equipment**, 608(1):99–106, 2009.

[117] L. Lewandowski. Optimization of the Pulse Shape Analysis for the Position-Sensitive γ-Ray Spectrometer AGATA. Master's thesis, Universiät zu Köln, 07 2014.

[118] B. Bruyneel, B. Birkenbach, J. Eberth, H. Hess, Gh. Pascovici, P. Reiter, A. Wiens, D. Bazzacco, E. Farnea, C. Michelagnoli, et al. Correction for hole trapping in AGATA detectors using pulse shape analysis. **The European Physical Journal A**, 49(5): 1–9, 2013.

[119] D.C. Radford. Radware05. `http://radware.phy.ornl.gov`.

[120] D. Bazzacco. Efficiency and P/T Ratio for the AGATA Demonstrator at Legnaro, 03 2013.

[121] femul subversion repository. `svn://gamma01.lnl.infn.it/agata/trunk/narval_emulator`.

[122] GammaWare - Agata Data Analysis. http://agata.in2p3.fr.

[123] ROOT - A Data Analysis Framework. URL `https://root.cern.ch/drupal`.

[124] R. Brun, F. Rademakers, S. Panacek, I. Antcheva, and D. Buskulic. The ROOT Users Guide. **CERN, http://root.cern.ch**, 03 2011.

[125] M.A. Baldin, V.I. Gol'Danskii, and I.L. Rozenthal. **Kinematics of nuclear reactions**. Pergamon Press, New York, 1 edition, 1961.

[126] G. Audi, F.G. Kondev, M. Wang, B. Pfeiffer, X. Sun, J. Blachot, and M. MacCormick. The NUBASE2012 evaluation of nuclear properties. **Chinese Physics C**, 36(12): 1157, 2012.

[127] L.C. Northcliffe and R.F. Schilling. Range and stopping-power tables for heavy ions. **Atomic Data and Nuclear Data Tables**, 7(3):233–463, 1970.

[128] A.B. Brown, C.W. Snyder, W.A. Fowler, and C.C. Lauritsen. Excited States of the Mirror Nuclei, ^{7}Li and^{7}Be. **Physical Review**, 82(2):159, 1951.

[129] A. Sonzogni et al. Nudat 2. `http://www.nndc.bnl.gov/nudat2`, 05 2014.

[130] L. Corradi, G. Pollarolo, and S. Szilner. Multinucleon transfer processes in heavy-ion reactions. **Journal of Physics G: Nuclear and Particle Physics**, 36:113101–113143, 2009.

[131] D. Montanari. **Reaction dynamics of neutron rich nuclei in Ca isotopes with heavy ions and gamma spectroscopy**. PhD thesis, Universita degli Studi di Milano, 2009.

[132] A. Fritzler. TV - Programm zur Analyse von Spektren und Matrizen. `http://www.ikp.uni-koeln.de/src/`, 09 2011.

[133] S.W. Yates, E.M. Baum, E.A. Henry, L.G. Mann, N. Roy, A. Aprahamian, R.A. Meyer, and R. Estep. Nuclear structure of ^{200}Pt from in-beam conversion-electron and γ-ray spectroscopy. **Physical Review C**, 37(5):1889, 1988.

[134] J.J. Valiente-Dobón. **Studies of Neutron-Rich Nuclei Using Deep Inelastic Collisions**. PhD thesis, University of Surrey, 05 2007.

[135] I.N. Bronstein, K.A. Semendjajew, G. Grosche, V. Ziegler, and D. Ziegler. **Taschenbuch der Mathematik**. Verlag Harri Deutsch, Frankfurt am Main, 5 edition, 2001.

[136] P.E. Haustein, E.-M. Franz, R.F. Petry, and J.C. Hill. New neutron-rich isotope: ^{196}Os. **Physical Review C**, 16:1559–1565, Oct 1977.

[137] C.J. Chiara, R. Broda, W.B. Walters, R.V.F. Janssens, M. Albers, M. Alcorta, P.F. Bertone, M.P. Carpenter, C.R. Hoffman, T. Lauritsen, et al. Low-spin states and the non-observation of a proposed 2202-keV, 0^+ isomer in ^{68}Ni. **Physical Review C**, 86 (4):041304, 2012.

[138] J.J. Valiente-Dobón, C. Wheldon, P.H. Regan, C.Y. Wu, D. Cline, C. Andreoiu, R. Chapman, P. Fallon, S.J. Freeman, A. Hayes, et al. Population of ^{195}Os via a deep-inelastic reaction. In **AIP Conference Proceedings**, volume 726, page 249, 2004.

[139] M.W. Reed, P.M. Walker, I.J. Cullen, Y.A. Litvinov, D. Shubina, G.D. Dracoulis, K. Blaum, F. Bosch, C. Brandau, J.J. Carroll, et al. Long-lived isomers in neutron-rich Z= 72–76 nuclides. **Physical Review C**, 86(5):054321, 2012.

[140] D. Shubina, R.B. Cakirli, Y.A. Litvinov, K. Blaum, C. Brandau, F. Bosch, J.J. Carroll, R.F. Casten, D.M. Cullen, I.J. Cullen, et al. Schottky mass measurements of heavy neutron-rich nuclides in the element range $70 \leq Z \leq 79$ at the GSI Experimental Storage Ring. **Physical Review C**, 88(2):024310, 2013.

[141] A.I. Morales, J. Benlliure, M. Gorska, H. Grawe, S. Verma, P.H. Regan, Zs. Podolyák, S. Pietri, R. Kumar, E. Casarejos, et al. β-delayed γ-ray spectroscopy of ^{203,204}Au and $^{200-202}$Pt. **Physical Review C**, 88(1):014319, 2013.

[142] B. Singh. Adopted Levels, Gammas for ^{190}Pt. **Nuclear Data Sheets**, 99:275, 2003.

[143] C.M. Baglin. Adopted Levels, Gammas for ^{192}Pt. **Nuclear Data Sheets**, 113:1871, 2012.

[144] B. Singh. Adopted Levels, Gammas for ^{194}Pt. **Nuclear Data Sheets**, 107:1531, 2006.

[145] S.J. Steer, Zs. Podolyák, S. Pietri, M. Górska, P.H. Regan, D. Rudolph, E. Werner-Malento, A.B. Garnsworthy, R. Hoischen, J. Gerl, et al. Single-particle behavior at $N = 126$: Isomeric decays in neutron-rich ^{204}Pt. **Physical Review C**, 78:061302, 2008.

[146] A.N Wilson, C.W. Beausang, N. Amzal, D.E. Appelbe, S. Asztalos, P.A. Butler, R.M. Clark, P. Fallon, and A.O. Macchiavelli. High-spin states following multi-nucleon transfer. **The European Physical Journal A-Hadrons and Nuclei**, 9(2):183–189, 2000.

[147] J. Van Roosbroeck, H. De Witte, M. Gorska, M. Huyse, K. Kruglov, D. Pauwels, J.-Ch. Thomas, K. Van de Vel, P. Van Duppen, S. Franchoo, et al. Evolution of the nuclear structure approaching ^{78}Ni: β decay of $^{74-78}$Cu. **Physical Review C**, 71(5): 054307, 2005.

[148] J. Van de Walle, F. Aksouh, T. Behrens, V. Bildstein, A. Blazhev, J. Cederkäll, E. Clement, T.E. Cocolios, T. Davinson, P. Delahaye, et al. Low-energy Coulomb excitation of neutron-rich zinc isotopes. **Physical Review C**, 79(1):014309, 2009.

[149] C. Louchart, A. Obertelli, A. Görgen, W. Korten, D. Bazzacco, B. Birkenbach, B. Bruyneel, E. Clément, P.J. Coleman-Smith, L. Corradi, et al. Collective nature of low-lying excitations in ^{70,72,74}Zn from lifetime measurements using the AGATA spectrometer demonstrator. **Physical Review C**, 87(5):054302, 2013.

[150] T. Faul. **Etude de la Structure des Noyaux Riches en Neutrons autour du Noyau Doublement Magique ^{78}Ni**. PhD thesis, Institut Pluridisciplinaire Hubert Curien (IPHC), 12 2007.

[151] N. Patronis, H. De Witte, M. Gorska, M. Huyse, K. Kruglov, D. Pauwels, K. Van de Vel, P. Van Duppen, J. Van Roosbroeck, J.-C. Thomas, et al. β-decay study of ^{77}Cu. **Physical Review C**, 80(3):034307, 2009.

[152] J.M. Daugas, R. Grzywacz, M. Lewitowicz, L. Achouri, J.C. Angelique, D. Baiborodin, K. Bennaceur, R. Bentida, R. Béraud, C. Borcea, et al. The 8^+isomer in ^{78}Zn and the doubly magic character of ^{78}Ni . **Physics Letters B**, 476(3):213–218, 2000.

[153] J.A. Winger, S.V. Ilyushkin, A. Korgul, C.J. Gross, K.P. Rykaczewski, J.C. Batchelder, C. Goodin, R. Grzywacz, J.H. Hamilton, W. Krolas, et al. Decay Studies of Very Neutron Rich Nuclei Near ^{78}Ni. **Acta Physica Polonica B**, 39(2):525, 2008.

[154] T.A. Shibata, H. Nakayama, T. Numao, and T. Yamazaki. Lifetimes of the 7^- states in ^{186,188}Os. **Nuclear Physics A**, 312(1):115–120, 1978.

[155] V. Modamio, A. Jungclaus, Zs. Podolyák, Y. Shi, F.R. Xu, A. Algora, D. Bazzacco, D. Escrig, L.M. Fraile, S. Lenzi, et al. Identification of yrast high-K intrinsic states in ^{188}Os. **Physical Review C**, 79:024310, 2009.

[156] A. Pakkanen, P. Puumalainen, H. Helppi, and T. Komppa. Isomeric transition in ^{198}Au. **Nuclear Physics A**, 206, 1973.

[157] M. Bonitz. Evidence for a 130 ns isomeric state in ^{198}Au. **Nuclear Physics A**, 118 (2):478–480, 1968.

[158] K.E.G. Löbner, J. Klöckner, H. Schimmer, and P. Kienle. Level scheme of ^{198}Au from γ-γ-coincidence measurements. **Zeitschrift für Physik A Atoms and Nuclei**, 235 (3):254–262, 1970.

[159] J.C. Cunnane and P.J. Daly. New High-Spin Isomer 2.3-Day ^{198}Au^m and the ^{198}Au Level Structure. **Physical Review C**, 6(4):1407, 1972.

[160] J.A. Mirza, K.E.G. Löbner, D. Breitig, H.A. Baader, H.R. Koch, and O.W.B. Schult. The nuclear structure of ^{198}Au from the reaction Au^{197}(n, γ) Au^{198}. **Zeitschrift für Physik A Atoms and Nuclei**, 272(2):175–187, 1975.

[161] M.G. Slocombe, J.O. Newton, and G.D. Dracoulis. A study of states in ^{201,203}Tl using the (d, 3nγ) reaction: A new $9/2^-$ band. **Nuclear Physics A**, 275(1):166–188, 1977.

[162] J.C. Hill, D.G. Shirk, R.F. Petry, and K.H. Wang. ^{200}Pt - ^{200}Au decay chain. **Physical Review C**, 13(6):2484, 1976.

[163] R.B. Duffield and S.H. Vegors Jr. Five New Isomers with Half-Lives between 10^{-6} and 10^{-1} Second. **Physical Review**, 112(6), 1958.

[164] N. Fotiades, R.O. Nelson, M. Devlin, and J.A. Becker. New levels and a lifetime measurement in ^{202}Tl. **Physical Review C**, 76(1):014302, 2007.

[165] B. Singh. Adopted Levels, Gammas for ^{188}Os. **Nuclear Data Sheets**, 95:387, 2002.

[166] B. Singh. Adopted Levels, Gammas for ^{190}Os. **Nuclear Data Sheets**, 99:275, 2003.

[167] C. M. Baglin. Adopted Levels, Gammas for ^{192}Os. **Nuclear Data Sheets**, 113:1871, 2012.

[168] H. Geissel, Armbruster P., K.H. Behr, A. Brünle, K. Burkard, M. Chen, H. Folger, B. Franczak, H. Keller, O. Klepper, et al. The GSI projectile fragment separator (FRS): a versatile magnetic system for relativistic heavy ions. **Nuclear Instruments and Methods in Physics Research Section B: Beam Interactions with Materials and Atoms**, 70(1):286–297, 1992.

[169] P. Spiller and G. Franchetti. The FAIR accelerator project at GSI. **Nuclear Instruments and Methods in Physics Research Section A: Accelerators, Spectrometers, Detectors and Associated Equipment**, 561(2):305–309, 2006.

[170] H. Geissel, H. Weick, M. Winkler, G. Münzenberg, V. Chichkine, M. Yavor, T. Aumann, K.H. Behr, M. Böhmer, A. Brünle, et al. The Super-FRS project at GSI. **Nuclear Instruments and Methods in Physics Research Section B: Beam Interactions with Materials and Atoms**, 204:71–85, 2003.

[171] M. Thoennessen. Plans for the facility for rare isotope beams. **Nuclear Physics A**, 834(1):688c–693c, 2010.

[172] R.C. York, G. Bollen, C. Compton, A.C. Crawford, M. Doleans, T. Glasmacher, W. Hartung, F. Marti, J. Popielarski, J.J. Vincent, et al. FRIB: a new accelerator facility for the production of rare isotope beams. **SRF2009, Berlin, September**, 2009.

[173] N. Alkhomashi, P.H. Regan, Zs. Podolyák, S. Pietri, A.B. Garnsworthy, S.J. Steer, J. Benlliure, E. Caserejos, R.F. Casten, J. Gerl, et al. β^--delayed spectroscopy of neutron-rich tantalum nuclei: Shape evolution in neutron-rich tungsten isotopes. **Physical Review C**, 80(6):064308, 2009.

[174] P.J.R Mason, Zs. Podolyák, N. Mărginean, P.H. Regan, P.D. Stevenson, V. Werner, T. Alexander, A. Algora, T. Alharbi, M. Bowry, et al. Half-life of the yrast 2^+ state in ^{188}W: Evolution of deformation and collectivity in neutron-rich tungsten isotopes. **Physical Review C**, 88(4):044301, 2013.

[175] G.J. Lane, G.D. Dracoulis, F.G. Kondev, R.O. Hughes, H. Watanabe, A.P. Byrne, M.P. Carpenter, C.J. Chiara, P. Chowdhury, R.V.F. Janssens, et al. Structure of neutron-rich tungsten nuclei and evidence for a 10^- isomer in ^{190}W. **Physical Review C**, 82(5):051304, 2010.

List of Figures

List of Tables

Acknowledgements

A three year long PhD passes fast. And if I look back, it was amazing and I am still astonished how much I learnt during these years. First of all I have to thank Daniele Mengoni and José Javier Valiente Dobón. Without their invitation to visit Legnaro, I would not have taken the decision to apply for a PhD in Padova. They naturally became my supervisors, together with Prof. Santo Lunardi. I could not imagine better supervisors than they are. They guided my through my PhD and were all the time available, helped me whenever I needed help, encouraged me and created the best opportunities for my PhD. I can not count how many fruitful discussions we had on the nuclear physics. Maybe they were as many as the typos and mistakes in the first draft of this thesis.

I would like to especially thank all the people, who proof read in addition to my supervisors parts or the complete draft of the thesis: Tomás Raúl Rodríguez Frutos, Aila Gengelbach and Lorenzo Fortunato.

All the theoretical interpretation in this thesis is based on the sophisticated calculations from Tomás Raúl Rodríguez Frutos. I have to thank him for all his work and in addition specially for the discussions on nuclear theory.

The analysis of the *AGATA* data would not be possible without the great support of Dino Bazzacco, maybe the nicest teacher of the world. He not only helped me with the analysis, but also introduced me to the complex treatment of digital signals in software.

Special thanks also to Carl Wheldon and Andres Gadea, who all the time followed the analysis and gave many great suggestions.

I went many times to GANIL for experiments, workshops and meetings. I learnt plenty of things there, so I would like to thank all for the hospitality and the pleasant time: Emmanuel Clement, Gilles de France, Antoine Lemasson, Maurycy Rejmund, Navin Alahari and Christelle Schmitt.

I also have to thank Prof. Dr. Dr. h.c. Norbert Pietralla, Dr. Jörg Leske, Dr. Oliver Möller, Dr. Babak Alikhani for introducing me into the fabulous world of nuclear physics. I would also like to thank all the PhD students in Darmstadt for the discussions in many places over the world, especially Christian Stahl, Michael Reese, Marc Lettmann, Mirko von Schmid and Michael Thürauf.

A special gracias to Victor Modamio for being such a nice office mate, for all the dis-

cussions on physics and many other topics but especially for the coffee invitations. All the other colleagues in my office were making it a pleasant time with many fruitful discussions Eda Şahin, Andrea Gottardo, Michele Gelain, Laura Grassi, Francesco Recchia and Enrico Farnea.

The gamma groups in Padova and Legnaro were welcoming me and I have to thank all for the support, suggestions, nice discussions and company during experiments: Giacomo de Angelis, Daniel Napoli, Silvia Lenzi, Roberto Menegazzo, Calin Ur, Roberto Isocrate, Diego Barrientos and all the others.

The analysis of the data would not be possible without the help and discussions with many other people, so I would like to thank also in addition Daniele Montanari, Tea Mijatović, Andreas Vogt, Benedikt Birkenbach, Aila Gengelbach, Caterina Michelagnoli, Lorenzo Corradi, Enrico Fioretto, Alberto Stefanini and Suzanna Szilner.

I have to thank all the other students PhD students in Padova and Ferrara, including Rosanna Depalo, Davide Cester, Laura Moschini, Alberto Boso, Franco Galtarossa, Marco Siciliano and Michele Gelain; also the PhD (and Master) students from Milano and Florence, Simone Bottoni, Simone Ceruti, Agnese Giaz, Riccardo Avigo, Giovanni Bocchi, Luna Pellegri and Marco Rocchini for the time during lectures, schools, experiments and conferences.

The Legnaro group of young people was amazing and grazie a tutti: Liliana, Oscar, Andrea, Olga, Daniel, Vlada, Mauri, Gabriele, Grześ, Tayfun, Bart, Alberto and many more

Besides all the nice people in Padova or Legnaro, I would like to thank also all the people, who made my stay at Padova unique. I know, that I forgot many, so thank you Chiara, Giada, Ian, Paola, Carmen, Steffi, Antonio, Emilia, Natalia, Diego, Teresa, Kayla, Niki, Fede, Luigi, Mateo, Argelia, Dijana, Marco, Nunzio, Domenico, Akos, Sandra, Marta, Aljona, Andrea, Vanessa, Elona, Patrizia, Angela, Elena, Simone, Djordja, ...
I have to say a big teşekkür ederim to the Turkish crew with Fatih (its life just try), Ekrem, Yeliz, Demet, Hülya, Canan, Oğuz, Bahar, Müge and Ileyna. You have brought me some Turkey back.

Vielen Dank auch an meine Familie und Freunde in Deutschland für die Unterstützung und Aufmunterungen.

And at the very end, I want to express my grateful thanks to all the anonymous people who actively convinced me in these 3 years to buy 5 new bicycles, 2 new Computers, 1 backpack and 2 new cellphones. And how could I forget to thank SITA for their splendid bus service, including the nice walking opportunities at the late evening? And at the very end, I want to thank you, for reading the whole thesis to the very end.